UNIVERSIDADE ESTADUAL DE CAMPINAS
Instituto de Geociências

PAOLA DE MELO SILVA

# EVOLUÇÃO GEODINÂMICA DO COMPLEXO DIVINÓPOLIS, SUL DO CRÁTON SÃO FRANCISCO

CAMPINAS
2020

PAOLA DE MELO SILVA

# EVOLUÇÃO GEODINÂMICA DO COMPLEXO DIVINÓPOLIS, SUL DO CRÁTON SÃO FRANCISCO

TESE APRESENTADA AO INSTITUTO DE GEOCIÊNCIAS DA UNIVERSIDADE ESTADUAL DE CAMPINAS PARA OBTENÇÃO DO TÍTULO DE DOUTORA EM CIÊNCIAS NA ÁREA DE GEOLOGIA E RECURSOS NATURAIS

ORIENTADOR: PROF. DR. WAGNER DA SILVA AMARAL

COORIENTADOR: PROF. DR. ELSON PAIVA DE OLIVEIRA

ESTE EXEMPLAR CORRESPONDE À VERSÃO FINAL DA TESE DEFENDIDA PELOA ALUNA PAOLA DE MELO SILVA E ORIENTADA PELO PROF. DR. WAGNER DA SILVA AMARAL

CAMPINAS

2020

Ficha catalográfica
Universidade Estadual de Campinas
Biblioteca do Instituto de Geociências
Cássia Raquel da Silva - CRB 8/5752

Silva, Paola de Melo, 1991-
Si38e Evolução geodinâmica do Complexo Divinópolis, sul do Cráton São Francisco / Paola de Melo Silva. – Campinas, SP : [s.n.], 2020.

Orientador: Wagner da Silva Amaral.
Coorientador: Elson Paiva de Oliveira.
Tese (doutorado) – Universidade Estadual de Campinas, Instituto de Geociências.

1. Crátons. 2. Geodinâmica. 3. Geocronologia. 4. Geoquímica. 5. Granito. I. Amaral, Wagner da Silva, 1979-. II. Oliveira, Elson Paiva de, 1947-. III. Universidade Estadual de Campinas. Instituto de Geociências. IV. Título.

Informações para Biblioteca Digital

**Título em outro idioma:** Geodynamic evolution of Divinópolis Complex, southern São Francisco Craton
**Palavras-chave em inglês:**
Cratons
Geodynamics
Geochronology
Geochemistry
Granite
**Área de concentração:** Geologia e Recursos Naturais
**Titulação:** Doutora em Ciências
**Banca examinadora:**
Wagner da Silva Amaral [Orientador]
Ticiano José Saraiva dos Santos
Valdecir de Assis Janasi
Vinícius Tieppo Meira
Luana Moreira Florisbal
**Data de defesa:** 24-11-2020
**Programa de Pós-Graduação:** Geociências

**Identificação e informações acadêmicas do(a) aluno(a)**

- ORCID do autor: https://orcid.org/0000-0001-9533-9637

- Currículo Lattes do autor: http://lattes.cnpq.br/141412146216400

**UNIVERSIDADE ESTADUAL DE CAMPINAS**
**INSTITUTO DE GEOCIÊNCIAS**

**AUTORA:** PAOLA DE MELO SILVA

# EVOLUÇÃO GEODINÂMICA DO COMPLEXO DIVINÓPOLIS, SUL DO CRÁTON SÃO FRANCISCO

# GEODYNAMIC EVOLUTION OF DIVINÓPOLIS COMPLEX, SOUTHERN SÃO FRANCISCO CRATON

**ORIENTADOR:** PROF. DR. WAGNER DA SILVA AMARAL
**COORIENTADOR:** PROF. DR. ELSON PAIVA DE OLIVEIRA

Aprovada em: 24/11/2020

**EXAMINADORES:**

Prof. Dr. Wagner da Silva Amaral – Presidente

Prof. Dr. Valdecir de Assis Janasi

Profa. Dra. Luana Moreira Florisbal

Prof. Dr. Ticiano José Saraiva dos Santos

Prof. Dr. Vinícius Tieppo Meira

*A Ata de Defesa assinada pelos membros da Comissão Examinadora consta no processo de vida acadêmica do aluno.*

Campinas, 24 de novembro de 2020.

## SÚMULA CURRÍCULAR

Graduada em geologia pela Universidade Federal de Mato Grosso (2009–2014), realizou seu Trabalho de Conclusão de Curso na porção leste da Província Aurífera de Alta Floresta (PAAF), norte de Mato Grosso, estudando os diques máficos da região de Peixoto de Azevedo.

Mestre em Geociências pela UNICAMP (2014 – 2016), desenvolveu sua dissertação na região de Pitangui (MG), conhecida pela exploração de ouro. Publicou dois artigos nessa linha de pesquisa, sendo o primeiro na *Lithos* (2017), apresentando dados de geoquímica acerca das rochas máficas do Greenstone belt Pitangui e implicações petrogenéticas. O segundo artigo foi publicado na *Journal of South American Earth Sciences* (2020) e apresenta dados geocronológicos e de proveniência sedimentar.

Doutora pelo Programa de Geociências da UNICAMP (2016–2020), foi professora temporária no curso de Geologia da Universidade Federal do Oeste da Bahia (UFOB) entre 2019 e 2020. Durante o período do doutorado e mestrado publicou resumos nos principais congressos do Brasil. Tem experiência no mapeamento de terrenos Arqueanos (Greenstone-TTG) e na linha de pesquisa de evolução crustal, integrando dados petrológicos, geoquímicos e datação U-Pb.

**" Você deve entender que há mais de um caminho para o topo da montanha."**

*Miyamoto Musashi*

Novamente dedico este trabalho aos meus pais,

que desde cedo me ensinaram a importância da educação.

## AGRADECIMENTOS

CAPES: "O presente trabalho foi realizado com apoio da Coordenação de Aperfeiçoamento de Pessoal de Nível Superior – Brasil (CAPES) - Código de Financiamento 001".

FAPESP: "O presente trabalho foi realizado com apoio da Fundação de Amparo à Pesquisa do Estado de São Paulo (FAPESP), processo nº 12/15824-6".

Agradeço meus orientadores, Prof. Wagner e Prof. Elson pelos ensinamentos e terem me acolhido desde o mestrado, quando eu mal sabia o que me esperava. Aos professores que avaliaram este trabalho: Ticiano e Jefferson, e ao pesquisador Cauê Cioffi (USP). A equipe do Instituto de Geociências da Unicamp, professores, técnicos e funcionários.

Ao Prof. Antonio García Casco por ter me recebido em Granada e pelas discussões, fundamentais nessa trajetória. Ao Programa Santander pelo período de mobilidade internacional com a parceria Brasil/Países Ibero-americanos.

Agradeço a minha família, que mesmo distantes, estão sempre comigo. Aos meus pais Consuelo e Cirus, por todo incentivo, meus irmãos Nicholas e Mirela. Catarina, por todos os anos de apoio!

Ao geólogo Marcelo Galé, companheiro de aventuras, geologia e o que der e vier! O caminho fica mais fácil sendo divido. Até que deu tudo certo!

Agradeço a todos os amigos e colegas do IG-Unicamp. Ao João Motta, pela amizade e pela integração dos dados geofísicos, essenciais para o desenvolvimento dessa tese. Aos amigos que dividiram a antiga salinha 14, Alice, Raisa, Verônica, Emanuel e Thais, pela amizade e pausas para o café. Aos amigos Isis, Igor, João Paulo, Felipe, Jéssica Mendes e Mariana Canevari, que também partilham da solitária jornada do cientista brasileiro. A Thais Murer pela parceria no Divinópolis que rendeu um TCC!

As meninas da rep Clã do Cangaço (versão 4.0) por tantas vezes terem me acolhido com alegria nessas idas e vindas da vida nômade. Aline, Alcione, Mayara, muito obrigada!

Aos amigos de Cuiabá, que mesmo longe (Karina B., Junior, Jovana, Karina K.) contribuem com incentivo e um pouco de sanidade mental!

Aos amigos e professores da Universidade de Granada que me receberam tão bem durante a curta e turbulenta estadia: José Maria, Nuria, Irene, Fabian. Gostaria de poder ter voltado!

Não caberiam todos aqui, mas diversas pessoas foram essenciais para a conclusão dessa pesquisa, afinal, "*nenhum homem é uma ilha*". Meu muito obrigado!

## RESUMO

O sul do Cráton do São Francisco é composto por uma variedade de complexos metamórfico-ígneos com afinidade cálcio-alcalina ou TTG, bordejado por greenstone belts, também arqueanos. O Complexo Divinópolis compreende um desses terrenos TTG-greenstone. Com o objetivo de desvendar a evolução geodinâmica deste complexo foram realizados estudos de campo, petrográficos, geoquímicos e geocronológicos dos gnaisses e granitoides félsicos. A suíte TTG caracteriza tonalitos, trondjhemitos e granodioritos peraluminosos, magnesianos e semelhantes a TTGs de baixa pressão. Esta suíte ocorre associada a uma suíte potássica (trondjhemitos e granodioritos) magnesiana a ferrosa e peraluminosa. Enquanto os TTGs podem ter se formado por fusão de uma crosta basáltica sem quantidades expressivas de granada (1000–850º C a 12 kbar), a suíte potássica provavelmente se formou por processos de assimilação crustal dos TTGs preexistentes (850–750º C a 12 kbar). As idades U-Pb em zircão corroboram esses dados, visto que a suíte TTG apresenta idades mais antigas de 2787 ± 9, 2779 ± 42 e 2782 ±6 Ma, enquanto a suíte potássica varia de 2731 ± 18 Ma, 2729 ± 31 Ma e 2673 ± 31 Ma. Ambas as suítes são intrudidas por granitos tardios divididos em médio a alto potássio. Os granitos de médio-K (granodioritos e monzogranitos) são peraluminosos e mais deformados, possuindo características similares as suítes TTGs e potássicas e se aproximando de monzogranitos Arqueanos do tipo I. Os granitos de alto-K (sienogranitos), por outro lado, são ferrosos e metaluminosos, não deformados, com assinatura mais próximas do tipo A. Integrando-se os dados do Complexo Divinópolis e as demais unidades Arquenas do sul do cráton São Francisco, um modelo geodinâmico é proposto. Processos de delaminação de litosfera basáltica causados por episódios de ascensão mantélica gerariam os primeiros TTGs de baixa pressão entre 2915–2860 Ma, formando os primeiros microcontinentes. Entre 2790 e 2770 Ma uma segunda geração de TTGs reflete mudanças na tectônica devido ao rápido crescimento de crosta que resultaria no imbricamento entre microcontinentes e crosta oceânica, eventualmente iniciando processos similares a subducção, além de colisão e acreção. Entre 2760 e 2715 Ma a produção de rochas potássicas predomina e seu retrabalhamento na crosta inferior geraria principalmente os monzogranitos de médio-K. Este período demarca bem o início de um evento colisional que se seguiu após o período de colagem. A partir de 2760 Ma, a crosta passa a perder calor e iniciam-se processos de extensão crustal, gerando os últimos pulsos graníticos pós-colisionais (granitos de alto-K) até 2610 Ma. Após 2,6 Ga o cráton passa por um período de estabilidade, sendo novamente reativado entre 2,1–1,9 Ga durante a colagem do Supercontinente Nuna/Columbia. Uma idade metamórfica foi obtida por monazita em 2062 ± 7 Ma em um leocossoma do Complexo Divinópolis, concordando com datações em monazita e titanita na região entre 2100 e 2050 Ma. O colapso do Orógeno Minas reativaria estruturas antigas e aqueceria o embasamento o suficiente para gerar monazita e titanita no núcleo dos microcontinentes mostrando que o metamorfismo sin-colisional foi regional e significativo.



**Palavras-chave:** Geodinâmica; retrabalhamento crustal; granitoides Arqueanos.

## ABSTRACT

The southern São Francisco Craton (3.2-2.6 Ga) - eastern Brazil - is composed of a variety of metamorphic-igneous complexes with TTG affinity, bordered by Archean greenstone belts. The Divinópolis Complex comprises one of these TTG-greenstone complexes. In order to unveil the geodynamic evolution of this complex, field, petrographic, geochemical and geochronological studies of the felsic granitoids were carried out. The TTG suite comprises peraluminous and magnesian tonalites, trondjhemites e granodiorites similar to low pressure TTGs. An associated potassic suite comprises magnesian to ferrous and peraluminous trondjhemites and granodiorites.While the TTGs may have been formed by partial melting of a basaltic crust without significant amount of garnet (1000-850º C at 12 kbar), the potassic suite may have formed by processes of crustal assimilation, including the pre-existing TTGs (850-750º C at 12 kbar). The U-Pb ages in zircon corroborate these data, where tonalites and trondjhemites of the TTG suite are older ( 2787 ± 9, 2779 ± 42 and 2782 ± 6 Ma), while the granodiorites of the potassic suite vary from 2731 ± 18 Ma, 2729 ± 31 Ma and 2673 ± 31 Ma. Both suites are intruded by late granites with medium to high potassic composition. Medium-K granites (granodiorites and monzogranites) are peraluminous and deformed. These granites have characteristics similar to TTGs, approaching Archean I-type monzogranites. High-K granites (syenogranites), on the other hand, are ferrous and metaluminous, non-deformed, and exhibiting A-type like signature. A geodynamic model is proposed for the southern São Francisco Craton, integrating the data from Divinópolis Complex. Delaminated basaltic lithosfere caused by episodes of mantle upwelling would generate the first low pressure TTGs between 2915–2860 Ma, forming the first microcontinents. Between 2790 and 2770 Ma a second generation of TTGs reflect change in the tectonic style due to the rapid development of new crust. This growth would result in the overlapping of microcontinents and oceanic crust, eventually initiating horizontal tectonics similar to subduction, in addition to collision and accretion. Between 2760 and 2715 Ma the production of potassic rocks predominates by reworking of the crust, forming the majority of the medium-K monzogranites. This period marks the beginning of a collision event that followed after microcontinent accretion. After 2760 Ma, the crust loses heat and a crustal extension processes begin during this post-collisional period, generating the last granitic pulses (high-K granites) at 2610 Ma. After 2.6 Ga the craton undergoes a period of stability, reactivated again between 2.1–1.9 Ga during the assemble of the Nuna/Columbia Supercontinent. A monazite from a leucosome is the only metamorphic age obtained for the Divinópolis crust so far, at 2062 ± 7 Ma. This shows that neosome crystallization occurred as a consequence of the Minas Orogeny, reactivating Archean structures and heating the basement enough to reset monazite and titanite in the microcontinent nucleus. This syn-collisional metamorphism and accretionary episode was widespread and significant in the southern São Francisco Craton.



**Keywords:** Geodynamics; crustal reworking; Archean granitoids.

# LISTA DE FIGURAS



## ANEXO 01

**ANEXO 02**

## LISTA DE TABELAS

### ANEXO 01



### ANEXO 02



### APÊNDICE A



### APÊNDICE B

**SUMÁRIO**

# 1. INTRODUÇÃO

## 1.1 – Introdução ao tema e relevância da proposta

O registro Arqueano (4,0–2,5 Ga) na Terra corresponde a um terço da história geológica do planeta e encontra-se preservado em terrenos cratônicos. Grande parte da crosta juvenil do nosso planeta foi formada durante este período (Rudnick & Gao, 2004), composta dominantemente por uma associação entre rochas máficas e ultramáficas, representada pelos *greenstone belts*, *e* complexos da série tonalito–trondhjemito–granidiorito (TTG). Porém, essa crosta antiga passou por múltiplos processos de retrabalhamento, deformação e tectonismo, descaracterizando suas feições primárias e, consequentemente, dificultando a interpretação dos processos genéticos das mesmas. Visto que uma porção da crosta foi retrabalhada e/ou consumida, parte do quebra-cabeça foi perdida. Outro desafio enfrentado no estudo de províncias Arqueanas se refere as condições tectônicas operantes, visto que os processos atuantes eram distintos e geraram associações petrogenéticas distintas em relação ao Fanerozoico. Um dos principais exemplos corresponde à série dos TTGs (Jahn et al., 1981), que representa uma quota significativa do Arqueano e compreende rochas sódicas pobres em potássio que se tornaram os primeiros embriões de crosta continental em um planeta até então dominado por crosta máfica (Martin et al., 2005; Moyen e Martin 2012; Dhuime et al., 2015).

Embora haja controvérsias, é amplamente aceito que a química dos TTGs requer uma fonte máfica pobre em potássio e sílica, onde um certo grau de hidratação é necessário para admitir que fusão parcial em alta pressão gere rochas félsicas (Rapp et al., 1995; Foley et al., 2002; Moyen, 2011). Diversos autores sugerem que essa fonte máfica seja toleiítica, densa e com alto conteúdo de MgO (e.g. Johnson et al., 2014; Hoffmann et al., 2019), gerada em um regime termal mais quente e distinto do atual devido ao calor resultante da acreção planetária e maior abundância de elementos radioativos (Bickle, 1986). Já no final do Arqueano (2,75–2,55 Ga), o expressivo surgimento de granitoides com assinatura de alto potássio – em contraste aos TTGs sódicos – marca a diferenciação progressiva do planeta para como o conhecemos hoje, com placas tectônicas e rochas félsicas diversificadas caracterizando continentes estáveis (e.g. Polat, 2012; Condie & Kröner, 2013; Turner et al., 2014; Moyen & Laurent, 2018).

O período exato dessa transição, no entanto, é tema de grande debate, assim como o ambiente de formação das rochas que compõem os crátons Arqueanos. Essa teorização resultou em duas principais vertentes científicas para a origem dessas rochas: uma uniformitarista, onde atuariam processos primitivos/distintos de subducção, com evidências de limites entre placas (e.g. Martin, 1994; Foley et al., 2002; de Wit, 2004; Furnes et al., 2014) e outra vertente que defende processos predominantemente

gravitacionais, portanto verticais, como plumas mantélicas e fusão parcial de espessos platôs máficos primitivos (Hamilton, 2011; Johnson et al., 2017; Bédard, 2018; Wyman, 2018). Trabalhos mais recentes têm sugerido uma abordagem dinâmica que engloba a atuação tanto de forças verticais quanto horizontais. Nestes modelos numéricos duais, uma variedade de ambientes tectônicos pode ter se formado na Terra primitiva devido a grande diferença no seu regime termal: delaminação de crosta máfica causado por convecção e/ou plumas mantélicas associados a episódios de subducção causados por impactos de meteoros e/ou colisão–acreção horizontal de crosta (e.g. Johnson et al., 2014; Sizova et al., 2015; Bédard, 2018; Moyen & Laurent, 2018; O'Neill & Zhang., 2019).

Tendo em vista este cenário, o estudo de terrenos *greenstone-TTG* é essencial para contribuir com o desenvolvimento do conhecimento sobre os estágios de evolução e formação da crosta terrestre e propor modelos para ambientes tectônicos primitivos. Os crátons *Pilbara, Western Australia, North Atlantic, Kaapvaal e Zimbabwe* estão entre os melhores terrenos ancestrais preservados, com rochas de idades entre 3,6–2,7 Ga. No Brasil, a crosta siálica do Cráton do São Francisco (Almeida, 1977) remonta a idades tão antigas quanto 3,5 Ga (Oliveira et al., 2020) até 2,6 Ga (Farina et al., 2015) (Figura 1.1), compreendendo uma das áreas de maior exposição de afloramentos ancestrais da Plataforma Sul Americana. Apenas recentemente a natureza geoquímica desses TTGs do sul do cráton começou a ser investigada (Farina et al., 2015; Simon et al., 2018). O Complexo Divinópolis é um desses terrenos Arqueanos margeado por *greenstone belt* e o tema de estudo desta tese, inserido na porção sul do Cráton do São Francisco (Figura 1.2). O propósito deste trabalho é caracterizar a evolução geodinâmica-crustal do Complexo Divinópolis no contexto regional do sul do cráton a partir da integração de dados geofísicos, petroquímicos e geocronológicos – desde sua natureza geoquímica e afinidade TTG, condições de pressão-temperatura, e idades de cristalização e metamorfismo. Buscando-se entender a gênese do magma e metamorfismo, um modelo geodinâmico dual é proposto para a formação da crosta Arqueana nesta região, onde atuariam tanto processos de delaminação por inversões de densidade anteriormente a 2,8 Ga, quanto episódios de colisão e inícios de proto-subducção, entre 2,7 e 2,6 Ga.

## 1.2 – Contexto geológico

A Plataforma Sul Americana é constituída essencialmente por núcleos cratônicos rodeados por faixas móveis e recoberta por bacias sedimentares (Alkmin & Noce, 2006). O Cráton do São Francisco (Figura 1.1) localiza-se na porção leste-central do Brasil e abrange em maior parte os estados de Minas Gerais e Bahia, sendo bordejado por cinturões móveis Brasilianos (e.g. Faixas Brasília, Rio Preto, Sergipana, Araçuaí e Ribeira) e recoberto por rochas sedimentares Proterozoicas a Fanerozoicas. Os núcleos arqueanos ocorrem tanto na porção norte (estado da Bahia) quanto sul (estado de Minas Gerais)

do cráton, tendo sido afetados por processos tectonomagmáticos Proterozoicos (Almeida, 1977; Teixeira et al., 1996; Machado & Carneiro, 1992; Alkmim, 2004). O núcleo Arqueano norte do cráton é segmentado nos blocos Gavião, Serrinha e Jequié, retrabalhados por eventos de metamorfismo entre 2,7 e 2.6 Ga (Santos-Pinto et al., 2012) e separados por zonas de suturas de ~2.1 Ga (Teixeira & Figueiredo, 1991; Barbosa & Sabaté, 2004; Aguilar et al., 2017). O Bloco Gavião apresenta as idades félsicas juvenis mais antigas de todo o cráton (3,6–3.2 – Nutman & Cordani, 1993; Dantas et al., 2013; Oliveira et al., 2020). Já o núcleo Arqueano sul tem idades de formação de crosta félsica relativamente mais jovens (3,2–2,6), sendo que o Complexo Santa Bárbara registra os núcleos mais antigos. O período de desenvolvimento crustal nessa porção foi dividido em quatro eventos magmáticos principais: (*i*) Santa Bárbara (3,22 – 3,20 Ga), (*ii*) Rio das Velhas I (2,92-2,85), (*iii*) Rio das Velhas II (2,85 – 2,76 Ga) e (*iv*) Mamona (2,76 – 2,61 Ga), sendo que os dois primeiros estão associados a geração de crosta TTG e *greenstone belts* (Teixeira et al., 1998; Noce et al., 2005; Lana et al. 2013; Farina et al., 2016), enquanto os dois últimos – de maior expressão – são responsáveis por formação de *greenstone belts* e granitoides potássicos.

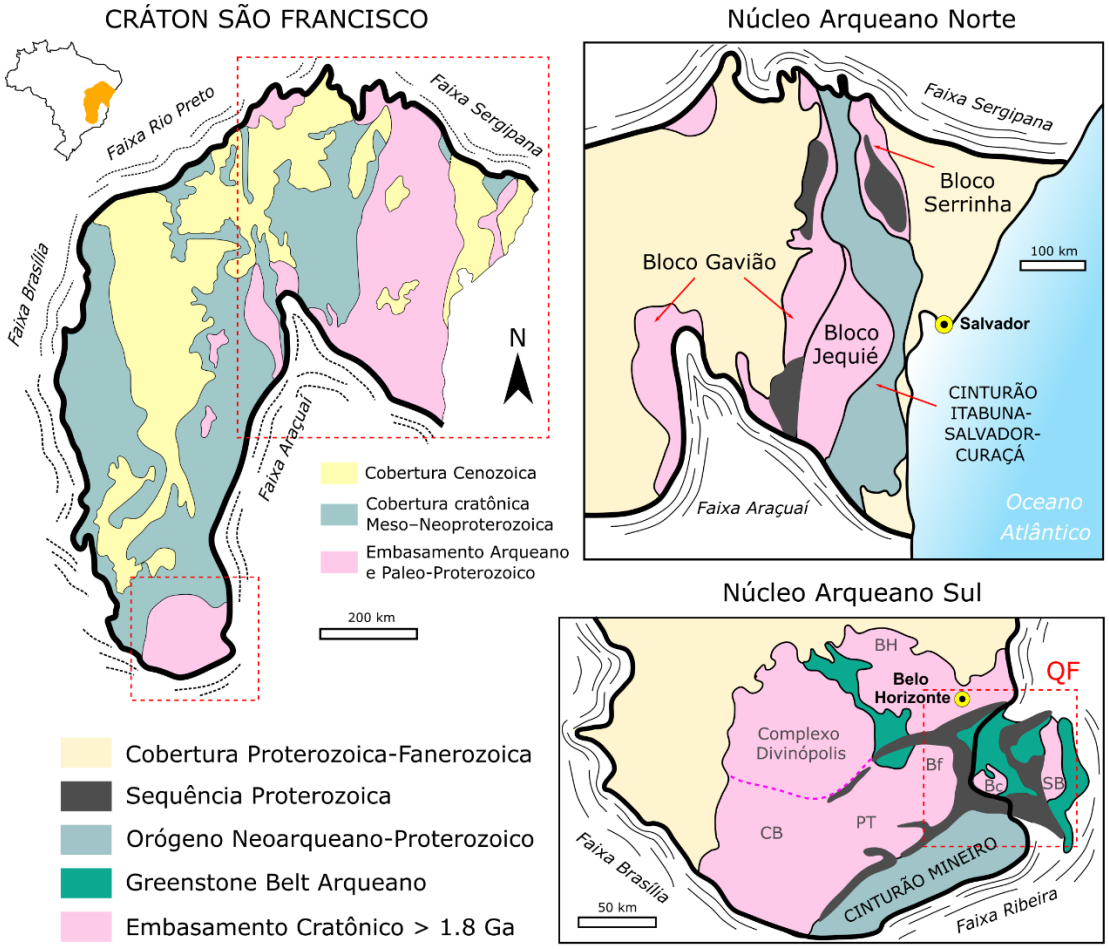


**Figura 1.1:** Mapa geológico do Cráton do São Francisco evidenciando-se os núcleos Arqueanos norte e sul (adaptado de Alkmin & Noce, 2006; Teixeira et al., 2017a). **CB**: Complexo Campo Belo, **PT**: Complexo Passa Tempo, **Bf**: Complexo Bonfim, **BH**: Complexo Belo Horizonte, **Bc**: Complexo Bação, **SB**: Complexo Santa Bárbara, **QF**: Quadrilátero Ferrífero.

### *1.2.1 – Geologia do sul do Cráton do São Francisco*

O sul do Cráton do São Francisco (Figura 1.2) pode ser dividido em quatro unidades principais, sendo estas: (*i*) o embasamento cratônico, formado por gnaisses Meso-Neoarqueanos (TTGs ou não); margeados por (*ii*) sequências metavulcanossedimentares Neorqueanas do tipo *greenstone belt* (Rio das Velhas e Pitangui); ambos intrudidos por (*iii*) granitoides Neoarqueanos; e sobrepostos por (*iv*) sequências metassedimentares Proterozoicas dos supergrupos Minas, Espinhaço e grupos Itacolomi e Bambuí (Dorr, 1969; Teixeira et al., 1998; Carneiro et al., 1998; Lobato et al., 2001; Baltazar & Zucchetti, 2007; Lana et al., 2013; Romano et al., 2013). O Cinturão Mineiro corresponde a borda mais meridional do cráton e representa um orógeno (2.6–2.0 Ga) que se formou como resultado da colisão dos núcleos cratônicos São Francisco–Congo durante o fechamento da Bacia Minas entre 2,1 e 2,0 Ga, sendo composto por rochas plutônicas e metassedimentares polideformadas e de alto grau, remanescentes de *greenstone belts* (e.g. Barbacena) e granitoides diversos (Dorr, 1969; Alkmim & Marshak, 1998; Alkmim & Teixeira, 2017; Aguilar et al., 2017).

A região sul do cráton é conhecida por sua importância metalogenética, com depósitos de ouro e ferro em escala global e bauxita e manganês hospedados em rochas máficas Arqueanas dos *greenstone belts* Rio das Velhas e Pitangui e nas sequências Paleoproterozoicas de Itabirito (Formações Ferríferas Bandadas do tipo *Lake Superior*) do Supergrupo Minas (Throman et al. 1986, Lobato et al. 2001). A configuração espacial das sequencias de Itabirito levou a denominação deste distrito metalogenético de Quadrilátero Ferrífero (Figura 1.1) e compreende geograficamente a região do *greenstone belt* Rio das Velhas; complexos Belo Horizonte, Bação, Bonfim, Santa Bárbara; e Supergrupo Minas. A região a oeste do Quadrilátero Ferrífero abarca o *greenstone belt* de Pitangui e o embasamento siálico é representado pelos complexos Divinópolis, Campo Belo e Passa Tempo.

O embasamento siálico compreende complexos ígneo-metamórficos com estruturação dômica (Divinópolis, Belo Horizonte, Campo Belo, Bonfim e complexos menores como Bação, Santa Bárbara e Passa Tempo) predominantemente formados por gnaisses sódicos com características de suítes TTGs, intrudidos por granitoides de ampla distribuição e predominantemente potássicos, não deformados ou menos deformados em relação aos gnaisses (Machado & Carneiro, 1992; Noce et al., 1998; Campos et al., 2003; Lana et al., 2013; Romano et al., 2013; Farina et al., 2016). Esses granitoides (desde diques a batólitos) são associados a distintos eventos de granitogênese Neoarqueanos. A geração mais antiga apresenta assinatura de médio potássio com idades em 2780–2760 Ma (U–Pb em zircão) e as gerações mais jovens são anorogênicas e de alto potássio, datadas em 2720–2700 Ma e 2600 Ma. A fusão de TTGs mais antigos e rochas máficas, com a adição de rochas metassedimentares dos *greenstone belts* pode ter gerado a assinatura de alto potássio nas unidades mais jovens (Lana et al., 2013; Romano et al., 2013; Farina et al., 2015; Moreno et al., 2017).

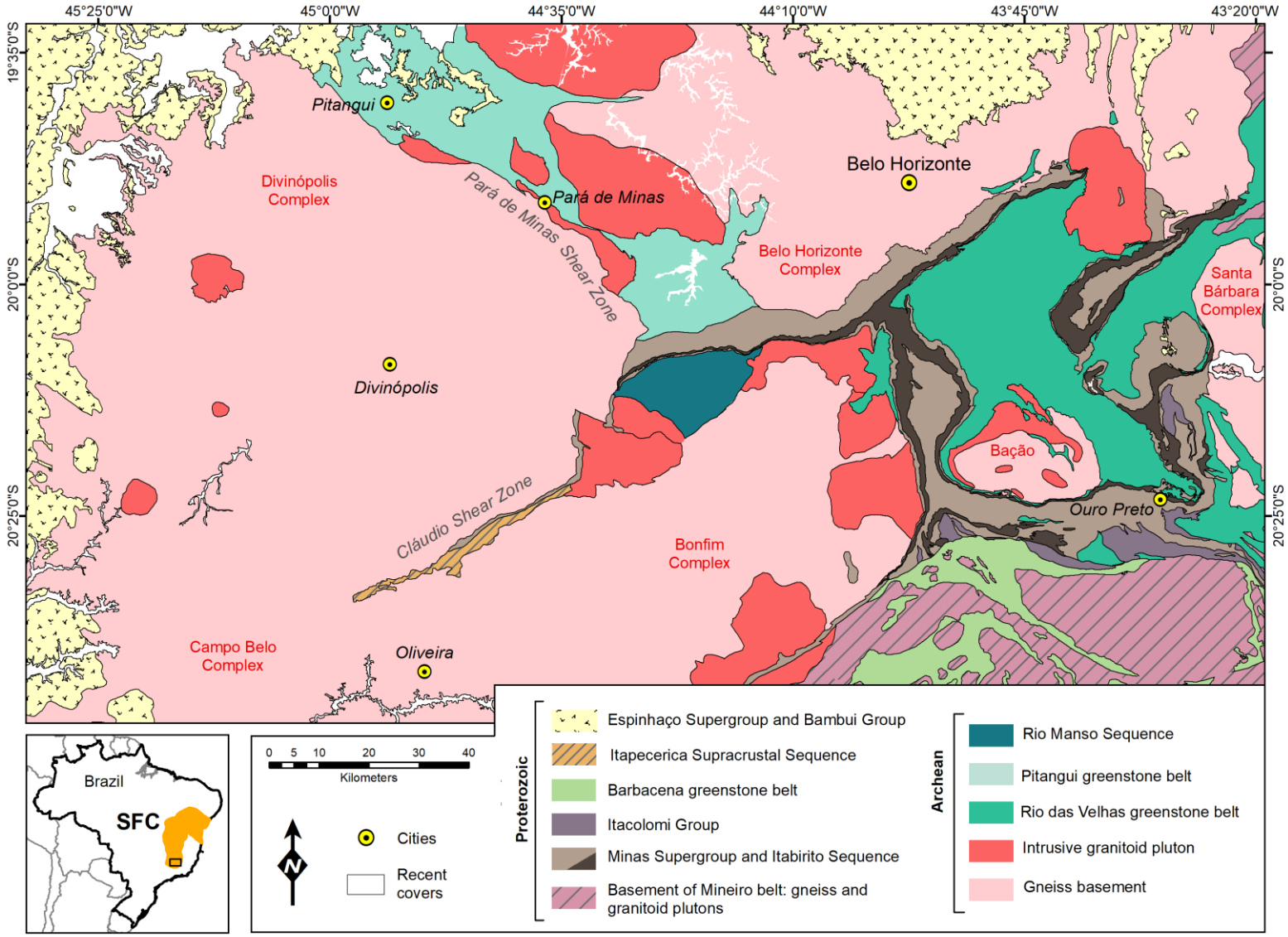


**Figura 1.2:** Mapa geológico da porção sul do Cráton do São Francisco (modificado de Pinto & Silva, 2014). Abaixo, a esquerda: mapa de localização do Cráton do São Francisco (SFC) no Brasil.

O *greenstone belt* Rio das Velhas compreende uma sequência de bacia oceânica, onde sua parte mais basal é composta por rochas vulcânicas máficas (incluindo komatiitos) e lentes de rochas ultramáficas que gradam para turbiditos e rochas metassedimentares clásticas e químicas (BIFs e *cherts*) em direção ao topo, formando o Grupo Nova Lima. O Grupo Maquiné sobrepõe o Nova Lima e representa uma associação fluvial marinha, composta por pelitos, quartzitos, grauvacas e conglomerados (Shorscher, 1978; Lobato et al., 2001a; Baltazar & Zucchetti, 2007). O *greenstone belt* Pitangui, por outro lado, representa um retro arco alongado com direção preferencial NW-SE, com uma unidade basal metavulcânica máfica-ultramáfica com lentes de BIFs e níveis de metapelitos que se torna predominantemente metassedimentar em direção ao topo (pelitos, grauvacas e arenitos), com metabasaltos associados (Romano 2007; Brando Soares et al., 2017; Fabricio-Silva et al., 2018; Melo-Silva et al., 2020). Apenas recentemente os *greenstone belts* Pitangui e Rio das Velhas têm sido abordados como unidades distintas (Melo-Silva et al., 2020; Brando Soares et al., 2020), tendo sido frequentemente correlatos na literatura (e.g. Alkmim & Noce, 2006; Romano, 2007; Romano et al., 2013; Pinto & Silva, 2014).

### *1.2.2 – Geologia do Complexo Divinópolis*

Os gnaisses cinzas e granitoides potássicos do Quadrilátero Ferrífero são consideravelmente mais estudados em relação aos complexos Passa Tempo, Campo Belo e Divinópolis, localizados a oeste do Quadrilátero Ferrífero. O Complexo Divinópolis, objeto de estudo desta tese, é um dos terrenos com menos informação e em trabalhos mais antigos é descrito como parte do Complexo Campo Belo ou separado em Campo Belo norte (Machado Filho et al. 1983; Teixeira et al., 1996; Teixeira et al., 1998; Fernandes & Carneiro, 2000), evidenciando lacunas em sua delimitação e abrangência. Apenas recentemente o Complexo Divinópolis passou a ser incluído como parte da crosta Arqueana do sul do cráton São Francisco (Albert et al., 2016; Farina et al., 2016, Teixeira et al., 2017a).

Estudos mais detalhados se restringem a sua borda mais meridional em contato com o Complexo Campo Belo (Oliveira, 2004; Carvalho *et al*., 2016; 2017a; Teixeira *et al*., 2017b) e a mapeamentos regionais realizados pela CPRM em seus extremos norte e sul, que visavam detalhamento do *greenstone belt* Pitangui e do Complexo Campo Belo (Romano, 2007; Carneiro et al., 2007). Romano (2007) dividiu os gnaisses do setor norte do complexo Divinópolis em uma unidade milonítica e uma migmatítica, sendo que o primeiro possui fraco caráter milonítico e ocorre em contato direto com o *greenstone belt* Pitangui, cuja foliação segue a direção preferencial do *greenstone* (NW–SE). O contato com o gnaisse migmatítico que ocorre mais ao centro do complexo não é nítido, evidenciando que as bordas foram mais afetadas por cisalhamento e milonitização (Melo-Silva et al., 2020). Uma datação direta foi realizada no setor norte do complexo, em contato com o *greenstone belt* Pitangui, obtendo-se uma

idade de 2878.5 ± 5.7 Ma (Melo-Silva et al., 2020). Essa porção norte do complexo engloba rochas leucocráticas com granulação grossa de composição granodiorítica a diorítica, e localmente porfiríticas, formando augen gnaisses com cristais de plagioclásio orientados (Romano, 2007; Melo-Silva et al., 2020). Assim sendo, o Complexo Divinópolis não possui correlação com dados de outros terrenos contíguos ou com a proposta de acreção de arcos vulcânicos definida para a porção do sul do cráton, interpretada como uma tectônica convergente durante o Arqueano (Lana et al., 2013; Romano et al., 2013; Farina et al., 2015; Moreira et al., 2016).

Zonas de cisalhamento e cavalgamento delimitam as margens com os domínios adjacentes, exceto em relação ao Grupo Bambuí, o qual recobre sua extensão oeste (Figura 1.2). A norte e nordeste faz contato com o *grenstone belt* de Pitangui, a Sequência Rio Manso e o Supergrupo Minas, e em sua borda sul faz contato com os complexos metamórficos Bonfim e Campo Belo pela Zona de Cisalhamento Cláudio e pelo cinturão kondalítico Paleoproterozoico denominado Sequência Supracrustal Itapecerica (Teixeira et al., 2017b; Coelho & Chaves, 2019). Em suas margens ocorrem ainda algumas sequências máficas acamadadas sem idade exata, como a Suíte Carmópolis de Minas, a Sequência Ribeirão dos Motas, a Sequência Rio Manso (Carneiro et al., 2004; Pinheiro & Nilson, 2000; Goulart et al., 2013). Na região de Oliveira e da Zona de Cisalhamento Cláudio (limite sul do complexo) um evento de fácies granulito é registrado em enderbitos e charnokitos, sendo estas rochas agrupadas na unidade Gnaisse Candeias (Corrêa da Costa, 1999; Oliveira, 2004), mais uma evidência do retrabalhamento expressivo nas bordas do complexo. Esse retrabalhamento foi datado em 2,0 Ga (Oliveira, 2004; Teixeira et al., 2017b), exposto também no leucossoma da pedreira Kinawa, localizada na Zona de Cisalhamento Cláudio e com idade similar (Carvalho et al., 2017a).

## 1.3 – Localização e Vias de Acesso

A área de estudo localiza–se no centro–sul de Minas Gerais, aproximadamente 120 km da capital Belo Horizonte, tendo o município Divinópolis a centro. O acesso até o município a partir de Campinas é feito pela rodovia SP–065 até a BR–381 (Fernão Dias) com destino a Minas Gerais, seguindo–se posteriormente pela BR–494 a partir do trevo com sentido à Oliveira (Figura 1.3). A área delimitada inclui as Folhas Belo Horizonte (SE.23) e Rio de Janeiro (SF.23) da CPRM (1:1.000.000), utilizadas como base para o mapeamento em conjunto com dados de geofísica (CODEMIG).

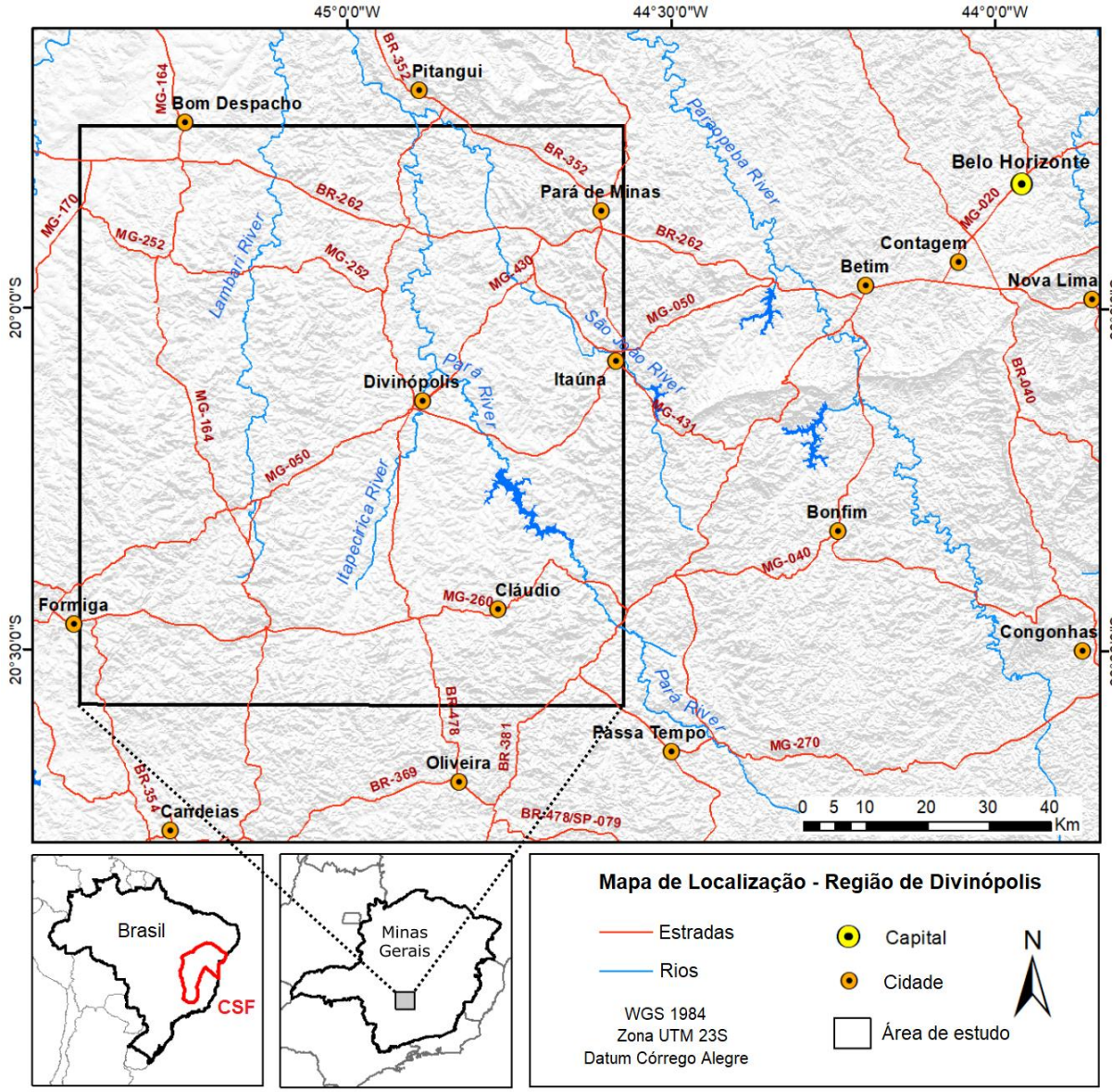


**Figura 1.3:** Mapa de localização da área de estudo com os principais municípios, vias de acesso e rede hidrográfica.

## 1.3 – Objetivos

O objetivo principal deste trabalho é caracterizar a evolução geodinâmica e crustal do Complexo Divinópolis. Para alcançar esta meta, os objetivos específicos incluem:

✓ Estabelecer a relação entre os diferentes litotipos da área; delimitando as principais litologias e estruturas da região;

✓ Identificar as assembleias minerais e as relações texturais e estruturais com intuito de caracterizar os processos petrogenéticos;

✓ Caracterizar a natureza química e afinidade TTG com intuito de identificar quais processos e ambientes de formação podem ter gerado as rochas do Complexo Divinópolis;

✓ Datar eventos de cristalização e metamorfismo e correlacioná–los aos eventos cronológicos da região;

✓ Discussão de um modelo de evolução tectônica para o Complexo Divinópolis e suas implicações para a evolução crustal do sul do Cráton São Francisco.

# 2. ESTRUTURAÇÃO DA TESE

O capítulo 1 compreende uma abordagem introdutória deste trabalho, situando a proposta e sua relevância, objetivos e contexto regional, enquanto o capítulo 2 aborda a estruturação da tese. O capítulo 3 expõe a metodologia empregada ao longo da pesquisa. Os produtos gerados a partir dos dados de sensoriamento remoto e aerogeofísica (gamaespectometria e magnetometria) são abordados no capítulo 4, apresentando-se os mapas gamaespectométricos, magnetométricos e do relevo sombreado. O capítulo 5 apresenta a integração das discussões e conclusões obtidas ao longo do trabalho, definindo a proposta final desta pesquisa. A apresentação dos resultados (petrográficos, geoquímicos e geocronológicos) foi dividida na forma de dois artigos inclusos como anexos neste documento (Anexos 1 e 2).

O artigo apresentado no Anexo 1 aborda os resultados obtidos por meio da caracterização geoquímica-petrográfica e detalha a ocorrência dos TTGs e rochas potássicas no Complexo Divinópolis, intitulado: "*Lithogeochemical evolution and petrogenesis of TTGs and potassic granites of Divinópolis Complex, São Francisco Craton (Brazil).*" O foco do trabalho são os processos petrogenéticos que originaram os gnaisses e granitos, além de discutir se estas rochas realmente podem ser caracterizadas como suítes TTGs. Processos de retrabalhamento crustal tiveram uma importante participação nessa porção do cráton, associados a evolução geodinâmica e maturação da crosta Arqueana.

O segundo artigo, apresentado no Anexo 2, aborda os dados geocronológicos obtidos por U-Pb em zircão e monazita (LA-FS-ICP-MS), intitulado: "*Emplacement of multistage Archean magmatism and Proterozoic reworking in Divinópolis Complex, southern São Francisco Craton*" e caracteriza os aspectos de campo e petrográficos, além da determinação de idades U-Pb absolutas de eventos magmáticos e metamórficos. Visto que o Complexo Divinópolis representava uma lacuna na relação de idades do sul do Cráton São Francisco, este artigo tem grande relevância no entendimento geodinâmico da evolução Arqueana da região. Eventos de diferenciação da crosta siálica são registrados nos gnaisses e granitos, além de uma sobreposição Paleoproterozoica datada em uma amostra de leucossoma e que se correlaciona com a acreção do Cinturão Mineiro a borda sul do Cráton do São Francisco.

# 3. MATERIAIS E MÉTODOS

## 3.1 – Trabalhos de campo

Os trabalhos de campo foram realizados em três etapas: julho de 2016, julho de 2017 e setembro de 2019, abrangendo um período de dezoito dias. Esta etapa consistiu no reconhecimento litoestrutural da área, além da coleta de amostras representativas para os estudos petrográficos, petroquímicos e geocronológicos. A coleta foi feita priorizando-se áreas não alteradas e diferentes porções do afloramento, cujas melhores exposições ocorrem em pedreiras. Para auxílio na etapa de campo foram utilizadas as folhas Belo Horizonte (SE23) e Rio de Janeiro (SF23), escala 1:100.000 (CPRM/UFMG) e dados de aeromagnetometria e aerogamaespectrometria.

## 3.2 – Aerogeofísica e sensoriamento remoto

Aerogeofísica e sensoriamento remoto foram utilizados como ferramentas para identificação das principais estruturas (rasas) e auxílio na individualização dos litotipos mapeados durante as etapas de campo. Os resultados obtidos a partir destes métodos foram integrados para confecção dos mapas litoestruturais. Os mapas magnetométricos, gamaespectométricos e relevo sombreado são apresentados no capítulo 4, tendo sido gerados através do programa ArcGIS (versões 10.6 e 10.7) e projetados em UTM – datum Córrego Alegre (zona 23S).

O banco de dados de aerogefísica (gamaespectrometria e magnetometria) utilizado nesse trabalho corresponde as áreas 2, 7 e 10 do Projeto de Levantamentos Aerogeofísicos de Minas Gerais (Projeto Pitangui–São João Del Rey–Ipatinga) conduzido pela CODEMIG, recobrindo o Quadrilátero Ferrífero e adjacências. Para a área 2, a altura do voo foi feita em 100 m, com espaçamento de linhas de voo em 250 m (N60W) e linhas de controle perpendiculares com espaçamento de 2500 m (N30E). Para a área 7, foi utilizado um espaçamento de 400 m para as linhas de voo com direção NW e um espaçamento de 8000 m para as linhas de controle perpendiculares, com altura do voo em 100 m. Para a área 10, foi utilizado um espaçamento de 500 m para as linhas de voo com direção N-S e um espaçamento de 1000 m para as linhas de controle perpendiculares, com altura do voo em 100 m.

### 3.2.1 – Gamaespectometria

Os dados de gamaespectometria foram interpolados pelo método da curvatura mínima, o qual gera uma superfície suavizada (Smith & Wessel, 1990) utilizando-se os canais de Potássio (eK), Tório

(eTh), Urânio (eU). O mapa ternário gerado foi do tipo U-Th-K no formato RBG como uma imagem em escala de cor (Figura 4.1), além da comparação com cada canal discriminado. O levantamento da área 10 não foi aproveitado para as interpretações gamaespectrométricas por destoar nos canais de Urânio e Tório, podendo não ter sido totalmente corrigido durante o levantamento. A influência do relevo sobre a resposta gamaespectrométrica também foi analisada, sendo sobrepostas imagens de RADAR (SRTM) à imagem RGB. Assim, os lineamentos que não estão expressos claramente na magnetometria puderam ser melhor delimitados.

3.2.2 – Magnetometria

A interpretação dos produtos magnetométricos envolveu uma análise visual, no qual se procurou utilizar as imagens tratadas (CPRM-CODEMIG) para definição das feições geológicas e estruturais mais relevantes da região. O método de amplitude do sinal analítico (ASA) foi utilizado por oferecer um bom balanço entre profundidades para uma análise estrutural qualitativa regional (Roest, 1992), influenciado pela inclinação magnética e pela profundidade do corpo (Li, 2006). Além disso, é bastante eficaz na identificação de rochas máficas. As estruturas isoladas correspondem as assembleias de fontes mais rasas do que 5 km apartir da filtragem por *band-pass* (Figura 4.2A). A Derivada Vertical Direcionada (VRD) também foi utilizada para realçar as anomalias rasas de alta frequência (Figura 4.2B).

3.2.3 – Sensoriamento Remoto

O sensor da missão Shuttle Radar Topography Mission (SRTM) da NASA é um dos mais conhecidos e confiáveis para aplicação de análise digital do terreno. O Modelo Digital de Elevação e dados geomorfométricos do Brasil são distribuídos na resolução de 30 m derivados da interpolação dos modelos de 90 m pelo Instituto Nacional de Pesquisas Espaciais (INPE), disponibilizados na plataforma do projeto TOPODATA (Valeriano & Rossetti, 2011). Foram utilizadas quatro imagens de relevo sombreado (RS) do sensor SRTM que correspondem aos recortes 19S45, 19S46, 20S45, 20S46 e que podem ser adquiridas gratuitamente, já corrigidas e projetadas para o datum UTM WGS84 (zona 23S) (Figura 4.3). Uma iluminação de 45º de elevação com direção norte é aplicada a essas imagens (Valeriano & Rossetti, 2011).

## 3.3 – Petrografia

Análises petrográficas foram realizas em um total de trinta e três lâminas delgadas por microscopia ótica convencional em luz transmitida (Microscópio Ótico *Zeiss Axiophot*) no Laboratório de Termometria do Instituto de Geociências (UNICAMP). A microscopia eletrônica de varredura (MEV) foi realizada em 11 lâminas polidas no Laboratório de

Microscopia Eletrônica de Varredura (IG/UNICAMP), em um espectrômetro de energia dispersiva (*Energy Dispersive X–Ray Spectrometer, EDS/Oxford Instruments*) acoplado a um MEV LEO 430i *Zeiss ac.* A metalização das lâminas polidas foi realizada por meio da evaporação de fibra de carbono (metalizador Q150T/ *Quorum Technologies*). A energia do feixe de elétrons utilizada foi 300 V a 30 kV e a corrente do feixe entre 1 pico–ampere e 1 micro–ampere, com foco fixado em 19 mm. As análises petrográficas tem como objetivo a identificação das assembleias minerais, composição modal, zoneamentos composicionais, intercrescimento e exsoluções, relações texturais e possíveis alterações.

### 3.4 – Geoquímica (FRX e ICP-MS)

Foram selecionadas 57 amostras para determinação de elementos maiores e menores por Fluorescência de Raios X (XRF) e elementos traço por espectrometria de ionização induzida por Plasma Acoplado (ICP–MS). As amostras foram preparadas no Laboratório de Preparação de Amostras do Instituto de Geociências da UNICAMP, a partir da britagem em um britador de mandíbulas (*Fritsh*, Alemanha), homogeneizadas e quarteadas, separando–se uma quantidade entre 50 e 70 g para moagem. A moagem é feita em um moinho planetário de ágata (*Fritsh*, Alemanha), operando durante 20 minutos com 200 rpm de rotação. A limpeza é feita com areia, operando durante 10 minutos e 200 rpm. As amostras resistentes a esta moagem passam por um moinho vibratório de anéis de ágata vibrando durante 5 a 7 minutos.

Para as análises de elementos maiores por FRX foram confeccionados discos de vidro e pastilhas prensadas para os elementos traço. As pastilhas prensadas foram preparadas com a mistura de 9,0 g da amostra moída e 1,5 g de cera em pó (*Hoechst,* Alemanha) em prensa hidráulica HTP 40 (*Herzog*, Alemanha) sob pressão de 119 Mpa, durante 1 minuto. Os discos de vidro foram confeccionados a partir da fusão de 6g de amostra com 1g de mistura fundente de metaborato e tetraborato de lítio (80/20 p/p – *Spectroflux 100B Johnson Mattey, USA*) a 1000º C em cadinhos de platina e resfriados em velocidade controlada em moldes circulares de platina. Foi utilizado o espectrômetro de Fluorescência de Raios X (*Philips*, PW 2404) do Laboratório de Geoquímica Analítica do Instituto de Geociências da UNICAMP. O controle de qualidade foi feito com a duplicação de uma amostra e a verificação do procedimento analítico foi feita com base na análise de discos de vidro de amostras de materiais de referência internacionais (GS–N, BRP-1, GRI-1 e RGM-1). A perda ao fogo foi realizada independentemente, com a queima de amostra seca em estufa por 4h a 1000ºC.

Foram selecionadas 23 amostras para determinação de elementos traços por ICP–MS. A dissolução da rocha foi feita com ataque ácido em 0,1 g de amostra para as amostras máficas e 0,04 g para as amostras félsicas em bombas de teflon PAAR identificadas e limpas, aquecidas em estufa a temperatura de 180º C por 5 dias, a partir da adição de 0,5 ml de $HNO_3$ e 2 ml de HF. A bomba é protegida por uma fita de teflon e fechada com uma jaqueta de metal. Após o resfriamento em temperatura ambiente, as amostras foram aquecidas em placa a 150º C até a quase dissolução, utilizando-se 0,5 ml de $HClO_4$ durante 4 horas. O procedimento completo utilizado para a dissolução está descrito em Cotta & Enzweiller (2010). As medições foram feitas no Laboratório de Geologia Isotópica do Instituto de Geociências da UNICAMP em um ICP–MS X *series* II (*Thermo*) equipado com CCT (*Collision Cell Technology*). O controle de qualidade foi feito com a duplicação de uma amostra, análise de materiais de referência internacionais (JGb–1, BRP–1) e um branco (uma bomba PAAR composta apenas por ácido).

Os dados obtidos foram aplicados em diagramas classificatórios a partir dos programas *Excel* 365© e *GCDKit* 4.1 (Janoušek *et al*. 2006) e as tabelas constam no Apêndice A (Tabela 1).

### 3.5 – Geocronologia (LA-FS-ICP-MS)

A geocronologia U–Pb foi feita para obtenção de idades de cristalização (em zircão) e de metamorfismo (em monazita). Foram datadas onze amostras no total, pelo método de ablação por *laser* acoplado ao ICP–MS. A preparação de amostras e análises foram feitas no Laboratório de Geologia Isotópica da UNICAMP. A separação do mineral é feita a partir da britagem em um britador de mandíbulas e moagem em moinho de discos. O bateamento para separação do concentrado é feito manualmente, assim como a separação magnética com imã de mão. O separador isodinâmico *Frantz* (LB–1, *S.G. Frantz Co., Inc*.) foi utilizado nas correntes 0,05, 0,1, 0,3, 0,7, 1,0 e 1,2 A e para separação por líquidos densos utilizou–se Iodeto de Metileno. A seleção dos grãos de zircão e monazita foi feita manualmente com lupa binocular.

Os minerais separados são colados em uma lâmina com fita dupla face, preenchidos com uma mistura de 5 g de araldite e 1 g de resina aradur em um molde etiquetado. A secagem é feita em 1 dia em estufa a 60ºC e os *mounts* são lixados e polidos com pasta diamantada e esterilizados. Para os grãos de zircão foram obtidas imagens de catodoluminescência (CL) e *backscattered electron* (BSE) em MEV para reconhecimento da estrutura interna dos minerais, auxiliando na escolha dos melhores *spots* a serem datados (identificação de borda e núcleo,

zoneamentos, intercrescimentos e fraturas), enquanto para os grãos de monazita, as imagens de BSE foram utilizadas para evitar inclusões e fraturas.

O equipamento de ablação a laser consiste em um Excite 193 (Photon Machines) equipado com uma célula de ablação de dois volumes (HelEx) acoplado ao ICP–MS (Element XR, Thermo Scientific). Os mounts são previamente limpos com 10% v/v HNO3 e água ionizada e inseridos no aparelho juntamente com os padrões de referência PEIXE e 91500 para os zircões (Wiedenbeck et al. 1995, Wiedenbeck et al. 2004) e Bananeira e USGS 44069 para as monazitas (Aleinikoff et al., 2006; Gonçalves et al., 2016) segundos os procedimentos de Navarro et al. (2015). O gás utilizado é He ultrapuro, a frequência do laser é 10 Hz e fluência de 4.74 J cm–2. O tamanho do spot foi definido para 25 µm. A redução dos dados foi feita com softwares Iolite 2.5 conforme método de Paton et al. (2010), a correção de Pb comum pelo software VizualAge 2014.10 (Petrus & Kamber 2012) e os diagramas Concordia foram feitos com o plugin Isoplot 4.15 para Excel© (Ludwig, 2012). As tabelas com os dados de U-Th-Pb constam no Apêndice B (Tabelas 2 a 12).

# 4. RESULTADOS GEOFÍSICOS

Mesmo considerando-se a boa área de exposição de rochas no sul do cráton do São Francisco, dados aerogeofísicos são uma importante ferramenta para entender a história policíclica desses terrenos, principalmente em relação ao arcabouço litoestrutural. Este capítulo apresenta as conclusões obtidas através do geoprocessamento de dados de gamaespectrometria, magnetometria e imagens de RADAR da região de Divinópolis.

Buscou-se primeiramente delimitar o terreno total do complexo a partir da relação de contato com as litologias adjacentes, como o *greenstone belt* Pitangui e as sequências máficas e supracrustais (e.g. Sequência Máfica de Cláudio, Sequência Supracrustal Itapecerica). A seleção da área foi feita visando-se um panorama amplo do Complexo Divinópolis, com enfoque em suas margens norte, leste e sul, onde é possível visualizar de modo bastante confiável as principais estruturas e contatos. Já a borda oeste do complexo é recoberta pelo Grupo Bambuí (Proterozoico).

A aerogamaespectrometria foi utilizada para identificação dos principais grupos de rochas a partir das distintas assinaturas de Tório, Urânio e Potássio, sendo possível identificar os gnaisses e migmatitos, os plútons tardios mais ricos em potássio, as rochas máficas, e unidades supracrustais. A magnetometria foi utilizada para identificação do arcabouço estrutural, obtendo-se informações de subsuperfície não reveladas no mapeamento geológico. Desse modo, o uso de dados de campo integrado aos mapas de aerogeofísica possibilitou a delimitação mais precisa das unidades e estruturas mapeadas.

O mapa final simplificado integrando os resultados obtidos é apresentado ao final do capítulo (Figura 4.4).

## 4.1 - Mapa gamaespecrométrico (RGB eK-eTh-eU)

É possível distinguir claramente no mapa gamaespectrométrico RGB (Figura 4.1) as bordas norte, leste e sul do complexo Divinópolis, que ocorrem respectivamente em contato com o *greenstone belt* Pitangui, o Supergrupo Minas e as rochas máficas da Sequência Cláudio. Tanto o contato com o *greenstone belt* Pitangui, quanto com a Sequência Máfica de Cláudio são marcados por zonas de cisalhamento, respectivamente, Pitangui (a norte) e Cláudio (a sul). Essas zonas são descritas na literatura (Romano, 2007; Carvalho et al., 2017a), enquanto as zonas de cisalhamento Itapecerica e Itaúna foram mapeadas durante este trabalho. A região oeste é balizada pela deposição de rochas sedimentares metamorfisadas do Grupo Bambuí, com tons de verde claro (resposta ao U e Th) na sobreposição com o Complexo Divinópolis (resposta ao Th e K) e tons de rosa na porção mais noroeste (resposta ao U e K).

O contato NW-SE com o *greenstone belt* Pitangui é bem demarcado devido ao baixo sinal de radiação gama emitido pelas rochas máficas e BIFs que mostram coloração vermelho-escuro a preto. A baixa radição em K, U e Th das rochas máficas fica visível também na anomalia emitida pela Sequência Máfica de Cláudio, na borda sul do complexo. Alguns diques máficos com orientação NW-SE e grande extensão (+150 km) também ficam visíveis como um risco mais escuro no mapa. Nesse aspecto, não apenas as rochas máficas são realçadas pelo mapa de gamaespectrometria, como também sua estruturação.

Observando-se o contraste entre os valores radiométricos foi possível dividir o Complexo Divinópolis em quatro setores distintos, caracterizando quatro domínios gamaespectométricos: Setor Nordeste (NES), Setor Central (CS), Setor Oeste (WS) e Setor Sul (SS) (Figura 4.1). De modo geral, a concentração de elementos radiogênicos coincide com contatos geológicos e zonas de cisalhamento são bem marcadas por contrastes de cor.

O Setor Nordeste é caracterizado por gnaisses com altos valores de U, K mediano e baixos valores de Th, resultando em uma coloração rosa e avermelhada bem distinta. Este setor forma uma faixa alongada com trend balizado pelo Lineamento Pitangui, cujo contato com o *greenstone belt* Pitangui resulta em uma zona milonítica. As intrusões graníticas que ocorrem neste domínio apresentam estruturação alongada conforme os trends estruturais NW-SE, aparecendo discretamente como corpos mais alaranjados devido ao teor de potássio. Este setor é separado do Setor Central por outra zona de cisalhamento, denominada Itaúna, onde ocorrem migmatitos e porções dioríticas metamorfisadas.

O Setor Central é caracterizado por significativa radiação de Th, assinalando cores verdes e amareladas características do embasamento gnáissico, cuja composição concentra minerais ricos em U e Th (zircão, titanita, apatita, monazita e epidoto). É possível identificar no Setor Central as anomalias das intrusões de granitos de alto-K, com característica estruturação elipsoide, representados pelas cores laranja e avermelhada, devido ao teor de potássio, resultado da presença de feldspato nessas rochas, por sua vez, mais susceptíveis ao intemperismo em relação aos gnaisses. Esses corpos elipsoides bem preservados são mais comuns na porção central, com 15 a 30 km de extensão, e em campo, esses granitos são pouco ou não deformados. No domínio central do Complexo Divinópolis concentram-se a maior parte das estruturas dômicas, seguido pelo domínio sul.

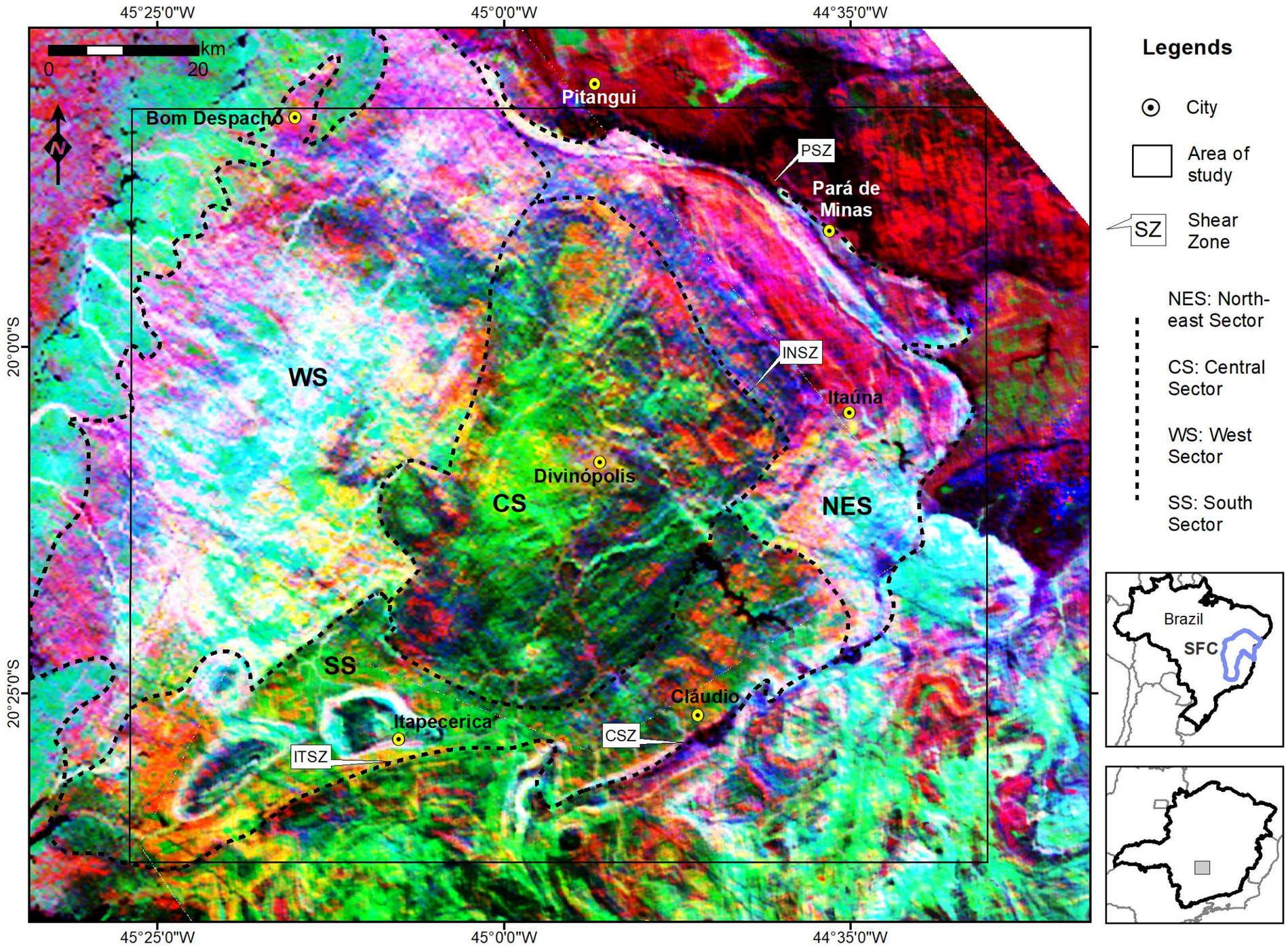


**Figura 4.1:** Mapa gamaespectrométrico da região de Divinópolis para a composição ternária eK-eTh-eU (RGB), mostrando os domínios gamaespectométricos (**NES**: Setor Nordeste, **CS**: Setor Central, **WS**: Setor Oeste, **SS**: Setor Sul). Os gnaisses e migmatitos são representados predominantemente pela cor verde (alto Th), enquanto as intrusões graníticas formam elipsoides com cor alaranjada-avermelhada (alto K). O *greenstone belt* Pitangui aparece em tons de vermelho e preto a norte (baixa radiação gama) e se estende com direção NW-SE. **PSZ**: Pitangui Shear Zone, **INSZ**: Itaúna Shear Zone, **ITSZ**: Itapecerica Shear Zone, **CSZ**: Cláudio Shear Zone, **SFC**: Cráton do São Francisco.

O Setor Sul apresenta assinaturas similares ao Setor Central, com composição rica em Th evidenciada nas colorações amarela e verde, porém é mais rica em afloramentos e os gnaisses não mostram estruturação dômica. O elemento Th pode concentrar-se nos mantos saprolíticos (Andersson *et al.*, 1995), podendo estar relacionado a erosão e exumação dos gnaisses que afloram de modo mais consistente na porção sul. Outra feição típica deste setor são as anomalias elípticas da Sequência Supracrustal Itapecerica descrita por Zacchi et al. (2007) e Teixeira et al. (2017b). O centro das elipses é formado por xistos Paleoproterozoicos ricos em grafite, com uma auréola de paragnaisses também Paleoproterozoicos (sudoeste da área, Figura 4.1). Essa porção do domínio sul é separada do Complexo Belo Horizonte pela Zona de Cisalhamento Itapecerica, enquanto na região da Sequência Máfica de Claúdio, é separada do Complexo Bonfim pela Zona de Cisalhamento Cláudio. Em ambas as zonas de cisalhamento é comum a ocorrência de rochas de alto grau metamófico, como paragnaisses, charnokitos, enderbitos e migmatitos, todos de idade Proterozoica (Corrêa da Costa, 1999; Oliveira et al., 2004; Carvalho et al., 2017a; Teixeira et al., 2017b).

O Setor Oeste é no geral caracterizado por gnaisses com altos teores de Th, U e K, emitindo uma coloração branco-azulada ou rosada, cuja anomalia radiométrica característica é muito similar a dos gnaisses Arqueanos que hospedam a Sequência Supracrustal Itapecerica. De fato, sua estruturação demonstra continuidade e foram classificados como o Gnaisse Itapecerica por Teixeira et al. (2017b), embora seja distinta do Gnaisse Itapecerica de Carneiro et al. (2007), o qual se aproxima mais dos gnaisses ricos em Th dos domínios sul e central. De modo mais discreto que nos demais setores é possível distinguir algumas anomalias dômicas de granitos potássicos, principalmente no contato com outros setores. É possível que uma zona de cisalhamento separe os domínios oeste e central, porém, não foi encontrada em campo. A região mais oeste da área de estudo tem influência da erosão das rochas do Grupo Bambuí.

À sul e sudeste do Complexo Divinópolis, rochas dos complexos Bonfim e Belo Horizonte exibem um padrão de dobramentos, e embora estas rochas não tenham sido amostradas em campo, são comumente descritas na região como charnokitos e enderbitos de idade Paleoproterozoica (Corrêa da Costa, 1999; Oliveira, 2004), associados a eventos de colisão do Cinturão Mineiro com o núcleo Arqueano do sul do Cráton do São Francico. Essa colisão está associada a importante zonas de cisalhamento, como o Lineamento Jeceaba-Bom Sucesso-Itubiruna e a Zona de Cisalhamento Lenheiros, que definem os limites sul do cráton (Campos & Carneiro, 2008; Barbosa et al., 2015). No domo Divinópolis esse evento está associado a zonas de cisalhamento Cláudio e Itapecerica, que acompanham a frente de deformação do Cinturão Mineiro com direção NE-SW.

## 4.2 - Mapas magnetrométricos (ASA e VDR)

A aeromagnetometria foi utilizada para traçar digitalmente os lineamentos e correlacionar anomalias magnéticas com o relevo e estruturas ao longo da área de estudo. Primeiramente caracterizou-se as principais anomalias magnéticas utilizando-se o método de amplitude do sinal analítico (ASA) para fontes mais rasas do que 5 km (Figura 4.2A). As fontes com altos valores de amplitude magnética são oriundas de rochas máficas e representadas em laranja e amarelo no mapa. As áreas em verde e azul possuem baixa susceptibilidade magnética e correspondem a gnaisses, granitos e rochas sedimentares.

O arco de alta magnetização na parte norte do mapa corresponde as rochas máficas do *Greenstone belt* Pitangui (e.g. basaltos, komatiitos e BIFs). Concomitantemente, as anomalias mais significativas correspondem as assinaturas geradas por BIF associado a rochas máficas e ultramáficas, evidente por exemplo, nas dobras anticlinais com eixo axial NW-SE próximas a cidade de Pará de Minas e Pitangui. Outra feição com alto sinal magnetométrico é visível na parte leste do mapa e corresponde ao Supergrupo Minas e suas sequências de Itabirito associadas (BIFs). Esse arco, no entanto, apresenta direção oposta ao do *Greenstone belt* Pitangui, com trend NE-SW. Estendendo-se com essa mesma direção afloram as rochas máficas da Sequência Cláudio (Couto & Carneiro, 2007) que delimitam a borda sudeste do Complexo Divinópolis. Essa região é demarcada por uma zona de cisalhamento dextral (Carvalho et al., 2016), representada em campo por gabros e basaltos indeformados. Na delimitação entre os setores nordeste e central, próximo a cidade de Itaúna uma anomalia magnética também é bem demarcada e vista em campo como dioritos bem deformados e foliados, com orientação de biotita e estiramento de quartzo e plagioclásio. É possível que essa zona represente a sutura de uma colagem, assim como a anomalia que separa os setores central e oeste, a oeste da cidade de Divinópolis. No entanto, mais estudos são necessários para confirmação dessa hipótese. As demais anomalias de rochas máficas são causadas por duas famílias de enxames de diques com orientação NW-SE (Pará de Minas) e E-W/NE-SW (Formiga) que correspondem a basaltos e diorito em campo.

Uma grande intrusão granítica ocorre no contato entre o *Greenstone belt* Pitangui e o Complexo Divinópolis, formando um corpo oval de aproximadamente 30 km de extensão. As bordas são delimitadas pelo sinal magnético mais elevado do *greenstone belt*, enquanto o corpo em si apresenta baixa suscetibilidade magnética. Essa intrusão é bem descrita na literatura como o corpo granítico Florestal (Romano, 2007; Farina et al., 2015). A área com menor suscetibilidade magnética (em azul) ocorre na parte oeste do mapa, anomalia característica das rochas sedimentares do Grupo Bambuí e que recobre toda a margem oeste do Complexo Divinópolis. Essas rochas são principalmente conglomerados, diamictitos, arenitos, calcários e pelitos com bandamento sedimentar horizontal preservado (Uhlein et al., 2016).

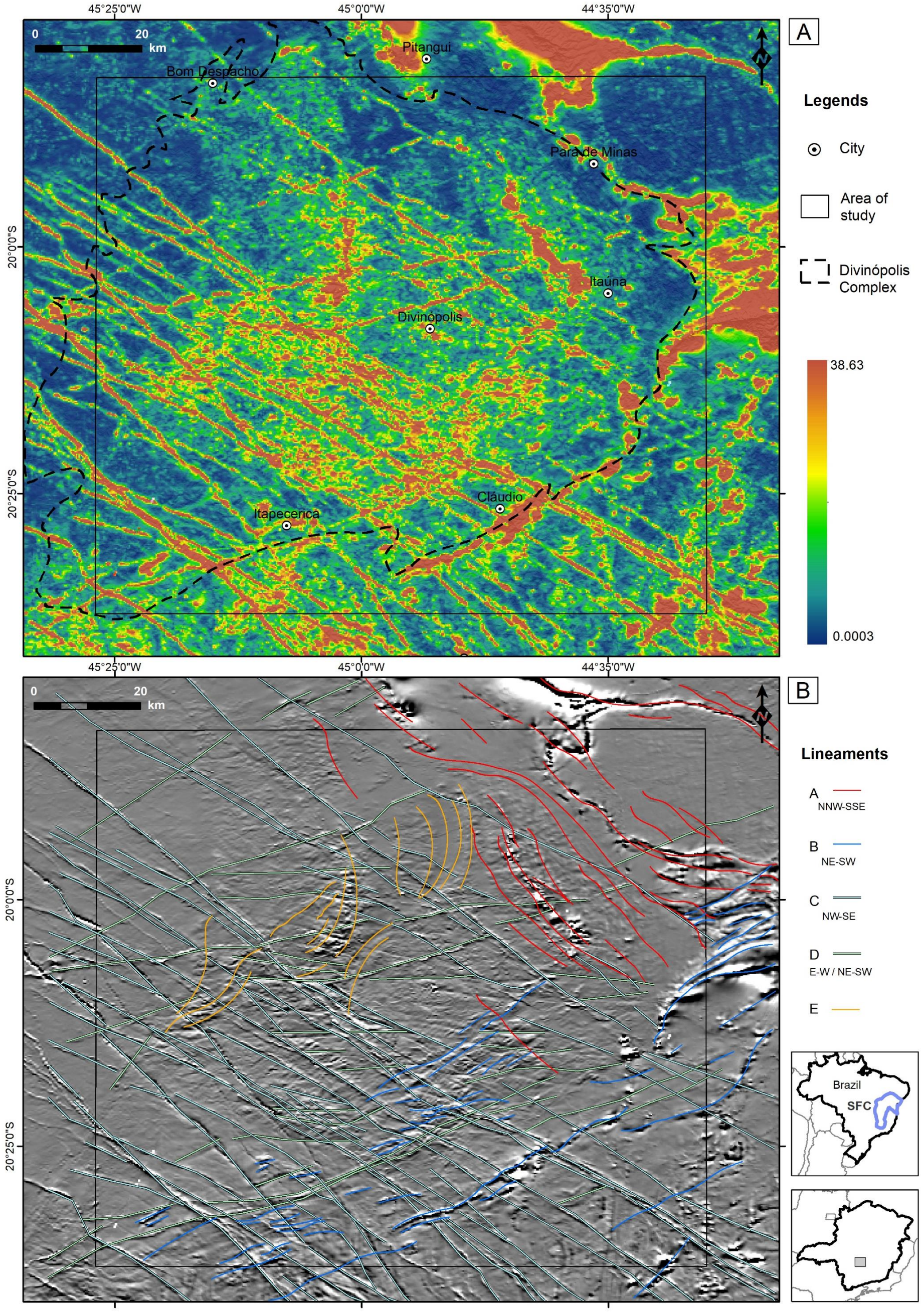


**Figura 4.2: A)** Mapa magnetométrico da região de Divinópolis para fontes rasas (< 5km) gerado pela imagem da amplitude do sinal analítico (ASA). As altas anomalias magnéticas são causadas principalmente por rochas máficas, enquanto as anomalias mais brandas são correlacionadas a rochas graníticas e sedimentares. **B)** Mapa da derivada vertical (VDR) com sombreamento em 45º mostrando os grupos de lineamentos magnéticos identificados. **SFC**: Cráton do São Francisco.

Utilizando-se o filtro da derivada vertical (VDR) foram traçados os lineamentos magnéticos (Figura 4.2B) auxiliado pelo mapa ASA. Duas direções preferenciais são predominantes (NW-SE e NE-SW) e os lineamentos foram separados em cinco grupos de acordo com sua ordem estrutural: A, B, C, D e E.

Os lineamentos do grupo A possuem direção preferencial NW-SE a NNW-SSE espaçadas entre 3 e 5 km formando linhas contínuas de 20 a 60 km, sendo observadas em rochas Arqueanas do norte do Complexo Divinópolis (gnaisses e milonitos) e ao longo do *Greenstone belt* Pitangui. Essa direção se correlaciona com o trend estrutural do *greenstone belt* e zonas de cisalhamento e zonas miloníticas associadas (e.g. Lineamento Pitangui) e é predominante no Setor Nordeste.

Na porção leste do mapa, os lineamentos A apresentam intersecção com os lineamentos B, que são mais novos. A direção preferencial dos lineamentos B segue um *trend* NE-SW composto por linhas segmentadas com 1 a 3 km de espaçamento e amplitude bastante variável, de 10 a 50 km de extensão. Ocorre em rochas preferencialmente Proterozoicas (e.g. Supergrupo Minas, na borda leste e Sequência Máfica de Cláudio na borda sudeste), porém também se replica nos gnaisses Arqueanos próximos os lineamentos Proterozoicos, sendo a estrutura predominante no Setor Sul.

Os lineamentos do grupo C correspondem a fontes contínuas e retas com orientação NW-SE, espessura de algumas dezenas a centenas de metros e extensão que varia de 50 a mais de 300 km. Esses lineamentos correspondem a um importante enxame de diques máficos denominado Pará de Minas e datado do Paleoproterozoico (Chaves et al., 2013), que intrudem o embasamento Arqueano dos complexos Divinópolis, Bomfim e Campo Belo. Os diques do grupo C podem ser deslocados pelos lineamentos D.

Os lineamentos D também correspondem a uma importante família de diques com direção E-W e NE-SW, deslocando a família anteriormente citada, o que leva a suposição de que seja mais nova, sendo atribuída ao enxame Formiga (Neoproterozoico) descrito por Chaves et al., (2013). Também correspondem a fontes contínuas e retas com alguns metros de espessura, porém a extensão desses diques é menor, ficando em torno de 20 a 100 km. Além da menor amplitude, os diques do grupo D parecem intrudir apenas o embasamento Arqueano do Complexo Divinópolis.

Os lineamentos do grupo E não possuem uma orientação preferencial, porém suas estruturas se aproximam dos *trends* N-S e NNE-SSW. Formam linhas sinuosas e anastomosadas relacionadas com a delimitação dos corpos graníticos Arqueanos que ocorrem principalmente na parte dômica do Setor Central do Complexo Divinópolis, a qual apresenta maior preservação de estruturas elipsoidais.

## 4.3 - Imagem de RADAR (SRTM)

A interpretação geomorfológica foi feita a partir da imagem de modelo numérico do terreno (SRTM), com o objetivo de compreender como o relevo da região se relacionada com as estruturas. Desse modo, os principais lineamentos estruturais foram extraídos através das quebras positivas e negativas de relevo que podem ser observadas nas imagens SRTM (Figura 4.3), sendo integradas posteriormente aos mapas geológicos (Anexos 1 e 2).

O mapa SRTM mostra o distinguível controle estrutural dos setores nordeste, sudeste e central do complexo Divinópolis. A zona de cisalhamento Pitangui associada ao *Greenstone belt* Pitangui no Setor Norte-Leste fica evidenciada por contínuos lineamentos com direção NW-SE, condizente com os dados de gamaespectometria e magnetometria. Toda a região sul mostra um controle estrutural NE-SW nas quebras negativas de relevo, condizente com a colisão dos blocos Divinópolis, Bonfim e Campo Belo e da influência do Cinturão Mineiro, bem marcado nas imediações da cidade de Cláudio.

Os lineamentos do Supergrupo Minas truncam estruturas Arqueanas do *Greenstone belt* Pitangui e Complexo Divinópolis, evidenciando sua colocação tardia (Proterozoica) em relação ao domo Arqueano. Um arcabouço do tipo domo-e-quilha é proposto para a região do Quadrilátero Ferrífero (Marshak et al., 1997; Cutts et al., 2019), onde estruturas Arqueanas são reativadas durante o Proterozoico (quilhas), truncando ou cortando os domos Arqueanos. Essas reativações geram auréolas de metamorfismo nas margens dos domos, enquanto os núcleos se mantêm relativamente preservados. Esse padrão se assemelha muito ao encontrado para o Complexo Divinópolis (domo) e sequências supracrustais adjacentes (quilhas).

A porção central do complexo não apresenta quebras de relevo significativas ou uma direção estrutural predominante, sendo representada por uma área mais aplainada. Há a presença de domos e estruturas circulares marcadas por quebras negativas de relevo. Com menor frequência, têm-se lineamentos NW-SE menos expressivos e concentrados, marcados pelas quebras positivas que representam zonas de cisalhamento locais. A porção noroeste da área é caracterizada como a região com menos quebras do relevo, associada a ocorrência das rochas metassedimentares do Grupo Bambuí. É possível distinguir uma leve erosão nas escarpas desse grupo, marcadas por lineamentos de menor intensidade.

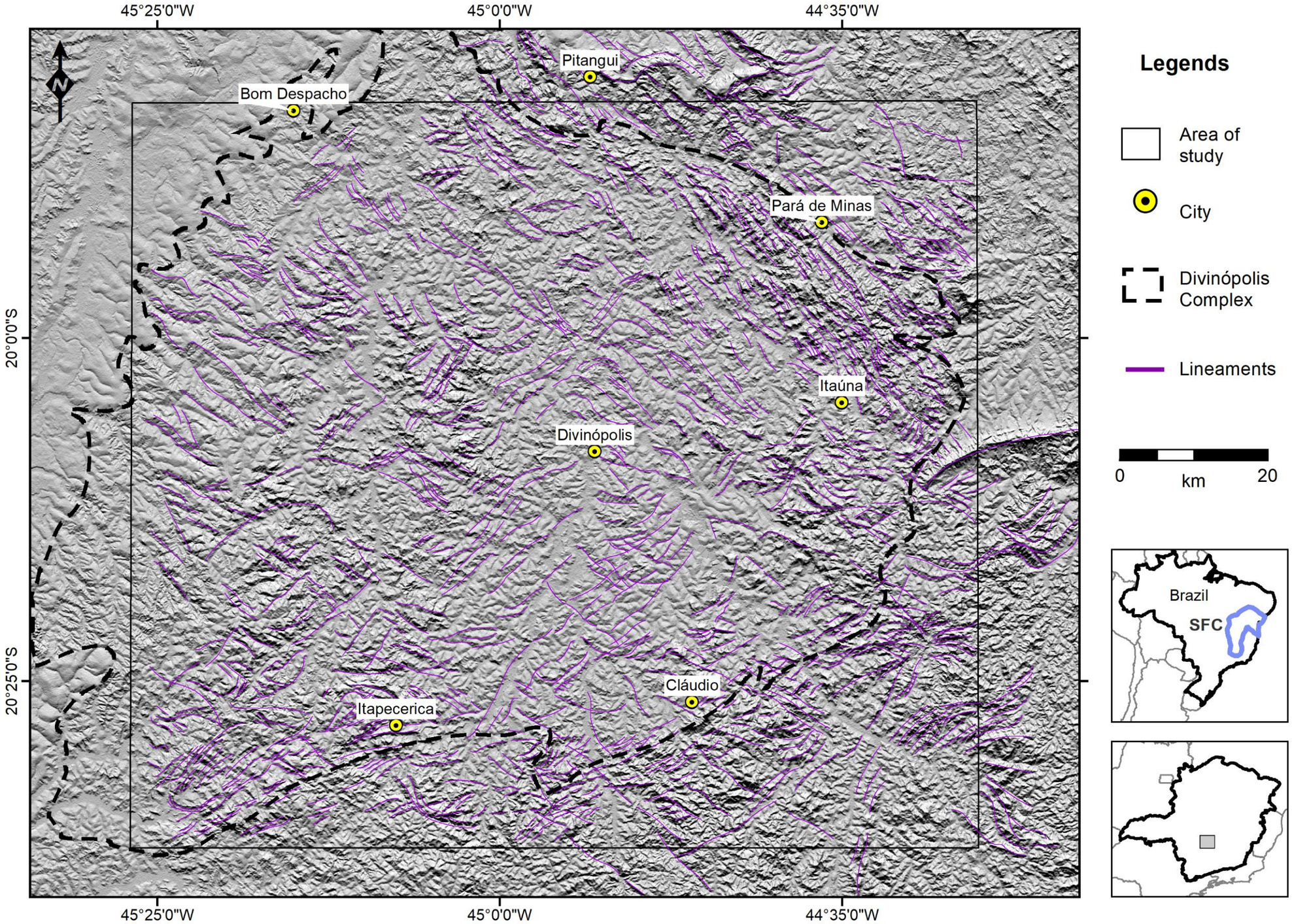


**Figura 4.1:** Imagem SRTM da região de Divinópolis e os principais lineamentos estruturais retirados a partir de quebras do relevo. **SFC**: Cráton do São Francisco.

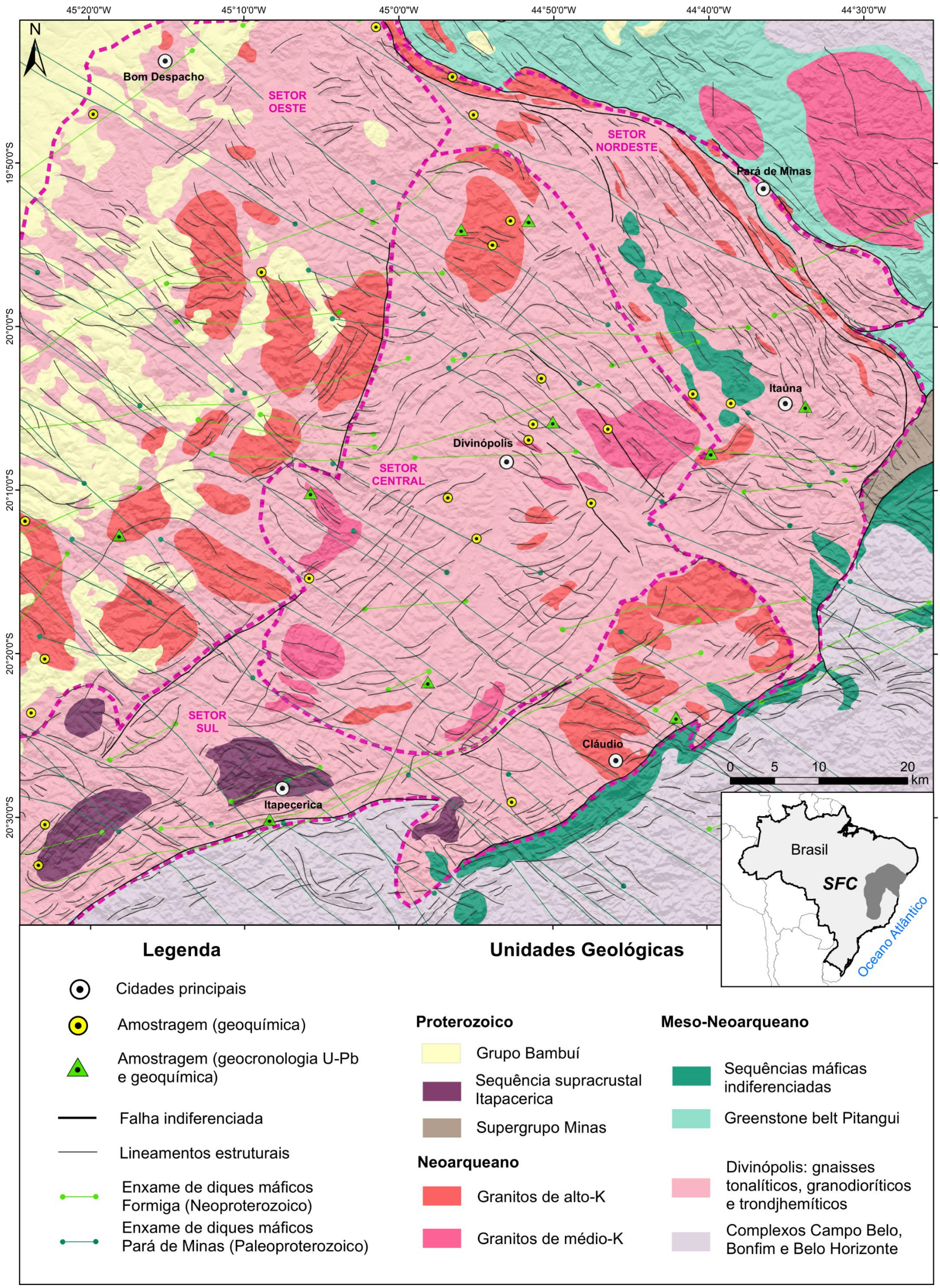


**Figura 4.4:** Mapa simplificado da área de estudo integrando-se os dados de campo e as imagens gamaespectométricas, magnetométricas e SRTM. Com base nesses dados, o Complexo Divinópolis foi dividido nos setores Nordeste, Central, Oeste e Sul.

# 5. SÍNTESE DAS DISCUSSÕES E CONCLUSÕES

- ✓ O Complexo Divinópolis compreende um núcleo Arqueano dômico bem preservado localizado no sul do Cráton São Francisco. É composto por uma suíte TTG (tonalitos-trondjhemitos-granodioritos) e uma suíte potássica (granodioritos), ambas intrudidas por uma suíte de granitos tardios (granodioritos, monzogranitos, sienogranitos) que podem perfazer até 30% do complexo. Os granitos foram agrupados em monzogranitos de médio-K e sienogranitos de alto-K.

- ✓ A suíte TTG é composta por dioritos, tonalitos, trondjhemitos e granodioritos de caráter cálcio-alcalino, magnesiano, peraluminosos a fracamente metaluminosos. Essas rochas exibem valores moderados de La/Yb e Sr/Y, baixo conteúdo de Sr e alto Mg, Cr e Ni. Tais assinaturas geoquímicas sugerem uma fonte basáltica sem conteúdo significativo de granada e temperaturas próximas a líquidos experimentais entre 1000–850º C a 12 kbar, além da participação de um componente mantélico. Este componente pode ter se formado tanto por fusão na presença de cunha mantélica em um ambiente similar a subducção quanto fusão parcial de crosta máfica por ascensões mantélicas.

- ✓ A idade de cristalização dos TTGs foi obtida em 2787 ± 9, 2782 ± 6 e 2779 ± 42 Ma, com uma idade herdada de 2860 ± 28 Ma. Idades similares foram encontradas na porção norte do complexo Divinópolis (2878 ± 5 Ma) e no greenstone belt Pitangui (2886 ± 10 Ma). A formação de TTGs no sul do cráton São Francisco pode ser dividida em dois períodos: 2915–2860 e 2790–2775 Ma, sendo que o primeiro período caracteriza o surgimento dos primeiros continentes estáveis enquanto o segundo caracteriza a principal crosta TTG atualmente preservada.

- ✓ A suíte potássica é formada por trondhjemitos, granodioritos e monzogranitos magnesianos a ferrosos com caráter peraluminoso bem definido, baixos valores de La/Yb, Sr/Y e um padrão plano de HREE. Anomalias negativas de Eu são mais significativas e apresentam similaridades com rochas potássicas Arqueanas. A geoquímica indica fonte sem granada formadas em um ambiente de baixa pressão com estabilidade de plagioclásio, com temperaturas próximas a líquidos experimentais entre 850–750º C a 12 kbar. O retrabalhamento progressivo e fusão parcial de rochas crustais (TTGs) gerou a suíte potássica.

- ✓ O magmatismo potássico se torna pervasivo no cráton São Francisco após 2.7 Ga, e as idades de cristalização obtidas para a suíte potássica foram de 2731 ± 18, 2729 ± 31, 2673 ± 33 e 2673 ± 31 Ma. Entre 2.8 e 2.7 Ga ocorre a mudança de um regime dominado predominantemente por fontes mantélicas

e/ou máficas para um regime dominado por fontes félsicas ricas em potássio oriundas do retrabalhamento de crosta preexistente.

- ✓ Os granitos de médio-K possuem geoquímica intermediária entre TTGs e rochas Arqueanas potássicas, sendo mais ricos em $K_2O$, peraluminosos e com baixos valores de Mg#, Cr e Ni. Considerando suas características geoquímicas, essas rochas se formaram em ambientes sem granada residual na fonte e rasos, em temperaturas mais baixas (~650º C), cuja fonte seriam as suítes TTGs e potássicas.

- ✓ Os granitos de médio-K ocorrem em todo o sul do cráton São Francisco, sendo que a geração mais antiga de granitoides dos complexos Campo Belo, Belo Horizonte e Bonfim (2755–2700 Ma) também apresentam afinidade com granitos de arco e colisionais em profundidade variável, similares a TTGs e adakitos. Os monzogranitos mais antigos do complexo Divinópolis apresentam idades similares (2733 ± 24 e 2729 ± 25 Ma).

- ✓ Os granitos de alto-K apresentam baixos valores de Sr e altos valores de $K_2O/Na_2O$ e LILE e compõem sienogranitos pouco deformados, ferrosos e preferencialmente metaluminous, podendo ser atribuídos a fontes potássicas rasas e de baixa pressão (~5 kbar).

- ✓ Uma idade de 2653 ± 13 Ma foi obtida para cristalização de um sienogranito não deformado, com uma idade herdada de 2709 ± 9 Ma. A constante presença de grãos herdados nesses granitos sugere uma fonte crustal reciclada.

- ✓ O cenário geodinâmico de formação das rochas félsicas do Complexo Divinópolis e do sul do cráton São Francisco mostra uma consistência das assinaturas geoquímicas em relação a geocronologia. Baseado nisso, um modelo geodinâmico é proposto para explicar a evolução da região.

- ✓ O primeiro estágio abrange o período anterior a 3,2 Ga (Evento Santa Bárbara), preservado majoritariamente como herança, idades $TDM_{Nd}$ ou zircões detríticos. Crosta com idade de 3,2 Ga é preservada apenas no Complexo Santa Bárbara o que sugere constante reciclagem para o manto. Ascensões mantélicas causariam delaminação da litosfera máfica resultando em fusão e geração de magma félsico alocado na crosta superior. Instabilidade gravitacional gera o afundamento de crosta mais densa, resultando no início de processos de diferenciação mantélica (Fig. 5.1a). Tais processos atuariam predominantemente por forças verticais e gravitacionais.

- ✓ Durante o segundo estágio (Evento Rio das Velhas I) parte da crosta máfica espessada é fundida, resultando nos primeiros TTGs a partir de 3,0 Ga. O primeiro pico de formação de micro continentes

félsicos pode ser registrado em 2915–2860 Ma, onde a fusão de uma fonte máfica sem granada oriunda do estágio anterior (a aproximadamente 12 kbar) resultaria em magmas TTGs de baixa e média pressão. Esses TTGs formariam os primeiros continentes, menos densos em relação as quilhas máficas e vulcanoclásticas e podem estar relacionados a formação da configuração de domos-e-quilhas do sul do cráton (Fig. 5.1b).

- ✓ Entre 2790 e 2775 Ma o segundo maior pico de formação de TTGs ocorre, representando o Evento Rio das Velhas II. Com o crescimento dos micro continentes, a deriva dos mesmos pode atuar como um agente tectônico causando colisões e imbricamento. Nestes casos, tanto processos de delaminação litosférica quanto inícios de subducção seriam responsáveis pela variação geoquímica vista no sul do cráton. Os processos associados a subducção estão relacionados a formação localizada de andesitos, adakitos e rochas similares a sanukitoides, enquanto ambientes intraplaca estariam relacionados a fusão de crosta máfica espessa e principalmente formação de TTGs de mais alta pressão (Fig. 5.1c). Neste cenário uma tectônica predominantemente horizontal atuaria e devido as condições termais elevadas e crosta menos rígida, pode-se esperar inícios de subducção de baixo ângulo e/ou quebra da crosta descendente (*slab break-off*).

- ✓ A partir de 2760 inicia-se o Evento Mamona, dividido neste trabalho em Mamona I (2760–2715 Ma) e Mamona II (2705–2680 Ma) com base nas duas fases de intrusões graníticas potássicas que se seguiram após a Orogenia Rio das Velhas. A fase mais antiga compreende monzogranitos foliados de médio-K com afinidade colisional que se formaram durante a colagem dos micro continentes. Episódios de amalgamação e acreção resultaram em granitos do tipo-I com afinidade colisional formados por retrabalhamento da crosta TTG e potássica (Fig. 5.1d).

- ✓ O Evento Mamona II, por outro lado, corresponde a fase extensional de relaxamento que se seguiu após a colagem dos blocos (Fig. 5.1e). A fusão por descompressão em níveis crustais mais rasos nesse ambiente resultou em granitos pós-colisionais ricos em potássio, oriundos de uma fonte híbrida, ou seja, fusão dos componentes anteriores. Distribuição semelhante ocorre nos granitos de alto-K dos complexos Bonfim, Campo Belo e Belo Horizonte, onde entre 2700 e 2600 Ma possuem afinidade pós-colisional e extensional. Os últimos pulsos de magmatismo potássico ocorrem de forma localizada em 2650 e 2610 Ma.

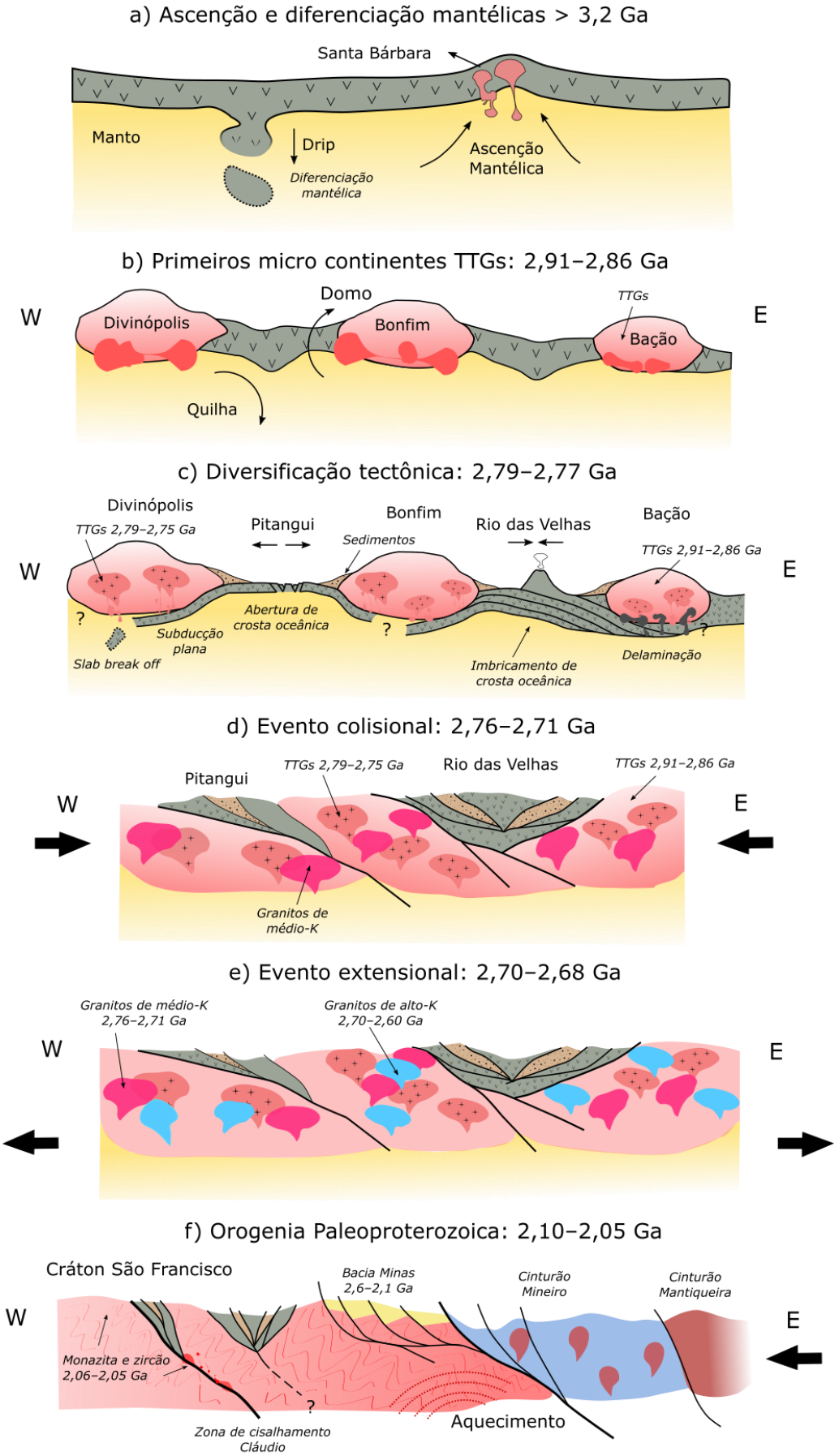


**Figura 5.1:** Desenho esquemático ilustrando o modelo de evolução geodinâmico do Complexo Divinópolis e terrenos adjacentes na região sul do cráton São Francisco.

- ✓ A maturação do sul do cráton São Francisco representa de modo consistente a transição de uma geodinâmica primitiva (TTGs sódicos) para cada vez mais evoluída (granitoides potássicos) e que se aproxima do estilo tectônico Fanerozoico, principalmente após 2,7 Ga. Esse longo período transicional pode ser correlacionado à interpretação de diversos autores como a explosão dos primeiros ambientes de subducção primitivas e colisão, conforme o planeta Terra busca atingir equilíbrio termal.

- ✓ Após 2,6 Ga a crosta passa por um período de estabilidade cratônica com a deposição do Supergrupo Minas até 2,1 Ga. A partir de então, a crosta é reativada pela Orogenia Minas, aquecendo o embasamento Arqueano o suficiente para resetar monazita e titanita entre 2100 e 2050 Ma (Fig. 5.1f). Em zonas onde a entrada de fluidos pode ser facilitada (ex. Zona de Cisalhamento Cláudio) pode ocorrer a cristalização de zircão. No Complexo Divinópolis, esse evento pode ser datado em monazita em 2062 ± 7 Ma em um gnaisse próximo a uma intrusão granítica no domínio central. Essa idade é uma das poucas obtidas no centro de um domo gnáissico, mostrando que a reativação da Orogenia Minas foi extensa e significativa, resultando em um metamorfismo sin-colisional regional, não se restringindo as bordas dos complexos gnáissicos.

# REFERÊNCIAS


**Albert, C., Farina, F., Lana, C., Stevens, G., Storey, C., Gerdes, A., Dopico, C. M. 2016.** Archean crustal evolution in the Southern São Francisco craton, Brazil: Constraints from U-Pb, Lu-Hf and O isotope analyses. *Lithos*, **266–267**: 64–86.

**Aleinikoff, J.N., Schenk, W.S., Plank, M.O., Srogi, L.A., Fanning, C.M., Kamo, S.L., Bosbyshell, H. 2006.** Deciphering igneous and metamorphic events in high-grade rocks of the Wilmington complex, Delaware: morphology, cathodoluminescence and backscattered electron zoning, and SHRIMP U–Pb geochronology of zircon and monazite. *Geological Society of America Buletin*, **118**: 39–64.

**Alkmim, F.F., Marshak, S. 1998.** Transamazonian orogeny in the southern São Francisco craton region, Minas Gerais, Brazil: evidence for Paleoproterozoic collision and collapse in the Quadrílatero Ferrífero. *Precambrian Research*, **90:** 29-58.

**Alkmim, F.F., Noce, C.M. (eds.) 2006.** The Paleoproterozoic Record of the São Francisco Craton. IGCP 509 Field workshop, Bahia and Minas Gerais, Brazil. Field Guide e Abstracts, 114 pp.

**Alkmim, F.F., Teixeira, W., 2017.** The Paleoproterozoic mineiro belt and the Quadrilátero Ferrífero. *In:* Heilbron, M., Alkmim, F.F., Cordani, U.G. (Eds.), The São Francisco Craton and its Margins, Eastern Brazil, Geology Review Series. Springer-Verlag, pp. 71-94.

**Almeida, F.F.M. 1977.** O Cráton do São Francisco. *Revista Brasileira de Geociências*, **7:** 349- 364.

**Aguilar, C., Alkmim, F.F., Lana, C., Farina, F., 2017.** Palaeoproterozoic assembly of the São Francisco craton, SE Brazil: new insights from U-Pb titanite and monazite dating. *Precambrian Research*, **289**: 95-115.

**Anderson, P., Wasserburg G., Chen, J., Papanastassiou, D., Ingri, J. 1995.** $^{238}$U-$^{234}$U and $^{232}$Th-$^{230}$Th in the Baltic Sea and in river water. *Earth and Planetary Science Letters*,**130:** 217–234.

**Anhaeusser, C. 2014.** Archaean *greenstone belts* and associated granitic rocks: a review. *Journal of African Earth Sciences*, **100:** 684-732.

**Baltazar, O.F. Zucchetti, M. 2007.** Lithofacies associations and structural evolution of the Archean Rio das Velhas *Greenstone belt*, Quadrilátero Ferrífero, Brazil: a review of the setting of gold deposits. O*re Geology Reviews*, **32**: 471–499.

**Barbosa, J.S.F., Sabaté, P., 2004.** Archean and Paleoproterozoic crust of the São Francisco craton, Bahia, Brazil: geodynamic features. *Precambrian Research*, **133**: 1-27.

**Barbosa, N.S., Teixeira, W., Ávila, C.A., Montecinos, P.M., Bongiolo, E.M., 2015**. 2.17–2.10 Ga plutonic episodes in the Mineiro belt, São Francisco Craton, Brazil: U–Pb ages, geochemical constraints and tectonics. *Precambrian Research*. 270, 204–225.

**Bédard, J.H. 2018.** Stagnant lids and mantle overturns: Implications for Archaean tectonics, magmagenesis, crustal growth, mantle evolution, and the start of plate tectonics. *Geoscience Frontiers*, **9**: 19–49.

**Brando Soares, M.B., Corrêa Neto, A.V., Zeh, A., Cabral, A.R., Pereira, L.F., Prado, M.G.B., Schlichta, T. M. 2017.** Geology of the Pitangui Greenstone Belt, Minas Gerais, Brazil: Stratigraphy, geochronology and BIF geochemistry. *Precambrian Research*, **291:** 17–41.

**Brando Soares, M., Corrêa Neto, A. V., Fabricio-Silva, W. 2020.** The development of a Meso- to Neoarchean rifting-convergence-collision-collapse cycle over an ancient thickened protocontinent in the south São Francisco craton, Brazil. *Gondwana Research*, **77:** 40–66.

**Bickle, M.J., 1986.** Implication of melting for the stabilization of lithosphere and heat loss in the Archaean. *Earth and Planetary Science Letters*, **80:** 314-324.

**Campos, J., Carneiro, M., Basei, M., 2003.** U-Pb evidence for Late Neoarchean crustal reworking in the southern São Francisco Craton (Minas Gerais, Brazil): In: Anais da Academia Brasileira de Ciências, 75: 497-511.

**Campos, J. C. S., & Carneiro, M. A. 2008**. Neoarchean and Paleoproterozoic granitoids marginal to the Jeceaba-Bom Sucesso lineament (SE border of the southern São Francisco craton): Genesis and tectonic evolution. *Journal of South American Earth Sciences*, **26(4):** 463–484.

**Carneiro, M.A., Teixeira, W., Carvalho Junior, I.M., Fernandes, R.A. 1998.** Ensialic Tectonic Setting of the Archaean Rio das Velhas Greenstone Belt: Nd and Pb Isotopic Evidence from the Bonfim Metamorphic Complex, Quadrilátero Ferrífero, Brazil. *Revista Brasileira de Geociências*, **28(2)**: 189–200.

**Carneiro, M.S, Teixeira, W., Carvalho-Júnior, I.M., Pimentel, M.M., Oliveira, A.H. 2004.** O comportamento dos sistemas Sm–Nd e Rb–Sr da Sequência Acamadada Máfico-Ultramafica Ribeirão dos Motas (Arqueano) Craton São Francisco Meridional: Evidências de Enriquecimento Mantélico e Fracionamento Isotópico. *Geologia USP, Série Científica*, **4:**13–26.

**Carneiro, M.A., Nalini Júnior, H.A., Endo, I., Suita, M.T.F., Castro, P. T.A., Barbosa, M.S.C., Campos, J.C.S., Goulart, L.E.A., Silva, E.F.S., Pereira, A.A., Tavares, T.D., Jiamelaro, F., Carneiro, J.M., Mariano, L.C., Miguel, F.P., Silva Junior, A.C., Barbosa, A.S., Prado, G.E.A., Santos, C., Urbano, E.E.M.C. 2007**. Nota explicativa das folhas Campo Belo (SF.23-V-B-VI) e Oliveira (SF.23-X-A-IV), escala 1:100.000. Minas Gerais, UFOP/CPRM, 114 p.

**Carvalho, B.B., Sawyer, E.W., Janasi, V.A. 2016.** Crustal reworking in a shear zone: Transformation of metagranite to migmatite. *Journal of Metamorphic Geology*, **34:** 237–264.

**Carvalho, B. B., Janasi, V. A., Sawyer, E. W. 2017a.** Evidence for Paleoproterozoic anatexis and crustal reworking of Archean crust in the São Francisco Craton, Brazil: A dating and isotopic study of the Kinawa migmatite. *Precambrian Research*, **291:** 98–118.

**Chaves, A.O., Oliveira, E.K., Garcia, L.R.A., 2013.** Desenvolvimento do método de datação química U-Th-Pb de monazita por microssonda eletrônica na UFMG. *Geonomos* **21(2):** 13–18.

**Chaves, A.O., Goulart, L. E. A., Coelho, R. M., Miranda, D. A., Aranda, R.O.A., Ramos, S.L.L.M. 2019.** High-pressure eclogite facies metamorphism and decompression melting recorded in paleoproterozoic accretionary wedge adjacent to probable ophiolite from Itaguara (southern São Francisco Craton - Brazil). *Journal of South American Earth Sciences*, **94:** 102226.

**Coelho, R. M., Chaves, A. O. 2019.** Pressure-temperature-time path of Paleoproterozoic khondalites from Claudio shear zone (southern São Francisco craton, Brazil): Links with khondalite belt of the North China craton. *Journal of South American Earth Sciences*, **94**: 102250.

**Condie, K. C., Kröner, A. 2013.** The building blocks of continental crust: Evidence for a major change in the tectonic setting of continental growth at the end of the Archean. *Gondwana Research*, **23(2):** 394–402.

**Corrêa da Costa, P.C. 1999.** Episódios de formação de crosta continental Arqueana no Cráton São Francisco Meridional: um exemplo a partir da região de Candeias – Campo Belo, MG. Dissertação de Mestrado. Departamento de Geologia da Escola de Minas da Universidade Federal de Ouro Preto, 151 p.

**Cotta, A.J.B. Enzweiler J. 2010.** Classical and New Procedures of Whole Rock Dissolution for Trace Element Determination by ICP-MS. *Geostandards and Geoanalytical Research*, **36:** 27-50.

**Couto, D.J.F, Carneiro, M.A. 2007.** The genesis of the metaultramafites from Cláudio (MG). *Geochimica Brasiliensis*, **21(1)**: 009 - 021, 2007

**Cutts, K., Lana, C., Alkmim, F., Farina, F., Moreira, H., Coelho, V. 2019.** Metamorphism and exhumation of basement gneiss domes in the Quadrilátero Ferrífero: Two stage dome-and-keel evolution? *Geoscience Frontiers*, **10:** 1765-1787.

**Dantas, E.L., Brito Neves, B.B., Fuck, R.A. 2013.** Looking for the Early Archean rocks in South America: U–Pb dating and Hf isotopes in zircons from the north São Francisco Craton, Brazil. *Geological Society of America, Annual Meeting*, 269: 5.

**de Wit, M.J. 2004.** Archean *greenstone belts* do contain fragments of ophiolites. *In:* T. M. Kusky (Ed.), *Precambrian Ophiolites and Related Rocks*, Amsterdam: Elsevier, p.: 599–614.

**Dhuime, B., Wuestefeld, A., Hawkesworth, C.J., 2015.** Emergence of modern continental crust about 3 billion years ago. *Nature Geoscience*, **8 (7):** 552-555.

**Door, J.V.N. 1969.** Physiographic, stratigraphic and structural development of the Quadrilátero Ferrífero, Minas Gerais, Brazil, *U.S.G.S. Professional Paper*, **614 –A**: 110 p.

**Fabricio-Silva, W., Rosière, C. A., Bühn, B. 2018.** The shear zone-related gold mineralization at the Turmalina deposit, Quadrilátero Ferrífero, Brazil: structural evolution and the two stages of mineralization. *Mineralium Deposita*.

**Farina, F., Albert, C., Lana, C. 2015.** The Neoarchean transition between medium-and high-K granitoids: Clues from the Southern São Francisco Craton (Brazil). *Precambrian Research*, **266:** 375-394.

**Farina, F., Albert, C., Martinez Dopico, C., Aguilar Gil, C., Moreira, H., Hippertt, J., Cutts, K., Lana, C., Alkmim, F.F., 2016.** The Archean-Paleoproterozoic evolution of the Quadrilátero Ferrífero (Brasil): current models and open questions. *Journal of South American Earth Sciences*, **68:** 4-21.

**Fernandes, R.A., Carneiro, M.A. 2000.** O Complexo Metamórfico Campo Belo (Cráton São Francisco Meridional) Unidades Litodêmicas e Evolução Tectônica. *Revista Brasileira de Geociências*, **30:** 671-678.

**Foley, S.F., Tiepolo, M., Vannucci, R. 2002**. Growth of early continental crust controlled by melting of amphibolite in subduction zones. *Nature*, **417:** 637–640.

**Furnes, H., Dilek, Y., De Wit, M. 2014.** Precambrian greenstone sequences represent different ophiolite types. *Gondwana Research*, **27:** 649–685.

**Gonçalves, G. O., Lana, C., Scholz, R., Buick, I. S., Gerdes, A., Kamo, S. L., Corfu, F., Marinho, M. M., Chaves, A. O., Valeriano, C., Nalini, H. A. 2016.** An assessment of monazite from the Itambé pegmatite district for use as U-Pb isotope reference material for microanalysis and implications for the origin of the "Moacyr" monazite. *Chemical Geology*, **424**: 30–50.

**Goulart, L.E.A., Carneiro, M.A., Endo, I., Suita, M.T.F. 2013.** New evidence of Neoarchean crustal growth in southern São Francisco Craton: the Carmópolis de Minas Layered Suite, Minas Gerais, Brazil. *Brazilian Journal of Geology*, **43(3):** 445–459.

**Hamilton, W.B. 2011.** Plate tectonics began in Neoproterozoic time, and plumes from deep mantle have never operated. *Lithos*, 123:1–20.

**Hoffmann, J. E., Zhang, C., Moyen, J.-F., Nagel, T. J. 2019.** The Formation of Tonalites–Trondjhemite–Granodiorites in Early Continental Crust. *In:* Earth's Oldest Rocks.

**Jahn, B., Glikson, A.Y., Peucat, J.-J., Hickman, A.H., 1981.** REE geochemistry and isotopic data of Archaean silicic volcanics and granitoids from the Pilbara block, western Australia: implications for early crustal evolution. *Geochimica et Cosmochimica Acta*, **45:** 1633–1652.

**Janoušek, V., Farrow, C.M., Erban, V. 2006.** Interpretation of whole-rock geochemical data in igneous geochemistry: introducing Geochemical Data Toolkit (GCDkit). *Journal of Petrology*, **47:**1255-1259.

**Johnson, T.E., Brown, M., Kaus, B.J., VanTongeren, J.A., 2014.** Delamination and recycling of Archaean crust caused by gravitational instabilities. *Nature Geoscience*, **7:** 47-52.

**Johnson, T. E., Brown, M., Gardiner, N. J., Kirkland, C. L., Smithies, R. H. 2017.** Earth's first stable continents did not form by subduction. *Nature*, **543 (7644)**, 239–242.

**Lana C., Alkmim F., Armstrong R., Scholz R., Romano R., Nalini H. 2013.** The ancestry and magmatic evolution of Archaean TTG rocks of the Quadrilátero Ferrífero province, southeast Brazil: *Precambrian Research*, **231:** 157-173.

**Li X. 2006.** Understanding 3D analytic signal amplitude. *Geophysics*, **71:**13-16.

**Lobato, L.M., Ribeiro-Rodrigues, L.C., Zuchetti, M., Noce, C.M., Baltazar, O.F., da Silva, L.C., Pinto, C.P. 2001a.** Brazil's premier gold province: part I: the tectonic, magmatic and structural setting of gold deposits in the Archean Rio das Velhas greenstone belt, Quadrilátero Ferrífero. *Mineralium Deposit*a, **36**: 249-277.

**Ludwig, K.R., 2012.** User's Manual for Isoplot Version 3.75-4.15: a Geochronological Toolkit for Microsoft Excel. *Berkeley Geochronological Center Special Publication*, **5**.

**Machado, N., Carneiro, M.A. 1992.** U–Pb evidence of late Archean tectono-thermal activity in the southern São Francisco shield, Brazil. Canadian Journal of Earth Science, 29: 2341–2346.

**Machado Filho L., Ribeiro, M.W., Gonzalez, S.R., Schenini C.A., Santos Neto, A.S., Barros Palmeira, R.C., Pires, J.L., Teixeira, W., Castro, H.E.F. 1983.** Geologia. *In:* Projeto RADAM Brasil, Folhas SF.23/24 Rio de Janeiro/Vitória, **32:** 36-45.

**Marshak, S., Tinkham, D., Alkmim, F.F., Brueckner, H., Bornhorst, T., 1997.** Dome-and-keel provinces formed during Paleoproterozoic orogenic collapse - core complexes, diapirs, or neither? Examples from the Quadrilátero Ferrífero and the Penokean Orogen. *Geology*, **25:** 415-418.

**Martin, H., 1994.** The Archean grey gneisses and the genesis of the continental crust. *In*: K. C. Condie (ed.) *Archean Crustal Evolution*. Elsevier, Amsterdam, pp.: 205–259.

**Martin, H., Smithies, R.H., Rapp, R., Moyen, J.F., Champion, D., 2005.** An overview of adakite, tonalite-trondhjemite-granodiorite (TTG), and sanukitoid: Relationships and some implications for crustal evolution: *Lithos*, **79:** 1–24.

**Melo-Silva, P., Amaral, W.S., Oliveira, E.P. 2020.** Geochronological evolution of the Pitangui Greenstone Belt, southern São Francisco Craton, Brazil: constraints from U-Pb zircon age, geochemistry and field relationships. *Journal of South American Earth Sciences*, **99:**102380.

**Moreira, H., Lana, C., Aria, S.H., Nalini Jr, H.A. 2016.** The detrital zircon record of an Archaean convergent basin in the. *Precambrian Research*, **275:** 84–99.

**Moreno, J. A., Baldim, M. R., Semprich, J., Oliveira, E. P., Verma, S. K., Teixeira, W. 2017.** Geochronological and geochemical evidences for extension-related Neoarchean granitoids in the southern São Francisco Craton, Brazil. *Precambrian Research*, **294:** 322–343.

**Moyen J.F. 2011.** The composite Archaean grey gneisses: Petrological significance, and evidence for a non-unique tectonic setting for Archaean crustal growth. *Lithos*, **123:** 21–36.

**Moyen, J. Martin, H. 2012.** Forty years of TTG research. *Lithos*, **148:** 312–336.

**Moyen, J.F., Laurent, O., 2018.** Archaean tectonic systems: a view from igneous rocks. *Lithos*, **302-303**: 99-125.

**Navarro, M.S., Tonetto, E.M., Oliveira, E.P., 2015.** LA-SF-ICP-MS U-Pb zircon dating at University of Campinas, Brazil. *In*: IAG, Geoanalysis. Leoben, Anais, CD-ROM.

**Noce, C.M., Machado, N., Teixeira, W. 1998.** U–Pb geochronology of gneisses and granitoids in the Quadrilátero Ferrífero (Southern São Francisco craton): age constraints for Archean and Paleoproterozoic magmatism and metamorphism. Revista Brasileira de Geociências 28: 95–102.

**Noce, C. M., Zuccheti, M., Baltazar, O. F., Armstrong, R., Dantas, E., Renger, F. E., Lobato, L. M. 2005.** Age of felsic volcanism and the role of ancient continental crust in the evolution of the Neoarchean Rio das Velhas *Greenstone belt* (Quadrilátero Ferrífero, Brazil): U-Pb zircon dating of volcaniclastic graywackes. *Precambrian Research*, **141:** 67–82.

**Nutman, A.P., Cordani, U.G. 1993.** SHRIMP U–Pb zircon geochronology of Archaean granitoids from the Contendas-Mirante area of the São Francisco craton, Bahia, Brazil. *Precambrian Research*, **63:** 179–188.

**O'Neill, C., Zhang, S. 2019.** Modeling Early Earth Tectonics. *In:* Earth's Oldest Rocks. Elsevier.

**Oliveira, E.A. 1999.** Geologia, Petrografia e Geoquímica do Maciço Granitóide de Cachoeira da Prata. Dissertação de Mestrado, Instituto de Geociências, Universidade Federal de Minas Gerais, 82 p.

**Oliveira, A.H. 2004.** Evolução tectônica de um fragmento do Cráton São Francisco Meridional com base em aspectos estruturais, geoquímicos (rocha total) e geocronológicos (Rb-Sr, Sm-Nd, Ar-Ar, U-Pb). Tese de Doutorado, Departamento de Geologia da Escola de Minas da Universidade Federal de Ouro Preto, 156 p.

**Oliveira, E.P., McNaughton, N.J., Zincone, S.A., Talavera, C. 2020.** Birthplace of the São Francisco Craton, Brazil: Evidence from 3.60 to 3.64 Ga Gneisses of the Mairi Gneiss Complex. *Terra Nova*, **32**:281–289.

**Paton, C., Woodhead, J.D., Hellstrom, J.C., Hergt, J.M., Greig, A., Maas, R. 2010.** Improved laser ablation U-Pb zircon geochronology through robust downhole fractionation correction. Geochemistry, Geophysics and Geosystems, 11: Q0AA06

**Petrus, J.A., Kamber, B.S., 2012.** VizualAge: a novel approach to laser ablation ICP-MS U–Pb geochronology data reduction. Geostandards and Geoanalytical Research, 36: 247–270.

**Pinheiro, S.O., Nilson, A.A., 2000.** Metakomatiitic and meta-ultramafic rocks from the Rio Manso region, Minas Gerais: geology, textures and metamorphism. *Revista Brasileira de Geociências*, **30:** 417–419

**Pinto, C.P., Silva, M.A. 2014.** Mapa Geológico do Estado de Minas Gerais. CODEMIG, Governo de Minas, CPRM, Secretaria de Geologia, Mineração e Transformação Mineral, Ministério de Minas e Energia, Governo Federal do Brasil.

**Polat, A. 2012.** Growth of Archean continental crust in oceanic island arcs. *Geology*, **40**, 383–384.

**Rapp, R.P., Watson, E.B. 1995.** Dehydration melting of metabasalt at 8–32 kbar: implications for continental growth and crust-mantle recycling. *Journal of Petrology*, **36**: 891–931.

**Roest, W.R.M.P. 1992.** Magnetic interpretation using the 3-D analytic signal. *Geophysics*, **57:** 116–125.

**Romano, A.W. 2007.** Nota explicativa da Folha Pará de Minas (SE-23-Z-C-IV) 1:100.000. CPRM-UFMG, 65p.

**Romano, R., Lana, C., Alkmim, F.F., Stevens G.S., Armstrong R. 2013.** Stabilization of the southern portion of the Sao Francisco Craton, SE Brazil, through a long-lived period of potassic magmatism. *Precambrian Research*, **224:** 143-159.

**Rudnick, R.L. Gao, S. 2004.** *Composition of the Continental Crust. In:* H.D. Holland e K.K. Turekian (eds). *Treatise of Geochemistry*. Elsevier, Amsterdam, pp.: 1–64

**Santos-Pinto, M., Peucat, J.J., Martin, H., Barbosa, J.S.F., Fanning, C.M., Cocherie, A., Paquette, J.L. 2012.** Crustal evolution between 2.0 and 3.5 Ga in the southern Gavião block (Umburanas-Brumado-Aracatu region) São Francisco Craton, Brazil. A 3.5–3.8 Ga proto-crust in the Gavião block? *Journal of South American Earth Sciences*, **40**: 129-142.

**Shorscher, J.H.D. 1978.** Komatiítos na estrutura "*greenstone belt*" Série Rio das Velhas, Quadrilátero Ferrífero, Minas Gerais, Brasil. *In:* SBG, 30º *Congresso Brasileiro de Geologia, Anais*, p. 292-293.

**Simon, M. B., Marques Bongiolo, E., Ávila, C. A., Oliveira, E. P., Teixeira, W., Stohler, R. C., e Soares de Oliveira, F. V. 2018.** Neoarchean reworking of TTG-like crust in the southernmost portion of the São Francisco Craton: U-Pb zircon dating and geochemical evidence from the São Tiago Batholith. *Precambrian Research*, **314:** 353–376.

**Sizova, E., Gerya, T., Stüwe, K., Brown, M., 2015.** Generation of felsic crust in the Archean: a geodynamic modeling perspective. Precambrian Research, **271:** 198–224.

**Smith, W.H.F., Wessel, P. 1990.** Gridding with continuous curvature splines in tension. *Geophysics*, **v.55, n.3**: p.293-305.

**Teixeira,W., Figueiredo, M.C.H. 1991.** An outline of Early Proterozoic crustal evolution in the Sao Francisco craton, Brazil: a review. *Precambrian Research*, **53:** 1-22.

**Teixeira, W., Carneiro, M.A., Noce, C.M., Machado, N., Sato, K., Taylor, P.N. 1996.** Pb, Sr and Nd isotopic constraints on the Archean evolution of gneissic-granitoid complexes in the southern São Francisco Craton, Brazil. *Precambrian Research*, **78:** 151–164.

**Teixeira, W., Cordani, U.G., Nutman, A.P., Sato, K. 1998.** Polyphase Archean evolution in the Campo Belo metamorphic complex, Southern São Francisco Craton, Brazil: SHRIMP U-Pb zircon evidence. *Journal of South American Earth Sciences*, **11:** 279-289.

**Teixeira, W., Oliveira, E.P., Marques, L.S., 2017a.** The nature and evolution of the Archean Crust of the São Francisco Craton. In: Heilbron, M., Alkmim, F., Cordani, U.G. (Eds.), São Francisco Craton, Eastern Brasil: tectonic genealogy of a miniature continent, *Regional Geology Review Series*. Springer-Verlag, pp. 29–56.

**Teixeira, W., Oliveira, E. P., Peng, P., Dantas, E. L., e Hollanda, M. H. B. M. 2017b.** U-Pb geochronology of the 2.0 Ga Itapecerica graphite-rich supracrustal succession in the São Francisco Craton: Tectonic matches with the North China Craton and paleogeographic inferences. *Precambrian Research*, **293**: 91–111.

**Thorman C., Ladeira E., Schnabel D., 1986.** Gold Deposits Related to Greenstone belts in Brazil - Deposit Modeling Workshop Part A - Excursions. In: *U.S. Geological Survey Bulletin* **1980-A**: 94 p.

**Turner, S., Rushmer, T., Reagan, M., e Moyen, J.-F. 2014**. Heading down early on? Start of subduction on Earth Geochemical stratigraphy of subduction initiation. *Geology*, **42 (2)**,139-142.

**Uhlein, G.J., Uhlein, A., Halverson, G.P., Stevenson, R., Caxito, F.A., Cox, G.M., Carvalho, J.F.M.G. 2016.** The Carrancas Formation, Bambuí Group: A record of pre-Marinoan sedimentation on the southern São Francisco craton, Brazil. *Journal of South American Earth Sciences*, **71:** 1–16.

**Valeriano, M.M., Rosetti, D.F. 2011.** Topodata: Brazilian full coverage refinement of SRTM data. *Applied Geography (Sevenoaks)*, **32:** 300-309.

**Wiedenbeck M., Allé P., Corfu F., Griffin W.L., Meier M., Oberli F., von Quadt A., Roddick J.C. Spiegel W. 1995.** Three natural zircon standards for U-Th-Pb, Lu-Hf, trace element and REE analyses. *Geostandards Newsletter*, **19:** 1-23.

**Wiedenbeck M., Hanchar J.M., Peck W.H., Sylvester P., Valley J., Whitehouse M., Kronz A., Morishita Y. Nasdala L., Fiebig J., Franchi I., Girard J.-P., Greenwood R.C., Hinton R., Kita N., Mason P.R.D., Norman M., Ogasawara M., Piccoli P.M., Rhede D., Satoh H., Schulz-Dobrick B., Skår Ø., Spicuzza M.J., Terada K., Tindle A., Togashi S., Vennemann T., Xie Q. Zheng Y.-F. 2004.** Further characterisation of the 91500 zircon crystal. *Geostandards and Geoanalytical Research*, **28:** 9-39.

**Wyman, D. 2018.** Do cratons preserve evidence of stagnant lid tectonics? *Geoscience Frontiers*, **9(1)**: 3–17.

**Zacchi E.N.P., Silva A.M., Toledo, C.L.B., Souza Filho, C.R. 2007**. As três anomalias elípiticas da porção sul do Cráton São Francisco: novos alvos para minerelização de grafita? *Brazillian Journal of Geophysics.* **25 (4):** 421-431.

# ANEXO 1: GEOQUÍMICA E PETROGÊNESE

Manuscrito: **“Lithogeochemical evolution and petrogenesis of TTGs and potassic granites of Divinópolis Complex, São Francisco Craton (Brazil)”**

# Lithogeochemical evolution and petrogenesis of TTGs and potassic granites of Divinópolis Complex, São Francisco Craton (Brazil)


## Abstract

The Archean core of São Francisco Craton in southeast Brazil is formed by Paleo- to Neoarchean granite-gneiss terrains surrounded by greenstone belts. The Divinópolis Complex is one of the preserved Neoarchean cores and is dominantly composed of tonalite-trondhjemite-granodiorite (TTG) gneiss suite and lesser granites (syeno to monzo), with preserved igneous portions. The TTGs of Divinópolis Complex correspond to the medium- and low-pressure groups, peraluminous and magnesian with moderate to low La/Yb ratio, negative Nb, Ta, and Ti, negative Eu anomalies and moderate fractionated REE pattern and HREE depletion. A portion of these TTGs are actually potassic gneisses, metaluminous and magnesian and more silica rich. They present a steeper HREE pattern, higher REE content and stronger Eu anomalies. While the TTG suite could have formed by melting of a basaltic crust without significant amounts of garnet (1000–850º C at 12 kbar) controlled by plagioclase in the source, the potassic suite probably formed by assimilation and partial melting of pre-existing TTGs, with addition of water and $K_2O$ (850–750º C at 12 kbar). The TTG and potassic suites are related to processes of delamination of thickened mafic lithosphere and shallow proto subduction during collision and accretion. Granitoid intrusions may compose 30% of Divinópolis Complex and were emplaced as two distinct phases. The first one is foliated and rich in plagioclase (medium-K granites), while the other is non-deformed and remarkably richer in alkali feldspar (high-K granites), with characteristics similar to the typical continental granite. The medium- and high-K granites derived from melting of a mix of TTG and potassic sources in the shallow crust. The medium-K granites (granodiorites and monzogranites) share similar characteristics with the TTG and potassic suite and their generation may be related to a collisional environment resulting in crustal thickening. The High-K granites (syenogranites) are ferroan and metaluminous, generated in a shallower environment in a post-collisional extensional environment. The felsic rocks of Divinópolis Complex illustrate a temporal evolution from sodic to potassic crust in a low- to medium-pressure environment transitional from vertical magmatism and gravitational processes to reworking of crust and primitive subduction, with horizontal accretion. They are a result of geodynamic diversification and thermal stabilization of the cratonic lithospheres in the Late Archean (~2.6 Ga).

## 1. Introduction

There is no general agreement about the operating tectonic conditions during the Archean, but the main models call for a hotter mantle that favors stronger plume activity dominated by vertical accretion (e.g. Stern, 2008; Hamilton, 2011), and a model that calls for episodic arc-continent accretion and plate motion analogous to modern ones (e.g. van Hunen and Moyen, 2012; Furnes et al., 2014; Condie, 2018). A third hypothesis suggests that both conditions were operating (Bédard et al., 2013; Bédard, 2018). The end of the Archean eon (3.0-2.5 Ga) was a period of change in many aspects of the geological record, with a substantial diversification in Earth's geodynamics (Laurent et al., 2014), such as the abrupt appearance of sanukitoids and disappearance of TTGs (Halla et al., 2016). This diversification is particularly recorded in the preserved ancient crust of Archean cratons. While greenstone belts have been investigated for decades due to their economic potential, only recently we began to recognize the complex evolution of gneisses and granitoids of Archean terrains, which includes variable geochemical traits (TTGs, potassic rocks, high-K granites) and a mix of operating and non-operating plate tectonics, providing a link to modern continental crust (Anhauesser, 2014; Moyen and Martin, 2012; Palin et al., 2016).

According to Moyen (2011) on a classical paper about Archean gneisses, the TTG series (s.l. and s.s.) can be classified in two main groups: a general LILE-enriched potassic group and a group of sodic TTGs that can be divided into low-, medium- and high-pressure that are essentially portions of a continuum with blurred boundaries. The high-pressure (HP) group has low HREE, Nb, Ta and high Sr. The low-pressure (LP) group shows higher HREE, Nb and Ta and lower Sr, while the medium-pressure (MP) group corresponds to an intermediate between previous ones. The sodic TTGs may still be divided into high-Al and low-Al groups, where the first mostly matches the HP TTGs, and the last, the LP and MP TTGs (Barker and Arth, 1976; Martin, 1994).

Following that approach, Laurent et al. (2014) revised the previous classifications of late-Archean granitoids into four different groups: 1) sodic granitoids (TTGs), 2) sanukitoids (*s.l.*), 3) biotite- and two-mica granites, and 4) hybrid granitoids, representing the dynamic evolution of late-Archean crust, from tonalite-trondhjemite suites to granodiorite-granite. Late-Archean granitoids with hybrid characteristics were identified in most cratons, such as Pilbara (Smithies et al., 2003), Kaapvaal (Sanchez-Garrido et al., 2011), Wyoming Province (Frost et al., 2006), the Tróia Massif (Ganade et al., 2017) and the São Francisco Craton in Brazil (Romano et al., 2013; Farina et al., 2015).

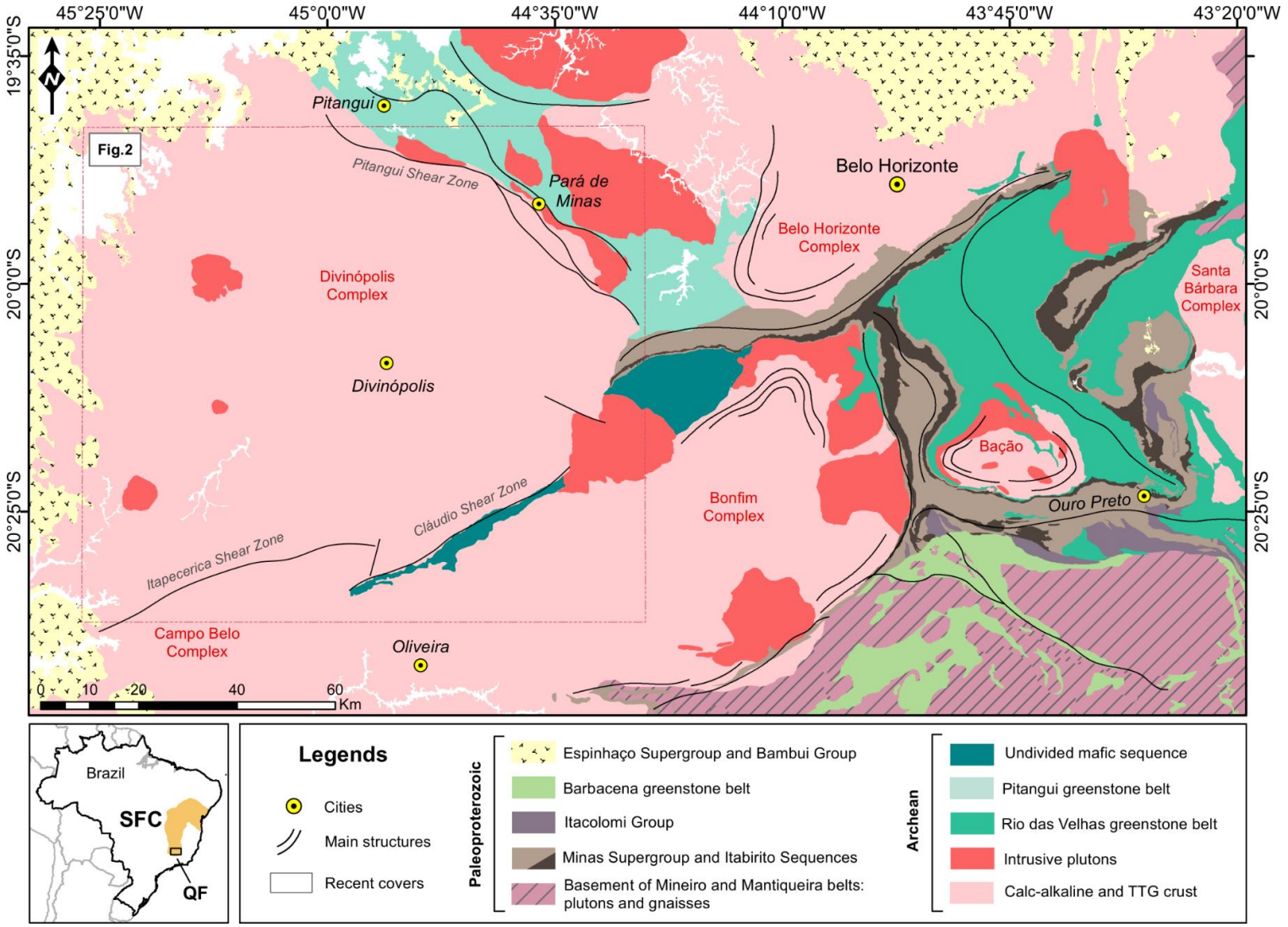


**Figure 1:** Regional geological setting of southern São Francisco Craton and Quadrilátero Ferrífero (modified after Pinto and Silva, 2014). The map shows the major gneiss-granite complexes (Bação, Bonfim, Belo Horizonte, Campo Belo, Divinópolis and Santa Bárbara) and Pitangui and Rio das Velhas greenstone belts. Lower left: localization of São Francisco Craton (SFC) in Brazil.

The São Francisco Craton is composed of a typical Archean association of granite-greenstone terrains that contain ancient crustal remnants as old as 3.8 Ga (Almeida, 1977; Hartmann et al., 2006; Alkmim and Noce, 2006). Despite the extensive geochronological data published (e.g. U-Pb and Lu-Hf in zircon, monazite, and titanite) (e.g. Barbosa and Sabaté, 2004; Noce et al., 2005; Farina et al. 2016), correlation between distinct events is not fully understood. A regional geochemical study was conducted by Farina et al. (2015) in the southern São Francisco Craton attesting a hybrid TTG nature for rocks of Bação, Bonfim and Belo Horizonte complexes, with source composition between partially melted metamafic crust and TTG rocks. The late potassic magmatism, on the other hand, evolved through partial melting of more fertile protoliths such as metagraywackes from the greenstone belts during crustal anatexis (Farina et al., 2015). Isotope signatures reveal that the most significant crustal growth occurred through a continuous evolution from 3.2 to 2.7 Ga (Lana et al., 2013; Albert et al., 2016).

The southern São Francisco Craton is known for its metallogenic potential with gold and iron deposits on a global scale associated with the Archean Rio das Velhas greenstone belt and the Proterozoic Minas Supergroup – the Quadrilátero Ferrífero mining district (Fig.1). The region west of the Quadrilátero Ferrífero (where Divinópolis Complex is located) has only gained importance more recently due to gold ore hosted in rocks of the Pitangui Greenstone Belt, named Turmalina and São Sebastião deposits (Brando Soares et al., 2018; Fabricio-Silva et al., 2018). The Divinópolis Complex, for instance, has been correlated to other complexes and left aside from the crustal evolution of southern São Francisco Craton. Late Archean felsic magmatism, including felsic granitoids of Divinópolis Complex, are responsible for part of the Turmalina and São Sebastião multistage gold mineralizations. Our work aims to characterize the Divinópolis Complex and its crustal evolution in the regional framework of the São Francisco Craton. Several questions must be addressed: What were the main sources of magma genesis? Can these rocks be interpreted as a typical TTG suite? Does it hold similarities with other gneiss complexes in the craton? What were the formation mechanisms of this Archean crust?

## 2. Geological background

The São Francisco Craton is one of the oldest segments of continental crust in South America, located in eastern Brazil. It is characterized by several Archean blocks bounded by Neoproterozoic fold belts (Heilbron et al., 2017) and partially covered by Phanerozoic sequences. Exposed areas of Archean crustal fragments in the São Francisco Craton are generally divided into northern and southern. The northern part is composed of the Gavião, Jequié, Serrinha and Itabuna-Salvador-Curaçá blocks. The southern São Francisco Craton is composed of granite-gneiss blocks (e.g. Divinópolis, Bonfim, Campo Belo, Belo Horizonte) separated by polydeformed, low-grade Archean to Proterozoic greenstone belts

(Pitangui and Rio das Velhas). The Archean basement and greenstone sequences are intruded by several generations of granitoid plutons (Fig.1).

Four main magmatic events were recognized in southern São Francisco Craton (Lana et al., 2013; Farina et al., 2015): Santa Bárbara (3220–3200 Ma), Rio das Velhas I (2920–2850 Ma), Rio das Velhas II (2800–2760 Ma), and Mamona (2760–2680 Ma). Santa Bárbara event is responsible for generation of juvenile sialic crust, recognized in zircon (U-Pb) of the Santa Bárbara Complex, in ancient detrital zircon from the Rio das Velhas and Pitangui Greenstone Belts (Hartmann et al., 2006; Melo-Silva et al., 2020) and from the Minas Supergroup (Moreira et al., 2016). The Rio das Velhas I and II events (Rio das Velhas Orogeny) are interpreted as a period of arc magmatism and crustal accretion (Machado et al., 1996; Silva et al., 2000; Noce et al., 2005), generating calc-alkaline plutonic and volcanic crust, TTG suites and high- to medium-K granitoids (Lana et al., 2013; Romano et al., 2013; Farina et al., 2015). The Mamona event corresponds to the final emplacement of voluminous potassic granitoids during stabilization of the craton (e.g. Teixeira et al., 1998; Campos et al., 2003; Lana et al., 2013; Romano et al., 2013). Available metamorphic Archean ages overlap the Rio das Velhas II event (Lana et al. 2013, Cutts et al., 2019).

Belo Horizonte Complex represents the largest segment of exposed crust in the southern São Francisco Craton. The granite-gneiss basement comprehends mostly banded orthogneisses intruded by coarser-grained granites, leucogranite and pegmatite dykes (Lana et al., 2013). The older gneisses and granitoids have regionally consistent trends of foliation, indicative of a pre- to syn-tectonic emplacement, while the younger granitoids are weakly to non-deformed (Machado et al., 1992; Romano et al., 2013). Farina et al. (2015) investigated the gneisses and granitoids of Bação, Bonfim and Belo Horizonte complexes (Quadrilátero Ferrífero region). These authors have found that the crust went through a major compositional change, from medium-K magmatism, responsible for the emplacement of Plg-rich granitoids during the Rio das Velhas Orogeny, to a high-K magmatism during the Mamona event, emplacing Kfs-rich granitoids. The southern domes (Bação and Bonfim) were intruded by medium-K granitoids between 2790–2770 Ma, being replaced by high-K granitoids at 2760–2680 Ma. This potassic magmatism event was termed Mamona and defined as transitional in the Belo Horizonte Complex, in which Pequi and Florestal batholiths show a mixed composition between TTG and partially melted metabasic oceanic crust (Farina et al., 2015).

The evolution of the southern São Francisco Craton is also attested in Albert et al. (2016), as well as the transition from sodic (TTG) to potassic magmatism (high-K granitoids), evidence of crustal maturation and differentiation. Albert et al. (2016) suggests that this transition is due to a geodynamic change around 2.9 Ga: distinct Paleoarchean proto-continents amalgamated during accretionary collision (possibly dominated by TTG), switching to an extensional Neoarchean regimen dominated by crustal reworking (Lana et al., 2013; Farina et al., 2015; Albert et al., 2016). This would generate the medium-K

magmas of Farina et al. (2015) by melting of old gneisses following the reworked high-K granitoids during depletion and stabilization of the crust (Lana et al., 2013; Romano et al., 2013).

Campo Belo, Divinópolis and Passa Tempo complexes are located west from Quadrilátero Ferrífero region and geographically, the delimitation of the Divinópolis Complex has not been precise. In the southern sector of the dome, where studies concentrate, Divinópolis is in contact with Bonfim and Campo Belo complexes, separated by Cláudio Shear Zone (Machado Filho et al., 1983; Oliveira, 2004; Carvalho et al., 2016; 2017a; Teixeira et al., 2017b) and Itapecerica Shear Zone (Fig.2, this work). In the Cláudio Shear Zone, protolith ages (granodiorite gneiss) were obtained for the Kinawa migmatite at 2794 ± 68, 2720 ± 28 and 2686 ± 18 Ma (Carvalho et al., 2017a). Very similar ages were found by Oliveira (2004) in the southern region of Cláudio Shear Zone, at 2749 ± 6, 2715 ± 86 and 2658 ± 7 Ma. Both authors similarly report a Proterozoic crystallization event at 2066 ± 24, 2048 ± 27 and 2034 ± 32 Ma, related to anatectic events in the shear zone, resulting in newly formed leucosome and charnokite. Only one U-Pb age for the north domain of Divinópolis Complex was obtained at 2878.5 ± 5.7 Ma, in the Pitangui Shear Zone, considerably older than the southern ages (Melo-Silva et al., 2020). The summary of available ages of Divinópolis Complex is shown in Table 1.

**Table 1.** Compilation of available ages (Ma) for the Divinópolis Complex. **SZ** = shear zone.

| Locality | Sample | Rock type | Age | | | Method | Reference |
|---|---|---|---|---|---|---|---|
| | | | Inherited | Magmatic | Metamorphic | | |
| Pitangui SZ | PM-17 | Diorite gneiss | | 2878 ± 5 | | LA-ICP-MS | [1] |
| Cláudio SZ | K82 | Diatexite protolith | | 2794 ± 68 | | SHRIMP | [2] |
| Cláudio SZ | K50A | Granodiorite gneiss | | 2704 ± 3 | | SHRIMP | [2] |
| Cláudio SZ | K25 | Monzogranite leucosome | 2686 ± 18 | 2048 ± 24 | | SHRIMP | [2] |
| Cláudio SZ | K4 | Green monzogranite | 2720 ± 28 | 2034 ± 32 | | SHRIMP | [2] |
| Cláudio SZ | AH11 | Gneiss migmatite | | 2749 ± 6 | | Ion Microprobe | [3] |
| Cláudio SZ | AH14 | Gneiss migmatite | | 2658 ± 7.2 | | Ion Microprobe | [3] |
| Cláudio SZ | AH15 | Gneiss migmatite | 2826 | 2715 ± 86 | | Ion Microprobe | [3] |
| Itapecerica SZ | CB-01 | Gneiss paleosome | | 2753 ± 81 | 2069 ± 84 | LA-ICP-MS | [4] |
| Itapecerica SZ | WM-1A | Candeias charnokite | | 2687 ± 61 | | LA-ICP-MS | [4] |
| Itapecerica SZ | FSTP-94 | Leucogranite | | 2705 ± 83 | | LA-ICP-MS | [4] |
| Itapecerica SZ | 3D | Quartzite | | 2129 ± 11 | | LA-ICP-MS | [4] |
| Itapecerica SZ | CB-3 | Paragneiss | | 2077 ± 20 | | LA-ICP-MS | [4] |
| Itapecerica SZ | PT-CB-3 | Schist | | 2122 ± 14 | | LA-ICP-MS | [4] |

[1] Melo-Silva et al. (2020), [2] Carvalho et al. (2017a), [3] Oliveira (2004), [4] Teixeira et al. (2017b).

The Rio das Velhas greenstone belt is an association of mafic and ultramafic rocks (komatiite–basalt), volcanic and volcaniclastic rocks (dacite), and immature clastic sedimentary rocks, subdivided in Nova Lima and Maquiné Groups (Dorr, 1969). The Pitangui Greenstone Belt is divided in a mafic metaigneous base (ultramafic-mafic metavolcanic rocks intercalated with metasedimentary rocks and BIF), that gradates to a middle metavolcanic-sedimentary sequence (clastic metasedimentary rocks and layers of mafic-intermediate metavolcanic rocks and metatuff), and an upper sequence composed of metaconglomerate and quartzite (Romano 2007; Fabricio-Silva et al., 2018; Melo-Silva et al., 2020). Traditionally, these greenstone belts have been considered to represent a single Archean basin but recently, a sedimentation time gap and the younger mafic magmatism of Pitangui (2740 Ma) suggests that they were formed as distinct units (Brando Soares et al., 2018; Melo-Silva et al., 2020). Whole-rock geochemical data also suggest a single evolution for the Pitangui Greenstone Belt, with LILE and HREE enrichment, flat REE pattern and a back-arc affinity (Verma et al., 2017; Brando Soares et al., 2020; Melo-Silva et al., 2020).

## 3. Methods and analytical techniques

Samples were collected from surface outcrops, avoiding weathered surfaces and targeting fresh rocks for petrography and geochemistry. Twenty-nine thin sections of diverse lithotypes were produced, from which textural relationships and mineralogy were obtained by optical mineralogy including modal point-counting.

Whole-rock analysis for major and trace elements was carried out on 36 selected samples and selected analyses are presented in Table 2, the complete dataset is presented in the Appendix A. X-ray fluorescence were made in a Philips PW 2404 spectrometer at the Geosciences Institute of University of Campinas. Approximately 500 g of sample was ground in an agate mill and made into fusion beads and pressed powder pellets. The quality control was made routinely through the analysis of duplicated samples, international reference materials (BRP-1, GRI-1, RGM-1 and ORTP-1) and a blank sample. From that, 17 samples were analyzed for trace elements on a Thermo (X series II) quadrupole ICP-MS with Collision Cell Technology at the Isotopic Geology Laboratory of the Geosciences Institute of University of Campinas. Dissolution was made after 0.5 ml of HNO3 and 2 ml of HF were added to 0.1 g of sample in Teflon bombs and the sample was heated at 180º C for 5 days, following the analytical procedures of Cotta and Enzweiller (2010). All samples have LOI between 0.21–1.44 wt.%.

**Table 2:** Geochemical analyses of selected major and trace element composition for samples of Divinópolis Complex gneisses.

| Sample | PD16-64A | PD16-51B | PD16-102 | PD17-89A | PD16-02D | PD16-29 |
|---|---|---|---|---|---|---|
| **Rock name** | Tonalite | Trondhjemite | Granodiorite | Granodiorite | Granodiorite | Granodiorite |
| **Group** | TTG | TTG | TTG | TTG | Potassic | Potassic |
| **Region** | Divinópolis | Bom Despacho | Divinópolis | Perdigão | Cláudio | Divinópolis |
| **Observation** | Hbl-bearing | | Grt-bearing | | | |
| **$SiO_2$** | 63.94 | 67.57 | 68.66 | 68.53 | 72.82 | 73.03 |
| **$TiO_2$** | 0.92 | 0.43 | 0.45 | 0.45 | 0.30 | 0.24 |
| **$Al_2O_3$** | 15.73 | 16.56 | 15.56 | 15.54 | 14.12 | 14.37 |
| **$FeO^t$** | 5.35 | 2.89 | 3.09 | 3.11 | 1.91 | 1.57 |
| **MnO** | 0.09 | 0.04 | 0.04 | 0.04 | 0.04 | 0.02 |
| **MgO** | 1.86 | 1.01 | 1.03 | 1.05 | 0.52 | 0.46 |
| **CaO** | 4.25 | 3.07 | 2.86 | 2.88 | 1.95 | 2.03 |
| **$Na_2O$** | 4.43 | 5.45 | 5.40 | 4.87 | 3.71 | 4.21 |
| **$K_2O$** | 2.08 | 1.47 | 2.21 | 2.20 | 3.91 | 3.20 |
| **$P_2O_5$** | 0.34 | 0.13 | 0.15 | 0.16 | 0.08 | 0.07 |
| **LOI** | 0.83 | 0.82 | 0.82 | 0.46 | 0.49 | 0.47 |
| **Total** | **99.82** | **99.43** | **100.28** | **99.28** | **99.84** | **99.68** |
| **Co** | 11.52 | 5.26 | 5.83 | n.d. | 2.73 | n.d. |
| **Ni** | 10.41 | 4.59 | 6.07 | 3.00 | 3.16 | 2.00 |
| **Cu** | 21.14 | 2.07 | 23.76 | 1.00 | 1.62 | 1.00 |
| **Zn** | 88.50 | 69.28 | 55.70 | 47.00 | 37.08 | 35.00 |
| **Rb** | 66.19 | 69.41 | 48.97 | 75.00 | 83.20 | 76.00 |
| **Sr** | 491 | 326 | 266 | 165 | 96.52 | 250 |
| **Ba** | 854 | 319 | 521 | 693 | 757 | 756 |
| **Pb** | 17.62 | 12.45 | 9.95 | 17.50 | 19.35 | 19.10 |
| **Th** | 11.09 | 5.12 | 9.74 | n.d. | 16.95 | 17.20 |
| **U** | 2.06 | 0.86 | 0.42 | n.d. | 1.05 | n.d. |
| **Nb** | 14.63 | 14.06 | 10.07 | 9.60 | 7.44 | 7.40 |
| **Ta** | 1.81 | 0.65 | 0.29 | n.d. | 0.33 | n.d. |
| **Zr** | 346 | 170 | 231 | 211 | 250 | 156 |
| **Hf** | 8.91 | 4.79 | 6.85 | n.d. | 6.90 | n.d. |
| **Cr** | 29.95 | 15.66 | 15.32 | 27.40 | 18.49 | 19.50 |
| **Sc** | 10.29 | 3.93 | 5.62 | n.d. | 1.86 | 3.00 |
| **V** | 57.29 | 24.59 | 40 | 16.30 | 19.32 | 16.40 |
| **Mo** | 0.69 | 0.37 | 0.21 | n.d. | 0.12 | n.d. |
| **Ga** | 19.61 | 22.73 | 20.51 | 19.50 | 17.21 | 18.40 |
| **Y** | 36.04 | 11.59 | 15.28 | 14.00 | 14.70 | 8.60 |
| **La** | 56.10 | 22.67 | 43.34 | n.d. | 41.08 | 23.00 |
| **Ce** | 111 | 44.97 | 58 | n.d. | 49.66 | 50.00 |
| **Pr** | 12.28 | 4.83 | 9 | n.d. | 7.88 | n.d. |
| **Nd** | 49.24 | 18.45 | 30.4 | n.d. | 28.46 | 19.00 |
| **Sm** | 9.48 | 3.66 | 5.3. | n.d. | 4.65 | n.d. |
| **Eu** | 2.14 | 1.01 | 0.97 | n.d. | 0.89 | n.d. |
| **Gd** | 8.34 | 3.45 | 4.8 | n.d. | 3.83 | n.d. |
| **Tb** | 1.21 | 0.49 | 0.67. | n.d. | 0.52 | n.d. |
| **Dy** | 7.00 | 2.59 | 3.47 | n.d. | 2.91 | n.d. |
| **Ho** | 1.36 | 0.46 | 0.63. | n.d. | 0.59 | n.d. |
| **Er** | 3.93 | 1.16 | 1.57 | n.d. | 1.75 | n.d. |
| **Tm** | 0.59 | 0.15 | 0.19. | n.d. | 0.24 | n.d. |
| **Yb** | 3.92 | 0.86 | 1.1 | n.d. | 1.54 | n.d. |
| **Lu** | 0.58 | 0.12 | 0.15 | n.d. | 0.23 | n.d. |

**Table 1:** Continuation

| Sample | PD17-97C | PD16-39 | PD16-18 | PD16-28 | PD16-69B | PD17-92 |
|---|---|---|---|---|---|---|
| **Rock name** | Trondhjemite | Trondhjemite | Syenogranite | Monzogranite | Granodiorite | Granodiorite |
| **Group** | Potassic | Potassic | Granitoid | Granitoid | Granitoid | Granitoid |
| **Region** | Pará de Minas | Pará de Minas | Formiga | Pedra do Indaiá | Itaúna | Perdigão |
| **Observation** | | | | Tit-bearing | | |
| **$SiO_2$** | 73.70 | 73.99 | 73.93 | 71.86 | 72.57 | 71.42 |
| **$TiO_2$** | 0.25 | 0.14 | 0.30 | 0.51 | 0.18 | 0.36 |
| **$Al_2O_3$** | 13.87 | 14.31 | 13.27 | 13.45 | 14.13 | 14.54 |
| **$FeO^t$** | 1.35 | 1.08 | 2.01 | 2.78 | 1.69 | 2.32 |
| **MnO** | 0.02 | 0.01 | 0.02 | 0.03 | 0.01 | 0.03 |
| **MgO** | 0.45 | 0.25 | 0.42 | 0.69 | 0.46 | 0.71 |
| **CaO** | 1.31 | 1.56 | 1.28 | 1.66 | 1.55 | 2.43 |
| **$Na_2O$** | 3.90 | 3.85 | 3.25 | 3.19 | 4.22 | 4.22 |
| **$K_2O$** | 4.43 | 4.58 | 4.92 | 4.98 | 4.14 | 2.89 |
| **$P_2O_5$** | 0.07 | 0.04 | 0.06 | 0.12 | 0.07 | 0.11 |
| **LOI** | 0.33 | 0.55 | 0.33 | 0.61 | 0.60 | 0.46 |
| **Total** | **99.67** | **100.35** | **99.79** | **99.88** | **99.62** | **99.49** |
| **Co** | n.d. | 13.30 | n.d. | 4.05 | 2.50 | 4.47 |
| **Ni** | 3.00 | 2.00 | 2.00 | 4.97 | 1.16 | 4.47 |
| **Cu** | 4.60 | 1.00 | 1.00 | 1.27 | 0.59 | 2.50 |
| **Zn** | 31.00 | 24.60 | 47.00 | 55.66 | 41.67 | 50.82 |
| **Rb** | 131 | 90.00 | 128 | 147 | 78.88 | 84.34 |
| **Sr** | 161 | 182 | 123 | 130 | 243 | 179 |
| **Ba** | 994 | 943 | 691 | 968 | 1220 | 670 |
| **Pb** | 35.00 | 22.40 | 44.00 | 25.07 | 23.00 | 16.14 |
| **Th** | n.d. | 17.00 | 65.00 | 30.51 | 29.33 | 16.75 |
| **U** | n.d. | n.d. | n.d. | 1.66 | 1.09 | 1.10 |
| **Nb** | 12.10 | 7.60 | 8.20 | 19.41 | 7.52 | 15.41 |
| **Ta** | n.d. | n.d. | n.d. | 1.06 | 0.39 | 0.54 |
| **Zr** | 154 | 108 | 205 | 481 | 194 | 243 |
| **Hf** | n.d. | n.d. | n.d. | 13.31 | 5.86 | 7.35 |
| **Cr** | 32.00 | n.d. | 28.60 | 21.90 | 6.98 | 15.95 |
| **Sc** | n.d. | 3.00 | 4.00 | 4.07 | 2.08 | 4.44 |
| **V** | 17.60 | 9.00 | 16.90 | 24.09 | 12.55 | 27.91 |
| **Mo** | n.d. | n.d. | n.d. | 4.48 | 0.12 | 0.22 |
| **Ga** | 18.30 | 18.70 | 16.80 | 16.55 | 18.76 | 20.49 |
| **Y** | 27.10 | 9.10 | 29.90 | 63.71 | 14.20 | 18.33 |
| **La** | n.d. | 31.00 | 144 | 111 | 110 | 52.76 |
| **Ce** | n.d. | 56.00 | 330 | 226 | 218 | 94.11 |
| **Pr** | n.d. | n.d. | n.d. | 23.09 | 22.79 | 12.05 |
| **Nd** | n.d. | 21.00 | 115 | 84.30 | 83.85 | 43.04 |
| **Sm** | n.d. | n.d. | n.d. | 15.28 | 13.67 | 8.26 |
| **Eu** | n.d. | n.d. | n.d. | 1.44 | 1.47 | 1.20 |
| **Gd** | n.d. | n.d. | n.d. | 14.21 | 10.01 | 7.15 |
| **Tb** | n.d. | n.d. | n.d. | 2.22 | 1.06 | 0.92 |
| **Dy** | n.d. | n.d. | n.d. | 13.13 | 4.25 | 4.60 |
| **Ho** | n.d. | n.d. | n.d. | 2.45 | 0.63 | 0.75 |
| **Er** | n.d. | n.d. | n.d. | 6.43 | 1.43 | 1.88 |
| **Tm** | n.d. | n.d. | n.d. | 0.80 | 0.16 | 0.22 |
| **Yb** | n.d. | n.d. | n.d. | 4.66 | 0.93 | 1.28 |
| **Lu** | n.d. | n.d. | n.d. | 0.63 | 0.14 | 0.18 |

## 4. Field relationships and petrography

Divinópolis Complex comprises a granitoid-gneiss dome surrounded by the amphibolite facies Pitangui Greenstone Belt, and Rio Manso and Cláudio mafic sequences (Fig. 2). It displays similar field relationship and rock associations with other Archean complexes of south São Francisco Craton, such as Belo Horizonte, Bonfim and Campo Belo, exposing a large area of low to high-grade granite-gneiss-migmatite mainly composed of tonalite-trondhjemite-granodiorite with minor diorite.

Granitoid intrusions occur along the complex and can form large batholiths and plutons, as well as small stocks, intruded in the gneisses. These intrusions are less deformed bodies of plg-rich to kfs-rich granitoids, generally more altered than the gneisses, most likely due to alkali-feldspar susceptibility to weathering. Their emplacement seems to be controlled by the reactivation of older structures in the northern and western sectors of the dome. These rocks are typically non-foliated to weakly foliated, with aligned crystals of biotite and stretched quartz or plagioclase. In the west limit, large, undeformed plutons are more frequent. These intrusions may comprise 30% of the dome.

Late leucocratic/aplitic sheets of veins and dikes oriented parallel or subparallel to the gneiss banding intrudes the gneisses and granitoids. The abundance of leucogranite dikes and veins increases eastward towards Itaúna and becomes most prominent south, in the Cláudio Shear Zone region.

The first deformation event of Divinópolis Complex is marked by the NE-SW trending foliation at the north and northeast portion of the dome (Fig. 2), with a moderate dipping (40 to 50º) plunging northeast. This structural arrangement reflects the influence of the Pitangui lineament (NW-SE), formed by multiple thrust and shear zones, controlling the relationship among TTGs and greenstone belt, with sheared slices of greenstone dipping 40 to 50º NE, defining a tectonic contact. This Neoarchean deformation is locally represented by rotation and displacement of the previous foliations with sinistral movements, pervasive stromatic migmatitic structures, and the gneissic foliation can be isoclinally folded.

The second major deformation event is registered in the southern portion of the dome, where structural controls take on a SE-NW direction, with several previous NW-SE structures being truncated by this subsequent event. Foliation dipping is moderate to W-S (20 to 40°) and this NE-SW direction can be correlated to the Cláudio and Itapecerica dextral shear zones.

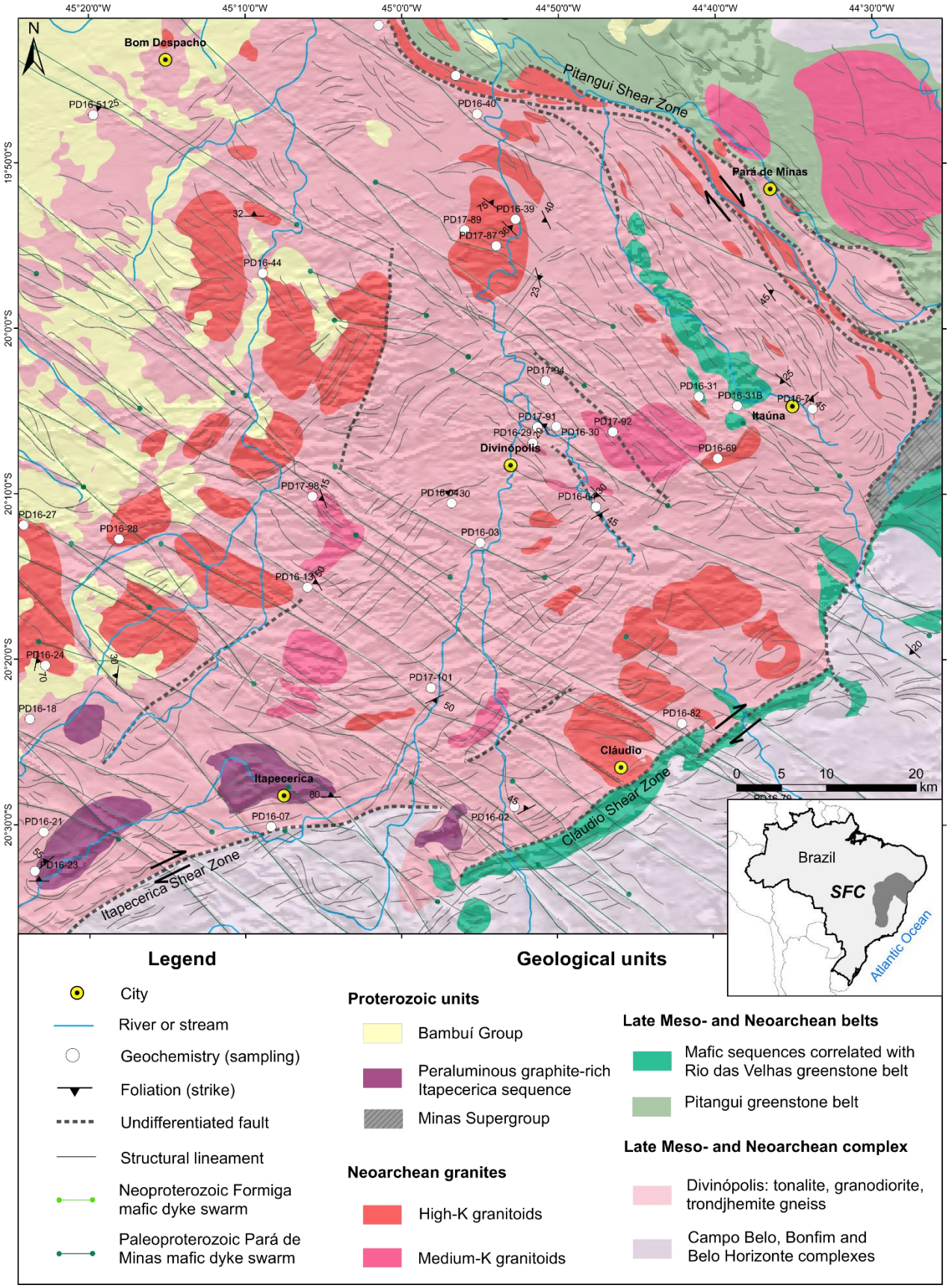


**Figure 2:** Geological map of Divinópolis Complex Archean–Proterozoic units and major tectonic features. Lithologies inferred from field mapping and gammaspectrometry. Structural lineaments extracted from field mapping, SRTM and magnetometry.

*4.1 Gneiss-migmatite association*

The Divinópolis dome is dominated by tonalite-trondhjemite-granodiorite grey gneisses. Trondhjemite and granodiorite are widely distributed, whereas tonalite is more localized. Based on previous works, the gneiss has similar characteristics to Cláudio and Itapecerica gneiss units (Oliveira, 2004; Carneiro et al., 2007). Although some differences between these units are described (more potassic *versus* less potassic), the gneisses of Divinópolis are discussed together in this paper. This suite comprises homogeneous orthogneiss typically foliated (Fig. 3a), but strongly banded rocks are uncommon. Complex compositional banding is found more often in the granodiorites and tight to isoclinal folds can develop in localized portions, following the main gneiss foliation. The gneisses are intruded by leucogranite, pegmatite and aplite veins that parallel and crosscut the gneiss bands. Late mafic dikes represented by Pará de Minas (NW-SE) and Formiga (E-W/NE-SW) swarms crosscut the units in the study area.

The *tonalites* are grey, mesocratic, showing a fine- to medium-grained texture and a gneissic structure with alternating bands that vary from 0.1 mm to 30 cm. The tonalite has a reasonably uniform mineralogy of oligoclase (50–60%), quartz (20–25%), biotite (10–15%) and hornblende (10–5%). Common accessory minerals include apatite, zircon, epidote, titanite, and ilmenite. The most prominent structure is the magmatic orientation of interstitial, fine-grained, biotite, associated with shear strain during dome emplacement (Fig. 4a and b). Leucocratic bands are slightly coarser-grained and more isotropic. Following Le Maitre (2002), they can be classified as hornblende-biotite tonalites.

The *trondhjemite* (Fig. 3a) is light grey, medium- to coarse-grained, locally intruded by pegmatite and aplite dikes. The trondhjemites are strongly banded with alternating melanocratic and leucocratic bands on a scale of centimeters to meters but over the entire dome it can grade into massive equigranular varieties. The main minerals are oligoclase (50–60%), quartz (25–30%) and biotite (10–20%). Monazite, allanite, zircon, apatite, and titanite are important accessory minerals and these rocks are classified as biotite-trondhjemites (Le Maitre, 2002). Calcite, sericite and clay minerals can replace plagioclase, especially the cores, suggesting some degree of plagioclase zonation. Aggregates of chlorite and epidote can replace primary amphibole, and this secondary paragenesis indicates greenschist-facies retrograde metamorphism. Although igneous textures are common, such as granular coarse-grained, the rocks have granoblastic texture and a faint foliation that is marked by the alignment of biotite grains (Fig. 4b).

The *granodiorite* is grey-pinkish, fine- to coarse-grained with melanocratic and leucocratic alternating bands that vary from 0.1 mm to 1 m. A complex intermingle between granodiorite-granite can be seen in a few outcrops, with pervasive stromatic structure boosted by the presence of melt (Fig. 3c). The granodiorites are primarily composed of oligoclase (35-60 %), quartz (25-30 %), biotite (7-20 %) and microcline (7-15%). Igneous alkali-feldspar is generally interstitial, while microcline can be a product of

hydrothermal alteration as inclusions in the center of plagioclase or quartz (Fig. 4c and 4d). Accessory phases include chlorite, epidote, allanite, apatite, zircon and opaque minerals. Atoll garnet (almandine) is a rare mineral and has minor inclusions of quartz and zircon (Fig. 4e) and a retrograde reaction is noted, as biotite grow at the expense of garnet.

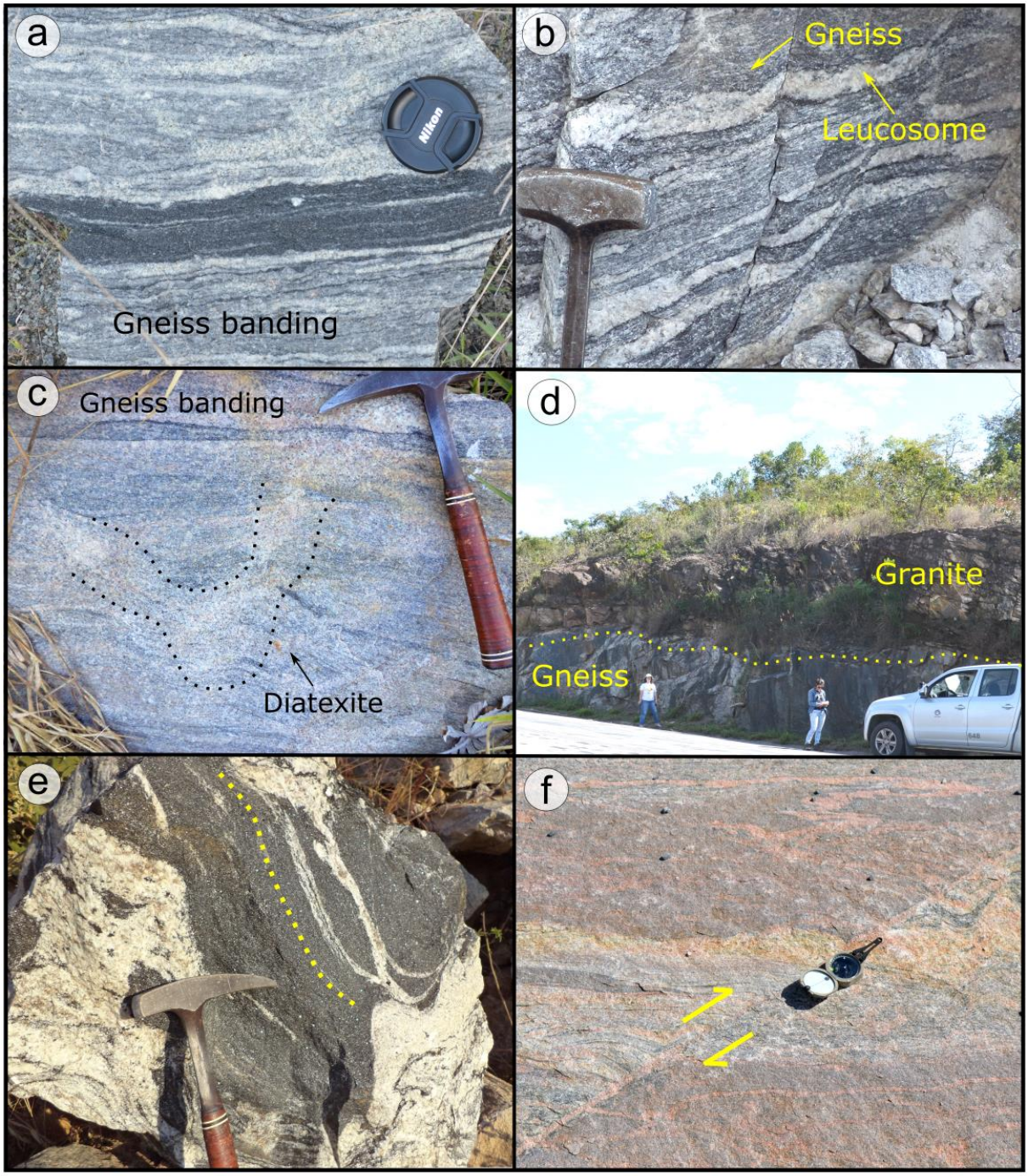


**Figure 3:** Field characteristics of Divinópolis Complex lithotypes. **a.** General aspect of the trondhjemite gneiss **b.** Tonalite gneiss with concordant leucosome dykes. **c.** Intermingle between a banded granodiorite gneiss and a diatexite observed in the anatectic region of a granite intrusion. **d.** Intrusive contact between TTG gneiss and altered granitoid pluton. **e.** Black schistose melanosome sample from Itaúna Migmatite, in contact with leucogranite neosome, exhibiting melting evidence. **f.** Brittle fault dislocating metatexite layers with dextral movement from the Kinawa Migmatite.

*Migmatites* show polydeformed and chaotic structures, with pink to white leucosomes and dismembered melanocratic fragments in the gneiss, varying from diatexite to metatexite (Sawyer, 2008). In the north and northeast domains, gray migmatites (Figs. 3e) preserve the main gneiss foliation (metatexites). In contrast, in the southern domain, partial melting is widespread and these diatexites have a pink color due to K-feldspar content (Figs. 3g). They have a leucogranite, monzogranite or granodiorite composition, and the pre-anatectic gneiss banding has been obliterated by a sub-vertical melt flux texture. In short, plg-rich leucosome is prevalent in the north and northeast, while kfs-rich leucosome is widespread in the south domain, close to the Cláudio and Itapecerica shear zones.

*4.2 Late granite intrusion association*

Late intrusive plutons are the second most widespread lithology of granitoids in Divinópolis Complex, distinguished from the older gneisses by their intrusive nature and well-defined pluton features associated with the TTGs. There is a geographic prevalence of non-deformed, equigranular to porphyritic syenogranites in the western domain, whereas slightly deformed, monzogranites predominate in any other domains. The intrusive contact between the gneiss and the granitoids can be seen in a few outcrops (Fig. 3d). Is notorious the elongate shape of the intrusions in the northeast portion of Divinópolis dome, following the Pitangui Lineament. The oldest intrusion phases are distinct foliated granodiorites and monzogranites whereas the latest plutons are non-foliated and show an increase in the K-feldspar content, varying from monzogranites to syenogranites.

The rocks are typically leuco to mesocratic, with a pink to greyish-pink color, medium- to coarse-grained and either equigranular or porphyritic. The rock-forming minerals are predominantly plagioclase (45–55%), quartz (25–35%), biotite (5–17%) and microcline (10–20%). Biotite is the only mafic mineral. Zircon, apatite, monazite, titanite, allanite and some opaques are common accessory minerals. The alkali feldspar is usually interstitial, and plagioclase can sometimes be characterized as phenocrysts, with perthite exsolution. The size and textures of plagioclase, quartz and biotite indicate that they belong to the original plutonic paragenesis, whereas all lithotypes are metamorphosed under low retrograde conditions, as evidenced by the change of biotite into chlorite and epidote (Fig. 4f).

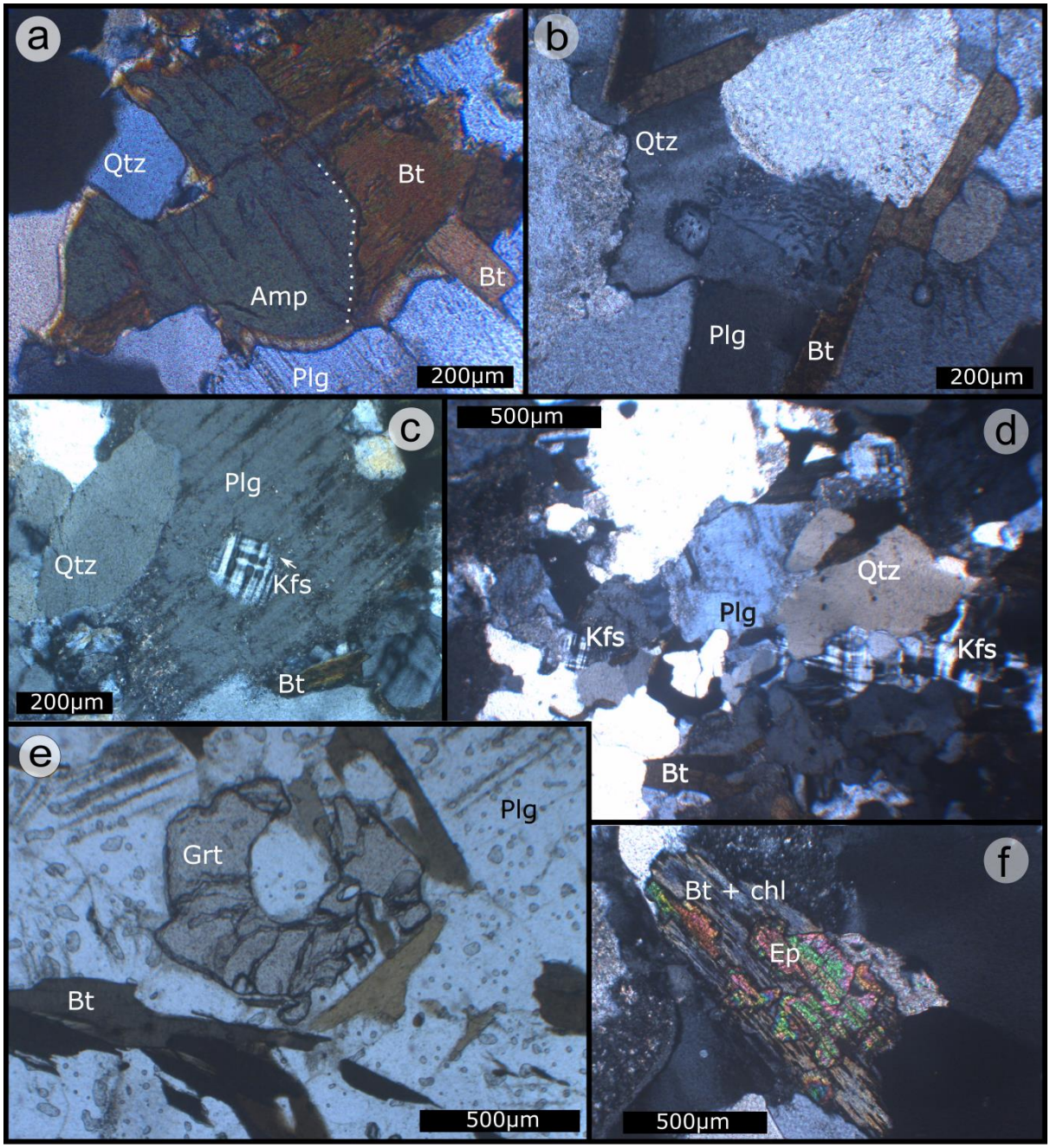


**Figure 4:** Microphotographs of petrological characteristics of the felsic rocks of Divinópolis Complex. **a)** The general feature of the trondhjemite, anhedral grains of plagioclase and quartz, with oriented interstitial tabular biotite and some degree of saussuritization of plagioclase. **b)** Amphibole intergrowth with biotite in tonalite, suggesting an early igneous crystallization. **c)** Hydrothermal microcline as inclusion in the center of plagioclase in granodiorite. **d)** Interstitial igneous microcline in granodiorite. **e)** Metamorphic garnet in association with biotite in granodiorite. **f)** Retrograde metamorphism of biotite in chlorite (blue) and epidote in a granodiorite sample.

## 5. Geochemistry

Some of the most relevant subdivision of Archean rocks include the work of Barker and Arth (1976) that subdivided trondhjemites based on their $Al_2O_3$ content: a high alumina group ($Al_2O_3$ >15 wt%) and a low alumina group ($Al_2O_3$ <15 wt%), whether Heilimo et al. (2010) divided TTGs into low-REE

and high-REE groups. Moyen (2011) describes at least four components: a sodic TTG group, divided into high-pressure (HP), medium-pressure (MP), and low-pressure (LP); and a potassic component suggesting low-pressure systems. Laurent et al. (2014) categorize the late Archean granitoids based on a petrogenetic classification: "TTGs", resulting from differentiation of tholeiitic and hydrous mafic rocks; "sanukitoids", encompassing rocks partially or totally derived from a mantellic component enriched in incompatible elements; "biotite- and two-mica granitoids", basically crust-derived granitoids; and "hybrid granitoids", a highly varied group formed through interaction between magmas of any of the previous groups. Indeed, there is no consensus on the nomenclature of Archean granitoids. Even though these rocks appear homogeneous at first, when investigated in further detail they embrace a varied group. In this paper, we integrate many of these characteristics and divided the felsic granitoids of Divinópolis Complex as follows:

1) TTG suite, which includes the most calcic and sodic gneisses.

2) Potassic suite, which comprises more potassic gneisses.

3) Late granitoid suite, including medium-K and high-K granitoids intruded into older gneisses.

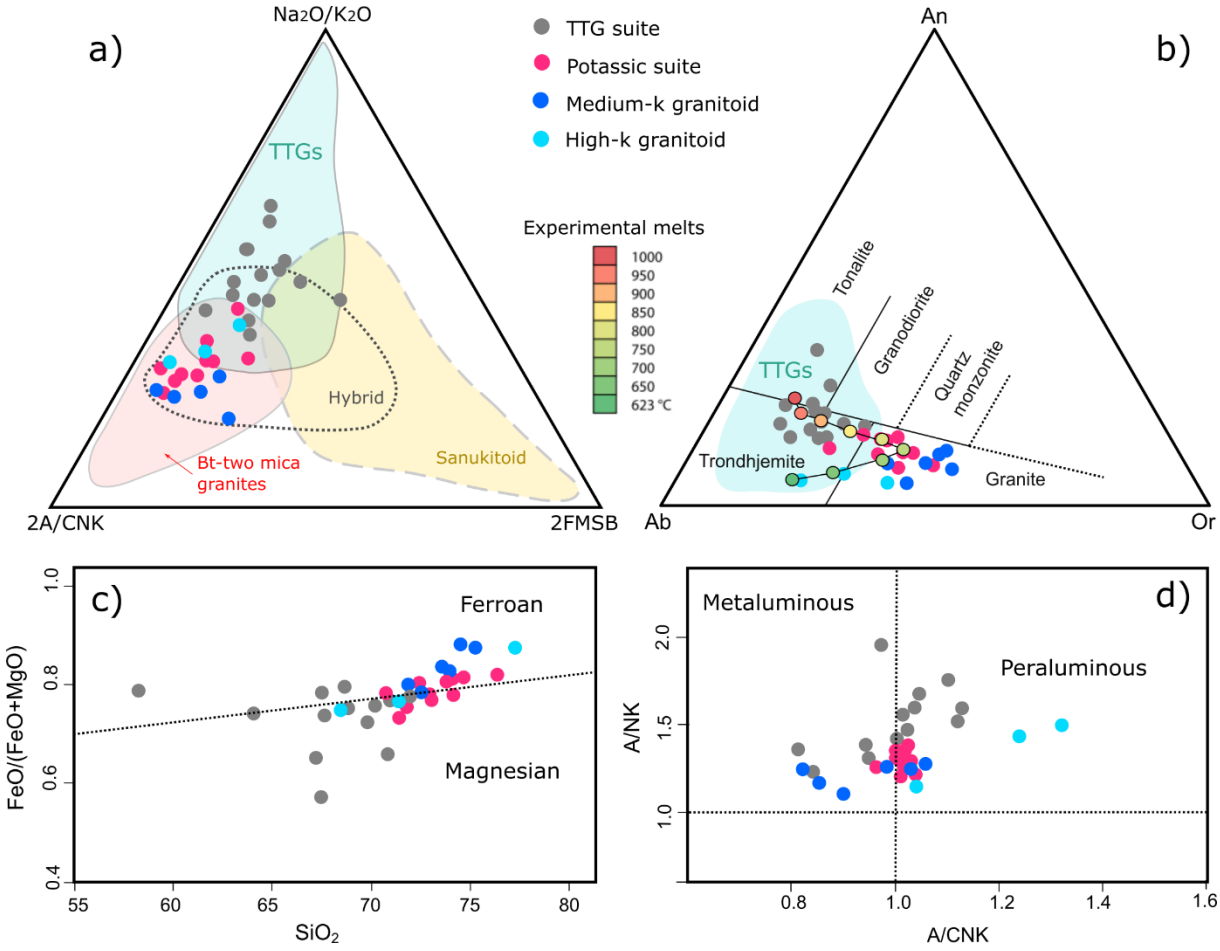


**Figure 5:** Distribution of felsic granitoids of Divinópolis Complex. **a)** Ternary $Na_2O/K_2O$–2*(molar $Al_2O_3/CaO + K_2O + Na_2O$)–2*(FeOt + MgO)*(Sr + Ba) classification diagram for Neoarchean granitoids after Laurent et al. (2014). **b)** Normative An-Ab-Or feldspar triangle (O'Connor, 1965). TTG field comparison with data of Moyen (2011) and crystallised melt derived from an enriched Archaean tholeiite protolith at 12 kbar (Palin et al., 2016). **c)** $SiO_2$ vs. FeO/(FeO+MgO) diagram and **d)** Molar A/CNK ($Al_2O_3$/ [CaO + Na2O + $K_2O$]) vs. A/NK ($Al_2O_3$/ [Na2O + $K_2O$]) after Frost et al., (2001).

### *5.1 TTG gneiss-migmatite suite*

On the ternary $Na_2O/K_2O$–2A/CNK–2FMSB diagram of Laurent et al. (2014) the TTG suite plot in typical Archean TTG field with the most mafic varieties superposing the sanukitoids series (Fig. 5a). Based on the normative mineralogy, the TTG group is made up of tonalites and trondhjemites (Fig. 5b). Their silica and alumina compositions range between 58.4 to 71.8 wt.% and 15 to 16.7 wt.%, respectively, and CaO content is high, from 2.2 to 5 wt.%. These rocks are essentially sodic (~4.9 wt. %) and magnesian, with peraluminous to slightly metaluminous affinity (Fig. 5c and 5d). The TTGs have average Mg (Mg#) number of 39. On Harker variation diagrams ($SiO_2$ versus major elements), these rocks exhibit a negative trend against the major elements, except for $K_2O$ (Fig. 6), with marked enrichment in the ferromagnesian elements. The TTGs have low Ni (~7.5), Ta (~0.88) and Nb (~12.3) contents, leading to negative Ta-Nb and Ti anomalies (Fig. 7a).

On the chondrite normalized rare earth element (REE) diagram, the TTGs display a fractionated pattern with negative Eu anomaly (Eu/Eu* = 0.41 to 1.05) and enrichment in LILE and depletion in HFSE. These rocks have moderate Y (~18 ppm) and Sr (~315 ppm), coupled with moderate La/Yb (~26) and low Sr/Y ratios (~22). Many Archean TTG suites are characterized by high Sr contents, typically greater than 400 ppm (Martin et al., 2005), the moderate Sr content and negative Eu anomaly is similar to those of low-pressure TTGs (Moyen, 2011), and the REE pattern is coherent with the low-pressure and medium-pressure TTGs of Moyen (2011) and the high-HREE of Heilimo et al. (2010).

### *5.2 Potassic gneiss-migmatite suite*

In the ternary diagram classification for late Archean rocks of Laurent et al., (2014) they exhibit a trend from TTGs to potassic granitoids, named "biotite and two micas granites" (Fig. 5a). We do not use this classification because the term 'biotite granite' can be too generic and adopted to any of the granitoid groups, as expressed by other authors (Halla et al., 2016). Based on the normative mineralogy, the Potassic suite is comprised by trondhjemites and granodiorites, distinct from the TTG suite (Fig. 5b). Enrichment towards K and Or express their potassic nature ($K_2O$ = 4.9–5.1 wt.%). Their silica and alumina compositions range between 70.8–74.6 wt.% and 14.12 to 14.6 wt.%, respectively. These rocks have a stronger peraluminous signature, slightly metaluminous, and varies from ferroan to magnesian (Fig. 5c and 5d). CaO content is low, from 2.1 to 1.1 wt.%, as well as content of ferromagnesian oxides. Average Mg number is 33 (molar Mg#).

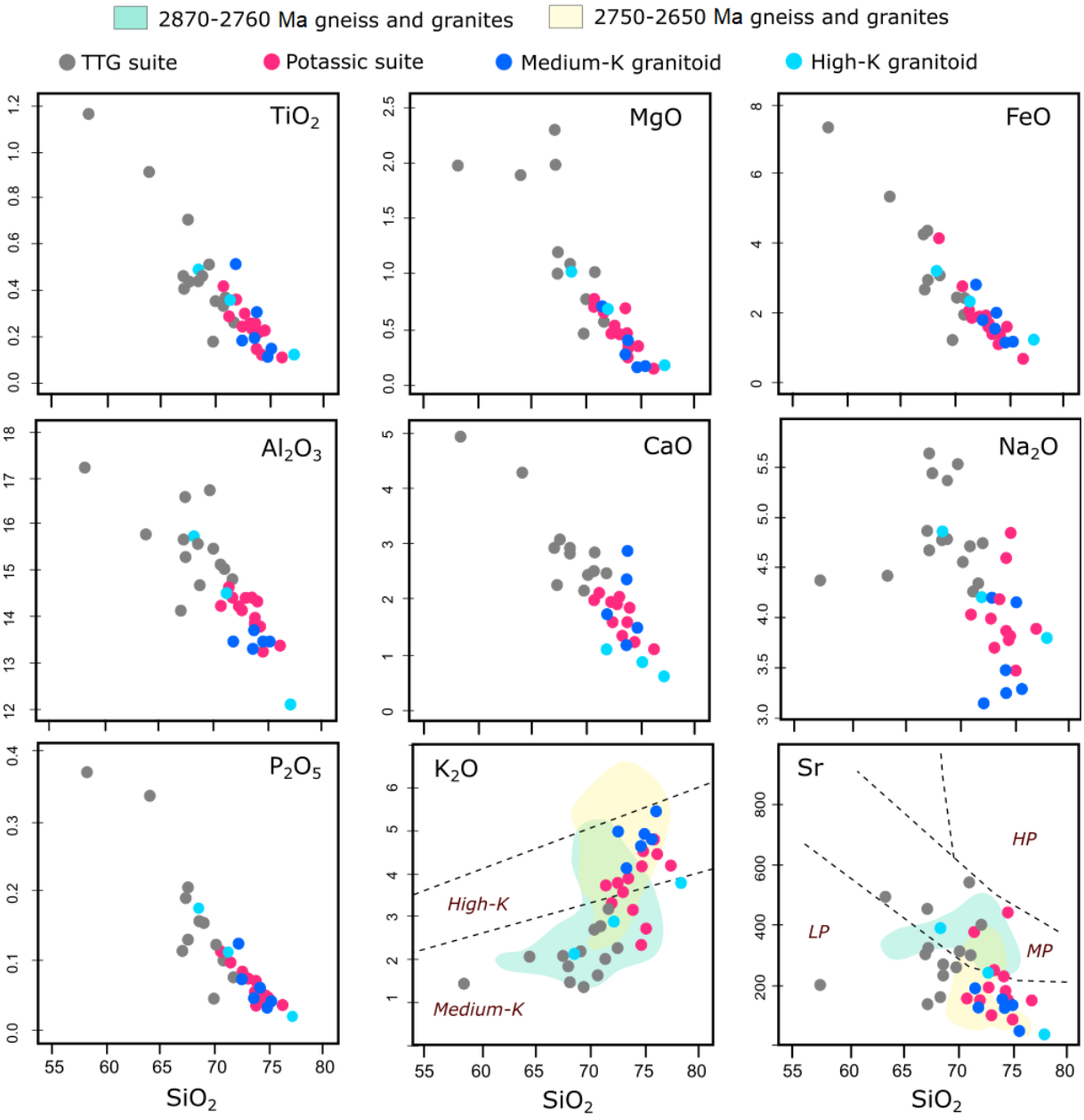


**Figure 6:** Harker diagrams showing the major elemental compositional variations among the felsic granitoids of Divinópolis Complex. Comparison with other felsic gneisses and granites of south São Francisco Craton. **LP:** Low-pressure TTGs. **MP:** Medium-pressure TTGs. **HP:** High-pressure TTGs (Moyen, 2011). Comparison data with gneisses and granites of distinct events in southern São Francisco Craton (Carneiro, 1992; Noce and Teixeira, 1997; Corrêa da Costa, 1999; Oliveira, 2004; Farina et al., 2015; Moreno et al., 2017; Simon et al., 2018; Brando Soares et al., 2020; Carvalho et al., 2017a).

On the Harker variation diagrams these rocks exhibit a negative trend against major elements, except for $K_2O$ (Fig. 6), and define a trend towards more silicic compositions when compared to the TTG suite. A steeper increase in $K_2O$ can be seen, as expected from the mineralogical appearance of K-feldspar and potassic enrichment. Sr is low (average of 200), and Cr (~26), Ni (~2.9), Nb (~8.4) and Ta (~0.3) are usually lower than the TTG suite and other Archean TTGs (e.g. Smithies, 2000; Moyen, 2011). On the chondrite normalized REE diagram (Fig. 7b), rocks of the potassic suite display a steeper fractionated

pattern with negative to positive Eu anomaly (Eu/Eu* = 0.6 to 1.4; positive in samples with garnet), LILE enrichment and HFSE depletion. La/Yb (~22) and Sr/Y ratios (~18) are lower than the TTGs and these gneisses share geochemical characteristics with low-pressure TTGs and potassic Archean crustal granitoids (Moyen, 2011; Laurent et al., 2014).

### *5.3 Late granite suite*

The late granite suite is geochemically diverse and can be classified as "hybrid granites" (Laurent et al., 2014), consisting of granodiorites, monzogranites and syenogranites (Fig. 6a and 6b). Geochemical differences have been recognized between the granitoids to divide them as a medium-K group ($K_2O$ = 2.2–3.8 wt.%) and a high-K group ($K_2O$ = 4.1–5.4 wt.%), based on their $K_2O$ content (Fig. 7). Farina et al. (2015) suggests that the granitoids of Quadrilátero Ferrífero are divided into a plagioclase-rich group named "medium-K granites" (3200 and 2760 Ma) and a K-feldspar-rich group (2760–2610 Ma), named "high-K granites". These groups are also reported as granitoids that intrudes Pitangui Greenstone Belt (Brando Soares et al., 2020) and São Tiago Batholith (Simon et al., 2018) in the Passa Tempo Complex.

#### *5.3.1 Medium-K monzogranites*

The medium-K monzogranites have low-MgO, silica composition between 68 and 77 wt.% and alumina composition vary from 15 to12 wt.%. Ferromagnesian content is variable, with samples having magnesian to ferroan signature, and a peraluminous affinity (A/CNK >1). In Harker variation diagrams, these granites show negative correlation of $SiO_2$ versus major oxides, except for $K_2O$ and have a regular trend that can be separated from the high-K granitoids (Fig. 6). These granites have Mg# ranging between 20 to 37, and show negative Ba, Nb, P and Ti anomalies. The most potassic samples have higher Y (34 ppm) and Rb (103 ppm), and low Sr values (40 ppm), whereas the most trondhjemitic ones have lower Y (13 ppm) and Rb (69 ppm), and high Sr (340 ppm). On the chondrite normalized REE diagram, these medium-K granitoids display LILE enrichment and HFSE depletion, with negative Eu anomalies (Eu/Eu* = 1.39), with a fractionated pattern (Fig. 7). Although some samples may resemble TTG-like rocks (Fig. 5a), their anorthite, $Al_2O_3$, CaO and MgO content is low, characterizing them, essentially, as monzogranites and syenogranites, similar to the monzogranites described by Joshi et al. (2016) at Bundelkhand Craton (India). These rocks also correlate well with the hybrid granitoids of (Laurent et al., 2014), and despite their more primitive kinship, cannot be classified as TTGs.

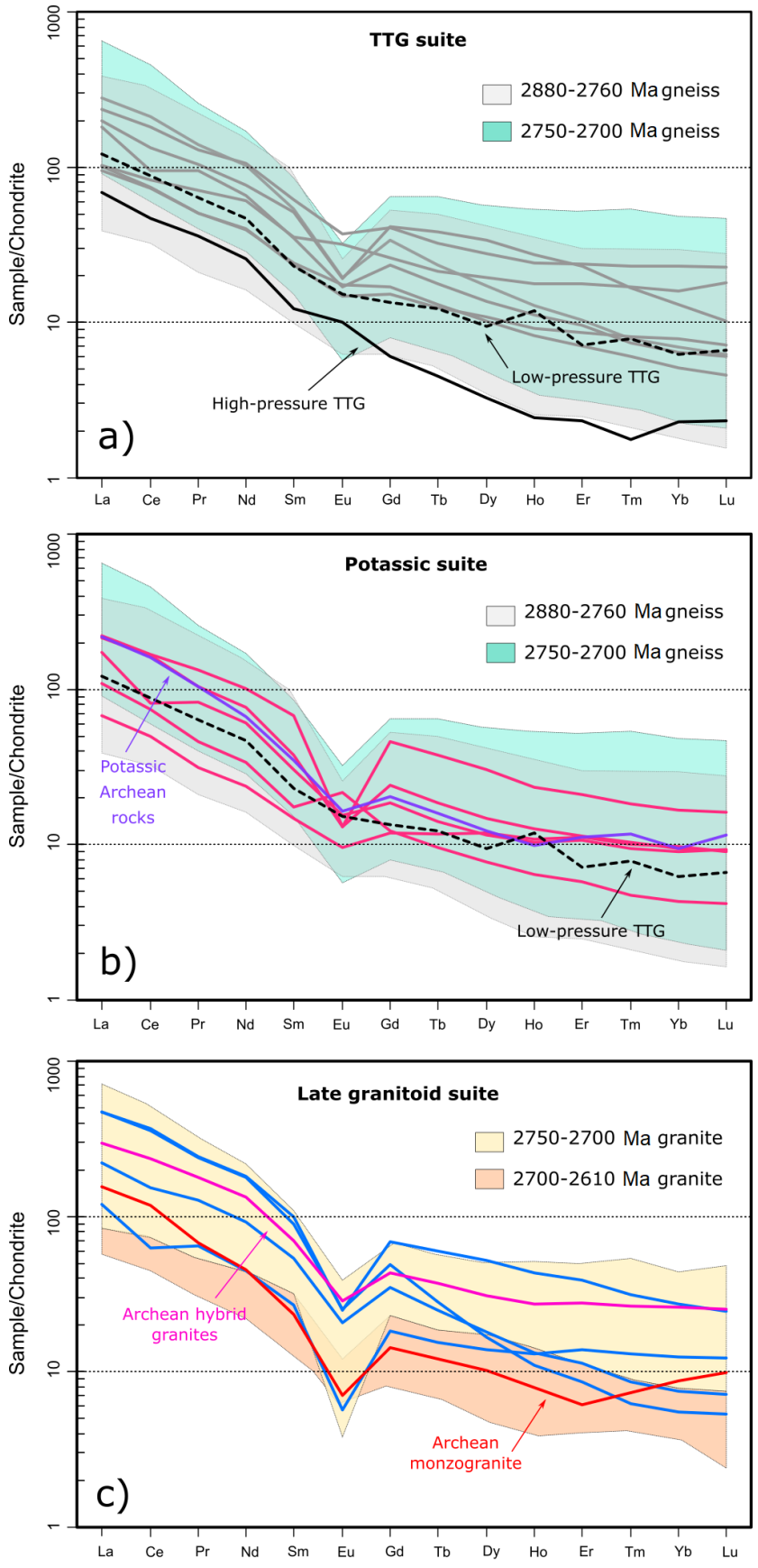


**Figure 7:** Chondrite normalized REE plot for the felsic granitoids of Divinópolis Complex (McDonough and Sun, 1995). Comparison data with average potassic Archean rocks (< 3.5 Ga), high-pressure TTGs and low-pressure TTGs of (Moyen (2011), and gneisses and granites from southern São Francisco Craton.

*5.3.2 High-K syenogranites*

The high-K syenogranites are chemically less diverse than the medium-K group, they plot in the granite field on the Ab-An-Or diagram and on the $Na_2O$-2A/CNK-2FMSB ternary diagram they plot in the hybrid granitoids field (Laurent et al., 2014) due to high $K_2O/Na_2O$ values (Fig. 5a and 5b). On the Alumina Saturation Index diagram, the high-K granitoids are peraluminous to metaluminous, with more affinity toward the latter. Mafic content and Mg number (Mg# = 19–32) are variable and these potassic rocks have a ferroan signature (Fig. 5c and 5d). The silica and alumina compositions of the high-K granites range between 72 and 75 and 13–14 wt.%, respectively. On Harker variation diagrams (Fig. 6), the less evolved samples have a similar composition to the TTG suite, whilst the monzogranites are more silica rich. Sr content is the lowest from all groups, from 47 to 240 ppm, lower $(La/Yb)_{PM}$ values and an increased Eu/Eu* negative anomaly, compared to any other groups. The samples have negative Ba, Nb-Ta, Sr, P and Ti anomalies and positive Th, Nd and Pb anomalies. On chondrite normalized REE plot these granites are depleted in Ni and enriched in LREE concerning the HREE, with a strongly fractionated elemental pattern, well-defined negative Eu anomaly (Fig. 7) and an intermediate trend between Archean hybrid granites (Laurent et al., 2014) and Archean monzogranites (Joshi et al., 2016).

## 6. Discussion

### *6.1 Crustal reworking and element mobility*

The gneisses and granitoids of Divinópolis Complex underwent metamorphism at amphibolite facies and anatexis and, therefore, element mobility must be discussed. The samples were preferentially collected on sites were deformation and anatexis were minor or absent, avoiding leucocratic veins and strongly banded varieties. The samples show low LOI values, from 0.4 to 0.9 wt.%, higher for samples with hornblende (0.8 to 1.7 wt.%). Minor or no Ce anomalies, combined with a consistent pattern for major and trace elements, low scatter of $Al_2O_3$, $K_2O$, $TiO_2$ and $P_2O_5$ suggest that these rocks were not affected by significant secondary processes such as metamorphism or hydrothermal alteration, also indicated by their mineralogy. Hence, mineralogy is representative of a very preserved igneous photolith Archean core in São Francisco Craton. Zr has been used to test mobility of other incompatible elements due to its relatively immobile nature (Pearce, 1982). On the plot of Zr versus selected major elements (Fig. 8), $Al_2O_3$, $Na_2O$ and $K_2O$ show scatter, while the less mobile elements such as MgO, $TiO_2$, $SiO_2$, $FeO^T$ present a good correlation. LILE also demonstrate a limited spread indicating that these elements remained relatively immobile during the alteration. REE, HFSE (Nb, La, Ti, Zr, Th, and Yb), and some transition metals (Co, Ni) have a good correlation with Zr and will be used to constrain the nature of petrogenetic

processes. But as stated by some authors the nature of the dominant sources is best demonstrated via major elements (Moyen et al., 2017; Johnson et al., 2019).

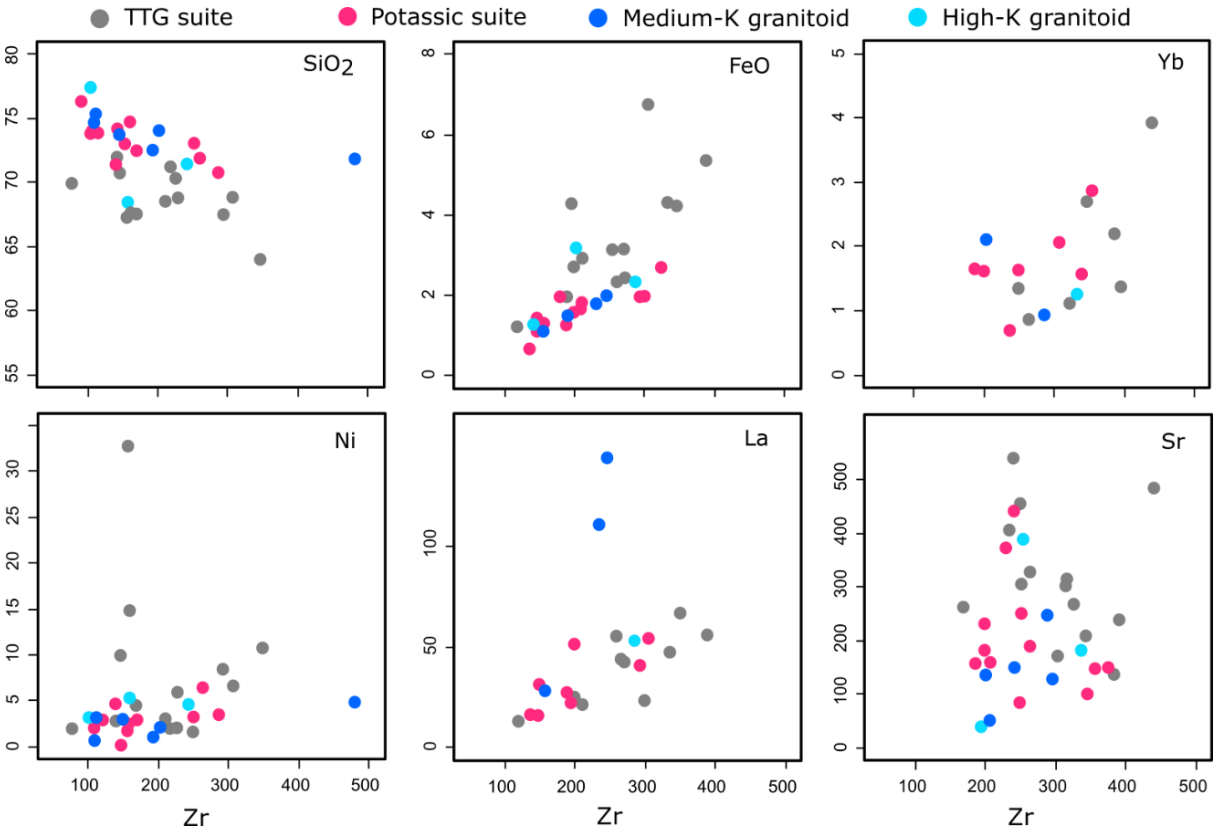


**Figure 8:** Covariation diagrams of Zr vs. selected major oxides and trace elements for the high-Al and low-Al gneisses and late granitoids of Divinópolis Complex.

### *6.2 TTG signature in the São Francisco Craton?*

Although the term grey gneiss is often used as a synonymous for most of the Archean basement, it contains a range of diverse components and the acronyms TTG (Jahn et al., 1981) has been overlapped by forementioned term. Some authors attest that potassic Archean rocks with a high content of heavy REE are technically not TTGs at all, but granitoids that could have formed by low-pressure melting in the absence of garnet, similar to some modern plagiogranites (e.g. Rollinson, 2009, Hoffmann et al., 2019). Moyen (2011) divides the TTGs based on plagioclase, rutile and garnet stabilities because these minerals are pressure-dependent and can provide depth information. The high- and medium-pressure groups are associated with melts in equilibrium with garnet and some rutile, but no plagioclase, typifying their fractionated REE pattern and depletion of HREE. Low-pressure TTGs and potassic granitoids, on the other hand, are associated with non-garnet controlled sources and plagioclase fractionation (Hoffmann et al., 2019). Trace elements are thus vital to constrain melt conditions in TTGs. For example, the partitioning

of Sr,Y, La, Yb or HREE are primarily linked to garnet abundance in the residue, since this mineral is linked to pressure gradients (Moyen, 2009; Hoffman et al., 2019).

Notably, all TTGs from Divinópolis Complex correspond to medium- and low-pressure groups (Fig. 6), with moderate to low La/Yb (average 26 ppm) and Sr/Y (average 22 ppm). They are characterized by negative Nb, Ta, and Ti. A decrease in the $(La/Lu)_N$ content with higher $SiO_2$ account for their fractionated REE pattern and moderate HREE depletion. It has been proposed that late-Archean TTGs (younger than 3.0 Ga) are poorer in Sr and HREE than older TTGs (Martin and Moyen, 2002), thus belonging to the low-pressure group. This is true for a varied of Archean rocks in southern São Francisco Craton, gneisses between 2880-2760 Ma can be classified as low-pressure TTGs (Fig. 6 and 7) as seen in our compilation data (Carneiro, 1992; Noce and Teixeira, 1997; Correa da Costa, 1999; Oliveira, 2004; Farina et al., 2015; Moreno et al., 2017; Carvalho et al., 2017a; Simon et al., 2018; Brando Soares et al., 2020). Particularly, the record of TTG magmatism in the southern São Francisco Craton is dominated by low- and medium-pressure sodic TTGs and potassic rocks with TTG-affinity (Fig. 8b and 8d). The production of such rocks is best explained by shallow evolution (≤10 kbar) (Hoffman et al., 2019). The TTGs of Divinópolis Complex demonstrate geochemical patterns likewise other low and medium pressure TTGs reported world-wide, whereas the gneisses of the potassic suite differ in many ways, and can be classified as potassic Archean gneisses, sharing similar traits to the Archean "biotite granites" of Moyen and Laurent (2018).

A compilation of experimental granitic melts (Moyen et al., 2017) was used to develop a Ca+Al –3Al+2(Na+K)–Al+(Na+K) projection to differentiate mafic and felsic sources of arc and collisional granites in the Paleozoic, further extending it to Archean granitoids (Moyen and Laurent, 2018). On this ternary source and tectonic diagram (Fig. 9a), the older gneisses and granites of the Rio das Velhas I and II events (2870–2760 Ma) are confined to the field expected for TTGs, deriving from mafic or intermediate sources (Moyen et al., 2017; Moyen and Laurent, 2018), as well as the TTGs of Divinópolis Complex. This agrees with data plotted in the source $CaO–Al_2O_3/(FeO+MgO)–K_2O/Na_2O$ ternary diagram in which the older gneisses and granites derive from low-K mafic rocks and tonalites (Fig. 9b). Younger gneisses and granites of the Mamona Event (2750-2650 Ma), on the other hand, plot in the expected fields for Archean biotite-granites (Fig. 9a) and show derivation from predominantly tonalitic and metasedimentary sources (Fig. 9b), in agreement with interpretations for the southern São Francisco Craton (Lana et al., 2013; Farina et al., 2015; Albert et al., 216). Hf isotopes for Bação, Bonfim and Belo Horizonte complexes suggest the involvement of Paleoarchean crust in their generation via crustal reworking processes with a metasedimentary component (Albert et al., 2016). The potassic suite of Divinópolis Complex does not hold this typical derivation from metasedimentary sources, and interestingly, the medium-K monzogranites marks a collision-related trend (discussion below).

In the north Paleoarchean nuclei of São Francisco Craton, low-HREE TTGs with garnet-bearing residue has been described in 3.4–3.3 Ga granitoids of the Sete Voltas, Bernarda, Boa Vista-Mata Verde, and Favelândia complexes, but high-pressure TTGs are not reported (Martin et al., 1997; Santos-Pinto et al., 2012; Barbosa et al., 2020). The oldest Eoarchean ages of the craton were recently dated at ca. 3600–3640 Ma in the Mairi Complex, and these felsic gneisses also share geochemical characteristics similar to low- and medium-pressure TTGs, with evidence of the existence of a depleted mantle (Oliveira et al., 2020). This raises the subject matter that even before 3.0 Ga, continental crust in São Francisco was not thick enough to stabilize great volumes of garnet, thus, resulting in low- and medium-pressure TTGs (Martin, 1993; Oliveira et al., 2020). High-pressure TTGs are only recorded in Bação Complex in the southern São Francisco Craton and could represent the partial melting of thick mafic pile heated up by mantle upwellings in an intra-plate environment (Albert et al., 2016).

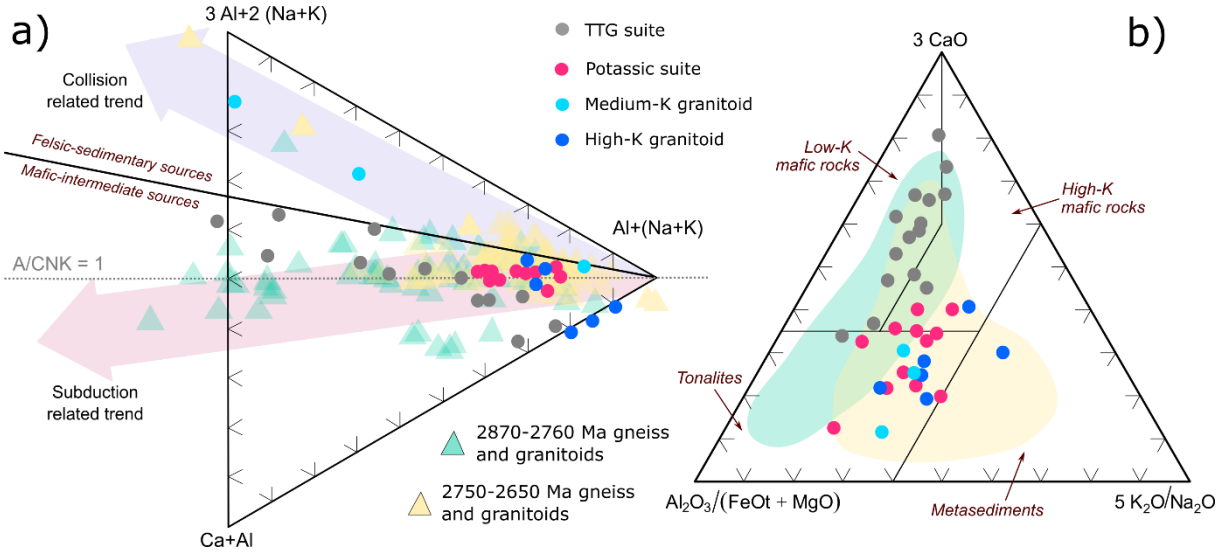


**Figure 9: a)** Ca+Al - 3Al+2(Na+K) - Al+(Na+K) projection diagram to differentiate sources and tectonic setting trends in Archean granites evolution (Moyen et al., 2017; Moyen and Laurent, 2018). **b)** Ternary diagram CaO–$Al_2O_3$/(FeO+MgO)–$K_2O/Na_2O$) representing the range of potential sources (tonalites, metasediments, low- and high-K mafic rocks) of Archean rocks (Laurent et al., 2014). Comparison data with gneisses and granitoids of distinct events in southern São Francisco Craton.

### *6.3 Petrogenesis and source of the TTG suite*

It is widely accepted that TTGs were generated by differentiation of a basaltic source, by partial melting or fractional crystallization of hydrated tholeiitic mafic crust (garnet-amphibolite), leaving a residue with hornblende and garnet to produce trondhjemitic liquids with HREE depletion (e.g. Barker and Arth, 1976; Martin, 1994; Rapp et al., 2003). The depletion on HREE is interpreted as being retained in residual phases, markedly garnet (Frost et al., 2006; Moyen and Martin, 2012), under high-pressure conditions (20-30 kbar) and many authors propose that despite the hotter Archean geotherm, some sort of subduction process would be involved (e.g. de Wit, 2004; Furnes et al., 2014; Condie, 2018). The

analogous Phanerozoic adakites are generated in modern plate tectonics, attributed to partial melting of a hydrated mafic crust with stable garnet, suggesting that a similar process generated the Archean TTGs (Frost et al., 2006). Intriguingly, Archean terrains do not preserve evidence of typical arc features such as true ophiolites, blueschists and elongated arc batholiths with compositional zoning seen in the modern tectonic register, usually calling for non-uniformitarian environments (Stern, 2005; Frost et al., 2006).

The use of REE, Sr and Y as proxies for pressure estimative has been widely applied on the petrogenetic models of such rocks (Rapp et al., 2003; Bédard, 2006; Halla et al., 2009; Hoffman et al., 2019). The less fractionated REE and low La/Yb and Sr/Y is indicative of plagioclase as a residual phase under lower pressure conditions (ca. 1.0 GPa), where plagioclase fractionation would reduce Sr, Sr/Y and Eu/Eu* (Martin et al., 2005; Clemens et al., 2006), accounting for the negative Eu anomaly in almost all samples. This is compatible with petrographic and textural evidence for the late crystallization of plagioclase in the rocks, where samples most depleted in Eu are also lacking Sr and $Al_2O_3$, which is best explained by prior removal of plagioclase.

Our dataset does not present HREE depletion and show moderate Sr values, suggesting that garnet was not stable in the residuum to retain these elements. But some of the TTGs are characterized by high $(La/Yb)_N$ and Sr/Y ratios and thus plot in the TTG–adakite field in the $(La/Yb)_N$–$(Yb)_N$ diagram, suggesting that they could be generated by melting of a basaltic source with no garnet, to maximum 5% of garnet (Fig. 10a). In Fig. 5b the pressure controls of crystallised melts of Palin et al. (2016) derived from an enriched Archaean tholeiitic protolith (Condie, 1981) points for higher temperature conditions for the TTGs than the other samples (1000–850º C at 12 kbar). In experimental studies of melting reactions in basalts, garnet grew between 9 and 14 kbar in the temperature interval 800–1000 ºC. The composition of this source is representative of basaltic underplate partially melted into an amphibolite with little garnet as a residual phase in the magma in thickened lower crust (Patiño Douce and Beard, 1995; Rapp and Watson, 1995; Vielzeuf and Schmidt, 2001; Palin et al., 2016).

Fractional crystallization of garnet increases Dy/Yb ratios and seems to be the dominant control in samples with lower silica (TTGs), not playing an important role in samples with higher silica (potassic suite and hybrid granitoids), where the chemical variation could be controlled by magma source (Ganade et al., 2017; Chen et al., 2019). The good correlation between differentiation indexes such as $SiO_2$ and Dy/Yb ratios could suggest that magma differentiation of a source with less than 5% of garnet in the residue can account for TTG formation (the most primitive gneisses in Divinópolis Complex) besides plagioclase fractionation and ruling out amphibole fractionation (Fig. 10b). The potassic and hybrid granitoids suites, on the other hand, show limited correlation between Dy/Yb and garnet fractionation, implying fractionation cannot adequately account for the whole variation seen in Divinópolis rocks.

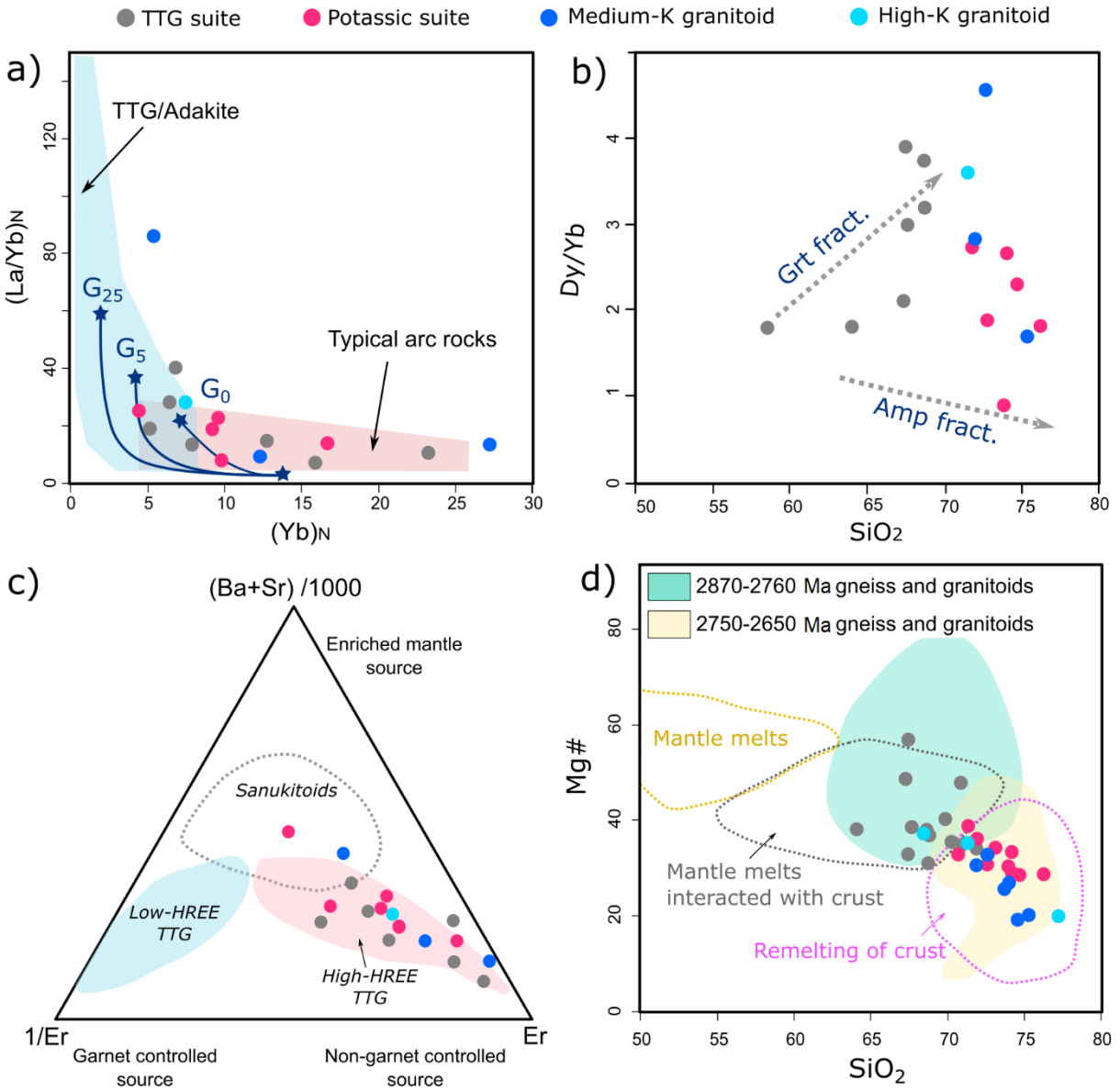


**Figure 10: a)** Co-variation diagrams of chondrite-normalized $(La/Yb)_N$ vs $(Yb)_N$ summarizing the different models for basalt melting (after Moyen and Martin, 2012). Batch melting curves for an E-MORB-like source after Wang et al. (2016). $G_0$ = 0% garnet, $G_5$ = 5% garnet, and $G_{25}$ = 25% garnet. **b)** Plot of Dy/Yb vs. $SiO_2$ showing that low silica samples (TTGs) have a garnet fractionation trend (after Chen et al., 2019). **c)** Ternary (Ba + Sr)/1000-1/Er-Er plot to discriminate between sanukitoids, Low-HREE TTGs and High-HREE TTGs (after Heilimo et al., 2010). **d)** Mg number (Mg#) vs. $SiO_2$ (after Peng et al., 2019).

When compared to the subdivision of Halla et al. (2009) and Heilimo et al. (2010), Divinópolis TTGs plot in the high-HREE field (Fig. 10c) and this group show lower $SiO_2$ and elevated Mg, Cr, Ni, and Mg# (Fig. 10d), which can be interpreted as a mantle-like signature and a mafic precursor, whereas the low-HREE TTG group with higher $SiO_2$ and lower Mg indicates an eclogitic parental melt in the garnet stability field under high-pressure conditions (Heilimo et al. 2010). The mantellic component can be observed as a discrete distribution of the samples towards sanukitoids field in Fig. 5a formed by the most primitive samples, with low silica. Although the felsic rocks of Divinópolis Complex don't fit under

the sanukitoids or M-type granitoids classification, this mantellic signature could be caused due to mantle upwellings that would melt pods of fusible metabasalts in the lower crust. Magma mixing zones between TTG and metabasaltic sources increases the proportion of felsic magma, such as in the model described by Bédard et al. (2018).

Thus, the suitable source lithology for TTGs of Divinópolis Complex is likely a garnet-free to maximum 5% garnet amphibolite. The compositional variation of mafic components and magnesium content imply an origin by involvement of mantle melts interacted with crustal melts (Fig. 10d) and such scenario can be envisaged by: i) partial melting of a MORB-like slab basalt depleted in incompatible elements in a hot environment during shallow subduction (Foley et al., 2003; Martin et al., 2014; Sizova et al., 2015) or ii) partial melting of the lower portion of an amphibolite mafic crust driven by heat from mantle-derived melts (Foley et al., 2003; Sizova et al., 2015).

### *6.4 Petrogenesis and source of the potassic suite*

The emplacement of late Archean components with a potassic affinity occurred extensively in most cratons worldwide, usually a result from geodynamic diversification, Earth's cooling and the transition to post-Archean tectonics (Smithies et al., 2003; Frost et al., 2006; Sanchez-Garrido et al., 2011; Romano et al., 2013; Laurent et al., 2014; Ganade et al., 2017). In many cratons, a second generation of TTG intrudes older ones, and the best explanation would be a process of partial melting of preexisting TTG source, as seen in other late Archean provinces. The Mamona Event (2.76–2.68 Ga) register this transition in the southern São Francisco Craton, showing a variety of sources, from mafic rocks – to tonalites – to metasedimentary rocks, attesting that a strong crustal component was involved in the genesis of these rocks (Farina et al., 2015; Albert et al., 2016).

The potassic suite of gneisses from Divinópolis Complex is constrained by trondhjemites, granodiorites and monzogranites, but particularly more peraluminous, with lower La/Yb (22 ppm) and Sr/Y (18 ppm) ratios, similar to the potassic group of Moyen (2011), or the "biotite granite" group of Laurent et al. (2014). The potassic suite occur spatially and temporally associated with TTGs with higher $K_2O/Na_2O$ ratios and LILE concentration. The similar temporal occurrence suggests that these magmas were generated in the same large-scale tectonic event, since they also preserve essentially similar bulk geochemistry. Gradational decreases in residual elements, such as Fe, Mg, Ca and Ti, and decreasing modal plagioclase is characteristic of magmatic differentiation from a common parental magma (Barker and Arth, 1976). But contrasting potassic and peraluminous affinities compared to the TTG suite suggests that these magmas were generated under different melting conditions and from distinct sources. The potassic suite is confined to non-garnet controlled sources (Fig. 10b and 10c) and this is supported by

negative Eu anomaly, low Sr content (avg. 202 ppm) and flat HREE pattern endorsing a source of shallow depth of melting at low-pressure conditions where plagioclase was stable. The granodiorite with garnet is an exception, showing enrichment in HREE and Eu since it retains those elements, but the atoll texture of these garnets and cross-cutting relationship with biotite (Fig. 4e) is indicative of a metamorphic origin, not reflecting the composition of the original magmatic source.

When considering the results of experimental melts (Palin et al., 2016) the potassic suite has lower temperature ranges than the TTGs (850–750º C) for conditions of 12 kbar (Fig. 5b). Silicic rocks have an extended temperature interval relative to more primitive compositions, allowing them to repeated open-system input and partial homogenization at higher melt fractions (Burgisser and Bergantz, 2011). Intermediate melts formed in the middle to lower crust derived from fractionation of underplated dry basaltic melts may hybridize with other melts, forming domes that rise diapirically in the upper crust. The lower part of these domes can remelt due to heat in the base of the crust by new mantle upwellings and/or delamination of the overlying mafic crust (Sizova et al., 2015). The progressive remelting will generate potassic Archean granitoids by remelting of the base of these TTG domes or magma chambers that remain partially molten at the bottom (Moyen and Martin, 2012; Sizova et al., 2015). In this model, the dome gneiss complexes that constitute the southern São Francisco Craton can be explained by vertical tectonic processes, similar to the model of Cutts et al. (2019) where gravitational inversions caused by heating and magmatism early in the evolution of the Quadrilátero Ferrífero crust build-up the initial dome-and-keel architecture.

Partial convective overturn results in upward of domes with TTG composition, and with subsequent mantle upwelling and delamination, they differentiate into potassic suites. Garnet fractionation would play an important role only in the beginning of differentiation of the TTGs and at small quantities (Fig. 10a and 10b), while latter on, partial melting becomes a dominant mechanism, with low degree of melting. The geochemical features of these rocks suggest that this parental magma has a crustal origin (Fig. 10d), most likely melting of already formed TTG magmas. Potassic felsic melts can also be produced by high degree of fractionation of hydrous medium- to high-K basaltic magmas, but requires high-pressure conditions (e.g. Sisson et al., 2005) and no such magmas are reported in the southern São Francisco Craton or befitting with the geochemical traits described here. High $SiO_2$ values also preclude this scenario. As suggested by some works, Archean granodiorites are most likely derived from the partial melting or fractional crystallization of tonalite–trondhjemite (e.g. Ridley et al., 1997). In this process, an interaction between mafic magma and tonalitic crust induces $H_2O$ and $K_2O$ transfer to produce granodiorite and granite melts (López et al., 2005).

The geochemical differences between the two groups of gneisses in the Divinópolis crust can be attributed to partial melting of a meta-igneous mafic protolith with low to moderate $K_2O$ contents (forming

the low- and medium-pressure TTGs), followed by differentiation and melting of more felsic crustal lithologies, such as TTGs, by addition of water and $K_2O$ during melt ascension, culminating in more evolved magmas. In the Neoarchean, a regime dominated by reworking processes is suggested for producing the variety of granitoids seen worldwide (e.g. Laurent et al., 2014) and also for the production of granitoids in Bação, Bonfim and Belo Horizonte complexes (Lana et al., 2013; Farina et al., 2015; Albert et al., 2016). The subchondritic Hf values and ancient TDMHf ages of Belo Horizonte and Bonfim complexes imply in multiple episodes of crustal reworking in the Paleo- and Mesoarchean (Albert et al., 2016).

### *6.5 Petrogenesis and source of the hybrid granites suite*

Hybrid Late-Archean granites are recognized in most cratons, formed through interaction between magmas of distinct compositions, such as TTGs, mantle, sanukitoids, potassic granites, etc., through distinct processes e.g. metasomatism, mingling, and mixing (Laurent et al., 2014). As a result, these granites have heterogeneous geochemical attributes. In the southern São Francisco Craton, this event is recorded in the granitoids of the Mamona Event (2760–2680 Ma - Lana et al., 2013; Farina et al., 2015). Farina et al. (2015) suggested that the Archean granitoids of Quadrilátero Ferrífero are divided into an older (i) banded gneiss + plagioclase-rich granitoids association and a younger (ii) Kfs-bearing gneiss + Kfs-rich granites association (Fig. 7c). It has been proposed that the Kfs-rich granitoids are product of mix of Archean metasedimentary rocks and older TTGs (Farina et al., 2016; Albert et al., 2016), consistent with the definition of "hybrid granites" of Laurent et al., (2014) and Moyen and Laurent et al., (2018).

In the Divinópolis Complex, the late granite suite was divided into a medium-K group and a high-K group, similar to the division of Farina et al., (2015) for granitoids of Bonfim, Belo Horizonte and Bação. The granites in the west sector of the complex are particularly Kfs-rich, coarse-grained and with no deformation, whilst the smaller plutons that intrude the north and central sectors are more deformed and less rich in alkali feldspar. Regarding their mineralogy, the medium-K group comprises granodiorites and monzogranites, while the high-K group consists of monzogranites and syenogranites. Remarkably, samples with a steeper REE fractionation also corresponds to the most foliated intrusions, localized in the north and central sectors of the dome. They also comprise the medium-K group, attesting their less evolved signature when compared to the high-K group that has much higher alkali feldspar content and almost no deformation. Variable incompatible elemental composition such as Ba (1200–600 ppm), Rb (185–69 ppm), Sr (390–40 ppm) and REE also reflect the heterogeneity of these granites. These hybrid granites have many similarities (Fig. 8c) with the medium-K granites and younger high-K granites of Farina et al., (2015).

*6.5.1 Medium-K granites*

The medium-K granites have geochemical characteristics close to the TTG suite but produce individual evolution trends as well as REE pattern (Fig. 8). These granites are more peraluminous (Fig. 5c), have relatively high $K_2O$ contents (2.2–3.8 wt. %) and lower Mg#, Cr and Ni contents (Table 2). The TTGs, on the other hand, have low $K_2O$ and higher MgO, Cr and Ni contents, which is attributed to their direct enriched metabasaltic source. These observations preclude a similar source for both TTG and medium-K granites (non-cogenetic). In the ternary diagram for discrimination of Archean granitoids composition (Fig. 5a), for example, the medium-K granites show characteristics closer to the potassic suite and on the An-Ab-Or diagram they have a unique trend that coincides with the lowest temperatures (620-650º C) calculated for partial melting of an $H_2O$ saturated enriched Archean tholeiite (Fig. 5b) modelled by Palin et al., (2016) considering 12 kbar.

Their negative Eu anomaly and REE content are intermediate between Archean potassic rocks (Moyen, 2011) and Archean monzogranites (Joshi et al., 2016). Low Sr/Y (9–28 ppm) and HREE pattern are indicative of non-residual garnet (e.g. Moyen, 2009). Felsic peraluminous compositions are dominantly generated in low-temperature systems as outcomes of partial melting of the crust at pressures below the garnet stability field, with only a minor contribution from sediments (Chappell et al., 2012). Experimental results suggest that Late Archean peraluminous, high-K and biotite granites are thought to derive from melting of pre-existing crustal lithologies (Fig. 5d), likely older TTGs, supracrustal rocks, potassic granites and sediments (Laurent et al., 2014).

Peraluminous granites of all ages typically form in collisional tectonic settings. The medium-K granites plot in the volcanic-arc and syn-collision field (Fig. 11a and 11b) in the (Y + Nb) vs. Rb and Nb vs. Y diagrams from Pearce et al. (1984). They also plot in the collision trend (Fig. 9a) in the ternary Ca+Al - 3Al+2(Na+K) - Al+(Na+K) projection (Moyen et al., 2017; Moyen and Laurent, 2018) to differentiate sources and tectonic setting trends in Archean granites. In collisional tectonic settings buried sedimentary material is heated until partial melting (e.g. Sylvester, 1998; Nabelek, 2019) and also in fore-arcs or back-arcs where mafic magmas heat sedimentary rocks (e.g. Lalonde, 1989; Bucholz and Spencer., 2019). The opening of the basin of the Pitangui Greenstone Belt is a possible explanation for heat production, resulting in continental collision through accretion of proto-continents (e.g. Divinópolis, Campo Belo, Bonfim, Belo Horizonte). This accretionary system would enable proto-subductions and the thermal anomaly generated during collision induces partial melting of the previously metasomatized mantle and interaction between crust and mantle components, resulting in diverse granites (Bonin, 2004; Laurent et al., 2014; Joshi et al., 2016; Moyen et al., 2017).

The evolution of the granites in Divinópolis Complex and south São Francisco craton can be best explained in an accretionary orogenic setting involving subduction and subsequent collision. The compositional heterogeneity of medium-K granites suggests that they can form at various stages between subduction and collision, various depths, and interaction between enriched mafic magmas with pre-existing felsic crust. As discussed above, multiple sources at variable depths were responsible for granitoid generation in the southern São Francisco Craton. As an example, the high Mg# of some samples (37–35) suggest a mantellic component (Fig. 10a) that could be achieved by interaction with the mantle wedge in a subduction setting or inherited from a metabasic source during crust delamination. In the same way, the peraluminous composition of the medium-K hybrid granitoids of Divinópolis Complex is attributed to the felsic crustal source (peraluminous magnesian TTGs and potassic rocks).

Taken together granitoids from Campo Belo, Belo Horizonte and Bonfim (Farina et al., 2015; Moreno et al., 2017; Brando Soares et al., 2020), the older generations (2755–2700 Ma) also have arc and collisional affinities in Pearce et al. (1984) discriminant diagrams (Fig. 11a and 11b). Many of these rocks are reported to have a TTG affinity or are closer to adakites and other arc-like settings (Silva et al., 2000; Farina et al., 2015; Albert et al., 2016; Brando Soares et al., 2020). These granitoids have many similarities with the medium-K granites of Divinópolis Complex. Pequi and Florestal intrusions (2755 Ma), for example, are interpreted to be product of melting of a hydrous amphibolitic source with garnet-rich and plagioclase-poor residue (Farina et al., 2015; Brando Soares et al., 2020), although the samples presented here preclude garnet pressure depths (Fig. 10c). Based on our data and compilation, a collisional event is argued for the emplacement of medium-K granites in the southern São Francisco Craton during the Mamona Event.

### *6.5.2 High-K granites*

The high-K granites are characterized by relatively high $K_2O/Na_2O$ ratios and LILE concentration. These syenogranites also define a trend towards more enriched compositions (Fig. 6) and are all ferroan, preferentially metaluminous (Fig. 5c and 5d). Eu depletion is typical of Post-Archean granites (Rapp et al., 2010) and these geochemical features can be attributed to enriched and relatively potassic sources (Moyen et al., 2007). Partial melting of potassic TTGs or Archean biotite-granites will generate melts enriched in $K_2O$ by the breakdown of amphibole and biotite (Watkins et al., 2007). The high-K syenogranites have lower concentrations of Sr (Fig. 6) and are characterized by negative Eu anomalies (Fig. 7c), indicating presence of plagioclase and absence of garnet in the source (Fig. 10b and 10c), best explained by parental melts resulting from relatively low-pressure and potassic sources. This includes middle to lower crust and supracrustal material, such as sediments, where progressive melting explains the

enrichment of alkalis and incompatible elements (Sawyer 1998; Moyen et al., 2007; Laurent et al., 2014; Farina et al., 2015).

The lack of aluminous minerals such as garnet, sillimanite and kyanite advise that these granites were not strictly formed as a product of crustal melting, but might result from the partial melting in the shallow to lower continental crust of a more potassic source, such as granodiorites of the potassic suite, with sodic melts involved (Hoffmann et al., 2019), like tonalites and trondhjemites of the TTG suite (Fig. 9b and 10d). Experimental results suggest that partial melting of calc-alkalic magnesian granitoids can produce ferroan metaluminous granitoids, especially at shallow depths up to 4 kbar (Skjerlie et al., 1993; Patiño Douce, 1997). An even shallower source (~5 kbar) is expected for these high-K granites in comparison with the medium-K granites (~10 kbar). Thus, the likely source of the high-K syenogranites are the granodiorites of the potassic suite as a result from melting in the shallow crust.

Farina et al. (2015) suggests that the high-K batholiths emplaced during the Mamona event require a source that is more enriched in K and LILE, and more fertile than the average continental crust, suggesting their derivation by melting of metasedimentary protoliths such as metagreywackes. As stated for the medium-K granites, petrography and geochemistry of the high-K granites does not suggest a metasedimentary derivation, unlike other gneisses and granitoids of the Mamona Event (2750–2650 Ma) that cluster between mafic, tonalitic and sedimentary sources (Fig. 9a). The absence of sedimentary supplies could reflect the fact that sites of sedimentary deposition was restricted, but it possible that small amounts of metagreywackes from Rio das Velhas and Pitangui Greenstone Belts influenced the composition of these hybrid granites.

Magnesian granite compositions often mark melts derived from post-collisional or earlier arc magmas (e.g. Frost and O'Nions, 1985), which agrees with data for the medium-K monzogranites. Ferroan granites, on the other hand, are often associated with evolved magmas in intraplate environments, usually a synonym for A-type granites that are considered to represent the final plutonic event in orogenic belts and anorogenic magmatism of shield areas (Frost and Frost, 2011). The difference between the medium-K and high-K intrusive suites are reinforced by tectonic diagrams (Fig. 11c). The ferroan features of the high-K granites make them somewhat similar to A-type granites (White and Chappell, 1983; Whalen et al. 1987), whereas the magnesian medium-K group features pushes these granites into I-type. A similar distribution is noted for the granitoids of Bonfim, Campo Belo and Belo Horizonte complexes, where the older generations (medium-K 2755–2700 Ma granitoids) can be classified as I-type granites and the younger generations (high-K 2700–2600Ma granitoids) exhibit A-type signatures. The older generation also shows a transitional setting from collisional and volcanic arc granites to within-plate granites, which is mor characteristic of the younger generation of high-K granites (Fig. 11a and 11b).

These monzogranites and syenogranites have no obvious geochemical signatures indicating melt-peridotite interaction, such as elevated Mg# and MgO, or Cr and Ni concentrations, which should be expected if these rocks were product of partial melting of a subducting crust or delaminated mafic crust (Bédard, 2006; Moyen and Martin, 2012; Sizova et al., 2015). Considering the A-type affinity of these rocks, a continental rift environment is inappropriate to explain the mafic-sodic-potassic trend envisaged as an evolution from mantellic to more crustal sources, reflecting progressive enrichment and shallowing of the depth of melting. Therefore, we suggest that a transition from collision to post-collisional extension is the best tectonic setting for the generation of these granites. After collision, the amalgamated micro-continental blocks would experience thermal relaxation, undergoing low degrees of partial melting as a result from decompression, resulting in the last potassic granites of the late granite suite.

The final cratonization stage is often marked by the generation of K-rich A-type granitoids in an extensional setting during crustal reworking. This major episode of high-K magmatism represents the period of thermal stabilization of the lithosphere and is reported in the São Francisco Craton (Romano et al., 2013, Albert et al., 2015; Moreno et al., 2017) and in the north Congo Craton (Shang et al., 2007). Such geodynamic change is attributed to the change in the nature and style of plate tectonics during the Archean-Proterozoic transition, with the involvement of collision and primitive episodes of subduction (Laurent et al., 2014) and these potassic granites can act as markers for the end of orogenic cycles and final stabilization of the Archean proto crust (Zhou et al., 2011; Zhang et al., 2012).

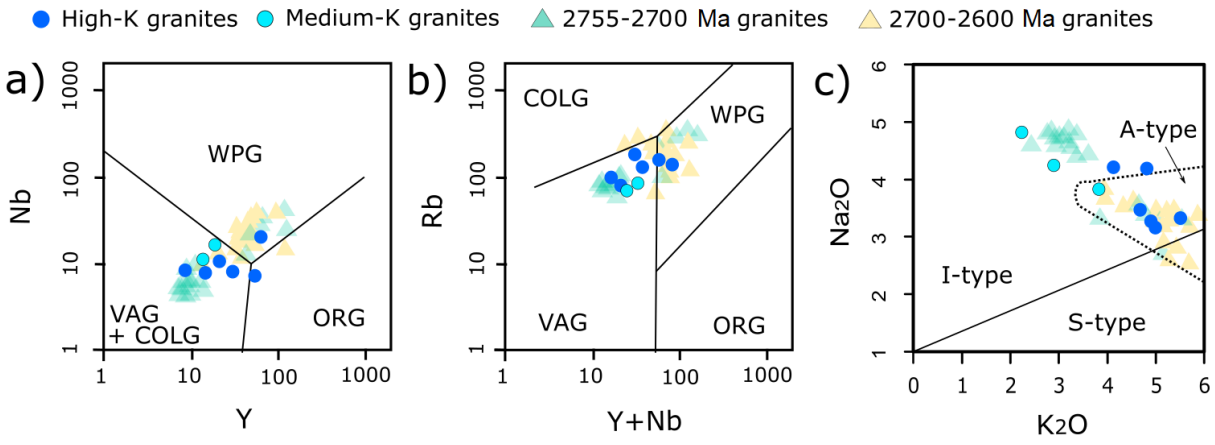


**Figure 11:** Classification diagrams of the hybrid granites. **a)** Nb vs. Y diagrams and **b)** Rb vs. Y+Nb from Pearce et al. (1984). **c)** $Na_2O$ v. $K_2O$ after White and Chappell (1983). Comparison data with granitoids from distinct events of southern São Francisco Craton (Farina et al., 2015; Moreno et al., 2017; Brando Soares et al., 2020). **FG**: fractionated felsic granites. **OGT**: unfractionated M-, I- and S-type granites. **A**: A-type granites. **COLG**: Syn-collision granite. **VAG**: Volcanic arc granite. **WPG**: Within plate granite. **ORG**: Ocean ridge granite.

*6.6 Geodynamic model*

The tectonic setting necessary to produce potassic and sodic Archean suites has proven to be diverse, accommodating many geodynamic environments, such as delamination, dripping, sagduction, subduction and subcretion, to cite a few (e.g. Lin et al., 2013; Sizova et al., 2015; Bédard, 2018; Moyen and Laurent et al., 2018). The occurrence of associated sodic and potassic magmatism worldwide and in the Divinópolis Complex is rather complex and we propose a three-stage tectonic model:

The **first stage** is represented by the formation of thick mafic lower crust that may have formed above mantle upwellings (Bédard, 2018). With subsequent gravitational instabilities, this crust begins to delaminate and overtake extensive mixing with the mantle (Johnson et al., 2014; Bédard, 2018), causing portions of mafic proto crust to differentiate into continental crust (Moyen and Laurent, 2018). This scenario is best envisaged by an intraplate environment, where pervasive mantle overturn recycles the lower crust (Bédard, 2006; Bédard, 2018), initiating the deep proto-cratonic root. This mafic proto crust source is chiefly mysterious in the Divinópolis Complex, but zircon grains of 3.8 to 3.2 Ga are recovered from the metasedimentary record of Pitangui Greenstone Belt (Hartmann et al., 2006; Brando Soares et al., 2020; Melo-Silva et al., 2020) and are present as inherited grains (3.2–3.0 Ga) in the southern Divinópolis sector (Carvalho et al., 2017a), Campo Belo Complex (Teixeira et al., 1998) and in the Itapecerica supracrustal succession (Teixeira et al., 2017b). In the north São Francisco Craton this crust is better exposed, which can have two explanations: 1) a simply sampling bias, for example, the Santa Bárbara Complex, which has the oldest ages in the southern São Francisco Craton was barely studied; or 2) a reworking bias, in which, for some, reason, the southern crust of the craton was extensively recycled back into the mantle before 3.2 Ga. One possibility does not exclude the other.

In the **second stage** of this model, part of the thickened crust melts, producing TTGs from a metabasaltic source with little to non-garnet composition at approximately 12 kbar. After the continental nuclei is formed, lithosphere deformation and mantle convection would take place spontaneously triggering: i) extensive remelting of pre-existing TTGs; ii) episodes of collision and accretion; and iii) the formation of unstable subduction zones at the edge of continental blocks (like the models proposed by Sizova et al., 2015 and Moyen and Laurent et al., 2018). Low- and medium-pressure TTG formation, in this case, can be triggered either by delamination of the lower mafic crust (enriched tholeiite) that sinks into the mantle or by the start of unstable subduction-like process as the system cools down and becomes more rigid. In our model, we suggest that both processes would occur, with thickened mafic crust first converted into TTG protocontinents by delamination. With the formation of these felsic protocontinents, the potential for horizontal mobility increases (Moyen and van Hunen, 2012), promoting accretion and collision of thick segments of mafic crust and felsic continental nuclei. This subduction-like processes

would favor flat configurations considering the hotter Archean gradient and thicker crust (Smithies et al., 2003; Herzberg et al., 2007; Palin et al., 2016). This geodynamic setting can lead to the formation of narrow oceanic areas (Bédard, 2018), such as the Pitangui Greenstone Belt (2740 ± 10 Ma, Melo-Silva et al., 2020). The accretion of this terrain against the border of Divinópolis is the main cause for the NW-SE deformation trend seen in the north sector, related to the collision and closure of the Pitangui basin, evidencing an Archean deformation front caused mostly by horizontal accretionary process. This collision resulted in a mylonite zone with augen gneiss and boudinage structures that exhibit kinematic structures consistent with thrusting towards SW. Continuation of overthrusting of thick oceanic and felsic crust would give rise to partial melting at different degrees, resulting in the potassic suite. This idea supports the coexistence of shallow subduction-like processes and crustal delamination with the coeval generation of TTGs and potassic rocks (Moyen, 2011; Johnson et al., 2014). Such model is described, for example, in the West Greenland. The gneisses are interpreted to represent a collage of terrains separated by mylonite zones and argued to have formed by shallow subduction during collisional orogenesis in the Archean (Nutman et al., 2007, 2013; Van Kranendonk, 2010).

In the **third stage** of this model, intrusion of potassic granitoids begins in the older TTG and potassic gneisses, as seen in most cratons worldwide by the end of the Archean (e.g. Laurent et al., 2014; Farina et al., 2015). The final evolution of the Archean crust involves massive transfer of material to the top of the crust, combined with loss of material to the mantle (Rudnick and Fountain, 1995). This results in potassium enrichment and fluid-mobile trace elements in the upper crust, following one of the last periods of global crustal growth (Arndt, 2013). As mentioned above, the granitoids of Divinópolis Complex vary from sodic TTGs, to potassic granodiorites, to monzogranites and potassic-rich granites. Such assemblage is comparable to Phanerozoic continental collisional belts, which encompass adakite, I-, S- and A-type granites through a wide compositional variation (e.g. Himalaya, Caledonian orogen). Together, the medium-K granites and high-K granites of the late granite suite were formed through an orogenic process involving transition from micro-continental collision to post-collisional extension. During amalgamation and accretion, the collisional medium-K granites are generated (2755–2710 Ma) by reworking of felsic crust and still under the influence of mantellic sources, with TTG-like signatures. The collisional event lead to significant crustal thickening. After collisional orogenesis, the amalgamated proto continents would go under extension and subsequent crustal thinning, forming the high-K granites by decompression melting (< 2.6 Ga) at shallow levels, resulting in the most evolved and potassic magmas.

The maturation of the southern São Francisco Craton crust towards more stable styles of plate tectonics as mantle temperature decayed is seen in the more primitive signature of Rio das Velhas I and II (2920–2760 Ma) gneisses and granitoids, corresponding to low- and medium-pressure TTGs, that transitions to the more evolved and potassic gneisses and granites of the Mamona Event (2760–2680 Ma),

that have a continental crust affinity. This long-term transition from Rio das Velhas Orogeny to Mamona can be correlated to the interpretation of many authors as the outburst of subduction and collision environments, as Earth acquires thermal equilibrium between 3.0 to 2.5 Ga (e.g. Cawood et al., 2013; Laurent et al., 2014; Halla et al., 2016; Moyen and Laurent, 2018; Condie, 2018).

## 7. Conclusions

- Field relationships and geochemical data indicate that the felsic gneisses and granitoids of Divinópolis Complex record three different geodynamic stages.
- TTGs (low and medium pressure) occur spatially and temporally associated with potassic gneisses, and the first is product of partial melting of hydrous mafic rocks with plagioclase as a residual phase and some mixing of mantle melts that could be related to processes of delamination of thickened mafic crust or shallow primitive subduction during proto continent accretion and collision.
- The potassic suite is associated with vigorous remelting of the older trondhjemite and tonalite TTGs during heating related to mantellic rises and crustal thickening, beginning the irreversible differentiation of the lithosphere. The generation of the TTG and potassic suite simply reflect the range of crustal thickness above hot zones and represents the potassic enrichment process of the crust.
- The hybrid granitoids were divided into an older foliated and medium-K generation and a younger, non-foliated high-K generation. Their source is a mix of partially melted TTG, potassic rocks and very small amounts of metasedimentary rocks. They represent a transition from collisional stage of thrusting and folding, resulting in crustal thickening (medium-K granites); to later post-collisional stage of extensional reflecting adjustment of the accreted blocks to tension loss and leading to final stabilization of the cratonic crust (high-K granites).
- The felsic suites of Divinópolis Complex and the São Francisco craton exemplify the temporal evolution from TTG-dominated crust to high-K dominated crust (sodic to potassic) as a result of continental crust diversification and thermal stabilization of the cratonic lithospheres in the Late Archean (~2.6 Ga).

## References

**Albert, C., Farina, F., Lana, C., Stevens, G., Storey, C., Gerdes, A., Dopico, C. M. 2016.** Archean crustal evolution in the Southern São Francisco craton, Brazil: Constraints from U-Pb, Lu-Hf and O isotope analyses. *Lithos*, **266–267**: 64–86.

**Almeida, F.F. 1977.** O Cráton do São Francisco. *Revista Brasileira de Geociências*, **7:** 349- 364.

**Alkmim, F.F., Noce, C.M. 2006.** The Paleoproterozoic Record of the São Francisco Craton. IGCP 509 Field workshop, Bahia and Minas Gerais, Brazil. Field Guide e Abstracts, 114 p.

**Anhaeusser, C., 2014.** Archaean *greenstone belts* and associated granitic rocks: a review. *Journal of African Earth Sciences*, **100:** 684-732.

**Arndt, N.T. 2013.** Formation and evolution of the continental crust. *Geochemical Perspectives*, **2(3).**

**Barbosa, J.S.F., Sabaté, P. 2004.** Archean and Paleoproterozoic crust of the São Francisco Craton, Bahia, Brazil: geodynamic features. *Precambrian Research*, **133**: 1–27.

**Barbosa, N., Menezes Leal, A. B., Debruyne, D., Bastos Leal, L. R., Barbosa, N. S., Marinho, M., Mercês, L., Barbosa, J. S., Koproski, L. M. 2020.** Paleoarchean to Paleoproterozoic crustal evolution in the Guanambi-Correntina block (GCB), north São Francisco Craton, Brazil, unraveled by U-Pb Geochronology, Nd-Sr isotopes and geochemical constraints. *Precambrian Research*, **340**: 105614.

**Barker, F., Arth, J.G., 1976.** Generation of trondhjemite–tonalite liquids and Archaean bimodal trondhjemite–basalt suites. *Geology*, **4**: 596–600.

**Bédard, J., 2006.** A catalytic delamination-driven model for coupled genesis of Archaean crust and sub-continental lithospheric mantle. *Geochimica et Cosmochimica Acta*, **70**: 1188–1214.

**Bédard, J.H., 2013.** How many arcs can dance on the head of a plume? A 'Comment' on: a critical assessment of neoarchean 'plume only' geodynamics: evidence from the Superior province, by Derek Wyman. *Precambrian Research*, **229:** 189-197.

**Bédard, J.H. 2018.** Stagnant lids and mantle overturns: Implications for Archaean tectonics, magmagenesis, crustal growth, mantle evolution, and the start of plate tectonics. *Geoscience Frontiers*, **9**: 19–49.

**Bonin, B., 2004.** Do coeval mafic and felsic magmas in post-collisional to within-plate regimes necessarily imply two contrasting, mantle and crustal, sources? A review. *Lithos*, **78**: 1–24.

**Brando Soares, M.B., Côrrea-Neto, A.V., Bertolino, L.C., Alves, F.E.A., de Almeida, A.M., da Silva, P.H.M., Mabubd, R.O.A., Manduca, L.G., Pamplona Araújo, I.M.C. 2018.** Multistage Mineralization at the Hypozonal São Sebastião Gold Deposit, Pitangui Greenstone Belt, Minas Gerais, Brazil. *Ore Geology Reviews*, **102:** 618–638.

**Brando Soares, M., Corrêa Neto, A. V., Fabricio-Silva, W. 2020.** The development of a Meso- to Neoarchean rifting-convergence-collision-collapse cycle over an ancient thickened protocontinent in the south São Francisco craton, Brazil. *Gondwana Research*, **77:** 40–66.

**Bucholz, C. E., Spencer, C. J. 2019.** Strongly Peraluminous Granites across the Archean-Proterozoic Transition. *Journal of Petrology*, **60:** 1299–1348.

**Burgisser, A., Bergantz, G.W. (2011).** A rapid mechanism to remobilize and homogenize highly crystalline magma bodies. *Nature*, **471:** 212–217.

**Campos, J.C.S., Carneiro, M.A., Basei, M.A.S. 2003.** U-Pb evidence for Late Neoarchean crustal reworking in the southern São Francisco Craton (Minas Gerais, Brazil): *In: Anais da Academia Brasileira de Ciências*, **75:** 497-511.

**Carvalho, B.B., Sawyer, E.W., Janasi, V.A. 2016.** Crustal reworking in a shear zone: Transformation of metagranite to migmatite. *Journal of Metamorphic Geology*, **34:** 237–264.

**Carvalho, B.B., Janasi, V.A., Sawyer, E.W., 2017a.** Evidence for Paleoproterozoic anatexis and crustal reworking of Archean crust in the São Francisco Craton, Brazil: a dating and isotopic study of the Kinawa migmatite. *Precambrian Research*, **291**: 98–118.

**Carneiro, M.A., 1992.** O Complexo Metamorófico Bonfim Setentrional (Quadrilátero Ferrífero, Minas Gerais): Litoestratigrafia e evolução geológica de um segmento de crosta continental do Arqueano. Ph.D. thesis (Unpublished), University of São Paulo, Brazil, 233p.

**Carneiro, M.A. 2007.** Nota explicativa Integrada das folhas Campo Belo e Oliveira (SF.23-V-BVI e SF.23-X-A-IV) escala 1:100.000. Programa Geologia do Brasil. CPRM-UFMG, 155p.

**Cawood, P.A., Hawkesworth, C.J., Dhuime, B., 2013.** The continental record and the generation of continental crust. *Geological Society of America Bulletin*, **125:**14-32.

**Chappell, B. W., Bryant, C. J., Wyborn, D. 2012.** Peraluminous I-type granites. *Lithos*, **153:** 142–153.

**Chen, Q., Sun, M., Zhao, G., Zhao, J., Zhu, W., Long, X., Wang, J. 2019.** Episodic crustal growth and reworking of the Yudongzi terrane, South China: Constraints from the Archean TTGs and potassic granites and Paleoproterozoic amphibolites. *Lithos*, **326–327**: 1–18.

**Clemens, J. D., Yearron, L. M., e Stevens, G. 2006.** Barberton (South Africa) TTG magmas: Geochemical and experimental constraints on source-rock petrology, pressure of formation and tectonic setting. *Precambrian Research*, **151**: 53–78.

**Condie K.C. 1981.** Archean Greenstone belts. *Elsevier*, Amsterdam, 434 pp.

**Condie, K. C. 2018**. A planet in transition: The onset of plate tectonics on Earth between 3 and 2 Ga? *Geoscience Frontiers*, **9,** 51–60.

**Corrêa da Costa, P.C. 1999.** Episódios de formação de crosta continental Arqueana no Cráton São Francisco Meridional: um exemplo a partir da região de Candeias – Campo Belo, MG. Dissertação de Mestrado. Departamento de Geologia da Escola de Minas da Universidade Federal de Ouro Preto, 151 p.

**Cotta A.J.B. e Enzweiler J. 2010.** Classical and New Procedures of Whole Rock Dissolution for Trace Element Determination by ICP-MS. *Geostandards and Geoanalytical Research*, **36:** 27-50.

**Cutts, K., Lana, C., Alkmim, F., Farina, F., Moreira, H., Coelho, V. 2019.** Metamorphism and exhumation of basement gneiss domes in the Quadrilátero Ferrífero: Two stage dome-and-keel evolution? *Geoscience Frontiers*, **10:** 1765-1787.

**de Wit M.J. 2004.** Archean *greenstone belts* do contain fragments of ophiolites. *In:* T. M. Kusky (Ed.), *Precambrian Ophiolites and Related Rocks*, Amsterdam: Elsevier, p.: 599–614.

**Door, J.V.N. 1969.** Physiographic, stratigraphic and structural development of the Quadrilátero Ferrífero, Minas Gerais, Brazil, U.S.G.S. Professional Paper 614 –A, 110 p.

**Fabricio-Silva, W., Rosière, C. A., Bühn, B. 2018.** The shear zone-related gold mineralization at the Turmalina deposit, Quadrilátero Ferrífero, Brazil: structural evolution and the two stages of mineralization. *Mineralium Deposita*.

**Farina, F., Albert, C., Lana, C. 2015.** The Neoarchean transition between medium-and high-K granitoids: Clues from the Southern São Francisco Craton (Brazil). *Precambrian Research*, **266:** 375-394.

**Farina, F., Albert, C., Martínez Dopico, C., Aguilar Gil, C., Moreira, H., Hippertt, J. P., Cutts, K., Alkmin, F. F., Lana, C. 2016.** The Archean–Paleoproterozoic evolution of the Quadrilátero Ferrífero (Brasil): Current models and open questions. *Journal of South American Earth Sciences*, **68:** 4–21.

**Foley, S.F., Tiepolo, M., Vannucci, R., 2002.** Growth of early continental crust controlled by melting of amphibolite in subduction zones. *Nature*, **417:** 637–640.

**Foley, S.F., Buhre, S., Jacob, D.E., 2003.** Evolution of the Archaean crust by lamination and shallow subduction. *Nature*, **421:** 249-252.

**Frost C.D., O'Nions R.K. 1985.** Caledonian magma genesis and crustal recyling. *Journal of Petrology*, **26:** 515–4

**Frost, B.R., Barnes, C.G., Collins, W.J., Arculus, R.J., Ellis, D.J., Frost, C.D., 2001.** A geochemical classification for granitic rocks. *Journal of Petrology*, **42:** 2033–2048.

**Frost, C. D., Frost, B. R., Kirkwood, R., Chamberlain, K. R. 2006.** The tonalite-trondhjemite-granodiorite (TTG) to granodiorite-granite (GG) transition in the late Archean plutonic rocks of the central Wyoming Province. Canadian Journal of Earth Sciences, 43(10), 1419–1444.

**Frost, C. D., Ronald Frost, B. 2011**. On ferroan (A-type) granitoids: Their compositional variability and modes of origin. *Journal of Petrology*, **52:** 39–53.

**Furnes, H., Dilek, Y., De Wit, M. 2014.** Precambrian greenstone sequences represent different ophiolite types. *Gondwana Research*, **27:** 649–685.

**Ganade, C. E., Basei, M. A. S., Grandjean, F. C., Armstrong, R., e Brito, R. S. 2017.** Contrasting Archaean (2.85–2.68 Ga) TTGs from the Tróia Massif (NE-Brazil) and their geodynamic implications for flat to steep subduction transition. *Precambrian Research*, **297**, 1–18.

**Hamilton, W.B. 2011.** Plate tectonics began in Neoproterozoic time, and plumes from deep mantle have never operated. *Lithos*, *123*:1–20.

**Hartmann L., Endo I., Suita M., Santos J., Frantz J., Carneiro M., McNaughton N., Barley M. 2006**. Provenance and age delimitation of Quadrilátero Ferrífero sandstones based on zircon U-Pb isotopes. *Journal of South American Earth Sciences*, **20:** 273-285.

**Halla, J., van Hunen, J., Heilimo, E., Hölttä, P., 2009.** Geochemical and numerical constraints on Neoarchean plate tectonics. *Precambrian Research*, **174:** 155–162.

**Halla, J., Whitehouse, M. J., Ahmad, T., Bagai, Z. 2016.** Archaean granitoids: An overview and significance from a tectonic perspective. *Geological Society Special Publication*, ***449*:** 1–18.

**Heilbron M., Cordani, U.G., Alkmim F.F., 2017**. The São Francisco Craton and its Margins. *In:* M. Heilbron, U.G. Cordani, F.F. Alkmim (eds.), *São Francisco Craton, Eastern Brazil*, Springer International Publishing, Switzerland, Regional Geology Reviews, pp. 3-13 p.

**Heilimo, E., Halla, J. & Hölttä P. 2010.** Discrimination and origin of the sanukitoid series: geochemical constraints from the Neoarchaean western Karelian Province (Finland). *Lithos*, **115:**

27–39.

**Herzberg, C., Asimow, P.D., Arndt, N., Niu, Y., Lesher, C.M., Fitton, J.G., Saunders, A.D., 2007.** Temperatures in ambient mantle and plumes: constraints from basalts, picrites, and komatiites. *Geochemistry, Geophysics, Geosystems*, **8**.

**Hoffmann, J.E., Zhang, C., Moyen, J.-F., Nagel, T.J. 2019.** The Formation of Tonalites–Trondjhemite–Granodiorites in Early Continental Crust. *In* Earth's Oldest Rocks.

**Jahn, B., Glikson, A.Y., Peucat, J.-J., Hickman, A.H., 1981.** REE geochemistry and isotopic data of Archaean silicic volcanics and granitoids from the Pilbara block, western Australia: implications for early crustal evolution. *Geochimica et Cosmochimica Acta,* **45:** 1633–1652.

**Johnson, T.E., Brown, M., Kaus, B.J., VanTongeren, J.A., 2014.** Delamination and recycling of Archaean crust caused by gravitational instabilities. *Nature Geoscience*, **7:** 47-52.

**Johnson, T.E., Kirkland, C.L., Gardiner, N.J., Brown, M., Smithies, R.H., Santosh, M. 2019.** Secular change in TTG compositions: Implications for the evolution of Archaean geodynamics. *Earth and Planetary Science Letters*, **505**, 65–75.

**Joshi, K.B., Bhattacharjee, J., Rai, G., Halla, J., Ahmad, T., Kurhila, M., Heilimo, E., Choudhary, A.K. 2017.** The diversification of granitoids and plate tectonic implications at the archaean-Proterozoic boundary in the Bundelkhand craton, central India. *Geological Society Special Publication*, **449:** 123–157.

**Lana C., Alkmim F., Armstrong R., Scholz R., Romano R., Nalini H. 2013.** The ancestry and magmatic evolution of Archaean TTG rocks of the Quadrilátero Ferrífero province, southeast Brazil: *Precambrian Research*, **231:** 157-173.

**Lalonde, A. E. 1989.** Hepburn intrusive suite: Peraluminous plutonism within a closing back-arc basin, Wopmay orogen, Canada. *Geology,* **17**: 261–264.

**Laurent, O., Martin, H., Moyen, J.F., Doucelance, R., 2014.** The diversity and evolution of late-Archean granitoids: evidence for the onset of 'modern-style' plate tectonics between 3.0 and 2.5 Ga. *Lithos*, **205:** 208-235.

**Le Maitre, R. W. 2002.** Igneous rocks a Classification and Glossary of Terms Recommendations of the International Union of Geological Sciences, Sub-Commission on the Systematics of Igneous Rocks, Cambridge University Press, 236p.

**Lin, S., Parks, J., Heaman, L.M., Simonetti, A., Corkery, M.T. 2013.** Diapirism and sagduction as a mechanism for deposition and burial of "Timiskaming-type" sedimentary sequences, Superior Province: Evidence from detrital zircon geochronology and implications for the Borden Lake conglomerate in the exposed middle to lower. *Precambrian Research*, **238:** 148–157.

**López, S., Castro, A., e García-Casco, A.** 2005. Production of granodiorite melt by interaction between hydrous mafic magma and tonalitic crust. Experimental constraints and implications for the generation of Archaean TTG complexes. *Lithos*, **79** (1-2 SPEC. ISS.), 229–250.

**Machado Filho L., Ribeiro M.W., Gonzalez S.R., Schenini C.A., Santos Neto A.S., Barros Palmeira R.C., Pires J.L., Teixeira W., Castro H.E.F. 1983.** Geologia. *In:* Projeto RADAM Brasil, Folhas SF.23/24 Rio de Janeiro/Vitória, **32:** 36-45.

**Machado N., Noce C., Ladeira E., Belo de Oliveira O. 1992**. U-Pb geochronology of Archean magmatism and Proteozoic metamorphism in the Quadrilátero Ferrífero, southern São Francisco

cráton, Brazil, *Geological Society of America Bulletin*, **104:** 721-727.

**Machado N., Schrank A., Noce C., Gauthier G. 1996.** Ages of detrital zircon from Archean-Paleoproterozoic sequences: Implications for *Greenstone belt* setting and evolution of a Transamazonian foreland basin in Quadrilátero Ferrífero, southeast Brazil: *Earth and Planetary Science Letters*, **141:** 259-276.

**Martin, H. 1993.** The mechanisms of petrogenesis of the Archean continental crust –comparison with modern processes. *Lithos*, **30:** 373–388.

**Martin H., 1994.** The Archean grey gneisses and the genesis of the continental crust. *In*: K. C. Condie (ed.) *Archean Crustal Evolution*. Elsevier, Amsterdam, pp.: 205–259.

**Martin, H., Peucat, J.J., Sabaté, P., Cunha, J.C., 1997.** Crustal evolution in early Archean of South America: exemple of Sete Voltas massif, Bahia state, Brazil. *Precambrian Research*, **82**: 35-62.

**Martin, H., Moyen, J.F., 2002.** Secular changes in TTG composition as markers of the progressive cooling of the Earth. *Geology*, **30:** 319–322

**Martin H., Smithies R.H., Rapp R., Moyen J.-F., Champion D., 2005.** An overview of adakite, tonalite-trondhjemite-granodiorite (TTG), and sanukitoid: Relationships and some implications for crustal evolution: *Lithos*, **79:** 1–24.

**Martin, H., Moyen, J.F., Guitreau, M., Blichert-Toft, J., Le Pennec, J. L., 2014.** Why Archean TTG cannot be generated by MORB melting in subduction zone. *Lithos*, **198-199**: 1-13

**McDonough W. F., Sun S.S. 1995.** Composition of the Earth. *Chemical Geology*, **120:** 223–253.

**Melo-Silva, P., Amaral, W.S., Oliveira, E.P. 2020.** Geochronological evolution of the Pitangui Greenstone Belt, southern São Francisco Craton, Brazil: constraints from U-Pb zircon age, geochemistry and field relationships. *Journal of South American Earth Sciences*, **99:** 102380.

**Moreira H., Lana C., Arias H., Nalini Jr H.A. 2016.** The detrital zircon record of an Archaean convergent basin in the. *Precambrian Research*, **275:** 84–99.

**Moreno, J.A., Baldim, M. R., Semprich, J., Oliveira, E.P., Verma, S.K., Teixeira, W. 2017.** Geochronological and geochemical evidences for extension-related Neoarchean granitoids in the southern São Francisco Craton, Brazil. *Precambrian Research*, **294,** 322–343.

**Moyen, J.F., 2009.** High Sr/Y and La/Yb ratios: the meaning of the "adakitic signature". *Lithos*, **112:** 556–574.

**Moyen, J.-F., Stevens, G., Kisters, A.F.M., Belcher, R.W., 2007.** TTG plutons of the Barberton granitoid-greenstone terrain, South Africa. *In:* Van Kranendonk, M.J., Smithies, R.H., Bennett, V. (Eds.), Earth's Oldest Rocks. Elsevier, pp. 606–668.

**Moyen J.F. 2011.** The composite Archaean grey gneisses: Petrological significance, and evidence for a non-unique tectonic setting for Archaean crustal growth. *Lithos*, **123:** 21–36.

**Moyen J., Martin H. 2012.** Forty years of TTG research. *Lithos*, **148:** 312–336.

**Moyen, J.F., van Hunen, J., 2012.** Short-term episodicity of Archaean plate tectonics. *Geology*, **40:** 451–454.

**Moyen, J.F., Laurent, O., Chelle-Michou, C., Couzinié, S., Vanderhaeghe, O., Zeh, A., Villaros, A., Gardien, V., 2017.** Collision vs. subduction-related magmatism: two contrasting ways of granite formation and implications for crustal growth. *Lithos*, **277:** 154–177.

**Moyen, J.F., Laurent, O., 2018.** Archaean tectonic systems: a view from igneous rocks. *Lithos*, **302-303**, 99-125.

**Nabelek, P.I. 2019.** Petrogenesis of leucogranites in collisional orogens. Geological Society, London, *Special Publications*, **491:** 181.

**Noce, C.M., Teixeira, W., Machado, N. 1997.** Geoquímica dos Gnaisses TTGs E Granitóides Neoarqueanos do Complexo Belo Horizonte, Quadrilátero Ferrífero, Minas Gerais. *Revista Brasileira de Geociências*, **27(1):** 25–32.

**Noce C. M., Zuccheti M., Baltazar O. F., Armstrong R., Dantas E., Renger F. E., Lobato L. M. 2005.** Age of felsic volcanism and the role of ancient continental crust in the evolution of the Neoarchean Rio das Velhas greenstone belt (Quadrilátero Ferrífero, Brazil): U-Pb zircon dating of volcaniclastic graywackes. *Precambrian Research*, **141:** 67–82.

**Nutman, A.P., Friend, C.R.L., 2007.** Terranes with ca. 2715 and 2650 Ma high-pressure metamorphisms juxtaposed in the Nuuk region, southern West Greenland: complexities of Neoarchaean collisional orogeny. *Precambrian Research*, **155:** 159-203.

**Nutman, A.P., Bennett, V.C., Friend, C.R.L., Hidaka, H., Yi, K., Lee, S.R., Kamiichi, T., 2013.** The Itsaq Gneiss Complex of Greenland: episodic 3900 to 3660 Ma juvenile crust formation and recycling in the 3660 to 3600 Ma Isukasian orogeny. *American Journal of Science*, **313:** 877–911.

**Oliveira A.H. 2004.** Evolução tectônica de um fragmento do Cráton São Francisco Meridional com base em aspectos estruturais, geoquímicos (rocha total) e geocronológicos (Rb-Sr, Sm-Nd, Ar-Ar, U-Pb). Tese de Doutorado, Departamento de Geologia da Escola de Minas da Universidade Federal de Ouro Preto, 156 p.

**Oliveira, E.P., McNaughton, N.J., Zincone, S.A., Talavera, C. 2020.** Birthplace of the São Francisco Craton, Brazil: Evidence from 3.60 to 3.64 Ga Gneisses of the Mairi Gneiss Complex. *Terra Nova*, **32**:281–289.

**O'Connor, J.T. 1965.** A classification of quartz rich igneous rock based on feldspar ratios. *US Geological Survey*, 525B, B79-B84.

**Palin, R.M., White, R.W., Green, E.C.R., 2016.** Partial melting of metabasic rocks and the generation of tonaliticetrondhjemiticegranodioritic (TTG) crust in the Archaean: constraints from phase equilibrium modelling. *Precambrian Research*, **287**: 73-90.

**Patiño Douce, A.E., Beard, J., 1995.** Dehydration-melting of biotite gneiss and quartz amphibolite from 3 to 15 kbar. *Journal of Petrology*, **36 (3)**: 707-738.

**Patiño Douce A. 1997.** Generation of metaluminous A-type granites by low-pressure melting of calc-alkaline granitoids, *Geology*, **25:** 743-746.

**Pearce, J.A., 1982.** Trace element characteristics of lavas from destructive plate boundaries. *In:* Thorpe, R.S. (Ed). *Orogenic andesites and related rocks*, John Wiley and Sons, pp. 528-548.

**Pearce, J.A., Harris, N.B.W. Tindle, A.G. 1984.** Trace element discrimination diagrams for the tectonic interpretation of granitic rocks. *Journal of Petrology*, **25**: 956–983.

**Peng, P., Qin, Z., Sun, F., Zhou, X., Guo, J., Zhai, M., Ernst, R. E. 2019.** Nature of charnockite and Closepet granite in the Dharwar Craton: Implications for the architecture of the Archean crust. *Precambrian Research*, **334**: 105478

**Pinto, C.P., Silva, M.A. 2014.** Mapa Geológico do Estado de Minas Gerais. CODEMIG, Governo de Minas, CPRM, Secretaria de Geologia, Mineração e Transformação Mineral, Ministério de Minas e Energia, Governo Federal do Brasil.

**Rapp R.P., Watson E.B. 1995.** Dehydration melting of metabasalt at 8–32 kbar: implications for continental growth and crust–mantle recycling. *Journal of Petrology*, **36:**891-931.

**Rapp, R.P., Shimizu, N., Norman, M.D., 2003.** Growth of early continental crust by partial melting of eclogite. *Nature*, **425,** 605-609.

**Rapp, R., Norman, M., Laporte, D., Yaxley, G., Martin, H., Foley, S., 2010.** Continent formation in the Archean and chemical evolution of the cratonic lithosphere: melt–rock reaction experiments at 3–4 GPa and petrogenesis of Archean Mg-diorites (sanukitoids). *Journal of Petrology*, **51**: 1237.

**Ridley, J.R., Vearcombe, J.R., Jelsma, H.A., 1997.** Relations between greenstone belts and associated granitoids. In: de Witt, M.J., Ashwall, L.D. (Eds.), Greenstone Belts. *Oxford Univ. Press*, Oxford, pp. 376–397.

**Rollinson, H.R., 2009.** New models for plagiogranites in the Oman ophiolite. *Lithos*, **112:** 603-614.

**Romano A.W. 2007.** Nota explicativa da Folha Pará de Minas (SE-23-Z-C-IV) 1:100.000. Programa Geologia do Brasil. CPRM-UFMG, 65p.

**Romano R., Lana C., Alkmim F. F., Stevens G., Armstrong R. 2013.** Stabilization of the southern portion of the São Francisco craton, SE Brazil, through a long-lived period of potassic magmatism. *Precambrian Research*, **224:** 143–159.

**Rudnick, R.L., Fountain, D.M. 1995.** Nature and composition of the continental crust: a lower crust perspective. *Reviews of Geophysics*, **33:** 267-309.

**Sanchez-Garrido, C.J.M.G., Stevens, G., Armstrong, R.A., Moyen, J.-F., Martin, H., Doucelance, R., 2011.** Diversity in Earth's early felsic crust: Paleoarchean peraluminous granites of the Barberton Greenstone Belt. *Geology*, **39**: 963–966.

**Sawyer E. W., Barnes S. J. 1988.** Temporal and compositional differences between subsolidus and anatectic migmatite leucosomes from the Quetico metasedimentary belt, Canada. *Journal of Metamorphic Geology*, **6:** 437–450.

**Sawyer E.W. 2008.**Working with migmatites: nomenclature for the constituent parts. In: Sawyer E.W. e Brown M. (Eds.). Working with migmatite: *Mineralogical Association of Canada. Short Course*, **38:**1-28.

**Shang, C.K., Liégeois, J.P., Satir, M., Frisch, W., Nsifa, E.N., 2010.** Late Archaean high-K granite geochronology of the northern metacratonic margin of the Archaean Congo craton, southern Cameroon: evidence for Pb-loss due to nonmetamorphic causes. *Gondwana Research*, **18,** 337–355.

**Silva L.C., Noce C. M., Lobato L.M. 2000.** Dacitic volcanism in the Course of the Rio das Velhas (2800-2690 Ma) Orogeny: A Brazilian Archean analogue (TTD) to the modern adakites. *Revista Brasileira de Geociências*, **30:** 384–387.

**Skjerlie, K.P., Patiño Douce, A.E., Johnston, A.D., 1993.** Fluid absent melting of a layered crustal protolith: implications for the generation of anatectic granites. *Contributions to Mineralogy and Petrology*, **114:** 365–378.

**Simon, M. B., Marques Bongiolo, E., Ávila, C. A., Oliveira, E. P., Teixeira, W., Stohler, R. C., e Soares de Oliveira, F. V. 2018.** Neoarchean reworking of TTG-like crust in the southernmost

portion of the São Francisco Craton: U-Pb zircon dating and geochemical evidence from the São Tiago Batholith. *Precambrian Research*, **314:** 353–376.

**Sisson, T., Ratajeski, K., Hankins, W., Glazner, A., 2005.** Voluminous granitic magmas from common basaltic sources. *Contributions to Mineralogy and Petrology*, **148**: 635–661.

**Sizova, E., Gerya, T., Stüwe, K., Brown, M., 2015.** Generation of felsic crust in the Archean: a geodynamic modeling perspective. Precambrian Research, **271:** 198–224.

**Smithies, R.H., 2000.** The Archaean tonalite–trondhjemite–granodiorite (TTG) series is not an analogue of Cenozoic adakite. *Earth Planetary Science Letters*, **182:** 115–125.

**Smithies, R.H., Champion, D.C., Cassidy, K.F., 2003.** Formation of Earth's early Archaean continental crust. *Precambrian Research*, **127:** 89-101.

**Smithies, R.H., 2000.** The Archean tonalite-trondhjemite-granodiorite (TTG) series is not an analogue of Cenozoic adakite. *Earth and Planetary Science Letters*, **182**: 115-125.

**Stern, R.J., 2005.** Evidence from ophiolites, blueschists, and ultra-high pressure metamorphic terranes that the modern episode of subduction tectonics began in Neoproterozoic time. Geology, **33:** 557–

**Sylvester P. J. 1998.** Post-collisional strongly peraluminous granites. *Lithos*, 45: 29–44.

**Stern, R. J. 2008**. Modern-style plate tectonics began in Neoproterozoic time: an alternative interpretation of Earth's tectonic history. *Geological Society of America Special Papers*, **440:** 265–280.

**Teixeira, W., Carneiro, M.A., Noce, C.M., Machado, N., Sato, K., Taylor, P.N. 1996.** Pb, Sr and Nd isotopic constraints on the Archean evolution of gneissic-granitoid complexes in the southern São Francisco Craton, Brazil. *Precambrian Research*, **78:** 151–164.

**Teixeira W., Cordani U.G., Nutman A.P., Sato K. 1998**. Polyphase Archean evolution in the Campo Belo metamorphic complex, Southern São Francisco Craton, Brazil: SHRIMP U-Pb zircon evidence. *Journal of South American Earth Sciences*, **11:** 279-289.

**Teixeira, W., Oliveira, E.P., Marques, L.S., 2017a.** The nature and evolution of the Archean Crust of the São Francisco Craton. In: Heilbron, M., Alkmim, F., Cordani, U.G. (Eds.), São Francisco Craton, Eastern Brasil: tectonic genealogy of a miniature continent, *Regional Geology Review Series*. Springer-Verlag, pp. 29–56.

**Teixeira, W., Oliveira, E. P., Peng, P., Dantas, E. L., Hollanda, M. H. B. M. 2017b.** U-Pb geochronology of the 2.0 Ga Itapecerica graphite-rich supracrustal succession in the São Francisco Craton: Tectonic matches with the North China Craton and paleogeographic inferences. *Precambrian Research*, **293**: 91–111.

**van Hunen J. e Moyen J-M. 2012.** Archean Subduction: Fact or Fiction? *Earth and Planetary Science, The Annual Review*, **40:**195-219.

**Van Kranendonk, M.J., 2010.** Two types of Archean continental crust: plume and plate tectonics on early earth. *American Journal of Science*, **310:** 1187-1209.

**Verma, S.K., Oliveira, E.P., Silva, P.M., Moreno, J.A., Amaral, W.S. 2017.**Geochemistry of komatiites and basalts from the Rio das Velhas and Pitangui Greenstone Belts, São Francisco Craton, Brazil: Implications for the origin, evolution, and tectonic setting. *Lithos*, **284–285:** 560–577.

**Vielzeuf, D., Schmidt, M.W., 2001**. Melting relations in hydrous systems revisited: application to metapelites, metagreywackes and metabasalts. *Contributions to Mineral Petrology,* **141:** 251–267.

**Whalen, J.B., Currie, K.L. Chappell, B.W. 1987.** A-type granites geochemical characteristics, discrimination and petrogenesis. *Contributions to Mineralogy and Petrology***, 95:** 407–419.

**Wang, C., Song, S., Niu, Y., Wei, C., Su, L. 2016.** TTG and potassic granitoids in the Eastern North China craton: Making Neoarchean upper continental crust during micro-continental collision and post-collisional extension. *Journal of Petrology*, **57:** 1775–1810.

**Watkins, J.M., Clemens, J.D. Treloar, P.J. 2007.** Archaean TTGs as sources of younger granitic magmas: melting of sodic metatonalites at 0.6–1.2 GPa. *Contributions to Mineralogy and Petrology*, **154**: 91–110.

**White, A.J.R. Chappell, B.W. 1983.** Granitoid types and their distribution in the Lachlan Fold Belt, southeastern Australia. In: Roddick, J.A. (ed.) Circum Pacific Plutonic Terranes. *Geological Society of America, Memoir*, **159:** 21–34.

**Zhang, C.L., Li, H.K., Santosh, M., Li, Z.X., Zou, H.B., Wang, H.Y., Ye, H.M., 2012**. Precambrian evolution and cratonization of the Tarim Block, NW China: Petrology, geochemistry, Nd-isotopes and U-Pb zircon geochronology from Archaean gabbro-TTG-potassic granite suite and Paleoproterozoic metamorphic belt. *Journal of Asian Earth Sciences*, **47:** 5–20.

**Zhou, Y.Y., Zhao, T.P., Wang, C.Y. Hu, G.H. 2011.** Geochronology and geochemistry of 25 to 24 Ga granitic plutons from the southern margin of the North China Craton: Implications for a tectonic transition from arc to post-collisional setting. *Gondwana Research*, **20:** 171–183

# ANEXO 2: GEOCRONOLOGIA E EVOLUÇÃO TECTÔNICA

Manuscript: "**Episodic crustal growth and reworking in the Archean Divinópolis Complex, southern São Francisco Craton (Brazil)**"

# Episodic crustal growth and reworking in the Archean Divinópolis Complex, southern São Francisco Craton (Brazil)

## Abstract

The Archean crust of the southern São Francisco Craton (3.2–2.6 Ga), eastern Brazil, is composed by a variety of metamorphic-igneous complexes with calcium-alkaline of TTG affinity forming a typical TTG-greenstone terrain. U-Pb ages (LA-ICP-MS) from zircon and monazite from the Divinópolis Complex reveals for the first time the polygenetic magmatic and metamorphic long-lived evolution of this dome. Our findings support a polycyclic evolution of the predominantly Neoarchean crust of the Divinópolis Complex, with inherited components from 3.2 to 2.8 Ga. The dome represents a well preserved late-Archean TTG suite, composed of tonalite-trondhjemite-granodiorite gneisses and subordinately, migmatites. Two generations of granite intrude the gneiss basement, an older foliated monzogranite generation and a younger isotropic syenogranite generation. The first period of felsic crust generation occurred from 2915 to 2860 Ma, represented by tonalites and trondhjemites. This event represents the rise of stable, long-lived felsic continents in the southern São Francisco Craton. From 2790 to 2775 Ma reworking process dominates, resulting in the extensive granodiorites and granites. Multiple collision of microcontinents (the domes in the southern São Francisco craton) would be triggered by growth of the newly formed felsic TTG crust, overriding adjacent mafic crust. Eventually this collisional phase would start short-term episodes of proto subduction and delamination of thick mafic crust, resulting in coeval periods of vertical and horizontal tectonics, representing a fundamental change in the geodynamic style of the southern São Francisco craton. The Mamona event (2760–2680 Ma) represents a period of progressive growth of continental crust and the Mamona I phase monzogranites (2760–2715) can be assigned to convergent margins or collisional settings, being consistently more deformed and less rich in potassium. The Mamona II phase syenogranites (2705–2680) likely formed during an extensional post collisional setting and comprise the potassic granites related to the irreversible differentiation and evolution of the crust, followed by a period of stability. The last potassic plutons characterize crust maturation and thermal stabilization of the São Francisco Craton. We propose a diachronic N to S maturation and stabilization of the São Francisco Craton. The Paleoproterozoic influence of the Mineiro Orogeny (2,1–1,9 Ga) was responsible for tectonic reactivation and development of important shear zones where water-fluxed melt can be facilitated, resulting in migmatite induction. During this period, reset of monazite and titanite occurred in the Archean nuclei as a result of crustal thickening and heating dated at 2062 ± 7 Ma in monazites from a leucosome of Divinópolis Complex. This syn-collisional metamorphism peaked at granulite facies.

## 1. Introduction

Earth's continental crust has evolved through time and about ~70% of it was formed by the end of the Archean (e.g. Taylor and McLennan, 1985; Dhuime et al., 2012). The dominant tonalite-trondhjemite-granodiorite series (TTG, Jahn et al., 1981) is amongst the oldest types of felsic magmas on Earth, estimated to make up around 50% to 70% of Archean juvenile continental crust (Moyen and Martin, 2012; Hoffman et al., 2019). They are typically composed of quartz, plagioclase, and biotite, with minor hornblende. These felsic rocks represent the transition from a dominantly mafic-ultramafic proto crust into an increasingly felsic continental crust and record the earliest stages of continent formation, composed by the TTG series (Martin et al., 2005; Hawkesworth et al., 2010; Moyen and Martin, 2012).

The most accepted models for TTG generation advocate a genesis from partial melting of relatively low-MgO hydrated basaltic rocks such as amphibolite (Foley et al., 2002; Johnson et al., 2014) at pressures sufficiently high to stabilize garnet (Moyen, 2011). The hydrated mafic source could be a partially melted subducting oceanic lithosphere in a process similar to adakite genesis (Arndt, 2013; Martin et al., 2005; Polat et al., 2015) or partially melted thick (>30 km) plateau-like mafic crust multiply reworked (Bédard, 2006; Sizova et al., 2015; Van Kranendonk et al., 2015).

In the Eo- and Paleoarchean, TTG suites are dominated by tonalites and trondhjemites, whereas towards Meso- and late Archean, they evolve away from typical TTGs and become increasingly granitic (Laurent et al., 2014). This transition is registered as a peak in igneous activity by the end of the Archean, with the massive generation of granodiorite and potassic granite batholiths linked to the stabilization of cratons (Taylor and McLennan, 1985; Tchameni et al., 2000; Romano et al., 2013; Laurent et al., 2014; Champion and Smithies, 2019). Some works propose an origin for the granodiorite batholiths by partial melting of previous TTG (Ridley et al., 1997; López et al., 2005), whereas the potassic granites characteristic of Late-Archaean (2.8–2.5 Ga) are represented by diverse rocks like sanukitoids, biotite granites, two mica granites, and are more complex to unravel, with their origin linked to subduction, collision, post-collision and intra-plate settings (Frost et al., 1998; Smithies, 2000; Laurent et al., 2014). The intrusion of Meso to Neoarchean granodiorite batholith is interpreted by some authors as favoring the idea of sporadic growth of continents (Taylor and McLennan, 1985; Condie, 1997). Other hypotheses suggest that granodiorites are products of recycled older crust, without additional crustal growth (Hawkesworth et al., 2009; Kemp et al., 2006).

In Brazil, the São Francisco Craton records a Paleo- to Neoarchean evolution of a TTG sialic crust and associated Meso-Neoarchean greenstone belts. In the northern portion of the craton, the Gavião Block hosts one of the oldest rocks of South America, in an ancient TTG nucleus of 3.5 to 3.2 Ga (Barbosa and Sabaté, 2004, Oliveira et al., 2020). The southern portion of the craton has considerably younger ages,

with the only Paleoarchean crust dated in Santa Bárbara Complex at 3220 Ma (Lana et al. 2013). The Rio das Velhas and Pitangui Greenstone Belts date at ca. 2900–2700 Ma, also younger than the northern Archean greenstone belts, such as Contendas–Mirante, Umburanas and Riacho de Santana at ca. 3200–2900 Ma (Nutman et al., 1994; Barbosa and Sabaté, 2004; Melo-Silva et al., 2020). Correlations between the southern and northern portions are practically non-existent, although some authors understand both to be contiguous (Romano et al., 2013).

Cratonic terrains are amongst the oldest records of continental formation and in many places, their origin is linked to the transition to modern-style process of magmatism and tectonics. We propose in this work that the multiple stages of magmatism during Meso- to Neoarchean are associated with mantellic differentiation in this sialic portion of south São Francisco Craton crust. This study establishes for the first time an expressive compilation of time interval events in Divinópolis Complex, these data have implications for temporal relationships to the regional crustal evolution in the southern São Francisco Craton. This contribution reports Laser Ablation-Sector Field Inductively Coupled Plasma Mass Spectrometer (LA-SF-ICPMS) ages of the unexplored sialic crust of the Divinópolis Complex in southern São Francisco Craton. The dating of zircon and monazite grains is used to constrain the timing of magmatism and metamorphism of the tonalites-trondhjemites-granodiorites and granites of the dome.

## 2. Geological framework of south São Francisco Craton

The São Francisco Craton (Fig. 1), located in center-east Brazil (Almeida, 1977) is composed of Archean nuclei bordered by Archean to Proterozoic mobile belts (e.g. Araçuaí, Ribeira and Brasília belts) and partially covered by sedimentary basins (São Francisco, Bambuí, Espinhaço). The Archean nuclei and belts were amalgamated and reworked in the Paleoproterozoic (Heibron et al., 2017), colliding against the south bounding accretionary Mineiro belt (Alkmim and Teixeira, 2017). The southern portion of the São Francisco Craton is formed by a sialic calc-alkaline crust with TTG affinity (Teixeira et al., 1996; 2017a) separated in granitic-gneiss-migmatite complexes around polydeformed belt sequences, between 3200 Ma and 2600 Ma (e.g., Noce, 2000; Teixeira et al., 1996; Machado et al., 1996; Lana et al., 2013; Farina et al., 2016). The best-studied complexes of south São Francisco Craton are geographically located in the Quadrilátero Ferrífero mining district of Minas Gerais state (Fig. 1). Many areas outside the district lack detailed geochemical and geochronological studies, which is the case of Divinópolis Complex, where works concentrate on its south border along the margins of Cláudio Shear Zone (Oliveira, 2004; Carvalho et al., 2017a) (Fig. 2). Divinópolis Complex has been correlated to Campo Belo in previous works (e.g. Teixeira et al., 1996; Fernandes and Carneiro, 2000) but more recently is has been reported as a separate unit (Albert et al., 2016; Farina et al., 2016, Teixeira et al., 2017a).

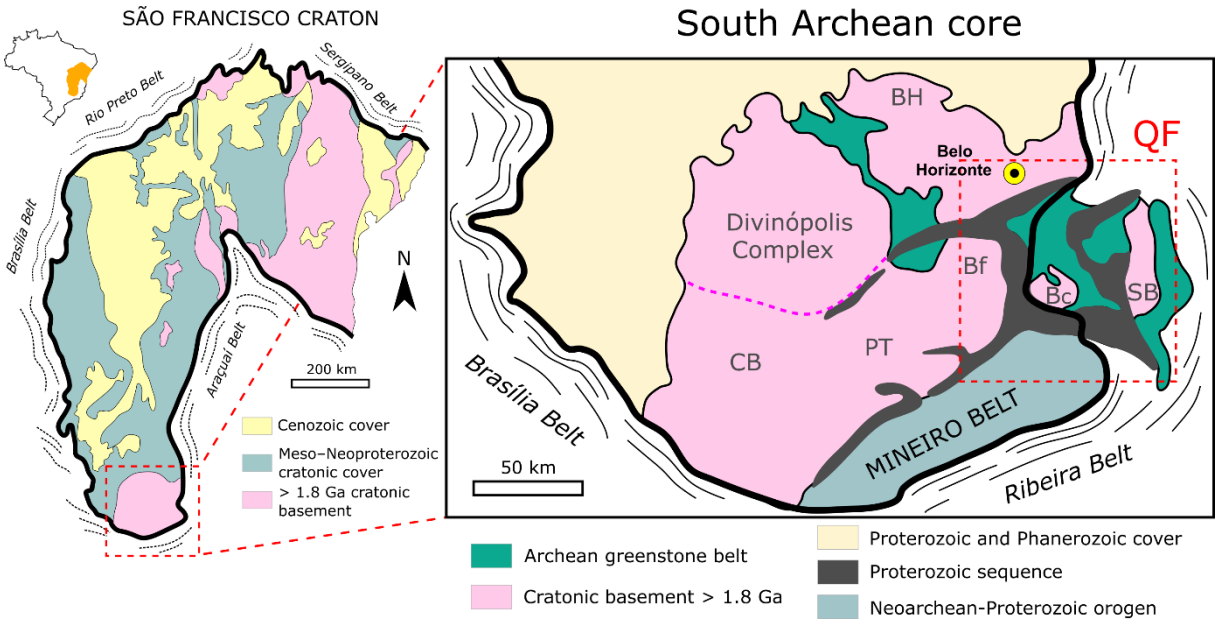


**Figure 1:** Geological map of the São Francisco Craton with focus on its southern Archean core (adapted from Alkmin and Noce, 2006; Teixeira et al., 2017a). **CB:** Campo Belo Complex, **PT:** Passa Tempo Complex, **Bf:** Bonfim Complex, **BH:** Belo Horizonte Complex, **Bc:** Bação Complex, **SB:** Santa Bárbara Complex, **QF:** Quadrilátero Ferrífero mining district.

The igneous-metamorphic crystalline basement of Southern São Francisco Craton is divided in gneiss-granitic complexes, such as Bação, Bonfim, Campo Belo, Belo Horizonte, Santa Bárbara, Passa Tempo and Divinópolis domes (Fig. 1) (Teixeira et al., 2017a; and references therein). The accretionary process that originated the continental cores of the Meso-Neoarchean domes are termed the Rio das Velhas I Event (2930–2850 Ma) in reference to the Rio das Velhas greenstone belt formation (Machado et al., 1996; Lobato et al., 2001; Noce et al., 2005; Baltazar and Zucchetti, 2007).

The domes are formed mainly by gneisses with mesocratic bands rich in plagioclase and biotite whereas the leucocratic ones are predominantly composed of plagioclase, quartz and minor microcline (Machado et al., 1996; Teixeira *et al.*, 1996; Noce et al., 1998; Lana et al., 2013; Farina et al., 2016). They are intruded by medium-coarse grained, mostly weakly foliated granites that form large batholiths (e.g. Mamona) or as smaller stocks with porphyritic textures ranging in composition from tonalite to syenogranite (Lana et al., 2013; Romano et al., 2013; Moreno et al., 2017). The granites were divided into Medium-K (plg-rich) and High-K (kfs-rich, Romano et al., 2013; Farina et al., 2015). The emplacement of Plg-rich granites (medium-K magmatism) is attributed to the Rio das Velhas II Event (2800–2760 Ma), while the transition to potassic magmatism and emplacement of high-K granites took place during the Mamona Event (2760–2680 Ma; Romano et al., 2013; Lana et al., 2013; Farina et al., 2015).

Santa Bárbara Complex preserves the oldest nucleus of Southern São Francisco Craton with constrained U–Pb ages between 3210 ± 8 and 3212 ± 9 Ma (Lana et al. 2013). This age interval gives the name of the Santa Bárbara Event (3220–3200 Ma), responsible for the first generation of juvenile sialic

crust recorded in south São Francisco Craton. In agreement, Paleo to Mesoarchean $T_{DM}$ ages (3400–3000 Ma) are evidence of older continental growth (Teixeira et al., 1996; Corrêa da Costa, 1999), also preserved in ancient detrital zircon age populations recovered from the metasedimentary rocks of Rio das Velhas greenstone belt (Hartmann et al., 2006), Pitangui Greenstone Belt (Melo-Silva et al., 2020) and from the Minas Supergroup (Moreira et al., 2016).

The southern São Francisco Craton is described as a typical Archean dome-and-basin terrain (e.g. Alkmim and Marshak, 1998). Together with Rio das Velhas and Pitangui Greenstone Belts, the gneiss domes make an extensive granite-greenstone terrain (Marshak et al., 1997; Noce et al. 2005; Cutts et al., 2019) with the enigmatic configuration of dome-and-keel geometry reported in numerous Archean cratons (Van Kranendonk et al., 2007; Sizova et al., 2015). The supracrustal sequences are the keels between the sialic crust and they are represented by the Rio das Velhas Supergroup (ca. 2900–2730 Ma), the Pitangui Greenstone Belt (2900–2690 Ma), the Minas Supergroup (ca. 2600–2100 Ma) and the Itacolomi Group (ca. 2100–2000 Ma). To west and north, the craton is covered by Proterozoic metasedimentary rocks of Espinhaço Supergroup and Bambuí Group.

The Paleoproterozoic Minas Supergroup is a package of clastic and chemical rocks (Dorr, 1969; Alkmim and Marshak, 1998) lying unconformably over the Rio das Velhas greenstone belt. It can be subdivided in two sequences, a lower one formed by continental to marine sediments of a passive margin basin (Dorr, 1969; Schorscher, 1992; Canuto, 2010) and an overlying sequence consisting of turbidites of a submarine fan deposit marking the inversion of the passive margin (Alkmim and Marshak, 1998; Alkmim and Martins-Neto, 2012). The dome-and-keel configuration of Quarilátero Ferrífero is interpreted to have formed in a two-stage process, where the first period occurred during orogenesis at 2770-2700 Ma and the second one at ca. 2050 Ma marked by compressional events related to the Minas Orogeny and the development of the Minas Supergroup (Cutts et al., 2019).

The Mineiro Belt (ca. 2.6–2.0 Ga) crops in the southern west margin of São Francisco Craton and corresponds to a sequence of high-grade, polydeformed plutonic and metasedimentary rocks, deformed greenstone belt remnants, and 2.3–2.0 Ga granitoids (Dorr, 1969; Alkmim and Marshak, 1998; Seixas et al., 2012; Teixeira et al., 2015). This belt lies in unconformably tectonic contact with the Rio das Velhas greenstone belt and is assumed to have formed through successive accretion of oceanic and continental arcs. Convergence and collision along the eastern margin of the Archean core of southern São Francisco Craton during the closure of the Minas Basin between 2.1 and 2.0 Ga led to the amalgamation of São Francisco and Congo cratons (Alkmim and Teixeira, 2017; Teixeira et al., 2017a; Aguilar et al., 2017). Related to this event, granulite-facies rocks are described along the anatectic region of Cláudio Shear Zone (ca. 2.06 Ga) interpreted to have formed due to granitoid dehydration (Corrêa da Costa, 1999; Oliveira, 2004).

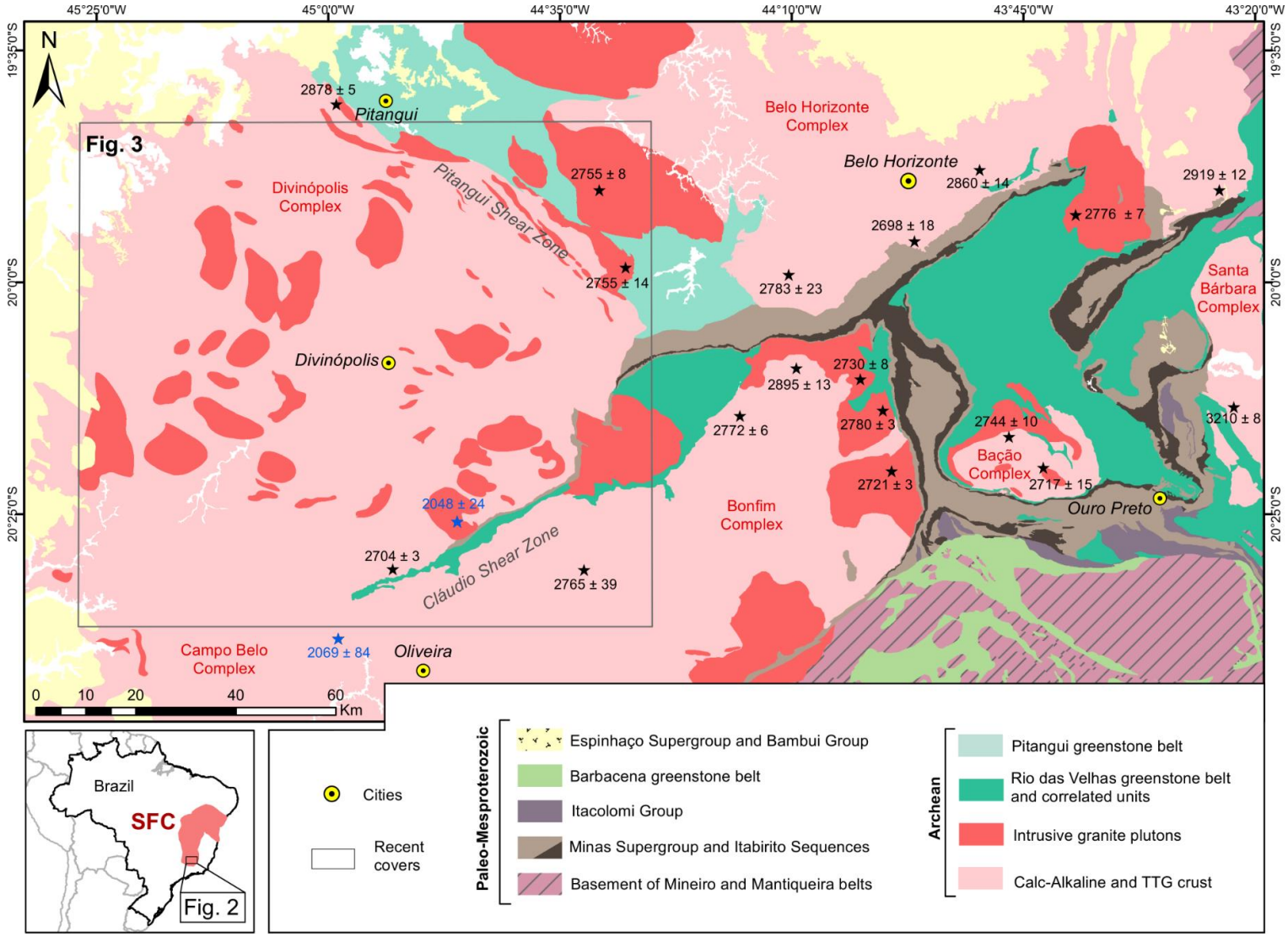


**Figure 2:** Geological map of Quadrilátero Ferrífero and Divinópolis Complex (modified from Pinto and Silva, 2014) showing previously published U-Pb ages (in Ma). Black stars indicate igneous ages and blue stars indicate metamorphic ages. Compiled from Machado et al. (1992); Machado and Carneiro (1992); Oliveira (2004); Lana et al. (2013); Romano et al. (2013); Farina et al. (2015); Carvalho et al., (2017a); Teixeira et al. (2017b).

Subsequent Paleoproterozoic reworking of the Archean crust has been pointed out by many authors. Carvalho et al. (2016; 2017a), based on the ca. 2.05 Ga anatectic event recorded in the Kinawa migmatite, correlated the collision of the Mineiro and Mantiqueira belts against the Archean core of south São Francisco Craton. Teixeira et al. (2017b) reported Paleoproterozoic ages (2.0 Ga) for the Itapecerica graphite-rich supracrustal succession as a response to this crustal reworking. Post-Archean events of crustal reworking between 2.1–2.0 Ga are also reported in metamorphic minerals at anatexis zones such as Jeceaba-Bom Sucesso and Lenheiros Shear Zones (Campos and Carneiro, 2008; Barbosa et al., 2015). The margins of SFC were affected by the Brasilian–Pan African orogeny Orogeny around 600–500 Ma during the assembly of West Gondwana (Alkmim and Noce, 2006). During this event, a passive margin of a carbonate-siliciclastic successions that covers part of the São Francisco Craton were deposited, named Bambuí Group (750–450 Ma) (Uhlein et al. 2016).

## 3. Analytical techniques

Detailed petrography under transmitted light was carried out on thirty thin sections, distributed throughout the dome. Additional mineralogical and textural characterization was made using a Scanning Electron Microscope (SEM) coupled with an Energy Dispersive Spectroscopy (EDS) at the University of Campinas (UNICAMP).

Ten samples were selected for U-Pb isotope zircon in gneiss and migmatite protoliths and one sample was selected for monazite analyses from a migmatite leucosome, conducted at the Isotopic Geology Laboratory of the Geosciences Institute of the University of Campinas by LA-SF-ICP-MS. Sampled sites are shown in Fig. 3 whereas their description is detailed in the next section. GPS coordinates of the samples are shown in Table 1 and result data is shown in Appendix B (Table 2). Zircon and monazite concentrates were extracted from approximately 5 to 1 kg of a sample that was crushed, milled and sieved. The grains were separated by conventional procedures using Frantz magnetic separator and heavy liquids after concentration by hand panning. Grains were extracted under a binocular microscope by hand-picking, mounted in eight epoxy disks and polished. Cathodoluminescence (CL) were obtained for analysis of internal structure and morphology in the zircon grains, while secondary electron images (BSE) helped avoid defects such as micro inclusions and microfractures in zircon and monazite grains.

The mounts were cleaned with $HNO_3$ and loaded into an Excite 193 Photon Machines linked to an Element XR, Thermo Scientific Multi-collector ICP-MS according to the procedures of Navarro et al. (2015). Ultrapure He was used as the carrier gas and the laser frequency was 10 Hz with a fluency of 4.74 J $cm^{-2}$. The reference material 91500 zircon (Wiedenbeck et al., 1995) was used as a primary standard for

data reduction (1065 Ma), and Peixe zircon standard (ID-TIMS age of 564 ± 4 Ma; cf. Dickinson and Gehrels, 2003) was used to monitor the quality of the reduction procedures. Three analytical sections were conducted and the results of the Peixe standard yielded weighted averages of 559.2 ± 4.2 (MSWD = 1.9, n = 15), 573.7±3.5 (MSWD = 0.98, n = 14) and 565.7 ± 4.5 Ma (MSWD = 1.2, n = 16). The analytical section of the monazite mount was standardized using the primary (505.7 ± 1.3 Ma, MSWD = 1.2, n = 30) reference material Bananeira (Gonçalves et al., 2016) and the accuracy of the results was confirmed using the USGS 44069 standard (426.5 ± 2.5 Ma, Aleinikoff et al., 2006). The spot size was set to 25 µm diameter and data reduction was made offline using Iolite 2.5 software, following the methods of Paton et al. (2010) and VizualAge 2014.10 software (Petrus and Kamber, 2012). The Concordia diagrams and histograms were made using Isoplot 4.15 excel plugin (Ludwig, 2012). Measurements with >1% common lead were excluded, and all uncertainties are reported as 2 sigma values.

## 4. Sample description and petrography

Divinópolis Complex is inserted in the context of the southern São Francisco Craton, west of Quadrilátero Ferrífero, being a composite dome formed by an orthogneiss-migmatite unit and a granite unit. The gneiss and migmatite unit encompass a tonalite, trondhjemite and granodiorite association, as many other TTG domes in the region (Campo Belo, Belo Horizonte, Bonfim, Bação) and worldwide. They exhibit alternating bands of light-colored and mesocratic material, very rarely melanocratic and punctually dioritic. Potassic granitoid intrusions occur along the complex and can form large batholiths and plutons, as well as small stocks, intruded into the gneisses. Their intrusion occurred in two phases: and older phase comprises foliated Plg-rich monzogranites; and a younger phase predominantly kfs-rich and non-deformed formed by syenogranites that are restricted to the west domain of the dome. These potassic granitoids cover somewhat 30% of Divinópolis dome and may display sharp contacts with the surrounding gneisses (Fig. 4).

### *4.1 Structural controls*

Many small-scale lineaments and three big regional-scale shear zones (Itapecerica, Cláudio, and Pitangui) define the tectonic boundaries and structural limits of Divinópolis Complex, on its northeast and southern borders. The nature and geometry of the west margin remains more enigmatic as it is covered by rocks of the Proterozoic Bambuí Group. Foliation defines a NW-SE trend in the north of Divinópolis Complex with moderate to steeply dipping to NE, and NE-SW trend in the south. In the center of the dome

the outcrops show no major faults and mostly showing igneous features with variable orientation of gneissose.

The northeast contact with the Pitangui Greenstone Belt is underlined by a strongly NW-SE sheared zone with mylonitic character. Deformation is mostly represented by augen gneiss, boudinage structures evidence a brittle to ductile deformation and cinematic indicators suggest a sinistral sense of movement for the Pitangui Shear Zone. This structural control is attributed to the collision of the Pitangui Greenstone Belt with Divinópolis continental crust, with the regional foliation related to tectonic imbrication during thrusting, parallel to the granitoid-greenstone contact (Pitangui Lineament). Compressional deformation is shown by the development of westward-facing isoclinal folds in the Pitangui Greenstone Belt. Structurally controlled orogenic gold deposits hosted in rocks of the Pitangui Greenstone Belt are associated with this event (Brando Soares et al., 2017; Fabricio-Silva et al., 2018). This northeast domain also hosts potassic granitoids which intrusions appears to be structurally controlled. Available data indicate that the Pitangui Greenstone Belt is a synclinal keel between Divinópolis and Belo Horizonte domes with mafic volcanic rocks near the greenstone–dome contacts, cored by metasedimentary rocks (Brando Soares et al., 2017; Melo-Silva et al., 2020).

In the southern limit, the dome is limited by the NE-SW Cláudio and Itapecerica shear zones. These south strike-slip shear zones have a dextral sense of movement, with pervasive foliation and lineation with a strong ductile character. Gneiss foliation shows a NE-SW trend and moderate dipping (20 to 50º), lineation and fold axial planes pitch constantly to NE. Small scale normal faults with low to high angle can disrupt the gneiss banding. The geometry and kinematics are consistent with the Mineiro Belt deformation front, exhibiting the same orientation of Jeceaba-Bom-Sucesso and Lenheiros Shear Zones (Campos and Carneiro, 2008; Barbosa et al., 2015). In this southern zone related to Cláudio and Itapecerica shear zones the degree of anatexis increases, resulting in widespread migmatite formation. The major structures that characterize the southern limit are dextral and coeval with peak granulite-facies metamorphism at 2.1 and 2.0 Ga (Carvalho et al.,2017; Teixeira et al., 2017) (Table 1).

Based on structural controls and airborne geophysical data, three distinct domains within the dome are defined (Fig. 4): a (1) northeast domain, where deformation is predominantly mylonitic with many small-scale shear zones and the granitoid intrusions have a strong structural control; a (2) central domain with predominantly ductile deformation or preserved igneous features, and localized shearing; a (3) west domain, partially covered by a Proterozoic basin (Bambuí Group) and where gneisses intercalated with migmatites are intruded by a series of non-deformed Kfs-rich granite bodies; and lastly, a (4) NE-SW south domain exhibiting a large anatectic zone in the southern contact with Campo Belo e Bonfim complexes.

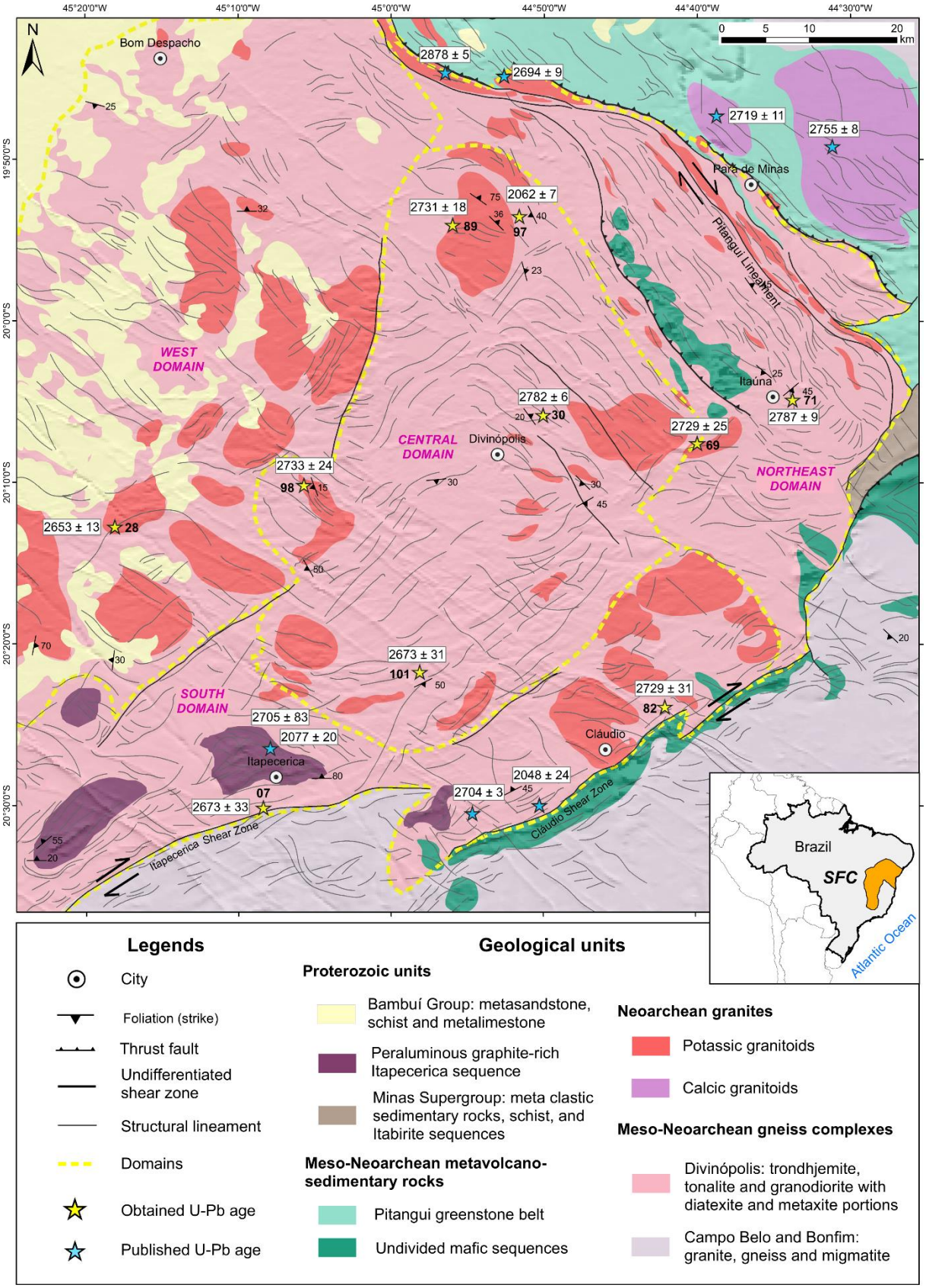


**Figure 3:** Geological map of the studied area, generated by field mapping and geophysical data. The ages represented by the yellow stars were obtained in this study, and the ages represented by the blue stars are from previously published work (Farina et al., 2015; Carvalho et al., 2017a; Teixeira et al., 2017a; Melo-Silva et al., 2020).

*4.2 Tonalite gneiss*

Divinópolis tonalite gneiss is dark grey, fine- to medium-grained, leucocratic (Fig. 4a). No abrupt contact between the tonalites, trondhjemites and granodiorites are observed. The tonalites are dominantly hornblende-biotite gneisses intruded by undeformed, layer-parallel or crosscutting leucogranite and pegmatite granite veins. These rocks contain oligoclase (52%) + quartz (24%) + biotite (10%) and amphibole (8%) as main minerals, with common chlorite and epidote as products of replacement of biotite. Zircon, apatite, titanite, allanite and some opaque minerals (ilmenite and rutile) are common accessory minerals, where rutile and ilmenite occur associated, usually around titanite and pargasite. Plagioclase is partly sericitized and saussuritized, with minor hydrothermal alteration and the amphibole is pargasite (Fig. 5a). Granoblastic texture is widespread and coarse-grained with sub grain recrystallization and melt at grain boundaries. The granoblastic domains comprise quartz and plagioclase layers with interlobate outlines and bulging. Textural controls indicate that pargasite formation followed replacement by biotite with the development of the discontinuous gneissic foliation. One sample of the tonalite was dated: sample 71D, represented by a tonalite gneiss with a banding defined by oriented biotite and stretched quartz. This tonalite was pervasively migmatized and is exposed in the Britadora RS Quarry, near Itaúna city, in the northeast sector of Divinópolis dome.

*4.3 Trondhjemite gneiss*

The trondhjemite gneiss is grey, medium-grained, leucocratic, sometimes inequigranular. The texture is granoblastic with a discontinuous foliation (Fig. 4b) defined by orientation of biotite. They are formed by oligoclase (56%) + quartz (26%) + biotite (18%), with monazite, allanite, titanite, zircon and opaque minerals as the main accessory minerals. Chloritization and saussuritization of biotite and plagioclase, respectively, are common. Intergrowths of quartz in alkali feldspar characterize granophyric texture and the trondhjemites are medium- to coarse-grained, with granoblastic interlobate and lepidoblastic texture. Higher strain zones develop metatexitic gneiss with segregate domains of granoblastic leucocratic minerals (quartz + plagioclase) and lepidoblastic domains of melanocratic minerals (biotite) that defines the main discontinuous foliation. Sample 30, a trondhjemite gneiss was collected for dating, representing a banded gneiss collected from MBL Quarry, north of Divinópolis city and located in the central domain. The rock displays strong foliation and mylonitic features, with augen texture and weak boudinage of the leucocratic bands.

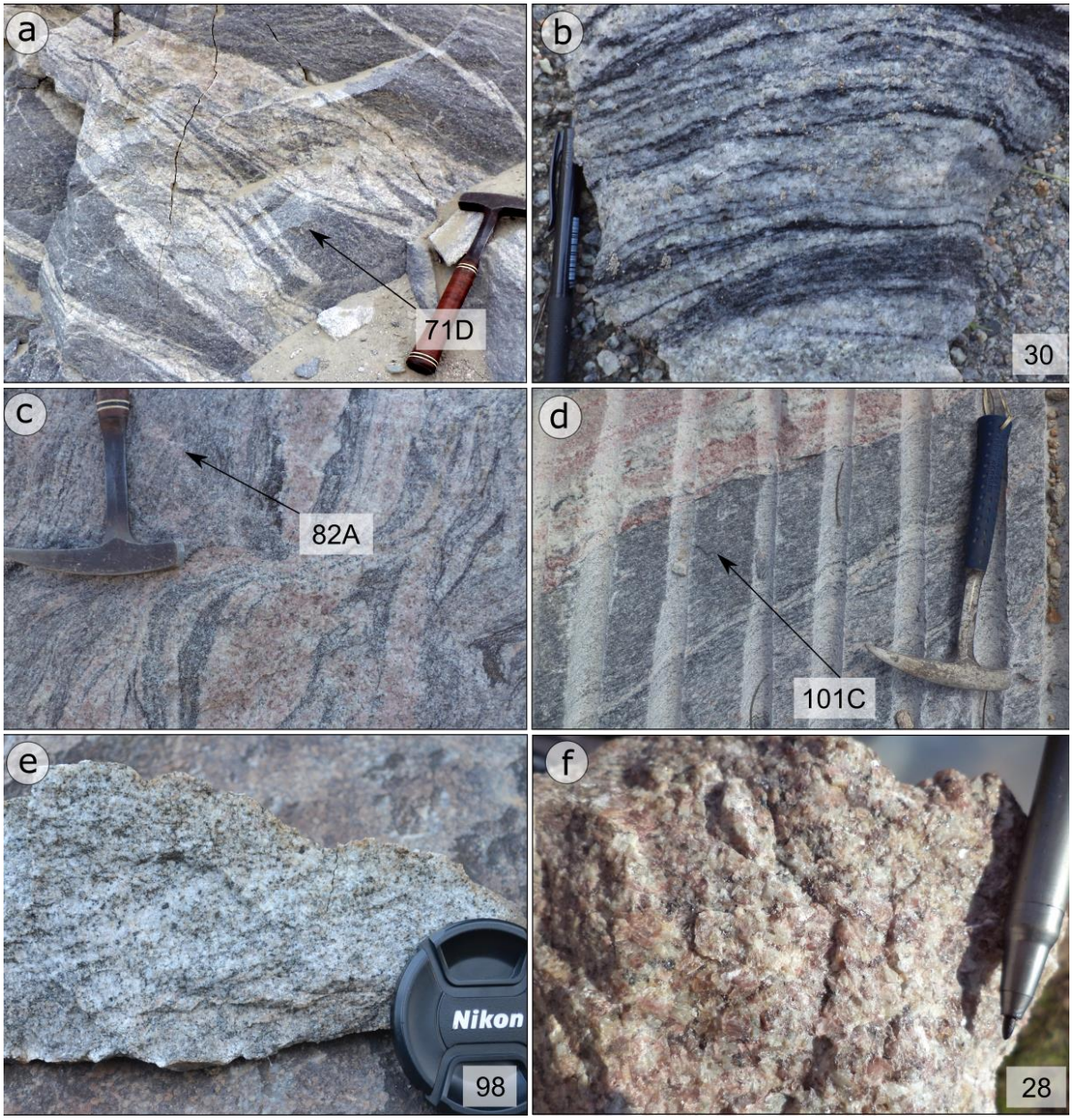


**Figure 4:** Main textural and structural features of the U-Pb dated samples. **a)** Tonalite gneiss collected from the North Domain, crosscut by leucocratic dyke. **b)** Trondhjemite gneiss with alternating leucocratic and melanocratic bands. **c)** Detailed photography of the granodiorite gneiss collected close to the Cláudio Shear Zone. **d)** Compositional variation recorded in the migmatite of sample 101C, collected from an abandoned quarry in the Central Domain. **e)** Foliated monzogranite of the Central Domain rich in plagioclase. **f)** Detailed image of the Kfs-rich isotropic syenogranite typical of the west domain.

### *4.4 Granodiorite gneiss*

The granodiorite gneiss has a pinkish color due to the occurrence of alkali feldspar (coarser-grained), they are fine- to coarse-grained, leucocratic and with more prominent banding and folding structures that can follow the main foliation. They are composed of oligoclase (40%) + quartz (31%) + biotite (13%) + microcline (10%) ± garnet, with titanite, allanite, zircon and opaque minerals as accessory minerals (Fig. 5b). Graphic quartz in alkali feldspar and perthite are common. Alteration is similar to the

tonalites and trondhjemites, with chloritization and epidotization of biotite, sericitized and saussuritized plagioclase and minor hydrothermalism. The occurrence of dark-green amphibolite boudins are localized, comprising elongated syn-tectonic bodies that follow the gneissic foliation. Melt-related textures are also localized and are represented by quartz and alkali feldspar films around the borders of crystals. One sample was used for U-Pb dating (**89C**), representing a banded granodiorite gneiss collected from Britadora Nova Serrana Quarry (Nova Brita - MBL), in the north sector of Divinópolis dome, proximate to a granite intrusion. This gneiss is a medium-grained granodiorite with grey leucocratic bands and pinkish portions, with a non-penetrative foliation. Abundant leucocratic and pegmatite veins crosscut or are parallel to the gneiss banding.

**Table 1:** Petrological features of the dated samples and their UTM coordinates (Datum Córrego Alegre 23S).

| Sample | Lithotype | Main mineralogy % | Accessory mineralogy[1] | Texture and structure | UTM |
|---|---|---|---|---|---|
| 71 | Tonalite gneiss | Plg, Qtz, Bt | Chl, Ep, Zr, Tit, Ser, Ap, Op | Non-penetrative foliation | 545812 7779435 |
| 30 | Trondhjemite gneiss | Plg, Qtz, Bt | Amp, Chl, Ep, Zr, Ser, Ap, Mz, Op | Inequigranular (phenocryst), banded (1 to 10 cm) | 517340 7777687 |
| 89 | Granodiorite gneiss | Plg, Qtz, Bt, Kfs | Chl, Ep, Zr, Ser, Ap,Op | Continuous well-developed foliation | 507015 7799377 |
| 07 | Granodiorite migmatite | Plg, Qtz, Bt, Kfs | Chl, Ep, Zr, Ser, Op | Non-penetrative foliation, mineral intergrowths | 485435 7732883 |
| 82 | Granodiorite migmatite | Plg, Qtz, Bt, Kfs | Chl, Ep, Zr, Ser, Ap, Op | Coarse-grained, non-penetrative foliation | 531235 7744394 |
| 101 | Monzogranite migmatite | Qtz, Pl, Bt, Kfs | Chl, Ep, Zr, Ser, Op | Incipient foliation, mineral intergrowths | 503262 7748349 |
| 69 | Foliated monzogranite | Qtz, Pl, Bt, Kfs | Chl, Ep, Zr, Ser, Op | Medium-grained, penetrative foliation | 534912 7774459 |
| 98 | Foliated monzogranite | Qtz, Pl, Bt, Kfs | Amp, Chl, Ep, Zr, Ser, Ap, Op | Medium-grained, non-penetrative foliation | 490037 7769692 |
| 28 | Syenogranite | Qtz, Pl, Bt, Kfs | Chl, Ep, Zr, Tit, Ap, Op | Medium-grained, inequigranular (porphyritic) | 468469 7764952 |
| 97 | Trondhjemite migmatite | Plg, Qtz, Bt | Chl, Ep, Zr, Ap, Ser, Mz, Tit | Medium to coarse-grained, inequigranular, foliated | 514611 7800370 |

[1] Mineral abbreviation after Whitney and Evans (2010).

*4.5 Monzogranites*

The first granite intrusion phase is characterized by biotite granites (granodiorite and monzogranite, grouped here as monzogranites). These granitoids are leucocratic, medium-grained, greyish-pink and weakly foliated foliated (Fig. 4e). They always show a stronger degree of weathering than the gneisses and are consisted of quartz (30–25%), plagioclase (40–30%), K-feldspar (35–20%) and biotite (11–8%) with accessory apatite, sericite, zircon, allanite and chlorite. The potassic feldspar commonly shows microcline cross-hatched twinning and crystallizes myrmekitic intergrowth textures in association with quartz yielding (Fig. 5c). Two samples were selected for zircon U-Pb dating: 98 and 69B. Sample 98 represents a more primitive granitoid intrusion, with relict hornblende, grey-pinkish color, being slightly foliated by a non-penetrative orientation of biotite and were collected from the central domain. Sample 69B is from a small batholith of the northern sector, leucocratic and pinkish with a pervasive foliation and higher K-feldspar content.

*4.6 Syenogranites*

The second granite intrusion phase is characterized by porphyritic coarse-grained syenogranites exposed in the west domain of Divinópolis Complex. These granites are leucocratic, pink and isotropic (Fig. 4f) and the second most widespread granite unit, with abundant K-feldspar porphyritic crystals. Coarse-grained syenogranites are described in the north-eastern part of the Pequi Batholith in the Belo Horizonte Complex (Farina et al., 2015). These granites form several large plutonic bodies and contain quartz (30%), plagioclase (30%), K-feldspar (35%) and biotite (5%) with accessory apatite, zircon, allanite, chlorite, rutile and titanite, a common accessory phase (Fig. 5d). There are abundant microcline grains with cross-hatched (tartan) multiple twinning, perthite and mymerkite exsolutions and granoblastic texture. Melt-related microstructures include cuspate terminations of K-feldspars crystals and pockets of K-feldspar, plagioclase and quartz along crystal borders. Sample 28 was selected for zircon U-Pb, comprising a more evolved granitoid with syenogranite composition collected from the west sector where large batholiths rich in K-feldspar crops out, exhibiting no deformation and coarser-grained texture.

*4.7 Migmatites*

Along Divinópolis dome, the orthogneisses show complex polydeformed and chaotic structural aspects, associated with anatexis that generates leucocratic and granitic material with dismembered alternating layers of leucocratic, mesocratic and melanocratic rocks, interpreted to represent melt-enriched

parts (leucosome) and melt-depleted parts (residual melanosome). These rocks are denominated migmatite and range from diatexites to metatexites (terminology from Sawyer, 2008). Two types of migmatite are recognized: the Itaúna Migmatite (Fig. 4e) and the Kinawa Migmatite (Fig. 4f). The Itaúna Migmatite generally has smaller grain size and higher biotite content, while the pink Kinawa Migmatite is coarser-grained and has higher alkali feldspar content. The Kinawa migmatite was described more recently by Carvalho et al. (2016) in the anatectic region of Cláudio Shear Zone.

*4.7.1 Itaúna Migmatite*

In the white-grey *Itaúna Migmatite*, no peritectic phase is observed, the leucosome is essentially plagioclase-rich with a trondhjemite composition. This leucosome can be *in source* or *in situ* and syn-anatectic migmatite structures include *schollen*, *schlieren*, veins and net. *In situ* partial melting is suggested by the composition of the residuum, similar to the adjacent leucosome. The main foliation is continuous to discontinuous, defined by biotite orientation and *schlieren* or *schollen* zones are typically oriented parallel to the contact. The fold axes are also parallel to the main foliation, that melting was syn-deformational, associated with shear planes. Diffuse contact on a centimeter scale occurs between the gneiss protolith and leucosome and diatexite portions can preserve pre-anatectic features and areas where the protolith magmatic rock is not migmatized. Films of melt on grain boundaries also result in small equant blobs of microleucosome. The foliated melanosome is black, predominantly formed by biotite and plagioclase. Newly formed biotite can also develop with perfect tabular habit included in quartz and plagioclase crystallized from the melt. Sample 71A was collected from the same quarry as sample 71D but represents a white-grey trondhjemite leucosome, medium-grained and intruded by layer-parallel or crosscutting leucogranite veins. Sample 97A represents a trondhjemite migmatitic gneiss, fine- to medium-grained, locally porphyritic. The neosome in this trondhjemite is also white-grey and can be folded locally.

*4.7.2 Kinawa Migmatite*

The *Kinawa Migmatite* presents a strong pink color due to the generation of melt rich in alkali feldspar and leucosome has varying modal contents of plagioclase, K-feldspar and quartz, giving rise to compositional variations such as granodiorite, monzogranite and syenogranite. Syn-anatectic migmatite structures include *schollen*, *schlieren*, stromatic, nebulitic, patches and dilatational. The main foliation is continuous to discontinuous, defined by biotite orientation and can be obliterated by an anatectic foliation of magmatic flux. Mafic boudins and enclaves present various sizes and have essentially amphibolite composition. Paleosome is diverse, with a black mafic residue composed essentially of biotite + plagioclase and minor quartz with a strong phyllosilicate foliation and unmelted portions of the tonalite-

trondhjemite-granodiorite protoliths. Small equant structures of microleucosome (string of beads) form by quartz and plagioclase on grain boundaries and pores (Fig. 5g) as a result from pseudomorphs of the melt (Sawyer, 2014). In the same way, solidifying intergrowth between quartz and alkali feldspar may result in granophyre texture. Garnet is a rare mineral in these migmatites with minor inclusions of quartz and zircon. SEM analyses show that they have an almandine composition and grew at the expense of biotite.

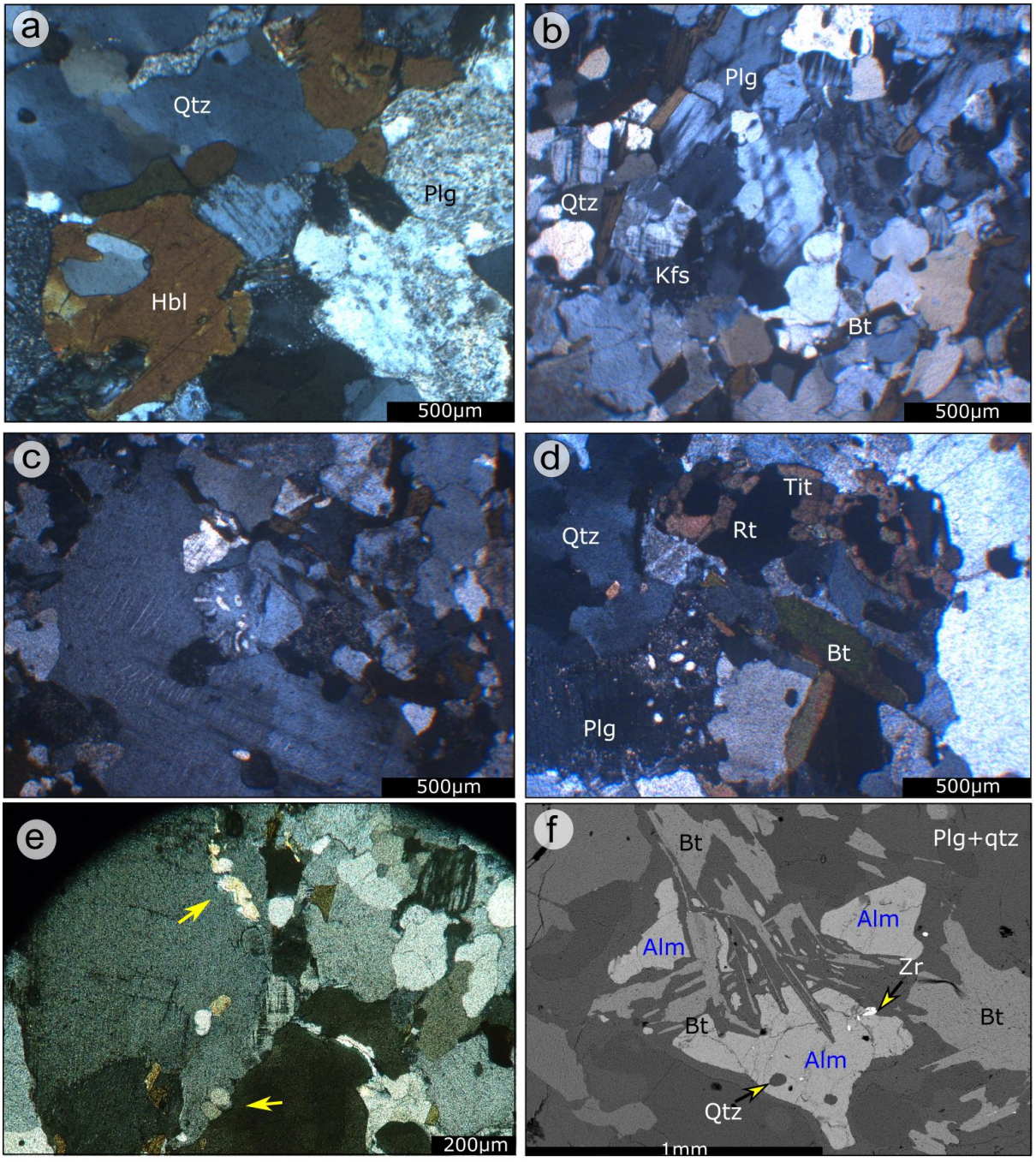


**Figure 5:** Representative photomicrographs of mineral assemblages of the felsic granitoids of Divinópolis Complex. **a)** Tonalite with quartz, plagioclase (saussuritized) and hornblende. **b)** Granodiorite with quartz, plagioclase, interstitial biotite and alkali-feldspar. **c)** Myrmekite intergrowth of quartz in plagioclase crystal in weak foliated monzogranite. **d)** Non-foliated syenogranite with quartz, plagioclase, alkali feldspar and titanite associated with rutile. **e)** Metatexite with microleucosome of plagioclase crystallized (yellow arrows) at grain boundaries (string of beads). **f)** Granodiorite migmatite with garnet (almadine), plagioclase, quartz and biotite (SEM image).

Three migmatite samples were collected for U-Pb geochronology. Sample 07C is a pinkish leucocratic granodiorite migmatite collected from an abandoned quarry, in the proximity of Itapecerica town, approximately 30 km west from the Kinawa mining pit, and 5 km south from the Itapecerica graphite mine. The rock has a strong metatexite foliation defined by oriented biotite and anatectic features (patch and stromatic). Sample 82A occurs in the anatectic region of Cláudio Shear Zone, northeast from Cláudio city and was also collected from an abandoned quarry, 20 km northeast from the Kinawa mine. This sample transitions from diatexite to metatexite, with a less prominent foliation defined by oriented biotite and evidence of partial melting of a syn-anatectic fabric. Sample 101C was collected at an abandoned quarry near Marilândia village and 20 km northwest of Kinawa mine. The rocks vary from gneiss protoliths with granodiorite composition to diatexite and metatexites (with tonalite to syenogranite composition). The photolith gneiss foliation can be overprinted by syn-anatectic foliation. All samples have similar characteristics with the Kinawa migmatite described by Carvalho et al. (2016).

## 5. U-Pb results

U–Pb isotope data for zircon and monazite are listed in the supplementary materials (Tables 2 - Appendix B) and illustrated on concordia diagrams (Figs. 7 to 10). Representative CL images of analyzed zircon grains with the corresponding spot ages are shown in Fig. 6. Zircon grains from migmatite leucosomes were opaque (milky-white or gray) and frail, resulting in highly discordant data. Instead, concordant data obtained from leucosomes actually represents the protolith ages (including samples 71A, 71D, 82A, 101C and 07C). This agrees with other studies in the southern portion of São Francisco Craton that attest that zircons with such features were likely altered by chemical weathering and U leaching, and thus, unreliable for U–Pb laser ablation (Romano et al., 2013; Lana et al., 2013). The only leucosome age in this study was obtained by monazite dating (Fig. 10).

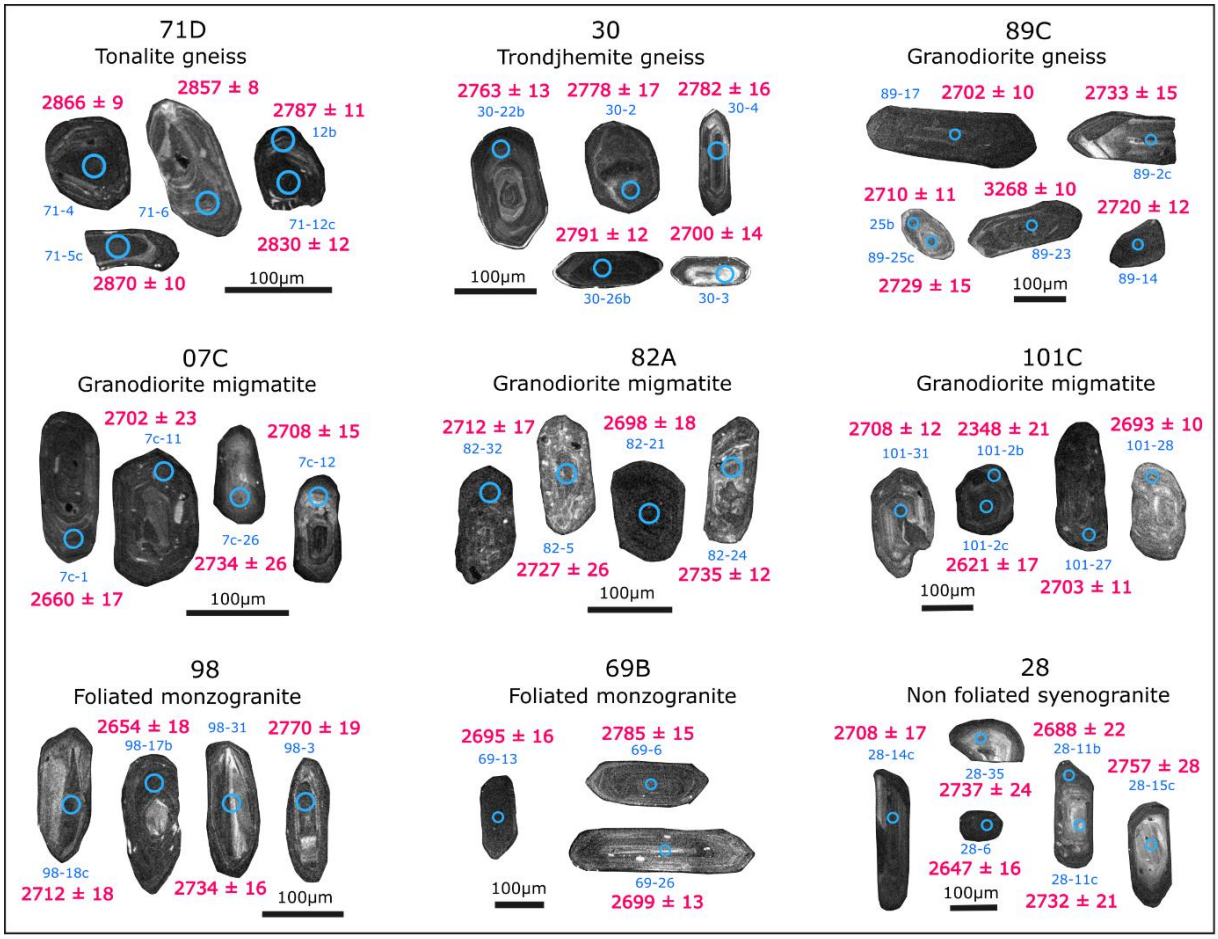


**Figure 6:** Representative cathodoluminescence image of zircon grains analyzed in this study. Spot size is 25 µm and age values reported are individual $^{207}Pb/^{206}Pb$.

## *5.1 Tonalite and trondhjemite*

**Tonalite gneiss 71D** contains zircons that are round to stubby and range in color from light pink to brown. They have concentrically oscillatory zoning, with dark structureless rims. Some grains have bright cores surrounding the nucleus and others have a bright domain separating a dark oscillatory zoned core from a dark oscillatory zoned rim (Fig. 6). The grains are 100 to 200 µm long and Th/U varies from 0.29 to 0.70. Regression of the analyses in a linear array, using all dated spots yielded an upper intercept age of 2862 ± 24 Ma but high MSWD (9.4). A better fit is constrained by using the most nine concordant grains (≥ 98%), which gives an upper intercept age of 2860 ± 28 Ma with an MSWD of 0.91. Their weighted average gives a similar age of 2861 ± 7 (MSWD = 1.7). Two younger concordant grains have $^{207}Pb/^{206}Pb$ ages of 2782 ± 13 (grain 71-12b) and 2787 ± 11 Ma (grain 71-26). Their Th/U ratios are, respectively, 0.21 and 0.44, typical of igneous rocks and they are 100% concordant. These two concordant grains could represent the age of igneous crystallization of sample 71D (2787 ± 9, MSWD = 0.06), whereas the 2860 ± 28 Ma age represents the inherited age of the gneiss (Fig. 7a).

**Trondhjemite gneiss 71A** zircon grains are light brown, dominantly long prismatic, with short-prismatic grains present, and bright internal oscillatory zoning typical of magmatic growth. They are anhedral to subhedral and most analyses reveal Th/U ratios between 0.23 and 1.3, with 100 to 300 width. Regression of the analyses in the discordia line yielded an upper intercept age of 2789 ± 37 (Fig. 7b) with a spurious MSWD. Using seven of the most concordat grains (≥ 98%), it gives a lower intercept of 2779 ± 49 (MSWD = 0.21), and an upper intercept of 3570 ± 120 (not shown). We believe that the lower intercept is the best estimate age of crystallization. This age is the same obtained for sample 71D, which agrees that the best estimative for crystallization of the tonalite gneiss is around 2.78 Ga.

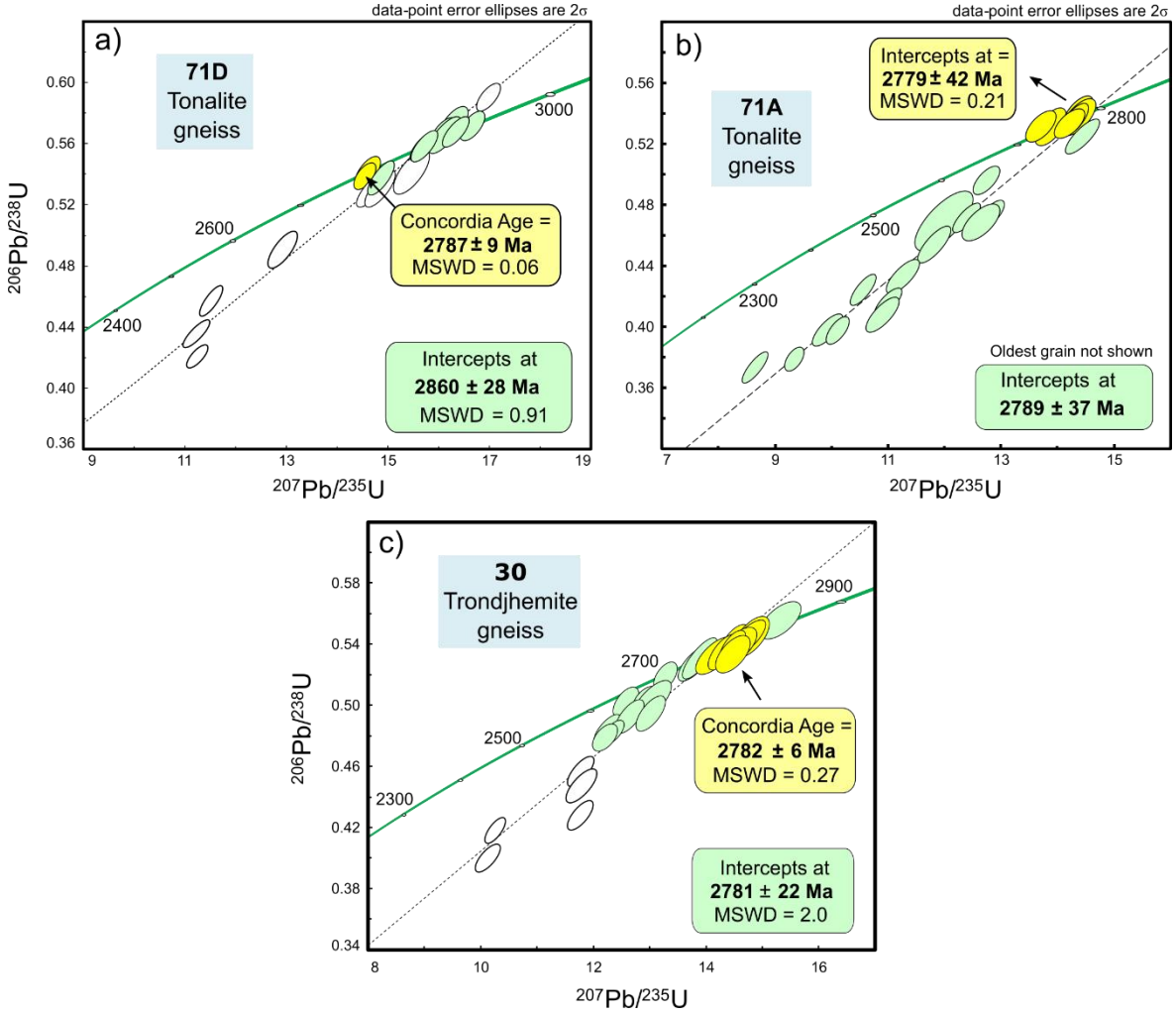


**Figure 7:** U-Pb Concordia diagrams of LA-ICPM-MS analyses of zircons from gneisses of Divinópolis Complex. **a)** Upper intercept (green = 98% conc.) and concordia age (yellow) of a mafic tonalite gneiss (sample 71D). **b)** Upper intercept (green = all grains) and concordia age (yellow) of a felsic tonalite gneiss (sample 71A). **c)** Upper intercept (green = 90% conc.) and concordia age (yellow) of a trondhjemite gneiss (sample 30).

Zircons from the **trondhjemite gneiss 30** are mostly light to dark brown, translucent, prismatic to slightly stubby, all with sub-rounded terminations. The grains have well-developed oscillatory zoning, rims are predominately brighter in CL, with less defined dark cores. Few grains are homogeneous and

dark, without visible domains, and one grain (30-3) has a bright core and a darker rim (Fig. 6). The grains are 50 to 150 µm long and Th/U values range from 0.26 to 0.53. The data show some scatter and variable discordance. The analyses of the most concordant grains (≥ 90%) defined an upper intercept of 2781 ± 22 and MSWD = 2.0, which is a robust result. This age is similar to the concordia obtained for the ten most concordant grains (100%) yielding an age of 2782 ± 6 Ma (MSWD = 0.27), making this the best estimative for the time of igneous crystallization (Fig. 7c).

*5.2 Granodiorite*

Zircon grains from the **granodiorite gneiss 89C** are prismatic to slightly stubby, with sub-rounded faces reaching lengths of 100 to 400 µm. They are translucent and light to dark brown. CL-images reveal internal oscillatory zoning and some homogeneous dark grains, and a few grains have complex, structureless cores surrounded by oscillatory rims. Their Th/U ratio varies from 0.12 to 0.77 and one analysis of 3268 ±10 (spot 89-23) represents an old inherited grain (99%), the only concordant Paleoarchean grain recorded in this study (Fig. 8a). The upper intercept gives the age of 2731 ± 18 Ma (MSWD = 3.7) for 19 grains, considered the time of igneous crystallization of the rock.

**Granodiorite gneiss 82A** contains translucent and mostly prismatic grains with well-defined oscillatory zoning in CL images (Fig. 6) with many inclusions and fractures, sub-rounded faces, dark to light brown and slightly stubby. Some grains have a bright core surrounded by a darker thin rim. The grains are 70 to 150 µm long with Th/U ratios of 0.25 to 0.94 and one discordant spot with 0.07 due to its extremely high U value and low Th (complete dark CL). All spot analysis yielded an upper intercept of 2704 ± 40 Ma (n = 18) with a very high MSWD (Fig. 8b). The seven most concordant points (≥ 95%) have $^{207}Pb/^{206}Pb$ ages from 2698 to 2735, and they give a robust upper intercept age of 2729 ± 31 Ma (MSWD = 0.67), but with high error. The most five concordant grains (≥ 98%), on the other hand, yielded a concordia age of 2712 ± 15 Ma (MSWD = 0.88), considered as the time of crystallization of the migmatite protolith.

**Granodiorite migmatite 07C** zircons grains are mostly prismatic, with sub-rounded faces, dark to light brown, and opaque to translucent similar to the grains of sample 82A. They are mostly 100–200 µm in length. Magmatic well-defined concentric zoning is common under CL, and a few samples have a bright core surrounded by a darker thin rim (grain 7c-26). Inclusions and fractures are also common, with Th/U ratios between 0.21 and 0.77. The spot analyses defined a regression line with an upper intercept at 2707 ± 32 (n = 26) and younger grains show Pb-loss towards 506 Ma along the discordia line (Fig. 8c). The data points without Pb-loss have $^{207}Pb/^{206}Pb$ ages between 2730 to 2660 Ma and the most concordant grains (≥ 98%, n = 7) intercept the concordia curve at 2673 ± 33 Ma with an MSWD of 0.23. This is a

robust age for the crystallization time of the granodiorite, similar to the weighted average of the most concordant grains (≥ 99%) that yielded an age of 2699 ± 11 Ma with MSWD of 3.5.

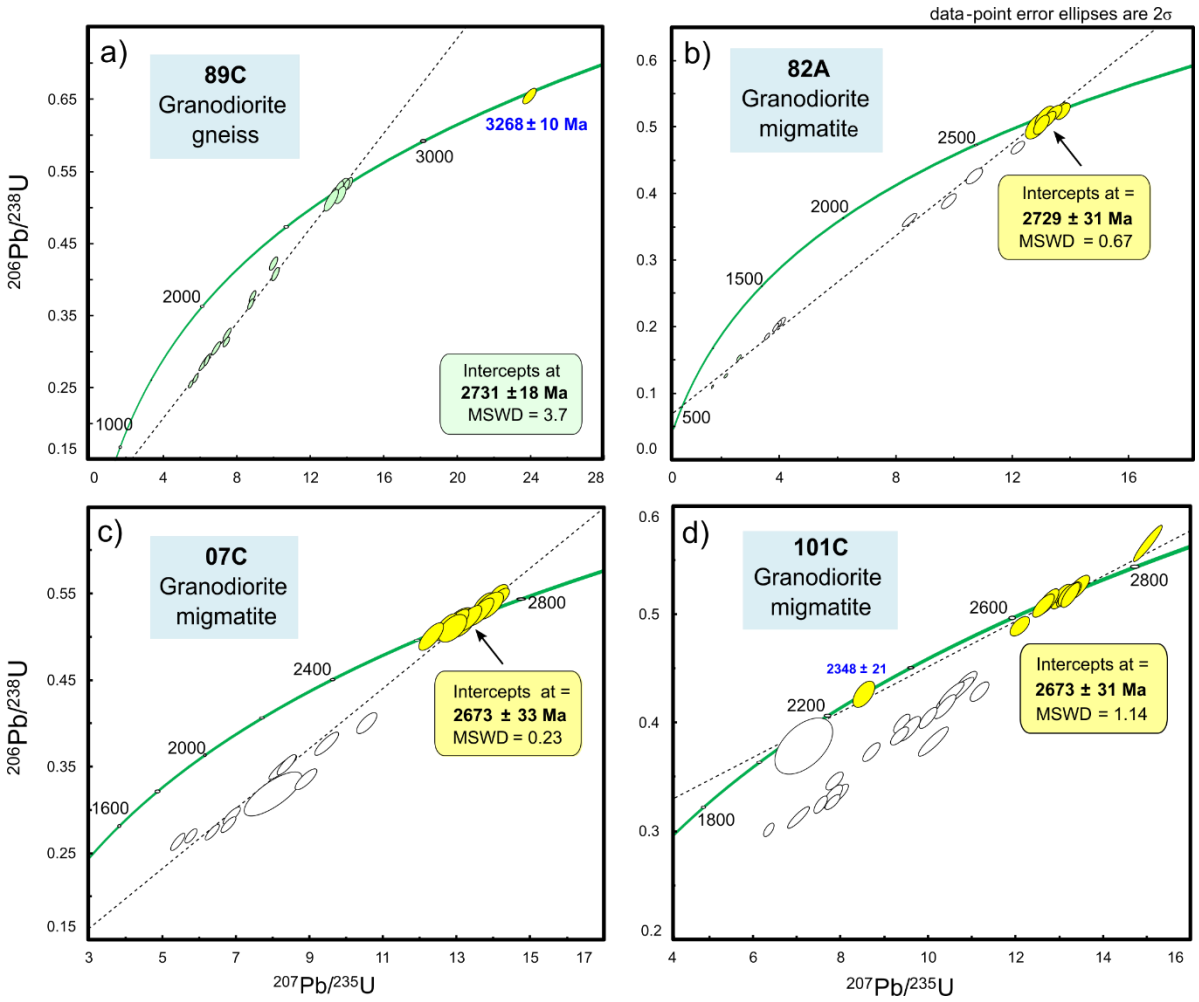


**Figure 8:** U-Pb Concordia diagrams of LA-ICPM-MS analyses of zircons from gneisses and migmatites of Divinópolis Complex. **a)** Upper intercepts (green = all grains; yellow = 95% conc.) of a granodiorite gneiss (sample 89C). **b)** Upper intercepts (green = all grains; yellow = 98% conc.) of a granodiorite migmatite leucosome (sample 82A). **c)** Granodiorite migmatite leucosome of sample 07C. **d)** Upper intercepts (green = all grains; yellow = 95% conc.) of a granodiorite migmatite leucosome (sample 101C).

**Granodiorite migmatite 101C** zircon grains have well-developed oscillatory zoning in CL images, with small inclusions (Fig. 6). Few grains have dark chaotic cores surrounded by grey rims and some have bright oscillatory zoning. The grains are sub-rounded and stubby, translucent and dark to light brown. Their length varies from 100 to 300 µm and this sample has anomalous high Th/U values, from 0.73 to 4.05 due to high Th content. A single grain (101-14b) has very low U content on its rim, with no obvious difference in appearance and it does record a fairly concordant Proterozoic age of 2227 ± 76 Ma (94% concordant), similar to the age obtained from the low-U rim of zircon 101-2b with a $^{207}Pb/^{206}Pb$ age of 2348 ± 21 Ma (98% concordance). These younger spots are shown in Fig. 8d where the data points are dispersed along the discordia line exhibiting an upper intercept of 2705 ± 38 (n = 30) and Pb loss towards

the lower intercept at approximately 676 Ma. The most concordant zircons (≥ 95%) yielded an upper intercept age of 2673 ± 31 Ma (MSWD = 1.14; n = 11), and it can be used as a good estimative for the protolith crystallization age (Fig. 8d), the same as the one reported for sample 101C (2673 ± 33).

*5.3 Intrusive granite plutons*

**Monzogranite 98** zircon grains are translucent to slightly turbid, light brown and light gray. The grains are dominantly long prismatic, although short-prismatic and rounded forms also occur. Inclusion is rare and fractures are not common. CL images exposed well-defined oscillatory zoning and clear core–overgrowth relationships (Fig. 6). Most cores are CL brighter than the rim overgrowth and rarely surrounded by bright rims. Overgrowth rims show perfect concentric oscillatory zoning with local intermediate resorption and a few xenocryst cores (grain 98-17). Zircon length is 100 to 320 µm long. Spot analyses in the cores and rims are fairly concordant, grouping in the upper intercept close to 2700 Ma. When all samples are plotted together, they present an upper intercept age of 2737 ± 13 Ma MSWD = 5, n = 32) and a lower intercept of 617 ± 110 Ma (Fig. 9a), which is a good estimate for the time of crystallization. Twenty-three of the most concordant points (95% confidence) were plotted yielding an upper intercept of 2733 ± 24 Ma (MSWD = 1.12). Since this age is the essentially the same as the upper intercept, it will be taken as the igneous crystallization age of this monzogranite (Fig. 9a).

Zircon crystals from **monzogranite 69B** are light brown, prismatic with rounded to sub-rounded facets, 200 to 500 µm long. CL imaging shows very clear oscillatory internal zoning with some dark-CL grains. Grains can have a rim of thin bright-CL overgrowths and a few present a very bright-CL xenocryst core. Most analyses reveal Th/U ratios that are between 0.12 and 1.42. The data show some scatter and variable discordance. Regression of the analyses of all spots group along with a strong Pb loss trend at 484 Ma, with an upper intercept of 2701 ± 82 and a spurious MSWD (n = 29). The best three concordant zircon grains provided a concordia age of 2729 ± 25 and MSWD of 2.7 which can be interpreted as the igneous crystallization age (Fig. 9b), correlating well with the previous monzogranite.

**Syenogranite 28** contains pink to medium brown elongate prismatic zircon grains ranging from 100–350 µm. The grains are moderately fractured, and inclusions are rare. Short-prismatic, rounded and few colorless grains can also occur, with several elongated xenocryst cores and concentric and well-developed oscillatory zoning overgrowths (Fig. 6). All cores are CL brighter than the rims and some grains do not have dark rims, only a bright CL oscillatory zoned response, with xenocrystal cores. Their high U (up to 240) and Th/U (up to 1.47) contents suggest that these late-developed rims are not metamorphic but formed by magmatic events. A total of thirty-four analyses were obtained and together, they plot in a discordia line with an upper intercept of 2698 ± 25 Ma (MSWD = 1.5) and lower intercept at 984 ± 270

Ma (Fig. 9c). These age calculations do not consider the oldest Mesoarchean grains preserved in the sample, respectively grain 28-13 (2918 ± 23) and 28-31 (2844 ± 21), considered inherited ages. Eighteen of the most concordant grains (99%) seem to indicate two single populations (Fig. 9d): an older one from magmatic cores and a younger one from magmatic overgrowths registered as dark rims. The concordia age for the oldest population was obtained at 2709 ± 7 Ma with an MSWD of 0.64 for eleven grains. The youngest population gives a concordia age of 2653 ± 13 Ma (MSWD = 0.27, n = 5) and is 55 Ma younger than the first crystallization event. We interpret the younger age as the crystallization event and the older one as inherited xenocrysts.

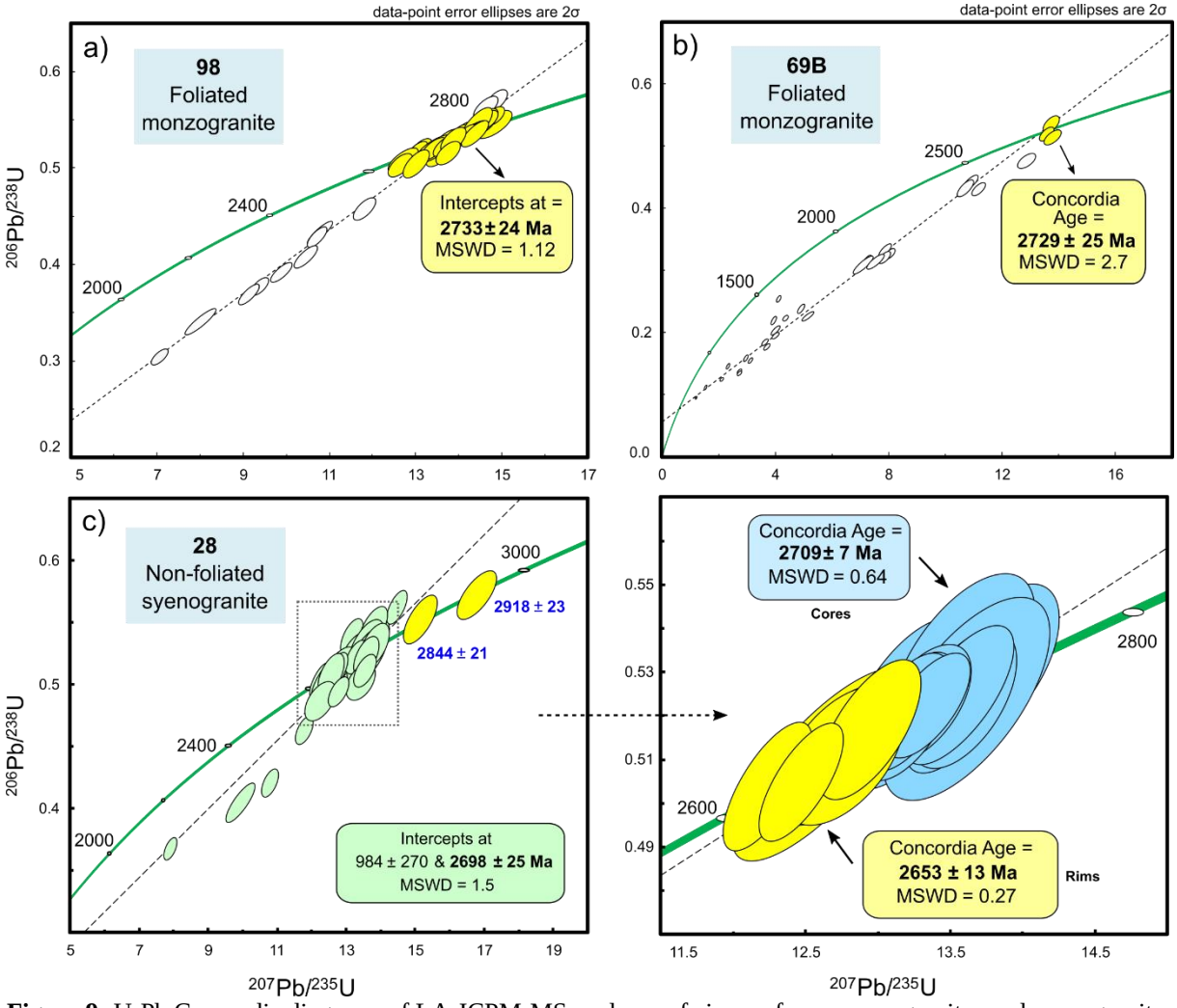


**Figure 9:** U-Pb Concordia diagrams of LA-ICPM-MS analyses of zircons from monzogranites and syenogranites of Divinópolis Complex. **a)** Upper intercepts (green = all grains; yellow = 95% conc.) of a foliated monzogranite of sample 98. **b)** Upper intercept (green = all grains) and concordia age (yellow) of a foliated monzogranite (sample 69B). **c)** Upper intercept (green = all grains, except inherited ones) and inherited zircon grains (yellow) of a non-foliated syenogranite (sample 28). **d)** Detailed concordia diagrams from sample 28. In blue: concordia age from zircon cores. In yellow: concordia age from zircon rims.

### *5.4 Migmatite leucosome*

Thirty monazite grains were dated from **sample 97B**, they are typically dark yellow to brown, transparent and irregular in shape, with rounded facets and 200 to 400 mm across. Under BSE imaging they show simple compositional zoning or no distinct structures, with no inherited cores. Parallel zoning to rational crystal faces indicates primary crystallization (Hawkins and Bowring, 1999). All thirty grains show good concordance values, with $^{207}Pb/^{206}U$ ages from 2128 to 2021 Ma and they plot in a coherent group. Twenty-seven of the most concordant grains within 5% of concordance yielded an upper intercept age of 3015 and a lower intercept of 2071 ± 40, with MSWD of 1.7. A concordia age could be obtained for the grains within 2% of concordance, yielding 2062 ± 7 Ma (MSWD of 2.6, n=18), which is interpreted as the age of crystallization of the leucosome and, therefore, of the anatexis event that generated the migmatite of the north domain.

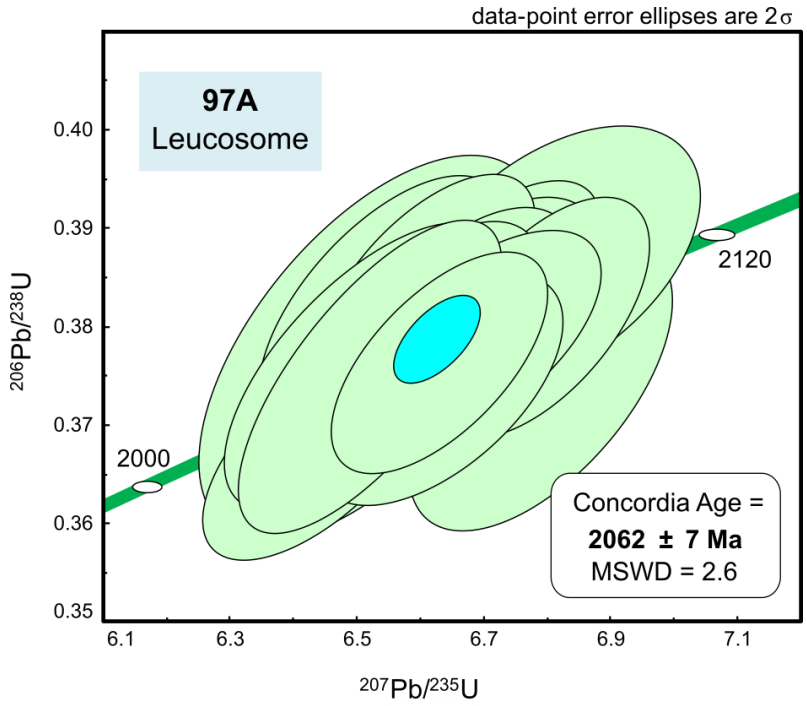


**Figure 10:** U-Pb Concordia diagram of LA-ICPM-MS analyses of monazites from a migmatite leucosome of Divinópolis Complex (sample 97A).

## 6. Discussion

### *6.1 Cryptic Paleoarchean record*

The Paleoarchean record in the southern São Francisco Craton is chiefly preserved in the Santa Bárbara Complex, where two crystallization ages were obtained at 3212 ± 9 and 3210 ± 8 Ma for a trondhjemite gneiss named Cachoeira Camargo (Lana et al., 2013). The complex gives names to the Santa

Bárbara event between 3220–3200 Ma (Lana et al., 2013), but it is noteworthy that no other ages or geochemistry are reported for this complex, representing an important gap in the region. This trondhjemite comprises the only significant peak of zircon growth at 3200 Ma (Fig. 10b). In our analyzed samples two Paleoarchean zircon grains of 3268 Ma (99% conc.) and 3378 Ma (98% conc.) were found in the granodiorite gneiss of samples 89C and the tonalite gneiss of sample 71A. These inherited grains are one of the few Paleoarchean ages recovered from the felsic sialic record in the southern São Francisco Craton besides the ages reported in the Santa Bárbara Complex (Lana et al. 2013). Inherited zircon grains of 3205 ± 17 Ma was recovered from a Campo Belo migmatite (Teixeira et al., 1998), a Belo Horizonte gneiss (3258 ± 14; Lana et al. 2013) and a leucosome of Divinópolis Complex (3227 ± 20; Carvalho et al. 2017a), all with good concordance and agreeing with the Santa Bárbara event. Albert et al. (2016) also report inherited zircon cores between 3515–3292 Ma (concordance values are not shown) and Brando Soares et al. (2020) recovered 3.5–3.0 Ga concordant grains (90–100%) from the Jaguara granitoid.

Besides these inherited grains obtained from felsic rocks, other > 3.2 Ga ages are only reported as detrital zircon grains or as $T_{DM}$ ages (Oliveira, 2004; Lana et al. 2013; Carvalho et al., 2017a; Melo-Silva et al., 2020). In the Pitangui and Rio das Velhas greenstone belts this detrital record is well represented (Fig. 10a), with minor peaks at 3230 and 3330 Ma (Hartmann et al., 2006; Brando Soares et al., 2020; Melo-Silva et al., 2020). The oldest grain recorded in the southern São Francisco Craton so far was dated by Hartmann et al. (2006) at 3.8 Ga (3% disc.) in a sandstone from the Rio das Velhas greenstone belt. This is the only U-Pb age older than 3.4 Ga and was not represented in the comparative relative probability diagrams of Fig. 10a due to scale. This constant recording of ages between 3.4 and 3.2 Ga is suggestive that a Paleoarchean crust developed in the southern São Francisco Craton extensive enough to be eroded and operate as a source of sediment. Enriched εHf values between 3.5 and 2.9 Ga suggests assimilation of older felsic crust by a mafic juvenile magma (Albert et al., 2016; Carvalho et al. 2017a).

Older ages (> 3.2) are more common in the TTGs of Gavião and Serrinha Blocks (Dantas et al. 2013; Zincone et al., 2016; Teixeira et al., 2017a), spanning back to 3.6 Ga (Oliveira et al., 2020). At 3.2 Ga the first episodes of crustal growth begin to emerge in the southern São Francisco Craton, 400 Ma later than the north São Francisco (Fig. 10e), but the lack of field exposition and more evidence preclude further interpretations. It is not clear whether this was the starting point of crustal development but ages around 3.2 Ga comprises a robust trend considering all complexes together (Fig. 10e). Considering that these ages are inherited, it suggests involvement of older Paleoarchean crust in the genesis of the younger magmas.

*6.2 Mesoarchean formation of TTG crust*

The oldest concordia ages found in our study corresponds to an inherited zircon population of 2860 ± 28 Ma (Fig. 7a) with well-defined oscillatory zoning that matches the interval of the Rio das Velhas I event (2930–2850 Ma). This intercept (2860 ± 28 Ma) corresponds essentially to the same age of a diorite of 2878 ± 5 Ma reported from the northern mylonite zone in contact with the Pitangui Greenstone Belt (Melo-Silva et al., 2020). The magmatic generation of this diorite represents one of the most ancient TTG pulses recorded so far in Divinópolis Complex, combined with their more primitive dioritic affinity. When comparing this age with zircon growth events in the southern São Francisco Craton, peaks of 2900 and 2850 Ma can be visualized in the gneisses of Bação, Bonfim, Belo Horizonte and Campo Belo complexes (Fig. 10b). Similarly, peaks of 2915 and 2875 Ma can be visualized in the granitoids (Fig. 10c), all within the Rio das Velhas I event. A similar age is reported in the Pitangui Greenstone Belt, where a metabasalt of 2740 Ma shows an inherited population at 2886 ± 10 Ma (Melo-Silva et al., 2020), supporting assimilation of previous crustal material (Mesoarchean) by magmas of Neoarchean age.

Igneous crystallization of TTG crust with 2.8 Ga (Fig. 10e) is documented in Bação, Bonfim, Belo Horizonte, Campo Belo, Passa Tempo and Divinópolis (Teixeira et al., 1998; Noce et al., 1998; Lana et al., 2013; Farina et al., 2015; Melo-Silva et al., 2020). The first exception would be the Santa Bárbara Complex, in which advent of felsic crust begun earlier, between 3220–3200 Ma (Lana et al., 2013). The second exception would be Campo Belo Complex, where Teixeira et al. (1996; 1998; 2017a) described an earlier magmatic event with homonymous name restricted to the Campo Belo Complex (3.2–2.92 Ga – Campo Belo Orogeny). These authors obtained three concordant ages from a migmatite sample: 3205 ± 25 Ma (interpreted as inherited age), 3047 ± 25 Ma (recording the main accretion episode), and 2840 ± 17 Ma (considered the crystallization age of the neosome). The 3.2 Ga age was discussed above and is one of the few Paleoarchean ages obtained from the felsic record. The 3.0 Ga age does not match any other crystallization event in the gneiss-granite terrains so far, but this age gap is well represented as $T_{DM}$ ages and in the detrital record of Pitangui and Rio das Velhas greenstone belts, yielding a peak at 3020 Ma (Fig. 10a) (Oliveira, 2004; Hartmann et al., 2006; Albert et al. 2016; Carvalho et al., 2017a; Brando Soares et al., 2020; Melo-Silva et al., 2020). This 3.0 Ga ages accounts for another "erased" period of crustal growth that was probably consumed before surviving and developing long enough to act as sediment source. And at last, the final 2.8 Ga age referred as the age of neosome formation matches the age of older TTG genesis (RVI) and is possible that it does not characterize the anatectic event, but protolith crystallization. In most of the southern São Francisco Craton, temperature and conditions were not enough to crystalize zircon in the gneiss-granite complexes, but only reset monazite (Cutts et al., 2019).

The Campo Belo Orogeny matches the end of the Santa Bárbara event and beginning of Rio das Velhas I and originated from accretionary process leading to continental cores (Teixeira et al., 2017a). Crust from this period was likely recycled and unpreserved in the same way as the 3.2 Ga crust. Thus, the first preserved phase of TTG formation at 2915–2860 Ma likely represents the emergence of stable felsic continents in the southern São Francisco Craton (Fig. 10e), consistent with the Rio das Velhas I event. The first steady pulses are preserved in this period in most of the gneiss-granite complexes suggesting the change from a reworking, hotter regime to a more stable regime with lower temperatures.

### *6.3 Early Neoarchean formation of TTG crust*

Zircon grains from tonalite and trondhjemite of the central and northeast domains furnish igneous crystallization ages between 2787 and 2779 Ma. These ages are essentially the same within errors and match the Rio das Velhas II event (2800–2760 Ma) recognized in the Quadrilátero Ferrífero and interpreted as a period of arc magmatism and crustal accretion (Machado et al., 1996; Noce et al., 2005), generation of TTG (Lana et al., 2013; Teixeira et al., 2017), calc-alkaline plutonic-volcanic crust (Silva et al., 2000) and emplacement of medium-K granitoids (Romano et al., 2013; Farina et al., 2015). This period between 2800 and 2760 Ma represents the second largest event of zircon growth, characterized as a peak of 2770 in the greenstone belts (Fig. 10a), a peak of 2780 in the gneisses (Fig. 10b) and a peak of 2775 in the granitoids (Fig. 10a). In the greenstone belts, the transition between Rio das Velhas II and Mamona (2760 Ma onward) is not clear, but in the felsic crust it is better constrained. This suggests that the sedimentation rate was continuous.

Considering this early Neoarchean (2790–2775 Ma) formation of TTG and the Mesoarchean one (2915–2875 Ma) it can be postulated that the TTG emplacement in the Divinópolis Complex occurred in two stages separated by ca. 100 Ma, corresponding to the Rio das Velhas I Orogeny and the Rio das Velhas II Orogeny. This age gap can also be inferred to the Bação and Bonfim domes, based on published ages (Noce et al., 1998; Lana et al., 2013; Farina et al., 2015). The crustal εHf signatures of Bonfim combined with their 3.5 to 3.1 Ga $Hf_{TDM}$ agree with a long episode of crustal reworking and εHf of the Bação suggests the involvement of reworked continental crust in their petrogenesis (Farina et al., 2015; Albert et al., 2016). It has been suggested by many authors that at least part of the Rio das Velhas Orogeny formed at a convergent setting (Silva et al., 2000; Lana et al., 2013; Albert et al., 2016; Moreno et al., 2017) and the Meso- and Neoarchean formation of TTGs can be linked to this scenario.

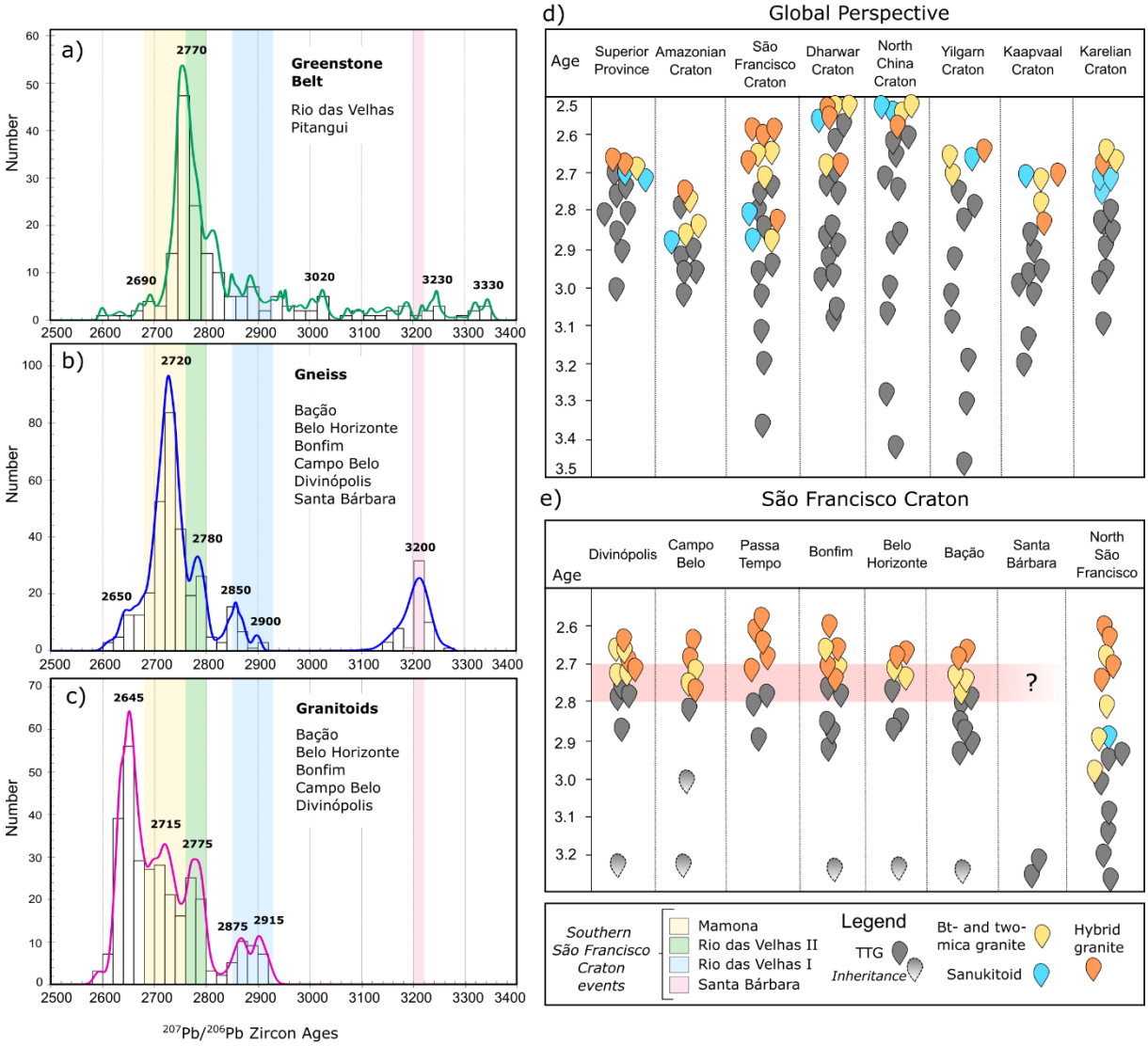


**Figure 11:** Comparative relative probability diagrams for **a)** detrital zircon grains from Pitangui and Rio das Velhas greenstone belt and for **b–c)** zircon crystallization ages from Bação, Belo Horizonte, Bonfim, Campo Belo and Santa Bárbara complex, plus the samples analysed in this work from Divinópolis Complex. Ages within 95% concordance were used ($^{207}Pb/^{206}Pb$). Simplified age distribution for TTG, Sanukitoid, Hybrid and Biotite-Two-mica granitoid rocks are show in **d)** selected cratons worldwide (modified after Heilimo et al., 2011; Singh et al., 2019a) and **d)** in the São Francisco Craton. References for the southern São Francisco Craton after Teixeira et al. (1998); Lana et al. (2013); Farina et al. (2015); Moreno et al. (2017). References for the northern São Francisco Craton after Medeiros et al. (2017), Barbosa et al. (2020). References for the Pitangui and Rio das Velhas greenstone belts after Hartmann et al. (2006); Brando Soares et al. (2017; 2020); Melo-Silva et al. (2020).

### *6.4 Transition to a potassic Neoarchean crust*

After the Rio das Velhas I and II, widespread potassic magmatism is recorded in the southern São Francisco craton named as Mamona event (2760–2680 Ma) after the homonymous granite (Lana et al., 2013). This magmatism is represented by the progressive emplacement of rocks with the potassic "biotite- and two-mica granites" affinity of Laurent et al. (2014), evolving into increasingly potassic granites, many of which are classified as "hybrid granites" (Laurent et al., 2014). In the Divinópolis Complex, the oldest

granodiorite matches the Mamona period with crystallization at 2731 ± 18 Ma and 2729 ± 31 Ma. This 2730 Ma age is similar to the most representative peak of zircon growth at 2720 Ma registered in the gneisses of Bação, Bonfim, Belo Horizonte and Campo Belo (Fig. 10b). This Archean potassic rocks (usually granodiorites) termed "biotite- and two-mica granites" first appear in the Bonfim and Bação complexes at 2.78–2.77 Ga (Farina et al., 2015). After 2.75 Ga their occurrence increase (Fig. 10e). It has implications that the highest point of crust formation in the southern São Francisco Craton occurred shortly after the generation of the 2790–2775 Ma TTGs. The inherited Paleo-Mesoarchean zircon grains preserved in many of the gneiss-granite complexes and as well in the Jaguara granitoid suggests the involvement of an older reworked source in the formation of this granodiorites and plg-rich granitoids.

The two monzogranites of the central and northeast domains are more primitive than the Kfs-rich syenogranites of the west domain, resembling the plg-rich gneisses and granites of Farina et al. (2015). The age of this foliated monzogranites overlap each other: 2733 ± 24 for the oldest one and 2729 ± 25 Ma for the younger. Their time of emplacement agree with their mineralogy, representing an older generation of intrusions, with rare hornblende and low alkali feldspar content when compared to the younger syenogranites of the western domain as well as the typical kfs-rich granitoids of the Mamona event (Romano et al., 2013; Farina et al., 2015). In the granitoids of southern São Francisco Craton this peak is analogous at 2715 Ma but smaller than the 2720 registered in the gneisses (Fig. 10c). Potassic magmatism pulses of 2760–2750 Ma and 2730–2700 Ma were the older granitoid bodies are foliated biotite-rich granodiorites were described by Romano et al. (2013).

When comparing Divinópolis data with the magmatic events of southern São Francisco Craton, this episode of 2730–2710 Ma magmatism intruding the older TTG gneiss (2870–2750 Ma) is well represented by the potassic magmatic pulse described by Romano et al. (2013), such as Mamona, Souza Noschese, Pequi, Santa Luzia and smaller granitoids from Bonfim and Bação (Machado et al., 1992; Farina et al., 2015). Some of these granitoids have medium-K affinity similar to tonalite–trondhjemite–granodiorite series (TTGs) and were generated by partial melting of metamafic rocks and recycled older TTG rocks up to 2730 Ma (Farina et al., 2015). The older foliated monzogranites of Divinópolis Complex characterizes an intermediate component between the transition from TTG suites to the typical K-rich late suites. Considering the ages presented here and the zircon peak growth published for the southern São Francisco Craton, it is proposed that this period of change roughly occurred between 2760–2710 Ma, that will be called Mamona I here, but the transition had begun as earlier as 2.78–2.77 Ga with the small occurrence of biotite-granites in Bação and Bonfim.

Between 2.8 and 2.7 Ga the crust record increases immensely and likely marks a change in the geodynamics of the southern São Francisco Craton (Fig. 10e), moving from a regime dominated by metamafic and/or mantellic sources (TTGs and biotite-granites with moderate potassium) to a regime

dominated by more felsic sources and recycled older TTG rocks (biotite-granites and hybrid granites more rich in potassium). This transition from Rio das Velhas to Mamona sets the widespread formation of potassic Neoarchean crust. A similar scenario can be seen in other Archean provinces worldwide, like the north Congo Craton (Shang et al., 2007), Superior Province, Yilgarn Craton and Kaapvaal Craton (Fig. 10e and references therein).

### *6.5 Late Neoarchean potassic magmatism*

The final magmatic pulses of Divinópolis are recorded in the late Neoarchean in granodiorites of the central and south domain, specifically on its southern border close to the anatectic region of Cláudio and Itapecerica shear zones. The protolith crystallization of these granodiorite migmatites could be well-constrained at 2673 ± 33 and 2673 ± 31 Ma (Fig. 8c and 8d). This region is very interesting because it defines the limits between the Archean Divinópolis, Campo Belo and Bonfim complexes and hosts two curious Proterozoic (2.01 Ga) supracrustal successions: the Itapecerica peraluminous graphite-rich succession (Teixeira et al., 2017b) and a khondalite belt-paragneiss succession (Coelho and Chaves, 2019). Besides that, in the Oliveira region (south of Cláudio and Itapecerica shear zones) a granulite facies event of 2.06 Ga is recorded as the enderbites and charnokites of the Candeias Gneiss unit (Corrêa da Costa, 1999; Oliveira, 2004), the only place where such rocks are described in the southern São Francisco Craton. Also, partial melting is widespread in the region, making it one of the most intricated succession of events occurring between Divinópolis, Campo Belo and Bonfim domes. Samples collected from the Kinawa Migmatite neosome could not be dated because the set of zircon grains had a chaotic, patchy and metamict nature, resulting in opaque milky grains with weak CL response and highly discordant spectra. This is reminiscent of structures formed by fluid-induced re-equilibration (Geisler et al., 2007; Kusiak et al., 2009), and likely affected by these multiple episodes.

The protolith age of the migmatites, gneisses and charnokites were dated between 2750 to 2650 Ma (Oliveira, 2004; Teixeira et al., 2017b; Carvalho et al., 2017a). Such ages can be divided into two distinct pulses. The first one, with crystallization of 2753 ± 81, 2749 ± 6 and 2720 ± 28 overlaps that of the Mamona I event and can include the age 2729 ± 31 of sample 82C, close to the Cláudio Shear Zone (Fig. 8a). The second pulse is more ubiquitous (2705 ± 83, 2704 ± 3, 2687 ± 61, 2686 ± 17, 2658 ± 7) and can include the two ages of 2673 Ma obtained in this study. The interval between 2705–2680 Ma where emplacement of biotite-granites and hybrid granite occur in Bonfim, Bação, Belo Horizonte, Campo Belo and Divinópolis will be called Mamona II here.

Besides the granodiorite migmatite protoliths, sample 28 also belongs to the period of late Neoarchean potassic magmatism. Said sample is a coarse-grained syenogranite from the west domain

with high alkali-feldspar content and no evidence of deformation. The zircon grains have perfect concentric oscillatory zoning with ages from 2758 to 2619 Ma and a few xenocrystic cores that yielded no-reliable ages. Two populations were obtained from this sample: 2709 ± 9, inherited from the source; and 2653 ± 13, the timing of crystallization, coinciding with small peaks of ca. 2650 Ma dated so far in Campo Belo (Moreno et al., 2017), Bonfim (Romano et al., 2013), Divinópolis (Oliveira, 2004; this work) and Passa Tempo (Campos and Carneiro, 2008; Simon et al., 2018). In contrast, although these peaks are small and localized, they represent the largest period of zircon growth in granites of the southern São Francisco, defined by the age 2645 Ma (Fig. 10c). It is interesting to note that the inherited age from the source was preserved on zircon cores, while the crystallization age was obtained from zircon rims. This is suggestive that temperature conditions were not high enough to prevent zircon dissolution, but the magma was saturated in zirconium, assimilating previous grains (Bea et al., 2007). The occurrence of inherited xenocrysts of 2918 and 2844 Ma (100% conc.) suggest recycling of older TTG crust in the genesis of the ca. 2709 Ma rocks, that were later assimilated by the 2653 Ma syenogranite.

The last magmatic emplacement of Kfs-rich hybrid granite is distributed in two small peaks at 2650 and 2610 Ma (Fig. 10e). The period between 2650–2610 Ma is a good estimative for the final potassic magmatism that affected the southern crust of São Francisco craton and marks the beginning of stabilization, a history similar to the Superior Province (Henry et al., 2000), Yilgarn Craton (Champion and Sheraton, 1997), North China Craton (Wang et al., 2016) and Kaapavaal Craton (Armstrong et al., 1990). In the north Archean nuclei of São Francisco, this transition begins earlier (ca. 2.9 Ga) and lasts longer (Fig. 10e). The maturation of the São Francisco occurred diachronically from N to S, with the final magmatic pulses recorded in the southern portion of Campo Belo, Passa Tempo and Divinópolis complexes (Moreno et al., 2017; Simon et al., 2018, this work).

### *6.6 Paleoproterozoic reactivation and exhumation*

In the Proterozoic, the São Francisco crust was reactivated and reworked, with the onset of the Minas Orogeny and collision with the Congo Craton between 2.1–1.9 Ga. This deformation front is imprinted in the southeast border of the craton, causing a NE-SW deformation trend developed in weaker areas of the crust, for example, the geological sutures that separates Campo Belo, Bonfim and Divinópolis complexes. The NE-SW Jeceaba-Bom Sucesso Lineament (Ávila et al., 2014) that separates Passa Tempo and Bonfim complexes from the Mineiro Belt is another example of this deformation front.

The Kinawa migmatite illustrates well this Proterozoic reworking of the Archean crust. The granodiorite protolith yielded the ages of 2704 ± 3 Ma and 2686 ± 18 Ma (Carvalho et al., 2017a), similar to the ones found in this work for granodiorites of the same region. This migmatization event is interpreted

to have formed by melting under water-induced anatexis in the shear zone at 2034 ± 32 Ma and 2048 ± 25 Ma at ca. 730º C and 5-6 kbar (Carvalho et al., 2016; 2017a). Similar age was found in the Itapecerica peraluminous graphite-rich succession in which the gneisses record a metamorphic overprint of 2069 ± 84 Ma (Teixeira et al., 2017b). Conditions in the Candeias Gneiss, south of the Cláudio Shear Zone were up to granulite facies, as recorded in the 2066 Ma felsic granulites interpreted to have formed due to granitoid dehydration during high-grade metamorphism (Corrêa da Costa, 1999; Oliveira, 2004). The $Nd_{TDM}$ ages of Kinawa Migmatite and Candeias granulites are correlated (3.4 to 3.0 Ga) and they also share similar $\varepsilon_{Nd}$ values of -3.6 to -11.7 (Oliveira, 2004; Carvalho et al., 2016; 2017a). It is possible that these rocks represent potential residues of gneiss dehydration due to anatectic segregation of migmatite melt.

The dated leucosome sample (97A) in this work records very similar age (2062 ± 7 Ma) with those published for the southern border of Divinópolis dome. This migmatite is Kfs depleted and does not present the strong pink color of neosome found in the migmatites of the anatectic region of the Cláudio Shear Zone. This suggests distinct events of anatexis and conditions for neosome formation. K-feldspar is expected as a peritectic phase resulting from hydrated conditions in the middle crust whereas during biotite dehydration melting, K-feldspar is absent (Carrington and Watt, 1995). The amount of Kfs also depends on protolith compositing (Weinberg and Hasalovà, 2015), and in the northeast and central domains trondhjemite and tonalite are the most common rocks, while along the southern border of the complex granodiorites are more common, what can explain the predominance of Itaúna and Kinawa migmatites on distinct domains. Sample 97A is located in the central domain, close to a granite intrusion and to the sheared mylonitic zone of the northeast domain. The gneisses in this region are essentially TTGs and the trondhjemite photolith is expected to have melted under congruent conditions since the leucosome and the melanocratic residuum have correspondent composition of a plg-rich trondhjemite with biotite, supporting an origin by in situ partial melting. Incongruent melt would not allow for the development of alkali-feldspar as a peritectic phase in the Itaúna migmatite.

Reactivation of shear zones and a transpressive system can facilitate water-fluxed zones of anatexis, where melt flow is interpreted to go upwards along the fabrics of the rocks (Brown et al., 2010). The contact zone between Pitangui and Divinópolis crust was caused by a shortening stage related to the closure of Pitangui Greenstone Belt basin, resulting in a series of small-scale shear zones replicating the main NW-SE direction trend of the Pitangui Lineament. In the same way, syntectonic intrusions associated with gold deposits and hydrothermal fluids occur in the northeast domain (e.g. Fabricio-Silva et al., 2018), close to the migmatite sample. During the 2100–2050 Ma collision-related tectonic exhumation decompression melting process started and could induce melting in these structures. Cutts et al., (2019) found the P-T conditions of ~17 kbar and ~680 °C for a similar setting in the Bação dome. Reactivation

of Archean structures during Proterozoic collision and exhumation could explain the migmatites of Divinópolis Complex. Migmatite induction is caused by destabilization of the crust. Deep structures may be more easily reactivated and hydrated, likewise what can be seen in the Kinawa migmatite. Carvalho et al. (2016) postulated that these rocks only experienced extensive melting due to the presence of water in the shear zone. One sample from the central domain show retrograde reactions, as biotite grow at the expense of garnet (Fig. 4e), typical of hydrous melting (Holness et al., 2011). Correspondingly, shallower crust levels may be more affected by dehydration reactions or not melt at all and, in this case, temperatures would be enough to result in significant zircon crystallization or monazite reset (Cutts et al., 2019). In the southern São Francisco Craton this syn-collisional metamorphism between 2100 and 2050 Ma is related to the Minas Orogeny and has been regionally imprinted in titanite and monazite, especially in the borders of the gneiss-granite complexes and the supracrustal successions between them (Campos and Carneiro, 2008; Aguilar et al., 2017; Chaves et al., 2019; Cutts et al., 2019). The amount of fluid available and depth were not amenable to growth new mineral in most of the Archean nuclei.

## 7. Tectonic implications

The zircon age data shows that major crust formation in the southern São Francisco Craton occurred trough a protracted time interval between 2.91 and 2.61 with minor contributions of material as old as 3.2 and 3.0 Ga. The first crust that formed at 3.2–3.0 Ga was not stable enough to constitute continents and would be constantly recycled back into the mantle, but, interestingly, it was preserved only in the Santa Bárbara dome or as inherited and detrital grains in other domes and greenstone belts. This ancient crust also shows TDM ages (Hf and Nd) varying from 3.4 to 3.0 Ga, usually with a long time of residence (Oliveira, 2004; Albert et al., 2016; Carvalho et al., 2016; 2017a). The metasedimentary sequences of the greenstone belts and the supracrustal successions preserve even older sources (up to 3.8 Ga), demonstrating that at least part of the crust survived long enough to work as a source of sediment. The best scenario to explain this constant recycle without fully developing would be the process of drip tectonics caused by mantle upwellings and resulting in partial melting of delaminated thick mafic proto crust. The drip residues that sink back into the mantle may guide new mantellic ascension causing additional melting. Eventually, the ascent of buoyant tonalitic magma into the upper crust would generate the first felsic crust. This period can be linked to the Santa Bárbara and Campo Belo events (Farina et al., 2015; Teixeira et al., 2017a).

The first period of TTG formation at 2915–2860 Ma likely represents the emergence of stable felsic continents in the southern São Francisco Craton. The buoyancy of felsic partially molten microcontinents of TTG between keels of thick successions of mafic and volcaniclastic rocks would

trigger the dome-and-keel structure of the southern São Francisco Craton (Marshak et al., 1997; Cutts et al., 2019). The detrital record on Pitangui and Rio das Velhas greenstone belts supports that they were a basin for sediments during this period (Brando Soares et al., 2020; Melo-Silva et al., 2020).

After ~70 Ma, the second generation of TTGs lasted from 2790 to 2775 Ma, coinciding with the Rio das Velhas II event and with fundamentals change in the tectonic style and geodynamics. It is suggested by some authors that subduction or subduction-like processes took place during this period, inferred by rocks with arc affinity such as the andesites of Pitangui and Rio das Velhas greenstone belt ca. 2.75 Ga (Silva, 2006; Brando Soares et al., 2020) and the adakites of the Rio das Velhas greenstone belt at ca. 2775 Ma (Silva et al., 2000). On the other hand, high-pressure TTGs are only recorded in Bação Complex, interpreted as melting of thick mafic pile in an intra-plate environment, and their juvenile $\varepsilon_{Hf}$ values agree with a low time of residence (Albert et al., 2016). We suggest that both regimes were taking place during the Rio das Velhas II and this period marks this transition. Multiple collision of microcontinents (Bação, Bonfim, Belo Horizonte, Passa Tempo, Divinópolis and Santa Bárbara) would be triggered by the growth of felsic proto continents, similar to the model proposed by Bédard et al. (2013) where drift of continental crust act as a tectonic agent overriding adjacent mafic oceanic crust or plateaus, producing multiple TTG generations. It is possible that these collisions would eventually trigger short-term episodes of proto subduction, mimicking plate tectonics style. If these short-term episodes would take place it likely would result in flat subduction or frequent slab break-off (van Hunen and Moyen, 2012; Laurent et al., 2014; Moyen and Laurent, 2018). In comparison, the higher thermal gradient (e.g. Bickle, 1986) and less stable regime were also more prone to mantle ascension and density inversions, resulting in delamination. The dome and keel configuration of the region is difficult to envisage if only collision and arc-like features were taking place in a series of paired arcs. Besides, rocks with typical arc signatures are very localized such as the adakites of Rio das Velhas greenstone belt (Silva et al., 2000) and the sanukitoids (*lato sensu*) of Passa Tempo Complex (Simon et al., 2018).

The Mamona event followed shortly after the Rio das Velhas Orogeny (2760–2680 Ma) and were divided here in Mamona I (2760 to 2715 Ma) corresponding to an older phase of intrusion of monzogranites that were subsequently foliated; and a younger phase of intrusions between 2705 to 2680 (Mamona II) composed of Kfs-rich granites. The results of our study support the episodic, rapid and progressive growth of continental crust during the Late Neoarchean. From 2760 Ma onward the widespread granodiorites and granites rich in alkali-feldspar predominate, requiring more enriched sources for producing large volumes of $K_2O$-rich magmas. The genesis of such potassic granite coupled with their inheritance support a silica rich crustal component (e.g. older TTGs, biotite-granites and even metasedimentary rocks). The Mamona I granitoids can be assigned to convergent or collisional settings that followed the period of collage of the microcontinental blocks, as suggested by some authors (Dopico

et al., 2017; Farina et al., 2015; Albert et al., 2016; Teixeira et al., 2017a; Brando Soares et al., 2020), while the Mamona II granitoids can be grouped as set of post collisional to extensional granites (e.g. Moreno et al., 2017; Cutts et al., 2019; Brando Soares et al., 2020) originated from hybrid sources from the reworked Meso-Neoarchean crust. This extensional magmatism would follow the post collisional setting, resulting in granites formed in shallower levels of the crust, within lower P-T conditions and more prone to a mix source. Their presence in Archean terranes can be used as an indicator of preexisting felsic crust and can be linked to the crustal evolution of a craton. In the Superior Province (Henry et al., 2000), Yilgarn Craton (Champion and Sheraton, 1997), Wyoming Province (Frost et al., 2006) and Carajás Province (Feio et al., 2013) similar generations of TTG and potassic granitoids are described (Fig. 10d).

The last potassic magmatic pulses occurred as localized intrusions of 2650 Ma and 2610 Ma and after that, the cratonic crust went through a period of stability with the deposition of the Minas Supergroup and the Itacolomi Group until ca. 2.1 Ga (Dorr, 1969; Machado et al., 1996; Alkmim and Martins-Neto, 2012; Dopico et al., 2017). In the Proterozoic, the crust was reactivated with the onset of the Minas Orogeny and formation of the Nuna-Columbia supercontinent between 2.1–1.9 Ga. This deformation front caused by the collapse of the Minas Orogen reactivated old Archean structures and crustal thickening heated the basement enough to crystallize monazite and titanite between 2100 and 2050 Ma (e.g. Cutts et al., 2019; Aguilar et al., 2017; this work). Deep structures where water percolates easier were able to crystallize zircon, such as in the Kinawa migmatite (Carvalho et al., 2016). The reactivation of the Archean dome-and-keel configuration of the craton (Marshak et al., 1997; Cutts et al., 2019) would explain the development of a varied of 2.1–1.9 Ga supracrustal successions between Divinópolis, Campo Belo and Bonfim complexes. This includes the Itapecerica peraluminous graphite-rich succession (Teixeira et al., 2017b), the khondalite belt-paragneiss succession of Cláudio Shear Zone (Coelho and Chaves, 2019) and the recently described Itaguara Ophiolite, associated with a Paleoproterozoic accretionary wedge and a paleo-subduction zone (Chaves et al., 2019b) between Divinópolis and Bonfim complexes.

## 8. Conclusions

Our findings support a polycyclic evolution for the southern São Francisco craton. This portion of Archean crust fits the classical model of granite-greenstone terrains with well-preserved Neoarchean rocks and a long-lived, multistage polygenetic genesis, highlighting five main events:

1) The first period of TTG formation at 2915–2860 Ma likely represents the rise of stable, long-lived felsic continents in the southern São Francisco Craton.
2) The second period of TTG formation from 2790 to 2775 Ma occurred during fundamental changes in the tectonic style and geodynamics of the southern São Francisco craton. Multiple

collision of microcontinents (the domes in the southern São Francisco craton) would be triggered by drift of the newly formed felsic crust, overriding adjacent mafic oceanic crust or plateaus. Eventually this accretionary phase would start short-term episodes of proto subduction and delamination of thick mafic crust, resulting in coeval periods of vertical and horizontal tectonics.

3) The Mamona event (2760 to 2680 Ma) represents a period of progressive growth of continental crust in the Late Neoarchean derived from reworked silica-rich crustal sources. The Mamona I phase monzogranites (2760 to 2715) can be assigned to convergent margins or collisional settings, being consistently more deformed and less rich in potassium. The Mamona II phase syenogranites (2705 to 2680) likely formed during an extensional post collisional setting and comprise the potassic granites related to the irreversible differentiation and evolution of the crust, followed by a period of stability.
4) The Proterozoic influence of the Mineiro Orogeny during the assembly of the Gondwana was responsible for tectonic reactivation of Archean structures and development of important shear zones and supracrustal successions, where water-fluxed melt can be facilitated, resulting in migmatite induction and granulite facies metamorphism at 2.06 to 2.04 Ga. During this period, reset of monazite and titanite also occurred in the Archean nuclei as a result of crustal thickening and heating.

## References

**Aguilar, C., Alkmim, F. F., Lana, C., Farina, F. 2017.** Palaeoproterozoic assembly of the São Francisco craton, SE Brazil: New insights from U–Pb titanite and monazite dating. *Precambrian Research*, **289:** 95–115.

**Aleinikoff, J.N., Schenk, W.S., Plank, M.O., Srogi, L.A., Fanning, C.M., Kamo, S.L., Bosbyshell, H. 2006.** Deciphering igneous and metamorphic events in high-grade rocks of the Wilmington complex, Delaware: morphology, cathodoluminescence and backscattered electron zoning, and SHRIMP U–Pb geochronology of zircon and monazite. *Geological Society of America Buletin,* **118:** 39–64.

**Almeida, F.F. 1977.** O Cráton do São Francisco. *Revista Brasileira de Geociências*, **7:** 349- 364.

**Alkmim, F.F. 2004.** O que faz de um cráton um cráton? O cráton do São Francisco e as revelações Almeidianas ao delimitá-lo. *In:* Mantesso-Neto V, Bartorelli A, Dal Ré Carneiro C (Eds.) Geologia do Continente Sul-Americano: Evolução da Obra de Fernando Flávio Marques de Almeida, Ed Beca, 17–34.

**Albert, C., Farina, F., Lana, C., Stevens, G., Storey, C., Gerdes, A., Dopico, C. M. 2016.** Archean crustal evolution in the Southern São Francisco craton, Brazil: Constraints from U-Pb, Lu-Hf and O isotope analyses. *Lithos*, **266–267**: 64–86.

**Alkmim, F.F., Marshak, S., 1998.** Tranzamazonian Orogeny in the southern São Francisco Craton region, Minas Gerais, Brazil: evidence of Paleoproterozoic collision and colapse in the Quadrilátero Ferrífero. *Precambrian Research,* **90,** 29–58.

**Alkmim F.F. Noce C.M. (eds.). 2006.** The Paleoproterozoic Record of the São Francisco Craton. IGCP 509 Field workshop, Bahia and Minas Gerais, Brazil. Field Guide & Abstracts, 114 pp.

**Alkmim, F.F., Martins-Neto, M.A. 2012.** Proterozoic first-order sedimentary sequences of the São Francisco craton, eastern Brazil. *Marine and Petroleum Geology,* **3:** 127–139.

**Alkmim, F.F., Teixeira, W., 2017.** The Paleoproterozoic Mineiro belt and the Quadrilátero Ferrífero. In: Heilbron, M., Alkmim, F., Cordani, U.G. (Eds.), The São Francisco Craton and its margins, Eastern Brazil, *Geology Review Series*. Springer-Verlag, pp. 71–94.

**Armstrong, R.A., Compston, W., de Wit, M.J., Williams, I.S., 1990.** The stratigraphy of the 3.5–3.2 Ga Barberton Greenstone Belt revisited: a single zircon ion microprobe study. *Earth and Planetary Sciences Letters,* **101:** 90–106.

**Arndt, N.T., 2013.** The formation and evolution of the continental crust. *Geochemical Perspectives,* **2**: 405.

**Ávila, C.A., Teixeira, W., Bongiolo, E.M., Dussin, I.A., Vieira, T.A.T. 2014.** Rhyacian evolution of subvolcanic and metasedimentary rocks of the southern segment of the Mineiro belt, São Francisco Craton, Brazil. *Precambrian Research*, **243:** 221–251.

**Baltazar, O.F. Zucchetti, M. 2007.** Lithofacies associations and structural evolution of the Archean Rio das Velhas *Greenstone belt*, Quadrilátero Ferrífero, Brazil: a review of the setting of gold deposits. O*re Geology Reviews,* **32**: 471–499.

**Barbosa, J.S.F., Sabaté, P. 2004.** Archean and Paleoproterozoic crust of the São Francisco Craton, Bahia, Brazil: geodynamic features. *Precambrian Research,* **133**: 1–27.

**Barbosa, N. S., Teixeira, W., Ávila, C. A., Montecinos, P. M., Bongiolo, E. M., e Craton, F. 2015.** 2.17–2. 10 Ga plutonic episodes in the Mineiro belt, São Francisco Craton, Brazil: U-Pb ages, geochemical constraints and tectonics. *Precambrian Research*, **270**: 204–225.

**Barbosa, N., Menezes Leal, A. B., Debruyne, D., Bastos Leal, L. R., Barbosa, N. S., Marinho, M., Mercês, L., Barbosa, J. S., Koproski, L. M. 2020.** Paleoarchean to Paleoproterozoic crustal evolution in the Guanambi-Correntina block (GCB), north São Francisco Craton, Brazil, unraveled by U-Pb Geochronology, Nd-Sr isotopes and geochemical constraints. *Precambrian Research*, **340**: 105614.

**Bea, F., Montero, P., Gonzalez Lodeiro, F., Talavera, C., 2007.** Zircon inheritance reveals exceptionally fast crustal magma generation processes in Central Iberia during the Cambro-Ordovician. *Journal of Petrology*, **48:** 2327–2339

**Bédard, J., 2006.** A catalytic delamination-driven model for coupled genesis of Archaean crust and sub-continental lithospheric mantle. *Geochimica et Cosmochimica Acta*, **70**: 1188–1214.

**Bédard, J.H., 2013.** How many arcs can dance on the head of a plume? A 'Comment' on: a critical assessment of neoarchean 'plume only' geodynamics: evidence from the Superior province, by Derek Wyman. *Precambrian Research,* **229:** 189-197.

**Bickle, M.J. 1986.** Implications of melting for stabilization of the lithosphere and heat loss in the Archean. *Earth Planetary Science Letters*, **80:** 314-324.

**Brando Soares, M., Corrêa Neto, A.V., Zeh, A., Cabral, A.R., Pereira, L.F., Prado, M.G.B., Almeida, A.M., Manduca, L.G., Silva, P.H.M., Mabub, R.O.A., Schlichta, T.M. 2017.** Geology of the Pitangui Greenstone Belt, Minas Gerais, Brazil: Stratigraphy, geochronology and BIF geochemistry. *Precambrian Research*, **291**: 17–41.

**Brando Soares, M., Corrêa Neto, A. V., e Fabricio-Silva, W. 2020.** The development of a Meso- to Neoarchean rifting-convergence-collision-collapse cycle over an ancient thickened protocontinent in the south São Francisco craton, Brazil. *Gondwana Research*, **77:** 40–66.

**Brown, M. 2010.** Melting of the continental crust during orogenesis: The thermal, rheological, and compositional consequences of melt transport from lower to upper continental crust. *Canadian Journal of Earth Sciences*, **47(5):** 655–694.

**Campos, J.C.S., Carneiro, M.A., 2008.** Genetic and tectonic implications of the Neoarchean and Paleoproterozoic granitoids marginal to the Jeceaba-Bom Sucesso Lineament, crustal segment of the Southern São Francisco Craton. *Journal of South American Earth Sciences,* **26:** 463–484.

**Canuto, J.R., 2010.** Estratigrafia de seqüencias em bacias sedimentares de diferentes idades e estilos tectônicos. *Revista Brasileira de Geociência*s, **40**: 537-549.

**Carrington, D.P. Watt, G.R. 1995.** A geochemical and experimental study of the role of K-feldspar during water undersaturated melting of metapelites. *Chemical Geology,* **122:** 59- 76.

**Carvalho, B.B., Sawyer, E.W., Janasi, V.A. 2016.** Crustal reworking in a shear zone: Transformation of metagranite to migmatite. *Journal of Metamorphic Geology*, **34:** 237–264.

**Carvalho, B.B., Janasi, V.A., Sawyer, E.W., 2017a.** Evidence for Paleoproterozoic anatexis and crustal reworking of Archean crust in the São Francisco Craton, Brazil: a dating and isotopic study of the Kinawa migmatite. *Precambrian Research*, **291**: 98–118.

**Campos, J.C.S., Carneiro, M.A., Basei, M.A.S., 2003.** U-Pb evidence for Late Neoarchean crustal reworking in the southern São Francisco Craton (Minas Gerais, Brazil): *In: Anais da Academia Brasileira de Ciências*, **75:** 497-511.

**Champion, D. C., Sheraton, J. W. 1997.** Geochemistry and Nd isotope systematics of Archean granites of the Eastern Gold-fields, Yilgarn craton, Australia: implications for crustal growth processes. *Precambrian Research*. **83:** 109-132.

**Champion, D. C., Smithies, R. H. 2019.** Geochemistry of Paleoarchean Granites of the East Pilbara Terrane, Pilbara Craton, Western Australia: Implications for Early Archean Crustal Growth. *In* Earth's Oldest Rocks.

**Chaves, A.O., Goulart, L. E. A., Coelho, R. M., Miranda, D. A., Aranda, R.O.A., Ramos, S.L.L.M. 2019.** High-pressure eclogite facies metamorphism and decompression melting recorded in paleoproterozoic accretionary wedge adjacent to probable ophiolite from Itaguara (southern São Francisco Craton - Brazil). *Journal of South American Earth Sciences*, **94:** 102226.

**Coelho, R. M., Chaves, A. O. 2019.** Pressure-temperature-time path of Paleoproterozoic khondalites from Claudio shear zone (southern São Francisco craton, Brazil): Links with khondalite belt of the North China craton. *Journal of South American Earth Sciences*, **94**: 102250.

**Condie, K.C., 1997.** Plate tectonics and crustal evolution. Butterworth Heinemann, Oxford. 282 pp.

**Corrêa da Costa, P.C. 1999.** Episódios de formação de crosta continental Arqueana no Cráton São Francisco Meridional: um exemplo a partir da região de Candeias – Campo Belo, MG. Dissertação de Mestrado. Departamento de Geologia da Escola de Minas da Universidade Federal de Ouro Preto, 151 p.

**Cutts, K., Lana, C., Alkmim, F., Farina, F., Moreira, H., Coelho, V. 2019.** Metamorphism and exhumation of basement gneiss domes in the Quadrilátero Ferrífero: Two stage dome-and-keel evolution? *Geoscience Frontiers*, **10:** 1765-1787.

**Dantas, E.L., Brito Neves, B.B., Fuck, R.A. 2013.** Looking for the Early Archean rocks in South America: U–Pb dating and Hf isotopes in zircons from the north São Francisco Craton, Brazil. *Geological Society of America*, Annual Meeting 2013, Paper 269-5.

**Dhuime, B., Hawkesworth, C.J., Cawood, P.A., Storey, C.D., 2012.** A change in the geodynamics of continental growth 3 billion years ago. *Science,* **335 (6074)**: 1334-1336.

**Dickinson, W.R., Gehrels, G. E. 2003.** U-Pb ages of detrital zircons from Permian and Jurassic eolian sandstones of the Colorado Plateau, USA: Paleogeographic implications. *Sedimentary Geology*, 163: 29–66.

**Door, J.V.N. 1969.** Physiographic, stratigraphic and structural development of the Quadrilátero Ferrífero, Minas Gerais, Brazil, U.S.G.S. Professional Paper 614 –A, 110 p.

**Dopico, C.I., Lana, C., Moreira, H.S., Cassino, L.F., Alkmim, F.F. 2017.** U–Pb ages and Hf-isotope data of detrital zircons from the late Neoarchean-Paleoproterozoic Minas Basin, SE Brazil. *Precambrian Research*, **291**: 143–161.

**Fabricio-Silva, W., Rosière, C. A., Bühn, B. 2018.** The shear zone-related gold mineralization at the Turmalina deposit, Quadrilátero Ferrífero, Brazil: structural evolution and the two stages of mineralization. *Mineralium Deposita*.

**Farina, F., Albert, C., Lana, C. 2015.** The Neoarchean transition between medium-and high-K granitoids: Clues from the Southern São Francisco Craton (Brazil). *Precambrian Research,* **266:** 375-394.

**Farina, F., Albert, C., Martínez Dopico, C., Aguilar Gil, C., Moreira, H., Hippertt, J. P., Cutts, K., Alkmin, F. F., Lana, C. 2016.** The Archean–Paleoproterozoic evolution of the Quadrilátero Ferrífero (Brasil): Current models and open questions. *Journal of South American Earth Sciences*, **68:** 4–21.

**Feio, G.R.L., Dall'Agnol, R., Dantas, E.L., Macambira, M.J.B., Santos, J.O.S., Althoff, F.J., Soares, J.E.B., 2013.** Archean granitoid magmatism in the Canaã dos Carajás area: implications for crustal evolution of the Carajás province, Amazonian craton, Brazil. *Precambrian Research,* **227:** 157–185.

**Fernandes, R., Carneiro, M. 2000.** O complexo metamórfico Campo Belo (Cráton São Francisco Meridional): unidades litodêmicas e evolução tectônica. *Brazilian Journal of Geology*, **30:** 671–678.

**Foley, S.F., Tiepolo, M., Vannucci, R., 2002.** Growth of early continental crust controlled by melting of amphibolite in subduction zones. *Nature*, **417**: 637-640.

**Frost, C. D., Frost, B. R., Chamberlain, K. R., e Hulsebosch, T. P. 1998.** The Late Archean history of the Wyoming province as recorded by granitic magmatism in the Wind River Range, Wyoming. *Precambrian Research*, **89(3–4)**: 145–173.

**Frost, C. D., Frost, B. R., Kirkwood, R., Chamberlain, K. R. 2006.** The tonalite-trondhjemite-granodiorite (TTG) to granodiorite-granite (GG) transition in the late Archean plutonic rocks of the central Wyoming Province. Canadian Journal of Earth Sciences, 43(10), 1419–1444.

**Geisler, T., Schaltegger, U., Tomaschek, F. 2007.** Re-equilibration of zircon in aqueous fluids and melts. *Elements*, **3 (1)**: 43-50.

**Gonçalves, G. O., Lana, C., Scholz, R., Buick, I. S., Gerdes, A., Kamo, S. L., Corfu, F., Marinho, M. M., Chaves, A. O., Valeriano, C., e Nalini, H. A. 2016.** An assessment of monazite from the Itambé pegmatite district for use as U-Pb isotope reference material for microanalysis and implications for the origin of the "Moacyr" monazite. *Chemical Geology,* **424:** 30–50.

**Hartmann L., Endo I., Suita M., Santos J., Frantz J., Carneiro M., McNaughton N., Barley M. 2006**. Provenance and age delimitation of Quadrilátero Ferrífero sandstones based on zircon U-Pb isotopes. *Journal of South American Earth Sciences*, **20:** 273-285.

**Hawkesworth, C.J., Cawood, P.A., Kemp, A.I.S., Storey, C.D., Dhuime, B., 2009**. A matter of preservation. *Science,* **323**: 49–50.

**Hawkesworth, C., Dhuime, B., Pietranik, A., Cawood, P., Kemp, T., Storey, C., 2010.** The generation and evolution of the continental crust. *Journal of the Geolofical Society of London* **167:** 229–248.

**Hawkins, D.P., Bowring, S.A. 1999.** U-Pb monazite, xenotime and titanite geochronological constraints on the prograde to post-peak metamorphic thermal history of Paleoproterozoicb migmatites from the Grand Canyon, Arizona. *Contributions to Mineralogy and Petrology*, **134:** 150–169.

**Heilbron M., Cordani, U.G., Alkmim F.F., 2017**. The São Francisco Craton and its Margins. *In:* M. Heilbron, U.G. Cordani, F.F. Alkmim (eds.), *São Francisco Craton, Eastern Brazil,* Springer International Publishing, Switzerland, Regional Geology Reviews, pp. 3-13 p.

**Heilimo, E., Halla, J., Huhma, H., 2011.** Single-grain zircon U-Pb age constraints of the western and eastern sanukitoid zones in the Finnish part of the Karelian Province. *Lithos* **12:** 87–99.

**Henry, P., Stevenson, R.K., Larbi, Y., Gariépy, C. 2000.** Nd isotopic evidence for Early to late Archean (3.4–2.7 Ga) crustal growth in the western Superior Province (Ontario, Canada). *Tectonophysics*, **322:** 135–151.

**Hoffmann, J. E., Zhang, C., Moyen, J.F., e Nagel, T. J. 2019.** The Formation of Tonalites–Trondjhemite–Granodiorites in Early Continental Crust. *In* Earth's Oldest Rocks.

**Holness, M. B., Cesare, B., Sawyer, E. W. 2011.** Melted rocks under the microscope: Microstructures and their interpretation. *Elements*, **7:** 247–252.

**Jahn, B., Glikson, A.Y., Peucat, J.-J., Hickman, A.H., 1981.** REE geochemistry and isotopic data of Archaean silicic volcanics and granitoids from the Pilbara block, western Australia: implications for early crustal evolution. *Geochimica et Cosmochimica Acta,* **45:** 1633–1652

**Johnson, T.E., Brown, M., Kaus, B.J., VanTongeren, J.A., 2014.** Delamination and recycling of Archaean crust caused by gravitational instabilities. *Nature Geoscience*, **7(1)**: 47-52.

**Kemp, A.I.S., Hawkesworth, C.J., Paterson, B.A., Kinny, P.D., 2006.** Episodic growth of the Gondwana super continent from hafnium and oxygen isotopes in zircon. *Nature,* **439**: 580–583.

**Kusiak, M.A, Whitehouse, M.J., Wilde, S.A., Nemchin, A.A., Clark, C. 2013.** Mobilization of radiogenic Pb in zircon revealed by ion imaging: Implications for early Earth geochronology. *Geology*; **41 (3)**: 291–294.

**Lana C., Alkmim F., Armstrong R., Scholz R., Romano R., Nalini H. 2013.** The ancestry and magmatic evolution of Archaean TTG rocks of the Quadrilátero Ferrífero province, southeast Brazil: *Precambrian Research*, **231:** 157-173.

**Laurent, O., Martin, H., Doucelance, R., Moyen, J.F., Paquette, J.L., 2011.** Geochemistry and petrogenesis of high-K "sanukitoids" from the Bulai pluton, Central Limpopo Belt South Africa: implications for geodynamic changes at the Archaean-Proterozoic boundary. *Lithos,* **123,** 73–91.

**Lobato L.M., Ribeiro-Rodrigues L.C., Zuchetti M., Noce C.M., Baltazar O.F., da Silva L.C., Pinto C.P. 2001**. Brazil's premier gold province: part I: the tectonic, magmatic and structural setting of gold deposits in the Archean Rio das Velhas *greenstone belt*, Quadrilátero Ferrífero. *Mineralium Deposita,* **36:** 249-277.

**López, S., Castro, A., e García-Casco, A.** 2005. Production of granodiorite melt by interaction between hydrous mafic magma and tonalitic crust. Experimental constraints and implications for the generation of Archaean TTG complexes. *Lithos,* **79** (1-2 SPEC. ISS.), 229–250.

**Ludwig, K.R., 2012.** User's Manual for Isoplot Version 3.75-4.15: a Geochronological Toolkit for Microsoft Excel. *Berkeley Geochronological Center Special Publication*, **5.**

**Machado, N., Noce, C.M., Ladeira, E.A., Belo de Oliveira, O.A. 1992.** U–Pb geochronology of Archean magmatism and Proterozoic metamorphism in the Quadrilátero Ferrífero, southern São Francisco craton, Brazil. *Geol Soc Am Bull 104*, **(9):** 1221–1227.

**Machado, N., Carneiro, M.A. 1992.** U − Pb evidence of late Archean tectono-thermal activity in the southern São Francisco shield, Brazil. *Canadian Journal of Earth Sciences*, **29**: 2341–2346

**Machado N., Schrank A., Noce C., Gauthier G. 1996.** Ages of detrital zircon from Archean-Paleoproterozoic sequences: Implications for *Greenstone belt* setting and evolution of a Transamazonian foreland basin in Quadrilátero Ferrífero, southeast Brazil: *Earth and Planetary Science Letters*, **141:** 259-276.

**Marshak, S., Tinkham, D., Alkmim, F.F., Brueckner, H., Bornhorst, T., 1997.** Dome-andkeel provinces formed during Paleoproterozoic orogenic collapse - core complexes, diapirs, or neither? Examples from the Quadrilatero Ferrifero and the Penokean Orogen. *Geology*, **25:** 415-418.

**Martin, H., Peucat, J.-J., Sabaté, P., Cunha, J.C., 1997.** Crustal evolution in Early Archaean of South America: example of the Sete Voltas Massif, Bahia, Brazil. *Precambrian Research,* **82**: 35–62.

**Martin H., Smithies R.H., Rapp R., Moyen J.-F., Champion D., 2005.** An overview of adakite, tonalite-trondhjemite-granodiorite (TTG), and sanukitoid: Relationships and some implications for crustal evolution: *Lithos,* **79:** 1–24.

**Medeiros, E.L.M., Cruz, S.C.P., Barbosa, J.S.F., Paquette, J.L., Peucat, J.J., Jesus, S.S.G.P., Barbosa, R.G., Brito, R.S.C., Carneiro, M.A. 2017.** The Santa Izabel Complex, Gaviao Block, Brazil: Components, geochronology, regional correlations and tectonic implications. *Journal of South American Earth Sciences*, **80:** 66–94.

**Melo-Silva, P., Amaral, W.S., Oliveira, E.P. 2020.** Geochronological evolution of the Pitangui Greenstone Belt, southern São Francisco Craton, Brazil: constraints from U-Pb zircon age, geochemistry and field relationships. *Journal of South American Earth Sciences*, **99:** 102380.

**Moreira, H., Lana C., Arias H., Nalini Jr H.A. 2016.** The detrital zircon record of an Archaean convergent basin in the. *Precambrian Research*, **275:** 84–99.

**Moreno, J. A., Baldim, M. R., Semprich, J., Oliveira, E. P., Verma, S. K., e Teixeira, W. 2017.** Geochronological and geochemical evidences for extension-related Neoarchean granitoids in the southern São Francisco Craton, Brazil. *Precambrian Research*, **294:** 322–343.

**Moyen J. F. 2011.** The composite Archaean grey gneisses: Petrological significance, and evidence for a non-unique tectonic setting for Archaean crustal growth. *Lithos*, **123:** 21–36.

**Moyen, J., Martin, H. 2012.** Forty years of TTG research. *Lithos*, **148**: 312–336.

**Moyen, J.F., Laurent, O., 2018.** Archaean tectonic systems: a view from igneous rocks. *Lithos,* **302-303**, 99-125.

**Navarro M.S., Tonetto E.M., Oliveira E.P., 2017.** Peixe zircon: new Brazilian reference material for U-Pb geochronology by LA-SF-ICP-MS. *Goldschmidt2017 Abstract*.

**Noce C.M., Machado N., Teixeira W. 1998.** U–Pb geochronology of gneisses and granitoids in the Quadrilátero Ferrífero (Southern São Francisco craton): age constraints for Archean and Paleoproterozoic magmatism and metamorphism. *Revista Brasileira de Geociências* **28:** 95–102.

**Noce C.M 2000.** Geochronology of the Quadrilátero Ferrífero: A review: *Geonomos*, **8:** 15-23.

**Noce C. M., Zuccheti M., Baltazar O. F., Armstrong R., Dantas E., Renger F. E., Lobato L. M. 2005.** Age of felsic volcanism and the role of ancient continental crust in the evolution of the Neoarchean Rio das Velhas greenstone belt (Quadrilátero Ferrífero, Brazil): U-Pb zircon dating of volcaniclastic graywackes. *Precambrian Research,* **141:** 67–82.

**Nutman, A.P., Cordani, U.G., Sabaté, P., 1994.** SHRIMP U–Pb ages of detrital zircons from the Early Proterozoic Contendas–Mirante supracrustal belt, São Francisco Craton, Bahia, Brazil. *Journal of South America Earth Sciences*, **7**: 109–114.

**Oliveira A.H. 2004.** Evolução tectônica de um fragmento do Cráton São Francisco Meridional com base em aspectos estruturais, geoquímicos (rocha total) e geocronológicos (Rb-Sr, Sm-Nd, Ar-Ar, U-Pb). Tese de Doutorado, Departamento de Geologia da Escola de Minas da Universidade Federal de Ouro Preto, 156 p.

**Oliveira, E.P., McNaughton, N.J., Zincone, S.A., Talavera, C. 2020.** Birthplace of the São Francisco Craton, Brazil: Evidence from 3.60 to 3.64 Ga Gneisses of the Mairi Gneiss Complex. *Terra Nova,* **32**:281–289.

**Paton C., Woodhead J.D., Hellstrom J.C., Hergt J.M., Greig A., Maas R. 2010.** Improved laser ablation U-Pb zircon geochronology through robust downhole fractionation correction. *Geochemistry, Geophysics and Geosystems*, **11:** Q0AA06.

**Petrus, J.A., Kamber, B.S., 2012.** VizualAge: a novel approach to laser ablation ICP-MS U–Pb geochronology data reduction. *Geostandards and Geoanalytical Research,* **36:** 247–270.

**Pinto, C.P., Silva, M.A. 2014.** Mapa Geológico do Estado de Minas Gerais. CODEMIG, Governo de Minas, CPRM, Secretaria de Geologia, Mineração e Transformação Mineral, Ministério de Minas e Energia, Governo Federal do Brasil.

**Polat, A. 2012.** Growth of Archean continental crust in oceanic island arcs. *Geology*, **40**, 383–384.

**Ridley, J.R., Vearcombe, J.R., Jelsma, H.A., 1997.** Relations between greenstone belts and associated granitoids. In: de Witt, M.J., Ashwall, L.D. (Eds.), Greenstone Belts. *Oxford Univ. Press*, Oxford, pp. 376–397.

**Romano R., Lana C., Alkmim F. F., Stevens G., Armstrong R. 2013.** Stabilization of the southern portion of the São Francisco craton, SE Brazil, through a long-lived period of potassic magmatism. *Precambrian Research,* **224:** 143–159.

**Sawyer E.W. 2008.**Working with migmatites: nomenclature for the constituent parts. In: Sawyer E.W. e Brown M. (Eds.). Working with migmatite: *Mineralogical Association of Canada. Short Course*, **38:**1-28.

**Schorscher, H.D., 1992.** Arcabouço petrográfico e evolução crustal dos terrenos pré-cambrianos do sudeste de Minas Gerais: Quadrilátero Ferrífero, Espinhaço Meridional, e domos granitoides-gnáissicos adjacentes. Livre Docência (Tese). Universidade de São Paulo USP, São Paulo, 393 p.

**Seixas, L.A.R., David, J., Stevenson, R. 2012.** Geochemistry, Nd isotopes and U–Pb geochronology of a 2350 Ma TTG suite, Minas Gerais, Brazil: implications for the crustal evolution of the southern São Francisco craton. *Precambrian Research*, **196-7:** 61-80.

**Shang, C.K., Satir, M., Nsifa, E.N., Liegeois, J.P., Siebel, W., Taubald, H., 2007.** Archaean high-K granitoids produced by remelting of the earlier Tonalite–Trondhjemite–Granodiorite (TTG) in the Sangmelima region of the Ntem complex of the Congo craton, southern Cameroon. *International Journal of Earth Sciences*, **96:** 817–842

**Silva L.C., Noce C. M., Lobato L.M. 2000.** Dacitic volcanism in the Course of the Rio das Velhas (2800-2690 Ma) Orogeny: A Brazilian Archean analogue (TTD) to the modern adakites. *Revista Brasileira de Geociências,* **30:** 384–387.

**Simon, M.B., Marques Bongiolo, E., Ávila, C.A., Oliveira, E.P., Teixeira, W., Stohler, R.C., Soares de Oliveira, F.V. 2018.** Neoarchean reworking of TTG-like crust in the southernmost portion of the São Francisco Craton: U-Pb zircon dating and geochemical evidence from the São Tiago Batholith. *Precambrian Research*, **314:** 353–376.

**Singh, P.K., Verma, S.K., Singh, V.K., Moreno, J.A., Oliveira, E.P., Mehta, P. 2019.** Geochemistry and petrogenesis of sanukitoids and high-K anatectic granites from the Bundelkhand Craton, India: Implications for late-Archean crustal evolution. *Journal of Asian Earth Sciences*, **174:** 263–282.

**Sizova, E., Gerya, T., Stüwe, K., Brown, M., 2015.** Generation of felsic crust in the Archean: a geodynamic modeling perspective. *Precambrian Research*, **271**: 198-224.

**Smithies, R.H., 2000.** The Archaean tonalite–trondhjemite–granodiorite (TTG) series is not an analogue of Cenozoic adakite. *Earth and Planetary Science Letters,* **182:** 115–125.

**Tchameni, R., Mezger, K., Nsifa, N.E., Pouclet, A., 2000.** Neoarchaean evolution in the Congo craton: evidence from K rich granitoids of the Ntem complex, Southern Cameroon. *Journal of African Earth Sciences*, **30**: 133–147.

**Taylor S.R., Mclennan S.M. 1985**. The Continental Crust: Its Composition and Evolution. Blackwell, Blackwell Scientific, Oxford, 311p.

**Teixeira, W., Carneiro, M.A., Noce, C.M., Machado, N., Sato, K., Taylor, P.N., 1996.** Polyphase crustal evolution in the late Archean: The case of the Campo Belo Metamorphic Complex. In: I Symposium of Archean Terranes of the South American Platform. Sociedade Brasileira de Geologia, Brasília, Anais, 63-64.

**Teixeira W., Cordani U.G., Nutman A.P., Sato K. 1998**. Polyphase Archean evolution in the Campo Belo metamorphic complex, Southern São Francisco Craton, Brazil: SHRIMP U-Pb zircon evidence. *Journal of South American Earth Sciences*, **11:** 279-289.

**Teixeira W., Ávila, C.A., Dussin, I.A., Corrêa Neto, A.V., Bongiolo, E.M., Santos, J.O.S., Barbosa, N. 2015.** Zircon U–Pb–Hf, Nd–Sr constraints and geochemistry of the Resende Costa Orthogneiss and coeval rocks: new clues for a juvenile accretion episode (2.36–2.33 Ga) in the Mineiro belt and its role to the long-lived Minas accretionary orogeny. *Precambrian Research*, **256:** 148-169.

**Teixeira, W., Oliveira, E.P., Marques, L.S., 2017a.** The nature and evolution of the Archean Crust of the São Francisco Craton. In: Heilbron, M., Alkmim, F., Cordani, U.G. (Eds.), São Francisco Craton, Eastern Brasil: tectonic genealogy of a miniature continent, *Regional Geology Review Series*. Springer-Verlag, pp. 29–56.

**Teixeira, W., Oliveira, E.P., Peng, P., Dantas, E.L., Hollanda, M.H.B.M. 2017b.** U-Pb geochronology of the 2.0 Ga Itapecerica graphite-rich supracrustal succession in the São Francisco Craton: Tectonic matches with the North China Craton and paleogeographic inferences. *Precambrian Research*, **293**: 91–111.

**Uhlein, G.J., Uhlein, A., Halverson, G.P., Stevenson, R., Caxito, F.A., Cox, G.M., Carvalho, J.F.M.G. 2016.** The Carrancas Formation, Bambuí Group: A record of pre-Marinoan sedimentation on the southern São Francisco craton, Brazil. *Journal of South American Earth Sciences*, **71:** 1–16.

**Wang, C., Song, S., Niu, Y., Wei, C., Su, L. 2016.** TTG and potassic granitoids in the Eastern North China craton: Making Neoarchean upper continental crust during micro-continental collision and post-collisional extension. *Journal of Petrology*, **57:** 1775–1810.

**Wiedenbeck M., Allé P., Corfu F., Griffin W.L., Meier M., Oberli F., von Quadt A., Roddick J.C. Spiegel W. 1995.** Three natural zircon standards for U-Th-Pb, Lu-Hf, trace element and REE analyses. *Geostandards Newsletter*, **19:** 1-23.

**Whitney. D.L. Evans B.W. 2010.** Abbreviations for names of rock-forming minerals. *American Mineralogist,* **95:** 185–187.

**Weinberg, R. F., Hasalová, P. 2015.** Water-fluxed melting of the continental crust: A review. *Lithos,* **212–215**: 158–188.

**van Hunen J. e Moyen J-M. 2012.** Archean Subduction: Fact or Fiction? *Earth and Planetary Science*, *The Annual Review*, **40:**195-219.

**Van Kranendonk, M.J., Smithies, R.H., Hickman, A.H., Champion, D.C., 2007.** Review: secular tectonic evolution of Archean continental crust: interplay between horizontal and vertical processes in the formation of the Pilbara Craton, Australia. *Terra Nova* **19:** 1-38.

**Van Kranendonk, M.J., Smithies, R.H., Griffin, W.L., Huston, D.L., Hickman, A.H., Champion, D.C., Anhaeusser, C.R., Pirajno, F., 2015.** Making it thick: a volcanic plateau model for Paleoarchean continental lithosphere of the Pilbara and Kaapvaal cratons. *In:* Roberts, N.M.W., Van Kranendonk, M., Parman, S., Shirey, S., Clift, P.D. (Eds.), Continent Formation through Time. Geological Society of London, pp. 83e112. Special Publications 389.

**Zeh, A., Gerdes, A. 2012.** U-Pb and Hf isotope record of detrital zircons from gold-bearing sediments of the Pietersburg Greenstone Belt (South Africa)-Is there a common provenance with the Witwatersrand Basin? *Precambrian Research*, **204–205**: 46–56.

**Zincone, S.A., Oliveira, E.P., Laurent, O., Zhang, H., Zhai, M., 2016.** 3.30 Ga high-silica intraplate volcanic–plutonic system of the Gavião Block, São Francisco Craton, Brazil: evidence of an intracontinental rift following the creation of insulating continental crust. *Lithos,* **266–267:** 414–434.

# APÊNDICE A

**Table 1:** Elementos maiores, traços e terras raras das rochas félsicas do Complexo Divinópolis.

| Amostra | PD16-03A | PD16-03B | PD16-40 | PD16-69B | PD17-89A | PD17-89C | PD16-07A |
|---|---|---|---|---|---|---|---|
| Rocha | Granodiorito | Granodiorito | Trondjhemito | Granodiorito | Granodiorito | Granodiorito | Granodiorito |
| Região | Divinópolis | Divinópolis | Pará de Minas | Itaúna | Pará de Minas | Pará de Minas | Itapecerica |
| Observação | Grt | Grt | | | Mais máfico | Mais félsico | |
| $SiO_2$ | 69.84 | 73.72 | 76.30 | 72.57 | 68.53 | 73.94 | 74.61 |
| $TiO_2$ | 0.17 | 0.22 | 0.11 | 0.18 | 0.45 | 0.22 | 0.23 |
| $Al_2O_3$ | 16.72 | 14.35 | 13.37 | 14.13 | 15.54 | 13.91 | 13.29 |
| $FeO^t$ | 1.21 | 1.47 | 0.67 | 1.69 | 3.11 | 1.34 | 1.49 |
| MnO | 0.03 | 0.04 | 0.01 | 0.01 | 0.04 | 0.01 | 0.03 |
| MgO | 0.46 | 0.68 | 0.15 | 0.46 | 1.05 | 0.32 | 0.34 |
| CaO | 2.15 | 1.84 | 1.06 | 1.55 | 2.88 | 1.58 | 1.18 |
| $Na_2O$ | 5.57 | 4.66 | 3.91 | 4.22 | 4.87 | 3.81 | 3.50 |
| $K_2O$ | 2.72 | 2.39 | 4.20 | 4.14 | 2.20 | 4.18 | 4.85 |
| $P_2O_5$ | 0.04 | 0.04 | 0.04 | 0.07 | 0.16 | 0.05 | 0.05 |
| LOI | 0.60 | 0.68 | 0.44 | 0.60 | 0.46 | 0.57 | 0.27 |
| **Total** | **99.52** | **100.08** | **100.25** | **99.62** | **99.28** | **99.93** | **99.83** |
| Co | | 2.82 | 0.35 | 2.50 | | | 1.85 |
| Ni | 2 | 2.13 | LD | 1.16 | 3 | 3 | 2.47 |
| Cu | 1 | 2.62 | 0.94 | 0.59 | 1 | 1 | 3.41 |
| Zn | 27 | 30.31 | 24.47 | 41.67 | 47 | 34 | 32.40 |
| Rb | 64 | 59.67 | 111.60 | 78.88 | 75 | 80 | 170.65 |
| Sr | 264 | 226.04 | 155.06 | 243.98 | 165 | 156 | 83.24 |
| Ba | 639 | 588.78 | 868.71 | 1220.49 | 693 | 814 | 621.26 |
| Pb | 35 | 29.92 | 44.27 | 23.00 | 17.50 | 19.50 | 31.05 |
| Th | 7.10 | 6.03 | 8.25 | 29.33 | | | 24.04 |
| U | | 0.87 | 3.55 | 1.09 | | | 2.11 |
| Nb | 6.40 | 5.96 | 4.87 | 7.52 | 9.60 | 7.50 | 8.41 |
| Ta | | 0.26 | 0.39 | 0.39 | | | 0.41 |
| Zr | 77 | 107.87 | 94.74 | 194.12 | 211 | 118 | 158.11 |
| Hf | | 3.65 | 3.50 | 5.86 | | | 5.09 |
| Cr | 20.40 | 18.20 | 20.57 | 6.98 | 27.40 | 25.40 | 24.73 |
| Sc | 4 | 2.97 | 0.98 | 2.08 | | | 5.08 |
| V | 14.70 | 14.11 | 7.02 | 12.55 | 16.30 | 11.80 | 14.63 |
| Mo | | 0.39 | 0.10 | 0.12 | | | 0.23 |
| Ga | 21.60 | 18.22 | 15.88 | 18.76 | 19.50 | 19.20 | 17.19 |
| Y | 6 | 9.07 | 18.12 | 14.20 | 14 | 9 | 18.90 |
| La | 13 | 17.72 | 16.13 | 110.98 | | | 50.70 |
| Ce | 13 | 27.86 | 30.29 | 218.67 | | | 101.57 |
| Pr | | 3.07 | 2.96 | 22.79 | | | 9.95 |
| Nd | 13 | 10.13 | 11.15 | 83.85 | | | 35.57 |
| Sm | | 1.77 | 2.27 | 13.67 | | | 5.81 |
| Eu | | 0.68 | 0.55 | 1.47 | | | 0.76 |
| Gd | | 1.44 | 2.45 | 10.01 | | | 4.97 |
| Tb | | 0.20 | 0.44 | 1.06 | | | 0.70 |
| Dy | | 1.34 | 3 | 4.25 | | | 3.73 |
| Ho | | 0.33 | 0.62 | 0.63 | | | 0.71 |
| Er | | 1.23 | 1.84 | 1.43 | | | 1.87 |
| Tm | | 0.22 | 0.26 | 0.16 | | | 0.26 |
| Yb | | 1.64 | 1.66 | 0.93 | | | 1.61 |
| Lu | | 0.26 | 0.23 | 0.14 | | | 0.23 |

| Amostra | PD16-07D | PD16-02D | PD16-82B | PD16-82D | PD17-101A | PD17-101B | PD17-101C |
|---|---|---|---|---|---|---|---|
| Rocha | Migmatito | Granodiorito | Migmatito | Migmatito | Migmatito | Migmatito | Migmatito |
| Região | Itapecerica | Cláudio | Cláudio | Cláudio | Marilândia | Marilândia | Marilândia |
| Observação | | | Leucossoma | Melanossoma | | | |
| $SiO_2$ | 74.40 | 72.82 | 67.33 | 49.57 | 72.70 | 71.66 | 72.34 |
| $TiO_2$ | 0.21 | 0.30 | 0.02 | 2.26 | 0.21 | 0.47 | 0.37 |
| $Al_2O_3$ | 13.38 | 14.12 | 19.39 | 12.05 | 14.12 | 13.26 | 13.69 |
| $FeO^t$ | 1.38 | 1.91 | 0.32 | 16.74 | 1.49 | 1.97 | 2.18 |
| MnO | 0.02 | 0.04 | 0.01 | 0.25 | 0.03 | 0.02 | 0.03 |
| MgO | 0.28 | 0.52 | 0.06 | 4.39 | 0.37 | 0.45 | 0.62 |
| CaO | 1.11 | 1.95 | 3.06 | 8.43 | 1.44 | 1.36 | 1.43 |
| $Na_2O$ | 3.46 | 3.71 | 6.70 | 2.68 | 3.78 | 3.10 | 4.28 |
| $K_2O$ | 5.01 | 3.91 | 2.67 | 1.26 | 4.93 | 5.32 | 4.25 |
| $P_2O_5$ | 0.04 | 0.08 | 0.03 | 0.23 | 0.06 | 0.09 | 0.09 |
| LOI | 0.28 | 0.49 | 0.62 | 0.21 | 0.39 | 0.62 | 0.37 |
| **Total** | **99.58** | **99.84** | **100.21** | **98.07** | **99.51** | **98.32** | **99.65** |
| Co | | 2.73 | | 54.06 | | 2.96 | |
| Ni | 2 | 3.16 | | 51.96 | 3 | 2.44 | 6.60 |
| Cu | 1 | 1.62 | 16.58 | 396.55 | 1 | 4.84 | 9.60 |
| Zn | 31 | 37.08 | 34.33 | 138.54 | 39 | 26.25 | 55 |
| Rb | 148 | 83.20 | 58.39 | 28.60 | 164 | 140.72 | 185 |
| Sr | 80 | 96.52 | 160.31 | 82.63 | 125 | 68.32 | 113 |
| Ba | 547 | 757.78 | 313.51 | 58.79 | 777 | 841.25 | 910 |
| Pb | 36 | 19.35 | 35.01 | 10.15 | 33 | 17.83 | 24.80 |
| Th | 26.80 | 16.95 | 19.29 | 0.79 | | 31.89 | |
| U | | 1.05 | 12.35 | 1.30 | | 0.65 | |
| Nb | 9.20 | 7.44 | 0.67 | 6.53 | 12 | 11.71 | 20.20 |
| Ta | | 0.33 | 0.08 | 0.77 | | 0.33 | |
| Zr | 152 | 250.78 | 18.64 | 100.46 | 134 | 464.24 | 312 |
| Hf | | 6.90 | 0.74 | 3.43 | | 13.20 | |
| Cr | 82 | 18.49 | 6.48 | 30.15 | 18.60 | 11.47 | 64 |
| Sc | 3 | 1.86 | LD | 37.26 | | 2.36 | |
| V | 10.70 | 19.32 | 4.08 | 351.14 | 13.30 | 29.55 | 37 |
| Mo | | 0.12 | 0.15 | 0.44 | | 1.97 | |
| Ga | 19.50 | 17.21 | 22.71 | 19.17 | 19.70 | 16.58 | 18.10 |
| Y | 20.10 | 14.70 | 8.08 | 45.43 | 12.40 | 15.30 | 22 |
| La | 59 | 41.08 | 33.69 | 7.81 | | 107.03 | |
| Ce | 99 | 49.66 | 65.26 | 20.14 | | 176.40 | |
| Pr | | 7.88 | 6.63 | 2.98 | | 21.52 | |
| Nd | 35 | 28.46 | 24.54 | 15.83 | | 69.67 | |
| Sm | | 4.65 | 4.37 | 5.04 | | 10.03 | |
| Eu | | 0.89 | 0.82 | 1.65 | | 0.70 | |
| Gd | | 3.83 | 3.56 | 6.40 | | 7.73 | |
| Tb | | 0.52 | 0.46 | 1.24 | | 0.84 | |
| Dy | | 2.91 | 2.21 | 8.71 | | 3.84 | |
| Ho | | 0.59 | 0.34 | 1.83 | | 0.64 | |
| Er | | 1.75 | 0.84 | 5.35 | | 1.68 | |
| Tm | | 0.24 | 0.09 | 0.82 | | 0.21 | |
| Yb | | 1.54 | 0.57 | 5.49 | | 1.22 | |
| Lu | | 0.23 | 0.07 | 0.83 | | 0.18 | |

| Amostra | PD17-101D | PD17-101D2 | PD17-101E | PD17-101P | PD17-101X | PD16-18 | PD16-23 |
|---|---|---|---|---|---|---|---|
| **Rocha** | Migmatito | Migmatito | Migmatito | Migmatito | Enclave | Granito | Granito |
| **Região** | Marilândia | Marilândia | Marilândia | Marilândia | Marilândia | Formiga | Formiga |
| **Observação** | Granodiorio | Granodiorito | Mais máfico | Melanossoma | Ultramáfica | | |
| **$SiO_2$** | 71.55 | 70.14 | 67.45 | 57.21 | 51.30 | 73.93 | 75.17 |
| **$TiO_2$** | 0.38 | 0.34 | 0.71 | 1.65 | 0.82 | 0.30 | 0.15 |
| **$Al_2O_3$** | 14.77 | 15.73 | 15.30 | 14.10 | 3.37 | 13.27 | 13.45 |
| **$FeO^t$** | 2.52 | 1.96 | 4.30 | 9.39 | 10.00 | 2.01 | 1.14 |
| **MnO** | 0.04 | 0.03 | 0.07 | 0.15 | 0.26 | 0.02 | 0.02 |
| **MgO** | 0.62 | 0.57 | 1.18 | 3.49 | 14.64 | 0.42 | 0.16 |
| **CaO** | 2.44 | 3.07 | 3.04 | 5.99 | 15.66 | 1.28 | 0.93 |
| **$Na_2O$** | 4.69 | 5.21 | 4.69 | 3.60 | 0.74 | 3.25 | 3.34 |
| **$K_2O$** | 2.32 | 1.45 | 1.87 | 1.73 | 0.71 | 4.92 | 5.49 |
| **$P_2O_5$** | 0.09 | 0.10 | 0.21 | 0.40 | 0.19 | 0.06 | 0.04 |
| **LOI** | 0.29 | 0.50 | 0.38 | 0.69 | 0.53 | 0.33 | 0.23 |
| **Total** | **99.70** | **99.10** | **99.19** | **98.39** | **98.21** | **99.79** | **100.11** |
| **Co** | | | 7.72 | | | | 0.64 |
| **Ni** | 3 | 3 | 8.64 | 38 | 352 | 2 | 0.58 |
| **Cu** | 1 | 1 | 5.76 | 186 | 8.40 | 1 | 0.89 |
| **Zn** | 62 | 50 | 98.38 | 169 | 179 | 47 | 12.60 |
| **Rb** | 99 | 63 | 94.58 | 80 | 34 | 128 | 185.92 |
| **Sr** | 132 | 205 | 138.45 | 217 | 17.80 | 123 | 47.41 |
| **Ba** | 295 | 259 | 276.53 | 365 | 42 | 691 | 609 |
| **Pb** | 18.20 | 16.90 | 13.66 | 14.50 | 8.30 | 44 | 24.15 |
| **Th** | | | 11.70 | | | 65 | 16.34 |
| **U** | | | 1.95 | | | | 3.65 |
| **Nb** | 16.40 | 15.30 | 23.46 | 19.80 | 7.80 | 8.20 | 9.97 |
| **Ta** | | | 1.18 | | | | 0.74 |
| **Zr** | 176 | 183.00 | 292.66 | 220 | 60 | 205 | 111.91 |
| **Hf** | | | 7.98 | | | | 4.03 |
| **Cr** | 20 | 15.90 | 23.49 | 69 | 2045 | 28.60 | 12.78 |
| **Sc** | | | 10.99 | | | 4 | 1.11 |
| **V** | 22.10 | 16.00 | 48.63 | 146 | 145 | 16.90 | 6.97 |
| **Mo** | | | 1.65 | | | | 0.11 |
| **Ga** | 22.50 | 22.00 | 23.89 | 16.80 | 8.90 | 16.80 | 16.63 |
| **Y** | 13.00 | 11.70 | 35.93 | 45 | 34 | 29.90 | 20.53 |
| **La** | | | 47.16 | | | 144 | 28.27 |
| **Ce** | | | 81.22 | | | 330 | 38.53 |
| **Pr** | | | 9.87 | | | | 6.18 |
| **Nd** | | | 35.82 | | | 115 | 20.87 |
| **Sm** | | | 7.87 | | | | 4.11 |
| **Eu** | | | 1.10 | | | | 0.33 |
| **Gd** | | | 8.55 | | | | 3.76 |
| **Tb** | | | 1.44 | | | | 0.58 |
| **Dy** | | | 8.58 | | | | 3.50 |
| **Ho** | | | 1.55 | | | | 0.74 |
| **Er** | | | 3.80 | | | | 2.30 |
| **Tm** | | | 0.43 | | | | 0.33 |
| **Yb** | | | 2.20 | | | | 2.11 |
| **Lu** | | | 0.26 | | | | 0.31 |

| Amostra | PD16-28 | PD16-44 | PD17-87B | PD17-92 | PD16-04A | PD16-04B |
|---|---|---|---|---|---|---|
| Rocha | Granito | Granito | Granito | Granito | Trondhjemito | Trondhjemito |
| Região | Formiga | Bom Despacho | Pará de Minas | Divinópolis | Divinópolis | Divinópolis |
| Observação | Tit | | | | Mais máfica | Mais félsica |
| $SiO_2$ | 71.86 | 74.58 | 73.71 | 71.42 | 68.68 | 70.99 |
| $TiO_2$ | 0.51 | 0.11 | 0.19 | 0.36 | 0.51 | 0.37 |
| $Al_2O_3$ | 13.45 | 13.42 | 13.68 | 14.54 | 14.63 | 15.05 |
| $FeO^t$ | 2.78 | 1.11 | 1.42 | 2.32 | 4.21 | 2.37 |
| MnO | 0.03 | 0.02 | 0.02 | 0.03 | 0.04 | 0.02 |
| MgO | 0.69 | 0.15 | 0.28 | 0.71 | 1.07 | 0.71 |
| CaO | 1.66 | 0.89 | 1.19 | 2.43 | 2.76 | 2.40 |
| $Na_2O$ | 3.19 | 4.19 | 3.49 | 4.22 | 5.40 | 4.28 |
| $K_2O$ | 4.98 | 4.81 | 4.68 | 2.89 | 1.44 | 3.21 |
| $P_2O_5$ | 0.12 | 0.03 | 0.05 | 0.11 | 0.16 | 0.11 |
| LOI | 0.61 | 0.48 | 0.59 | 0.46 | 0.49 | 0.42 |
| **Total** | **99.88** | **99.79** | **99.29** | **99.49** | **99.38** | **99.93** |
| Co | 4.05 | | | 4.47 | 7.06 | |
| Ni | 4.97 | 3 | 3 | 4.47 | 6.48 | 2 |
| Cu | 1.27 | 1 | 1 | 2.50 | 6.69 | 1.60 |
| Zn | 55.66 | 37 | 33 | 50.82 | 98.41 | 53 |
| Rb | 147.20 | 154 | 93 | 84.34 | 47.07 | 66 |
| Sr | 130.89 | 132 | 151.00 | 179.88 | 239.65 | 300 |
| Ba | 968.60 | 610 | 824 | 670.43 | 326.64 | 859 |
| Pb | 25.07 | 43 | 25.50 | 16.14 | 11.85 | 17 |
| Th | 30.51 | | | 16.75 | 9.54 | 13.70 |
| U | 1.66 | | | 1.10 | 0.53 | |
| Nb | 19.41 | 7.50 | 8 | 15.41 | 12.41 | 9.70 |
| Ta | 1.06 | | | 0.54 | 0.46 | |
| Zr | 481.66 | 109 | 149 | 243.39 | 305.41 | 220 |
| Hf | 13.31 | | | 7.35 | 7.67 | |
| Cr | 21.90 | 16.40 | 15 | 15.95 | 31.76 | 22.30 |
| Sc | 4.07 | | | 4.44 | 4.56 | 4 |
| V | 24.09 | 7 | 10.30 | 27.91 | 52.05 | 29.60 |
| Mo | 4.48 | | | 0.22 | 0.45 | |
| Ga | 16.55 | 20.20 | 16.90 | 20.49 | 22.68 | 20.10 |
| Y | 63.71 | 51.00 | 8.20 | 18.33 | 17.78 | 12.90 |
| La | 111.97 | | | 52.76 | 66.13 | 56 |
| Ce | 226 | | | 94.11 | 129.72 | 103 |
| Pr | 23.09 | | | 12.05 | 13.21 | |
| Nd | 84.30 | | | 43.04 | 47.83 | 40 |
| Sm | 15.28 | | | 8.26 | 8.19 | |
| Eu | 1.44 | | | 1.20 | 1.13 | |
| Gd | 14.21 | | | 7.15 | 6.95 | |
| Tb | 2.22 | | | 0.92 | 0.87 | |
| Dy | 13.13 | | | 4.60 | 4.36 | |
| Ho | 2.45 | | | 0.75 | 0.72 | |
| Er | 6.43 | | | 1.88 | 1.71 | |
| Tm | 0.80 | | | 0.22 | 0.20 | |
| Yb | 4.66 | | | 1.28 | 1.17 | |
| Lu | 0.63 | | | 0.18 | 0.16 | |

| Amostra | PD16-30A | PD16-30B | PD16-39 | PD16-39B | PD17-91A | PD17-91C |
|---|---|---|---|---|---|---|
| Rocha | Trondhjemito | Trondhjemito | Trondhjemito | Trondhjemito | Granodiorito | Trondhjemito |
| Região | Divinópolis | Divinópolis | Pará de Minas | Pará de Minas | Divinópolis | Divinópolis |
| Observação | Mais máfica | | | | | |
| $SiO_2$ | 67.18 | 71.35 | 73.99 | 72.54 | 74.86 | 70.81 |
| $TiO_2$ | 0.46 | 0.28 | 0.14 | 0.24 | 0.23 | 0.41 |
| $Al_2O_3$ | 14.09 | 14.63 | 14.31 | 14.20 | 13.13 | 14.23 |
| $FeO^t$ | 4.27 | 1.96 | 1.08 | 1.82 | 1.53 | 2.71 |
| MnO | 0.07 | 0.03 | 0.01 | 0.02 | 0.02 | 0.03 |
| MgO | 2.29 | 0.70 | 0.25 | 0.46 | 0.37 | 0.76 |
| CaO | 2.91 | 2.12 | 1.56 | 1.93 | 1.46 | 1.97 |
| $Na_2O$ | 4.89 | 4.34 | 3.85 | 4.02 | 3.48 | 4.05 |
| $K_2O$ | 2.13 | 3.35 | 4.58 | 3.55 | 4.31 | 3.70 |
| $P_2O_5$ | 0.11 | 0.10 | 0.04 | 0.08 | 0.05 | 0.11 |
| LOI | 0.98 | 0.53 | 0.55 | 0.68 | 0.42 | 0.58 |
| **Total** | **99.38** | **99.38** | **100.35** | **99.53** | **99.85** | **99.37** |
| Co | | | 13.30 | | | |
| Ni | 33 | 4.80 | 2 | 3 | 3 | 3.40 |
| Cu | 27.70 | 6.80 | 1 | 1 | 1 | 1.60 |
| Zn | 89 | 44 | 24.60 | 41 | 33 | 55 |
| Rb | 93 | 114 | 90 | 68 | 122 | 109 |
| Sr | 304 | 375 | 182 | 191 | 100 | 150 |
| Ba | 607 | 1164.00 | 943 | 913 | 465 | 499 |
| Pb | 17.30 | 20.70 | 22.40 | 19.50 | 21.60 | 22.20 |
| Th | | | 17 | | | |
| U | | | | | | |
| Nb | 18.10 | 10.50 | 7.60 | 10.10 | 9 | 11.40 |
| Ta | | | | | | |
| Zr | 158 | 137 | 108.00 | 169 | 126 | 285 |
| Hf | | | | | | |
| Cr | 75 | 54 | | 22.20 | 25.60 | 36 |
| Sc | | | 3.00 | | | |
| V | 65 | 23.10 | 9.00 | 13.10 | 14.70 | 26.70 |
| Mo | | | | | | |
| Ga | 20 | 19.80 | 18.70 | 19.60 | 18.40 | 20.20 |
| Y | 34 | 11.40 | 9.10 | 12.30 | 9.00 | 13.80 |
| La | | | 31 | | | |
| Ce | | | 56 | | | |
| Pr | | | | | | |
| Nd | | | 21 | | | |
| Sm | | | | | | |
| Eu | | | | | | |
| Gd | | | | | | |
| Tb | | | | | | |
| Dy | | | | | | |
| Ho | | | | | | |
| Er | | | | | | |
| Tm | | | | | | |
| Yb | | | | | | |
| Lu | | | | | | |

| Amostra | PD17-91D | PD17-94 | PD17-102 | PD16-71A | PD16-71B | PD16-71D | PD17-97A |
|---|---|---|---|---|---|---|---|
| Rocha | Trondhjemito | Trondhjemito | Tonalito | Migmatito | Migmatito | Migmatito | Migmatito |
| Região | Divinópolis | Divinópolis | Divinópolis | Itaúna | Itaúna | Itaúna | Pará Minas |
| Observação | | | Hbl | Leucossoma | Trondhjemito | Melanossoma | Trondhjemito |
| $SiO_2$ | 71.84 | 70.79 | 68.66 | 76.75 | 67.38 | 61.45 | 71.82 |
| $TiO_2$ | 0.26 | 0.32 | 0.45 | 0.07 | 0.40 | 0.75 | 0.36 |
| $Al_2O_3$ | 14.79 | 15.12 | 15.56 | 12.17 | 15.67 | 15.69 | 14.36 |
| $FeO^t$ | 1.96 | 1.92 | 3.09 | 0.55 | 2.66 | 5.55 | 2.01 |
| MnO | 0.03 | 0.02 | 0.04 | 0.00 | 0.04 | 0.10 | 0.02 |
| MgO | 0.57 | 1.00 | 1.03 | 0.32 | 1.98 | 3.12 | 0.64 |
| CaO | 2.44 | 2.81 | 2.86 | 0.49 | 2.26 | 5.03 | 1.62 |
| $Na_2O$ | 4.77 | 4.73 | 4.80 | 1.97 | 5.67 | 4.31 | 4.24 |
| $K_2O$ | 2.27 | 2.04 | 2.21 | 7.12 | 1.89 | 2.24 | 3.79 |
| $P_2O_5$ | 0.07 | 0.10 | 0.15 | 0.05 | 0.19 | 0.35 | 0.12 |
| LOI | 0.49 | 0.50 | 0.50 | 0.42 | 1.44 | 0.72 | 0.50 |
| **Total** | **99.49** | **99.36** | **99.36** | **99.91** | **99.58** | **99.31** | **99.49** |
| Co | | | 5.83 | 1.03 | 7.88 | 16.45 | 3.26 |
| Ni | 3 | 9.90 | 6.07 | 1.80 | 14.92 | 23.02 | 6.36 |
| Cu | 1.60 | 5.60 | 23.76 | 1.44 | 3.43 | 15.33 | 2.84 |
| Zn | 45 | 42 | 55.70 | 12.60 | 65.37 | 86.75 | 43.60 |
| Rb | 67 | 69 | 48.97 | 144.12 | 101.89 | 80.04 | 116.91 |
| Sr | 403 | 541 | 266.47 | 411.34 | 456.39 | 470.89 | 149.78 |
| Ba | 570 | 758 | 520.98 | 2150.58 | 608 | 592.17 | 787.37 |
| Pb | 16.80 | 12.90 | 9.95 | 24.59 | 10.12 | 14.74 | 30.36 |
| Th | | | 9.74 | 1.71 | 5.58 | 5.03 | 27.54 |
| U | | | 0.42 | 0.93 | 1.29 | 4.91 | 2.25 |
| Nb | 9.90 | 8.30 | 10.07 | 0.97 | 7.03 | 8.06 | 13.66 |
| Ta | | | 0.29 | 0.12 | 0.71 | 1.37 | 0.40 |
| Zr | 144 | 147 | 231.07 | 27.56 | 158.37 | 149.30 | 261.72 |
| Hf | | | 6.85 | 1.04 | 4.52 | 4.45 | 8.25 |
| Cr | 41 | 85 | 15.32 | 21.95 | 38.62 | 62.99 | 22.82 |
| Sc | | | 5.62 | 0.01 | 4.11 | 11.03 | 3.03 |
| V | 17.50 | 24.70 | 40.01 | 10.36 | 38.52 | 81.41 | 26.03 |
| Mo | | | 0.21 | 0.08 | 0.19 | 0.26 | 0.33 |
| Ga | 20.40 | 19.90 | 20.51 | 10.39 | 19.52 | 17.45 | 21.83 |
| Y | 10.80 | 12.10 | 15.28 | 4.18 | 13.78 | 23.54 | 33.40 |
| La | | | 43.34 | 4.59 | 23.98 | 20.17 | 52.94 |
| Ce | | | 58.06 | 8.80 | 45.29 | 43.87 | 103.45 |
| Pr | | | 9.02 | 0.94 | 4.80 | 5.20 | 12.76 |
| Nd | | | 30.44 | 3.99 | 18.73 | 22.87 | 46.84 |
| Sm | | | 5.30 | 0.86 | 3.57 | 5.05 | 10.36 |
| Eu | | | 0.97 | 0.81 | 0.86 | 1.39 | 0.76 |
| Gd | | | 4.80 | 0.87 | 3.10 | 4.86 | 9.40 |
| Tb | | | 0.67 | 0.13 | 0.47 | 0.76 | 1.41 |
| Dy | | | 3.47 | 0.75 | 2.76 | 4.67 | 7.76 |
| Ho | | | 0.63 | 0.14 | 0.52 | 0.90 | 1.32 |
| Er | | | 1.57 | 0.41 | 1.43 | 2.52 | 3.48 |
| Tm | | | 0.19 | 0.05 | 0.21 | 0.38 | 0.46 |
| Yb | | | 1.10 | 0.37 | 1.33 | 2.59 | 2.83 |
| Lu | | | 0.15 | 0.05 | 0.18 | 0.37 | 0.41 |

| Amostra | PD16-51A | PD16-51B | PD17-97C | PD16-64A | PD16-29 | PD17-98 |
|---|---|---|---|---|---|---|
| Rocha | Trondjhemito | Trondjhemito | Trondjhemito | Tonalito | Trondjhemito | Granito |
| Região | Bom Despacho | Bom Despacho | Pará Minas | Divinópolis | Divinópolis | Formiga |
| Observação | | | Mais félsico | Hbl | | Hbl |
| $SiO_2$ | 70.23 | 67.57 | 73.70 | 63.94 | 73.03 | 68.42 |
| $TiO_2$ | 0.34 | 0.43 | 0.25 | 0.92 | 0.24 | 0.49 |
| $Al_2O_3$ | 15.44 | 16.56 | 13.87 | 15.73 | 14.37 | 15.71 |
| $FeO^t$ | 2.43 | 2.89 | 1.35 | 5.35 | 1.57 | 3.16 |
| MnO | 0.03 | 0.04 | 0.02 | 0.09 | 0.02 | 0.04 |
| MgO | 0.76 | 1.01 | 0.45 | 1.86 | 0.46 | 1.06 |
| CaO | 2.45 | 3.07 | 1.31 | 4.25 | 2.03 | 2.99 |
| $Na_2O$ | 4.58 | 5.45 | 3.90 | 4.43 | 4.21 | 4.80 |
| $K_2O$ | 2.80 | 1.47 | 4.43 | 2.08 | 3.20 | 2.21 |
| $P_2O_5$ | 0.12 | 0.13 | 0.07 | 0.34 | 0.07 | 0.17 |
| LOI | 0.67 | 0.82 | 0.33 | 0.83 | 0.47 | 0.54 |
| **Total** | **99.85** | **99.43** | **99.67** | **99.82** | **99.68** | **99.60** |
| Co | | 5.26 | | 11.52 | | |
| Ni | 2 | 4.59 | 3 | 10.41 | 2 | 5 |
| Cu | 1.10 | 2.07 | 4.60 | 21.14 | 1 | 1 |
| Zn | 54 | 69.28 | 31 | 88.50 | 35 | 66 |
| Rb | 80 | 69.41 | 131 | 66.19 | 76 | 69 |
| Sr | 315 | 326.48 | 161 | 491.24 | 250 | 390 |
| Ba | 796 | 319.71 | 994 | 854.84 | 756 | 602 |
| Pb | 16.80 | 12.45 | 35 | 17.62 | 19.10 | 17.30 |
| Th | 16.80 | 5.12 | | 11.09 | 17.20 | |
| U | | 0.86 | | 2.06 | | |
| Nb | 11 | 14.06 | 12.10 | 14.63 | 7.40 | 10.50 |
| Ta | | 0.65 | | 1.81 | | |
| Zr | 225 | 170.21 | 154 | 346.87 | 156 | 160 |
| Hf | | 4.79 | | 8.91 | | |
| Cr | 26.70 | 15.66 | 32 | 29.95 | 19.50 | 55 |
| Sc | 3 | 3.93 | | 10.29 | 3 | |
| V | 26.60 | 24.59 | 17.60 | 57.29 | 16.40 | 47 |
| Mo | | 0.37 | | 0.69 | | |
| Ga | 20.30 | 22.73 | 18.30 | 19.61 | 18.40 | 21.70 |
| Y | 14.40 | 11.59 | 27.10 | 36.04 | 8.60 | 13.90 |
| La | 45 | 22.67 | | 56.10 | 23 | |
| Ce | 83 | 44.97 | | 111.48 | 50 | |
| Pr | | 4.83 | | 12.28 | | |
| Nd | 38 | 18.45 | | 49.24 | 19 | |
| Sm | | 3.66 | | 9.48 | | |
| Eu | | 1.01 | | 2.14 | | |
| Gd | | 3.45 | | 8.34 | | |
| Tb | | 0.49 | | 1.21 | | |
| Dy | | 2.59 | | 7.00 | | |
| Ho | | 0.46 | | 1.36 | | |
| Er | | 1.16 | | 3.93 | | |
| Tm | | 0.15 | | 0.59 | | |
| Yb | | 0.86 | | 3.92 | | |
| Lu | | 0.12 | | 0.58 | | |

# APÊNDICE B

**Table 2:** Resultados U-Pb para as onze amostras de zircão e monazita datadas.

| Amostra 71D | | | | | | | | | | | | | | | | | | | |
|---|---|---|---|---|---|---|---|---|---|---|---|---|---|---|---|---|---|---|---|
| **Zircão** | ***f*206** | **(μg.g$^{-1}$)** | | | | | **Razão isotópica** | | | | | | | **Idade (Ma)** | | | | | | **Conc** |
| **spot** | **(%)** | **U** | **Th** | **Pb** | **Th/U** | **$^{206}$Pb/$^{204}$Pb** | **$^{207}$Pb/$^{206}$U** | **2σ** | **$^{207}$Pb/$^{235}$U** | **2σ** | **$^{206}$Pb/$^{238}$U** | **2σ** | **Rho** | **$^{207}$Pb/$^{206}$Pb** | **2σ** | **$^{206}$Pb/$^{238}$U** | **2σ** | **$^{207}$Pb/$^{235}$U** | **2σ** | **(%)** |
| 71D-5 | 0.02 | 233 | 163 | 228 | 0.70 | 109650 | 0.2044 | 0.0022 | 16.09 | 0.20 | 0.5685 | 0.0075 | 0.64 | 2870 | 10 | 2903 | 31 | 2884 | 12 | 101 |
| 71D-6 | 0.02 | 220 | 102 | 147 | 0.46 | 100000 | 0.2030 | 0.0019 | 15.67 | 0.19 | 0.5583 | 0.0074 | 0.73 | 2857 | 8 | 2862 | 31 | 2857 | 12 | 100 |
| 71D-8 | 0.03 | 208 | 21 | 18 | 0.10 | 73950 | 0.1852 | 0.0020 | 11.22 | 0.22 | 0.4360 | 0.0075 | 0.83 | 2702 | 11 | 2323 | 34 | 2534 | 19 | 86 |
| 71D-9 | 0.01 | 303 | 135 | 191 | 0.45 | 134500 | 0.2027 | 0.0017 | 15.69 | 0.15 | 0.5590 | 0.0062 | 0.68 | 2857 | 7 | 2860 | 26 | 2856 | 10 | 100 |
| 71D-4 | 0.03 | 146 | 93 | 139 | 0.64 | 68450 | 0.2039 | 0.0022 | 15.71 | 0.22 | 0.5587 | 0.0083 | 0.73 | 2866 | 9 | 2861 | 34 | 2859 | 13 | 100 |
| 71D-2 | 0.02 | 253 | 107 | 153 | 0.42 | 111750 | 0.1992 | 0.0022 | 14.86 | 0.22 | 0.5379 | 0.0090 | 0.76 | 2836 | 11 | 2771 | 38 | 2804 | 14 | 98 |
| 71D-10 | 0.02 | 210 | 65 | 97 | 0.31 | 89500 | 0.1889 | 0.0018 | 14.37 | 0.17 | 0.5499 | 0.0070 | 0.71 | 2740 | 10 | 2825 | 29 | 2775 | 11 | 103 |
| 71D-12b | 0.03 | 135 | 28 | 40 | 0.21 | 53550 | 0.1941 | 0.0022 | 14.54 | 0.18 | 0.5393 | 0.0072 | 0.61 | 2787 | 11 | 2782 | 30 | 2782 | 12 | 100 |
| 71D-12c | 0.02 | 287 | 215 | 325 | 0.75 | 115000 | 0.2006 | 0.0025 | 14.84 | 0.25 | 0.5310 | 0.0100 | 0.76 | 2830 | 12 | 2745 | 44 | 2801 | 16 | 97 |
| 71D-13 | 0.03 | 145 | 43 | 61 | 0.29 | 58250 | 0.2071 | 0.0021 | 16.33 | 0.22 | 0.5683 | 0.0082 | 0.74 | 2893 | 9 | 2900 | 34 | 2895 | 13 | 100 |
| 71D-15 | 0.02 | 255 | 153 | 150 | 0.60 | 77700 | 0.1935 | 0.0020 | 11.24 | 0.17 | 0.4211 | 0.0062 | 0.74 | 2779 | 11 | 2264 | 28 | 2540 | 14 | 81 |
| 71D-17 | 0.03 | 141 | 73 | 105 | 0.52 | 59900 | 0.2068 | 0.0021 | 16.98 | 0.19 | 0.5908 | 0.0076 | 0.68 | 2892 | 9 | 2986 | 31 | 2929 | 11 | 103 |
| 71D-19 | 0.05 | 98 | 38 | 58 | 0.39 | 38750 | 0.2089 | 0.0024 | 16.65 | 0.20 | 0.5719 | 0.0079 | 0.62 | 2902 | 11 | 2910 | 32 | 2914 | 11 | 100 |
| 71D-20 | 0.02 | 284 | 171 | 244 | 0.60 | 107000 | 0.2053 | 0.0034 | 15.45 | 0.29 | 0.5420 | 0.0120 | 0.70 | 2875 | 16 | 2786 | 51 | 2836 | 18 | 97 |
| 71D-24 | 0.02 | 325 | 141 | 198 | 0.43 | 118000 | 0.1988 | 0.0024 | 14.70 | 0.27 | 0.5310 | 0.0100 | 0.79 | 2826 | 11 | 2743 | 42 | 2798 | 18 | 97 |
| 71D-25 | 0.03 | 137 | 74 | 102 | 0.54 | 54700 | 0.2042 | 0.0027 | 16.28 | 0.24 | 0.5731 | 0.0097 | 0.65 | 2872 | 12 | 2919 | 39 | 2894 | 14 | 102 |
| 71D-26 | 0.02 | 219 | 96 | 135 | 0.44 | 76400 | 0.1936 | 0.0026 | 14.59 | 0.21 | 0.5416 | 0.0087 | 0.63 | 2782 | 13 | 2783 | 36 | 2787 | 14 | 100 |
| 71D-27 | 0.03 | 224 | 63 | 79 | 0.28 | 68450 | 0.1808 | 0.0020 | 11.51 | 0.19 | 0.4576 | 0.0080 | 0.80 | 2668 | 11 | 2424 | 36 | 2561 | 16 | 91 |
| 71D-28 | 0.01 | 334 | 231 | 252 | 0.69 | 126250 | 0.2021 | 0.0023 | 16.12 | 0.26 | 0.5660 | 0.0100 | 0.76 | 2858 | 11 | 2888 | 42 | 2886 | 15 | 101 |
| 71D-29 | 0.02 | 378 | 138 | 207 | 0.36 | 117500 | 0.1902 | 0.0026 | 12.92 | 0.24 | 0.4910 | 0.0100 | 0.74 | 2750 | 12 | 2566 | 44 | 2672 | 18 | 93 |

Amostra 71A

| Zircão | $f$206 | (μg.g$^{-1}$) | | | | | Razão isotópica | | | | | | | Idade (Ma) | | | | | | Conc |
|---|---|---|---|---|---|---|---|---|---|---|---|---|---|---|---|---|---|---|---|---|
| spot | (%) | U | Th | Pb | Th/U | $^{206}Pb/^{204}Pb$ | $^{207}Pb/^{206}U$ | 2σ | $^{207}Pb/^{235}U$ | 2σ | $^{206}Pb/^{238}U$ | 2σ | Rho | $^{207}Pb/^{206}Pb$ | 2σ | $^{206}Pb/^{238}U$ | 2σ | $^{207}Pb/^{235}U$ | 2σ | (%) |
| 71-1 | 0.07 | 137 | 90 | 95 | 0.65 | 27500 | 0.1916 | 0.0023 | 12.82 | 0.20 | 0.4743 | 0.0078 | 0.71 | 2762 | 11 | 2503 | 34 | 2664 | 15 | 91 |
| 71-2b | 0.17 | 57 | 25 | 23 | 0.44 | 10800 | 0.1906 | 0.0034 | 12.64 | 0.27 | 0.4692 | 0.0098 | 0.64 | 2774 | 18 | 2471 | 42 | 2646 | 20 | 89 |
| 71-4 | 0.10 | 96 | 61 | 72 | 0.64 | 19000 | 0.1870 | 0.0028 | 11.81 | 0.24 | 0.4547 | 0.0097 | 0.78 | 2722 | 14 | 2409 | 43 | 2579 | 20 | 89 |
| 71-5 | 0.06 | 143 | 97 | 108 | 0.68 | 33000 | 0.1891 | 0.0025 | 14.36 | 0.22 | 0.5407 | 0.0093 | 0.65 | 2742 | 12 | 2791 | 39 | 2772 | 14 | 102 |
| 71-6 | 0.08 | 136 | 147 | 111 | 1.08 | 22150 | 0.1648 | 0.0023 | 8.64 | 0.19 | 0.3741 | 0.0085 | 0.82 | 2533 | 14 | 2041 | 39 | 2291 | 20 | 81 |
| 71-7b | 0.11 | 93 | 55 | 51 | 0.59 | 17600 | 0.1842 | 0.0025 | 11.25 | 0.24 | 0.4336 | 0.0091 | 0.75 | 2707 | 14 | 2323 | 41 | 2543 | 19 | 86 |
| 71-8 | 0.10 | 111 | 145 | 151 | 1.30 | 19400 | 0.1800 | 0.0028 | 9.93 | 0.22 | 0.3983 | 0.0087 | 0.76 | 2662 | 14 | 2165 | 39 | 2421 | 20 | 81 |
| 71-9 | 0.06 | 129 | 102 | 113 | 0.79 | 29150 | 0.1935 | 0.0028 | 14.37 | 0.25 | 0.5383 | 0.0097 | 0.66 | 2769 | 13 | 2769 | 41 | 2773 | 16 | 100 |
| 71-13 | 0.06 | 144 | 61 | 62 | 0.42 | 29550 | 0.1855 | 0.0022 | 12.74 | 0.19 | 0.4966 | 0.0077 | 0.67 | 2709 | 10 | 2598 | 34 | 2657 | 14 | 96 |
| 71-15 | 16.73 | 75 | 54 | 433 | 0.72 | 112 | 0.2925 | 0.0078 | 27.40 | 1.10 | 0.6820 | 0.0160 | 0.86 | 3378 | 38 | 3313 | 61 | 3326 | 37 | 98 |
| 71-18 | 0.08 | 139 | 47 | 57 | 0.34 | 24000 | 0.1794 | 0.0023 | 10.55 | 0.19 | 0.4250 | 0.0083 | 0.78 | 2664 | 12 | 2272 | 37 | 2480 | 17 | 85 |
| 71-21b | 0.11 | 84 | 49 | 55 | 0.59 | 17100 | 0.1921 | 0.0024 | 14.21 | 0.22 | 0.5341 | 0.0080 | 0.64 | 2769 | 12 | 2758 | 34 | 2762 | 15 | 100 |
| 71-24b | 0.10 | 126 | 340 | 124 | 2.70 | 19550 | 0.1819 | 0.0024 | 10.10 | 0.17 | 0.3981 | 0.0073 | 0.67 | 2682 | 13 | 2161 | 34 | 2439 | 16 | 81 |
| 71-27 | 0.06 | 150 | 94 | 104 | 0.63 | 29050 | 0.1888 | 0.0031 | 13.87 | 0.23 | 0.5320 | 0.0100 | 0.62 | 2754 | 15 | 2741 | 44 | 2742 | 15 | 100 |
| 71-28b | 0.05 | 207 | 127 | 138 | 0.62 | 40500 | 0.1913 | 0.0023 | 14.30 | 0.20 | 0.5369 | 0.0086 | 0.70 | 2761 | 10 | 2770 | 36 | 2770 | 13 | 100 |
| 71-31b | 0.11 | 120 | 88 | 77 | 0.73 | 17600 | 0.1882 | 0.0025 | 10.99 | 0.20 | 0.4163 | 0.0079 | 0.75 | 2742 | 12 | 2245 | 36 | 2514 | 17 | 82 |
| 71-31c | 0.06 | 186 | 80 | 62 | 0.43 | 33200 | 0.1874 | 0.0021 | 12.39 | 0.20 | 0.4724 | 0.0080 | 0.78 | 2725 | 10 | 2493 | 35 | 2636 | 15 | 91 |
| 71-32 | 0.06 | 161 | 83 | 108 | 0.52 | 31700 | 0.1963 | 0.0023 | 14.44 | 0.25 | 0.5254 | 0.0094 | 0.80 | 2819 | 11 | 2718 | 40 | 2775 | 17 | 96 |
| 71-33 | 0.11 | 128 | 33 | 34 | 0.26 | 17350 | 0.1759 | 0.003 | 9.34 | 0.1 | 0.3795 | 0.006 | 0.6 | 2629 | 14 | 2068 | 29 | 2369 | 14 | 79 |
| 71-34b | 0.26 | 40 | 9 | 12 | 0.23 | 7150 | 0.1887 | 0.0072 | 11.99 | 0.42 | 0.4700 | 0.0160 | 0.72 | 2673 | 26 | 2492 | 72 | 2579 | 35 | 93 |
| 71-34c | 0.11 | 121 | 62 | 61 | 0.52 | 17550 | 0.1931 | 0.0028 | 10.90 | 0.24 | 0.4085 | 0.0092 | 0.76 | 2774 | 13 | 2206 | 43 | 2512 | 20 | 80 |

Amostra 30

| Zircão | $f$206 | (μg.g$^{-1}$) | | | | | Razão isotópica | | | | | | | Idade (Ma) | | | | | | Conc |
|---|---|---|---|---|---|---|---|---|---|---|---|---|---|---|---|---|---|---|---|---|
| spot | (%) | U | Th | Pb | Th/U | $^{206}Pb/^{204}Pb$ | $^{207}Pb/^{206}U$ | 2σ | $^{207}Pb/^{235}U$ | 2σ | $^{206}Pb/^{238}U$ | 2σ | Rho | $^{207}Pb/^{206}Pb$ | 2σ | $^{206}Pb/^{238}U$ | 2σ | $^{207}Pb/^{235}U$ | 2σ | (%) |
| 30-2 | 0.044 | 197 | 63 | 104 | 0.32 | 42 100 | 0.192 | 0.003 | 15.31 | 0.30 | 0.5560 | 0.0099 | 0.62 | 2778 | 17 | 2799 | 47 | 2798 | 17 | 101 |
| 30-3 | 0.113 | 86 | 28 | 34 | 0.32 | 16 535 | 0.183 | 0.003 | 12.20 | 0.18 | 0.4793 | 0.0074 | 0.54 | 2700 | 14 | 2523 | 32 | 2622 | 14 | 93 |
| 30-4 | 0.106 | 77 | 20 | 25 | 0.26 | 17 600 | 0.193 | 0.003 | 15.31 | 0.30 | 0.5560 | 0.0099 | 0.62 | 2782 | 16 | 2773 | 44 | 2780 | 18 | 100 |
| 30-6c | 0.046 | 197 | 63 | 81 | 0.32 | 40 550 | 0.179 | 0.002 | 12.24 | 0.19 | 0.4846 | 0.0079 | 0.74 | 2662 | 11 | 2551 | 34 | 2624 | 15 | 96 |
| 30-6b | 0.053 | 182 | 64 | 79 | 0.35 | 35 550 | 0.183 | 0.002 | 12.64 | 0.21 | 0.4931 | 0.0090 | 0.69 | 2699 | 13 | 2584 | 39 | 2654 | 16 | 96 |
| 30-7 | 0.063 | 152 | 43 | 52 | 0.28 | 29 700 | 0.182 | 0.002 | 12.34 | 0.16 | 0.4827 | 0.0065 | 0.64 | 2691 | 11 | 2535 | 28 | 2628 | 12 | 94 |
| 30-9b | 0.087 | 107 | 39 | 44 | 0.37 | 21 420 | 0.180 | 0.003 | 12.57 | 0.19 | 0.5022 | 0.0081 | 0.55 | 2660 | 14 | 2617 | 35 | 2646 | 14 | 98 |
| 30-9c | 0.066 | 144 | 62 | 74 | 0.43 | 28 300 | 0.183 | 0.002 | 12.91 | 0.17 | 0.5048 | 0.0067 | 0.58 | 2690 | 12 | 2634 | 28 | 2671 | 12 | 98 |
| 30-12 | 0.041 | 253 | 131 | 149 | 0.52 | 45 150 | 0.185 | 0.002 | 11.77 | 0.19 | 0.4569 | 0.0081 | 0.73 | 2713 | 11 | 2422 | 35 | 2584 | 15 | 89 |
| 30-13 | 0.061 | 142 | 59 | 74 | 0.41 | 30 885 | 0.191 | 0.003 | 15.31 | 0.30 | 0.5560 | 0.0099 | 0.62 | 2758 | 14 | 2760 | 42 | 2757 | 19 | 100 |
| 30-14 | 0.060 | 199 | 90 | 93 | 0.45 | 30 950 | 0.180 | 0.003 | 10.12 | 0.18 | 0.4003 | 0.0076 | 0.72 | 2664 | 13 | 2168 | 35 | 2444 | 16 | 81 |
| 30-15 | 0.034 | 282 | 72 | 90 | 0.25 | 55 000 | 0.188 | 0.003 | 13.01 | 0.21 | 0.4950 | 0.0093 | 0.67 | 2731 | 15 | 2583 | 40 | 2682 | 15 | 95 |
| 30-19 | 0.096 | 90.7 | 28 | 40 | 0.31 | 19 450 | 0.195 | 0.003 | 15.31 | 0.30 | 0.5560 | 0.0099 | 0.62 | 2798 | 15 | 2854 | 41 | 2832 | 18 | 102 |
| 30-21 | 0.046 | 207 | 74 | 123 | 0.36 | 40 500 | 0.184 | 0.003 | 13.03 | 0.28 | 0.5030 | 0.0110 | 0.72 | 2706 | 17 | 2636 | 47 | 2680 | 20 | 97 |
| 30-22b | 0.035 | 256 | 51 | 70 | 0.20 | 53 350 | 0.191 | 0.003 | 15.31 | 0.30 | 0.5560 | 0.0099 | 0.62 | 2763 | 13 | 2764 | 39 | 2766 | 14 | 100 |
| 30-24b | 0.131 | 67 | 26 | 31 | 0.38 | 14 310 | 0.195 | 0.003 | 15.31 | 0.30 | 0.5560 | 0.0099 | 0.62 | 2794 | 15 | 2757 | 44 | 2775 | 17 | 99 |
| 30-24 | 0.104 | 100 | 48 | 55 | 0.48 | 18 000 | 0.190 | 0.003 | 11.78 | 0.22 | 0.4475 | 0.0091 | 0.73 | 2764 | 15 | 2385 | 40 | 2582 | 18 | 86 |
| 30-26b | 0.030 | 311 | 189 | 233 | 0.61 | 63 150 | 0.195 | 0.003 | 15.31 | 0.30 | 0.5560 | 0.0099 | 0.62 | 2791 | 12 | 2776 | 36 | 2779 | 13 | 99 |
| 30-27 | 0.042 | 208 | 74 | 95 | 0.36 | 44 150 | 0.193 | 0.002 | 15.31 | 0.30 | 0.5560 | 0.0099 | 0.62 | 2778 | 11 | 2777 | 36 | 2782 | 13 | 100 |
| 30-28 | 0.049 | 236 | 126 | 133 | 0.53 | 37 950 | 0.176 | 0.002 | 10.25 | 0.15 | 0.4185 | 0.0070 | 0.72 | 2631 | 11 | 2254 | 32 | 2455 | 14 | 86 |
| 30-31b | 0.032 | 285 | 121 | 149 | 0.42 | 57 600 | 0.192 | 0.003 | 15.31 | 0.30 | 0.5560 | 0.0099 | 0.62 | 2770 | 11 | 2792 | 35 | 2782 | 13 | 101 |
| 30-33 | 0.061 | 143 | 46 | 60 | 0.32 | 30 800 | 0.195 | 0.003 | 15.31 | 0.30 | 0.5560 | 0.0099 | 0.62 | 2787 | 13 | 2800 | 43 | 2796 | 18 | 100 |
| 30-36 | 0.068 | 170 | 54 | 107 | 0.32 | 27 700 | 0.198 | 0.003 | 11.76 | 0.19 | 0.4284 | 0.0079 | 0.71 | 2806 | 14 | 2301 | 35 | 2578 | 15 | 82 |

| Amostra 89C | | | | | | | | | | | | | | | | | | | |
|---|---|---|---|---|---|---|---|---|---|---|---|---|---|---|---|---|---|---|---|
| **Zircão** | ***f*206** | **(μg.g$^{-1}$)** | | | | | **Razão isotópica** | | | | | | | **Idade (Ma)** | | | | | | **Conc** |
| **spot** | **(%)** | **U** | **Th** | **Pb** | **Th/U** | **$^{206}$Pb/$^{204}$Pb** | **$^{207}$Pb/$^{206}$U** | **2σ** | **$^{207}$Pb/$^{235}$U** | **2σ** | **$^{206}$Pb/$^{238}$U** | **2σ** | **Rho** | **$^{207}$Pb/$^{206}$Pb** | **2σ** | **$^{206}$Pb/$^{238}$U** | **2σ** | **$^{207}$Pb/$^{235}$U** | **2σ** | **(%)** |
| 89-2 | 0.08 | 113 | 81 | 91 | 0.72 | 23115 | 0.1871 | 0.0029 | 13.65 | 0.24 | 0.5184 | 0.0097 | 0.60 | 2733 | 15 | 2685 | 41 | 2723 | 17 | 98 |
| 89-3 | 0.05 | 332 | 255 | 171 | 0.77 | 36150 | 0.1544 | 0.0024 | 6.29 | 0.26 | 0.2861 | 0.0099 | 0.93 | 2406 | 17 | 1607 | 49 | 1961 | 35 | 67 |
| 89-4c | 0.08 | 220 | 59 | 53 | 0.27 | 23700 | 0.1582 | 0.0024 | 6.39 | 0.13 | 0.2894 | 0.0059 | 0.72 | 2451 | 14 | 1635 | 29 | 2025 | 18 | 67 |
| 89-4b | 0.04 | 314 | 75 | 72 | 0.24 | 45200 | 0.1682 | 0.0020 | 8.89 | 0.15 | 0.3776 | 0.0067 | 0.77 | 2549 | 10 | 2067 | 31 | 2322 | 15 | 81 |
| 89-8 | 0.05 | 275 | 150 | 127 | 0.54 | 37650 | 0.1707 | 0.0021 | 8.77 | 0.13 | 0.3668 | 0.0059 | 0.72 | 2581 | 11 | 2010 | 28 | 2312 | 14 | 78 |
| 89-11 | 0.05 | 220 | 25 | 32 | 0.12 | 40600 | 0.1838 | 0.0030 | 13.17 | 0.31 | 0.5110 | 0.0120 | 0.76 | 2700 | 17 | 2659 | 51 | 2693 | 22 | 98 |
| 89-12 | 0.06 | 265 | 87 | 56 | 0.33 | 29600 | 0.1678 | 0.0024 | 7.44 | 0.15 | 0.3141 | 0.0056 | 0.72 | 2551 | 15 | 1759 | 27 | 2162 | 18 | 69 |
| 89-13 | 0.08 | 205 | 100 | 93 | 0.49 | 23150 | 0.1591 | 0.0025 | 6.90 | 0.21 | 0.3055 | 0.0079 | 0.86 | 2482 | 18 | 1710 | 39 | 2087 | 28 | 69 |
| 89-14 | 0.06 | 161 | 95 | 121 | 0.59 | 32800 | 0.1862 | 0.0023 | 13.57 | 0.23 | 0.5267 | 0.0092 | 0.71 | 2720 | 12 | 2722 | 39 | 2722 | 16 | 100 |
| 89-16 | 0.05 | 373 | 261 | 152 | 0.70 | 36350 | 0.1566 | 0.0021 | 5.78 | 0.11 | 0.2637 | 0.0050 | 0.74 | 2435 | 14 | 1511 | 25 | 1945 | 16 | 62 |
| 89-17 | 0.05 | 212 | 104 | 117 | 0.49 | 40000 | 0.1834 | 0.0022 | 13.31 | 0.18 | 0.5200 | 0.0073 | 0.66 | 2702 | 10 | 2704 | 31 | 2701 | 12 | 100 |
| 89-21 | 0.04 | 235 | 137 | 152 | 0.58 | 45050 | 0.1902 | 0.0019 | 13.98 | 0.16 | 0.5313 | 0.0071 | 0.67 | 2745 | 10 | 2742 | 30 | 2746 | 11 | 100 |
| 89-22 | 0.06 | 221 | 105 | 104 | 0.47 | 33950 | 0.1790 | 0.0023 | 10.13 | 0.17 | 0.4086 | 0.0077 | 0.73 | 2653 | 11 | 2207 | 35 | 2445 | 16 | 83 |
| 89-23 | 0.02 | 329 | 184 | 255 | 0.56 | 78150 | 0.2622 | 0.0028 | 23.93 | 0.30 | 0.6554 | 0.0091 | 0.70 | 3268 | 10 | 3243 | 35 | 3266 | 12 | 99 |
| 89-25c | 0.07 | 139 | 118 | 143 | 0.85 | 28500 | 0.1874 | 0.0031 | 13.77 | 0.26 | 0.5301 | 0.0098 | 0.64 | 2729 | 15 | 2745 | 41 | 2745 | 18 | 101 |
| 89-25b | 0.03 | 387 | 253 | 298 | 0.65 | 73950 | 0.1846 | 0.0024 | 13.64 | 0.22 | 0.5232 | 0.0086 | 0.71 | 2710 | 11 | 2722 | 36 | 2720 | 15 | 100 |
| 89-27 | 0.07 | 163 | 72 | 86 | 0.44 | 26150 | 0.1722 | 0.0024 | 10.01 | 0.19 | 0.4229 | 0.0076 | 0.73 | 2584 | 14 | 2271 | 34 | 2430 | 18 | 88 |
| 89-28 | 0.05 | 288 | 60 | 69 | 0.21 | 36550 | 0.1640 | 0.0020 | 7.48 | 0.18 | 0.3252 | 0.0072 | 0.85 | 2505 | 13 | 1812 | 35 | 2157 | 22 | 72 |
| 89-29c | 0.05 | 236 | 90 | 85 | 0.38 | 35900 | 0.2230 | 0.0025 | 13.08 | 0.17 | 0.4236 | 0.0061 | 0.68 | 3004 | 10 | 2279 | 27 | 2687 | 12 | 76 |
| 89-29b | 0.08 | 246 | 154 | 96 | 0.63 | 23100 | 0.1529 | 0.0021 | 5.51 | 0.10 | 0.2559 | 0.0044 | 0.68 | 2387 | 14 | 1467 | 22 | 1899 | 15 | 61 |
| 89-33 | 0.05 | 179 | 75 | 88 | 0.42 | 34750 | 0.1896 | 0.0022 | 14.12 | 0.18 | 0.5343 | 0.0069 | 0.61 | 2755 | 10 | 2760 | 29 | 2756 | 12 | 100 |

Amostra 82A

| Zircão | $f$206 | (μg.g$^{-1}$) | | | | | Razão isotópica | | | | | | | Idade (Ma) | | | | | | Conc |
|---|---|---|---|---|---|---|---|---|---|---|---|---|---|---|---|---|---|---|---|---|
| spot | (%) | U | Th | Pb | Th/U | $^{206}Pb/^{204}Pb$ | $^{207}Pb/^{206}U$ | 2σ | $^{207}Pb/^{235}U$ | 2σ | $^{206}Pb/^{238}U$ | 2σ | Rho | $^{207}Pb/^{206}Pb$ | 2σ | $^{206}Pb/^{238}U$ | 2σ | $^{207}Pb/^{235}U$ | 2σ | (%) |
| 82-1 | 0.04 | 480 | 82 | 127 | 0.17 | 46100 | 0.124 | 0.002 | 2.59 | 0.06 | 0.1539 | 0.0037 | 0.77 | 2031 | 22 | 918 | 21 | 1279 | 17 | 45 |
| 82-2 | 0.02 | 747 | 393 | 312 | 0.53 | 97300 | 0.141 | 0.002 | 3.85 | 0.09 | 0.1994 | 0.0051 | 0.80 | 2256 | 17 | 1165 | 27 | 1583 | 18 | 52 |
| 82-5 | 0.02 | 349 | 125 | 230 | 0.36 | 104600 | 0.188 | 0.005 | 12.83 | 0.32 | 0.5030 | 0.0160 | 0.59 | 2726 | 26 | 2601 | 69 | 2663 | 23 | 95 |
| 82-6 | 0.02 | 673 | 511 | 341 | 0.76 | 86800 | 0.141 | 0.002 | 4.04 | 0.11 | 0.2072 | 0.0058 | 0.76 | 2236 | 18 | 1201 | 30 | 1619 | 22 | 54 |
| 82-7 | 0.03 | 228 | 196 | 279 | 0.86 | 58000 | 0.177 | 0.003 | 10.68 | 0.23 | 0.4270 | 0.0100 | 0.67 | 2652 | 18 | 2283 | 45 | 2490 | 20 | 86 |
| 82-11 | 0.02 | 1 142 | 77 | 86 | 0.07 | 123150 | 0.139 | 0.002 | 3.56 | 0.08 | 0.1858 | 0.0043 | 0.77 | 2222 | 15 | 1092 | 23 | 1527 | 17 | 49 |
| 82-18 | 0.02 | 282 | 180 | 326 | 0.64 | 80850 | 0.189 | 0.003 | 13.72 | 0.22 | 0.5250 | 0.0100 | 0.59 | 2734 | 15 | 2719 | 41 | 2724 | 15 | 99 |
| 82-19 | 0.04 | 178 | 113 | 184 | 0.63 | 52100 | 0.185 | 0.003 | 13.41 | 0.24 | 0.5210 | 0.0100 | 0.62 | 2725 | 16 | 2703 | 45 | 2707 | 17 | 99 |
| 82-20 | 0.03 | 238 | 142 | 216 | 0.60 | 65450 | 0.187 | 0.003 | 13.22 | 0.22 | 0.5122 | 0.0097 | 0.66 | 2725 | 15 | 2661 | 41 | 2697 | 15 | 98 |
| 82-21 | 0.03 | 212 | 165 | 308 | 0.78 | 59200 | 0.185 | 0.004 | 13.09 | 0.27 | 0.5170 | 0.0130 | 0.65 | 2698 | 18 | 2682 | 53 | 2685 | 20 | 99 |
| 82-24 | 0.02 | 340 | 75 | 136 | 0.22 | 92000 | 0.187 | 0.002 | 13.65 | 0.20 | 0.5274 | 0.0090 | 0.65 | 2735 | 12 | 2720 | 38 | 2723 | 14 | 99 |
| 82-25 | 0.03 | 309 | 132 | 170 | 0.43 | 60200 | 0.168 | 0.002 | 8.44 | 0.20 | 0.3613 | 0.0081 | 0.85 | 2546 | 12 | 1983 | 39 | 2276 | 22 | 78 |
| 82-29c | 0.04 | 246 | 63 | 163 | 0.26 | 49700 | 0.183 | 0.003 | 9.81 | 0.21 | 0.3894 | 0.0090 | 0.75 | 2682 | 16 | 2105 | 41 | 2416 | 19 | 78 |
| 82-29b | 0.03 | 226 | 139 | 293 | 0.61 | 55050 | 0.188 | 0.002 | 12.18 | 0.19 | 0.4698 | 0.0079 | 0.69 | 2740 | 12 | 2479 | 35 | 2617 | 15 | 90 |
| 82-30c | 0.02 | 1 272 | 992 | 418 | 0.78 | 82900 | 0.120 | 0.002 | 2.13 | 0.06 | 0.1271 | 0.0029 | 0.75 | 1972 | 21 | 770 | 17 | 1151 | 18 | 39 |
| 82-30b | 0.04 | 912 | 394 | 174 | 0.43 | 50900 | 0.109 | 0.002 | 1.67 | 0.04 | 0.1103 | 0.0024 | 0.75 | 1790 | 19 | 673 | 14 | 990 | 14 | 38 |
| 82-31 | 0.04 | 520 | 490 | 308 | 0.94 | 52300 | 0.142 | 0.002 | 3.96 | 0.09 | 0.2045 | 0.0047 | 0.73 | 2264 | 17 | 1194 | 25 | 1618 | 17 | 53 |
| 82-32 | 0.02 | 394 | 99 | 174 | 0.25 | 95600 | 0.187 | 0.003 | 12.98 | 0.22 | 0.5040 | 0.0120 | 0.60 | 2712 | 17 | 2619 | 49 | 2675 | 16 | 97 |

| Amostra 07C | | | | | | | | | | | | | | | | | | | | |
|---|---|---|---|---|---|---|---|---|---|---|---|---|---|---|---|---|---|---|---|---|
| **Zircão** | **ƒ206** | **(μg.g$^{-1}$)** | | | | | **Razão isotópica** | | | | | | | **Idade (Ma)** | | | | | | **Conc** |
| **spot** | **(%)** | **U** | **Th** | **Pb** | **Th/U** | **$^{206}$Pb/$^{204}$Pb** | **$^{207}$Pb/$^{206}$U** | **2σ** | **$^{207}$Pb/$^{235}$U** | **2σ** | **$^{206}$Pb/$^{238}$U** | **2σ** | **Rho** | **$^{207}$Pb/$^{206}$Pb** | **2σ** | **$^{206}$Pb/$^{238}$U** | **2σ** | **$^{207}$Pb/$^{235}$U** | **2σ** | **(%)** |
| 7-1 | 0.02 | 234 | 149 | 246 | 0.64 | 88500 | 0.1793 | 0.0032 | 12.31 | 0.28 | 0.5010 | 0.0130 | 0.73 | 2660 | 17 | 2617 | 55 | 2632 | 21 | 98 |
| 7-4b | 0.05 | 86 | 157 | 248 | 1.83 | 36300 | 0.1878 | 0.0024 | 14.19 | 0.21 | 0.5468 | 0.0085 | 0.65 | 2729 | 13 | 2809 | 35 | 2761 | 14 | 103 |
| 7-4c | 0.07 | 123 | 32 | 53 | 0.26 | 26400 | 0.1532 | 0.0025 | 5.78 | 0.13 | 0.2707 | 0.0065 | 0.74 | 2412 | 18 | 1537 | 33 | 1928 | 20 | 64 |
| 7-5 | 0.03 | 136 | 245 | 412 | 1.80 | 55500 | 0.1842 | 0.0032 | 12.94 | 0.32 | 0.5160 | 0.0140 | 0.77 | 2701 | 17 | 2675 | 57 | 2676 | 23 | 99 |
| 7-8 | 0.08 | 127 | 189 | 205 | 1.49 | 24150 | 0.1730 | 0.0028 | 6.80 | 0.17 | 0.2837 | 0.0071 | 0.80 | 2600 | 17 | 1604 | 36 | 2079 | 22 | 62 |
| 7-10 | 0.07 | 76 | 152 | 221 | 2.00 | 26800 | 0.1858 | 0.0032 | 13.74 | 0.24 | 0.5380 | 0.0110 | 0.64 | 2722 | 15 | 2772 | 45 | 2728 | 16 | 102 |
| 7-11 | 0.18 | 32 | 52 | 82 | 1.62 | 10395 | 0.1827 | 0.0042 | 12.89 | 0.31 | 0.5110 | 0.0130 | 0.53 | 2702 | 23 | 2665 | 53 | 2664 | 22 | 99 |
| 7-12 | 0.08 | 69 | 97 | 144 | 1.41 | 22150 | 0.1852 | 0.0030 | 13.16 | 0.24 | 0.5180 | 0.0110 | 0.71 | 2708 | 15 | 2686 | 46 | 2688 | 17 | 99 |
| 7-13b | 0.09 | 90 | 76 | 148 | 0.84 | 20100 | 0.1926 | 0.0035 | 8.90 | 0.24 | 0.3363 | 0.0099 | 0.81 | 2767 | 18 | 1856 | 48 | 2313 | 24 | 67 |
| 7-13c | 0.05 | 116 | 176 | 285 | 1.52 | 39000 | 0.1865 | 0.0031 | 13.36 | 0.27 | 0.5220 | 0.0120 | 0.69 | 2724 | 17 | 2700 | 50 | 2703 | 19 | 99 |
| 7-14b | 0.07 | 152 | 119 | 136 | 0.78 | 27250 | 0.1672 | 0.0027 | 6.35 | 0.16 | 0.2752 | 0.0074 | 0.83 | 2534 | 16 | 1553 | 37 | 2015 | 23 | 61 |
| 7-15 | 0.06 | 93 | 242 | 352 | 2.62 | 30450 | 0.1827 | 0.0032 | 12.83 | 0.25 | 0.5110 | 0.0120 | 0.68 | 2680 | 16 | 2664 | 50 | 2665 | 18 | 99 |
| 7-16 | 0.11 | 50 | 79 | 120 | 1.58 | 17365 | 0.1863 | 0.0029 | 14.13 | 0.22 | 0.5495 | 0.0094 | 0.60 | 2730 | 15 | 2817 | 39 | 2751 | 15 | 103 |
| 7-17b | 0.05 | 103 | 139 | 216 | 1.35 | 35600 | 0.1824 | 0.0027 | 13.15 | 0.23 | 0.5190 | 0.0110 | 0.69 | 2691 | 15 | 2687 | 46 | 2689 | 17 | 100 |
| 7-17c | 0.08 | 111 | 122 | 159 | 1.10 | 24800 | 0.1740 | 0.0025 | 8.38 | 0.21 | 0.3528 | 0.0095 | 0.84 | 2612 | 14 | 1931 | 45 | 2264 | 23 | 74 |
| 7-20 | 0.10 | 73 | 83 | 149 | 1.13 | 18400 | 0.1912 | 0.0032 | 10.56 | 0.22 | 0.4010 | 0.0100 | 0.73 | 2785 | 17 | 2172 | 46 | 2478 | 19 | 78 |
| 7-23 | 0.05 | 114 | 204 | 326 | 1.79 | 34300 | 0.1827 | 0.0036 | 12.71 | 0.27 | 0.5120 | 0.0130 | 0.70 | 2690 | 20 | 2658 | 57 | 2656 | 20 | 99 |
| 7-24 | 0.06 | 129 | 117 | 167 | 0.91 | 29000 | 0.1661 | 0.0027 | 8.28 | 0.31 | 0.3500 | 0.0110 | 0.90 | 2526 | 19 | 1924 | 53 | 2207 | 35 | 76 |
| 7-26 | 0.35 | 19 | 19 | 30 | 1.00 | 5305 | 0.1869 | 0.0051 | 13.10 | 0.34 | 0.5170 | 0.0140 | 0.48 | 2734 | 26 | 2671 | 59 | 2672 | 24 | 98 |
| 7-27 | 0.12 | 95 | 158 | 166 | 1.67 | 16150 | 0.1715 | 0.0033 | 6.88 | 0.19 | 0.2941 | 0.0078 | 0.82 | 2600 | 19 | 1649 | 38 | 2079 | 24 | 63 |
| 7-30 | 0.13 | 98 | 56 | 44 | 0.58 | 14700 | 0.1474 | 0.0027 | 5.42 | 0.16 | 0.2639 | 0.0079 | 0.82 | 2335 | 19 | 1504 | 41 | 1875 | 26 | 64 |
| 7-31 | 0.12 | 51 | 86 | 122 | 1.69 | 15700 | 0.1853 | 0.0040 | 13.88 | 0.32 | 0.5370 | 0.0130 | 0.61 | 2727 | 23 | 2761 | 56 | 2730 | 22 | 101 |
| 7-32b | 0.09 | 92 | 117 | 175 | 1.27 | 19700 | 0.1825 | 0.0030 | 9.46 | 0.27 | 0.3770 | 0.0110 | 0.85 | 2700 | 16 | 2035 | 52 | 2360 | 26 | 75 |
| 7-33b | 0.55 | 18 | 1 | 55 | 0.04 | 3380 | 0.1880 | 0.0110 | 8.01 | 0.64 | 0.3190 | 0.0210 | 0.76 | 2738 | 63 | 1770 | 100 | 2183 | 76 | 65 |

| | | | | | | | | | | | | | | | | | | | |
|---|---|---|---|---|---|---|---|---|---|---|---|---|---|---|---|---|---|---|---|
| 7-35 | 0.06 | 114 | 159 | 236 | 1.39 | 33400 | 0.1849 | 0.0030 | 13.66 | 0.29 | 0.5300 | 0.0130 | 0.74 | 2707 | 16 | 2734 | 52 | 2720 | 20 | 101 |
| 7-36 | 0.03 | 195 | 313 | 434 | 1.61 | 54950 | 0.1826 | 0.0024 | 13.12 | 0.21 | 0.5189 | 0.0096 | 0.72 | 2682 | 13 | 2685 | 40 | 2689 | 16 | 100 |

Amostra 101C

| Zircão | $f$206 | (µg.g$^{-1}$) | | | | | Razão isotópica | | | | | | | Idade (Ma) | | | | | | Conc |
|---|---|---|---|---|---|---|---|---|---|---|---|---|---|---|---|---|---|---|---|---|
| spot | (%) | U | Th | Pb | Th/U | $^{206}Pb/^{204}Pb$ | $^{207}Pb/^{206}U$ | 2σ | $^{207}Pb/^{235}U$ | 2σ | $^{206}Pb/^{238}U$ | 2σ | Rho | $^{207}Pb/^{206}Pb$ | 2σ | $^{206}Pb/^{238}U$ | 2σ | $^{207}Pb/^{235}U$ | 2σ | (%) |
| 101-1b | 0.08 | 97 | 117 | 109 | 1.21 | 22350 | 0.1631 | 0.0023 | 7.86 | 0.16 | 0.3468 | 0.0069 | 0.72 | 2517 | 14 | 1921 | 33 | 2215 | 18 | 76 |
| 101-1c | 0.05 | 131 | 457 | 466 | 3.50 | 36700 | 0.1760 | 0.0022 | 10.00 | 0.17 | 0.4049 | 0.0078 | 0.77 | 2635 | 12 | 2193 | 36 | 2433 | 16 | 83 |
| 101-2b | 0.08 | 81 | 59 | 64 | 0.73 | 22850 | 0.1493 | 0.0036 | 8.54 | 0.20 | 0.4270 | 0.0100 | 0.55 | 2348 | 21 | 2291 | 46 | 2302 | 22 | 98 |
| 101-2c | 0.04 | 179 | 309 | 344 | 1.73 | 46950 | 0.1749 | 0.0024 | 10.62 | 0.35 | 0.4280 | 0.0120 | 0.91 | 2621 | 17 | 2285 | 56 | 2446 | 34 | 87 |
| 101-3 | 0.05 | 131 | 377 | 415 | 2.87 | 36650 | 0.1822 | 0.0022 | 10.39 | 0.21 | 0.4155 | 0.0090 | 0.82 | 2675 | 11 | 2232 | 41 | 2468 | 18 | 83 |
| 101-5 | 0.03 | 197 | 552 | 665 | 2.80 | 65200 | 0.1819 | 0.0024 | 12.74 | 0.21 | 0.5120 | 0.0100 | 0.75 | 2676 | 13 | 2662 | 43 | 2662 | 16 | 99 |
| 101-6 | 0.04 | 135 | 373 | 395 | 2.76 | 44050 | 0.1836 | 0.0020 | 13.08 | 0.16 | 0.5196 | 0.0069 | 0.65 | 2694 | 10 | 2693 | 29 | 2686 | 11 | 100 |
| 101-7 | 0.05 | 118 | 402 | 479 | 3.40 | 40050 | 0.1837 | 0.0023 | 13.43 | 0.22 | 0.5251 | 0.0092 | 0.74 | 2703 | 11 | 2712 | 39 | 2707 | 15 | 100 |
| 101-10 | 0.06 | 116 | 245 | 264 | 2.12 | 28950 | 0.1748 | 0.0026 | 9.57 | 0.21 | 0.3949 | 0.0092 | 0.77 | 2630 | 15 | 2143 | 43 | 2391 | 20 | 81 |
| 101-12 | 0.06 | 156 | 418 | 402 | 2.68 | 30150 | 0.1725 | 0.0021 | 7.83 | 0.14 | 0.3275 | 0.0057 | 0.74 | 2600 | 12 | 1828 | 27 | 2211 | 16 | 70 |
| 101-14b | 0.58 | 15 | 4 | 14 | 0.28 | 3230 | 0.1390 | 0.0100 | 7.17 | 0.54 | 0.3790 | 0.0210 | 0.51 | 2227 | 76 | 2089 | 96 | 2129 | 63 | 94 |
| 101-15b | 0.06 | 122 | 290 | 255 | 2.38 | 29350 | 0.1694 | 0.0022 | 9.40 | 0.15 | 0.3995 | 0.0071 | 0.73 | 2550 | 13 | 2164 | 33 | 2372 | 14 | 85 |
| 101-16b | 0.08 | 137 | 138 | 125 | 1.01 | 22600 | 0.1525 | 0.0021 | 6.37 | 0.10 | 0.3018 | 0.0050 | 0.65 | 2402 | 15 | 1697 | 25 | 2029 | 14 | 71 |
| 101-17b | 0.02 | 263 | 835 | 951 | 3.17 | 76050 | 0.1852 | 0.0023 | 13.26 | 0.18 | 0.5183 | 0.0094 | 0.74 | 2707 | 12 | 2689 | 40 | 2699 | 13 | 99 |
| 101-18b | 0.07 | 145 | 528 | 426 | 3.65 | 26250 | 0.1687 | 0.0030 | 7.82 | 0.18 | 0.3325 | 0.0088 | 0.75 | 2577 | 16 | 1838 | 42 | 2203 | 22 | 71 |
| 101-19 | 0.07 | 122 | 448 | 406 | 3.68 | 25750 | 0.1728 | 0.0024 | 9.35 | 0.17 | 0.3884 | 0.0070 | 0.72 | 2591 | 14 | 2110 | 32 | 2369 | 16 | 81 |
| 101-21b | 0.06 | 154 | 366 | 317 | 2.37 | 30600 | 0.1694 | 0.0022 | 8.71 | 0.16 | 0.3734 | 0.0069 | 0.75 | 2563 | 13 | 2040 | 32 | 2308 | 17 | 80 |
| 101-22 | 0.06 | 184 | 58 | 88 | 0.32 | 30050 | 0.1668 | 0.0026 | 7.55 | 0.13 | 0.3249 | 0.0064 | 0.69 | 2551 | 17 | 1810 | 31 | 2172 | 16 | 71 |
| 101-23b | 0.09 | 87 | 242 | 241 | 2.78 | 21550 | 0.1778 | 0.0024 | 12.10 | 0.18 | 0.4898 | 0.0073 | 0.59 | 2642 | 14 | 2561 | 32 | 2609 | 14 | 97 |
| 101-24 | 0.06 | 147 | 355 | 461 | 2.41 | 31300 | 0.1902 | 0.0025 | 10.13 | 0.28 | 0.3830 | 0.0110 | 0.89 | 2755 | 13 | 2071 | 53 | 2431 | 26 | 75 |
| 101-26b | 0.05 | 180 | 552 | 590 | 3.06 | 40300 | 0.1781 | 0.0021 | 10.87 | 0.21 | 0.4377 | 0.0083 | 0.80 | 2649 | 11 | 2330 | 38 | 2507 | 18 | 88 |
| 101-26c | 0.06 | 177 | 415 | 281 | 2.35 | 30550 | 0.1720 | 0.0024 | 7.97 | 0.17 | 0.3350 | 0.0075 | 0.79 | 2581 | 14 | 1851 | 36 | 2222 | 19 | 72 |
| 101-27b | 0.07 | 176 | 626 | 449 | 3.57 | 27800 | 0.1616 | 0.0021 | 7.04 | 0.20 | 0.3129 | 0.0082 | 0.89 | 2483 | 14 | 1748 | 40 | 2102 | 25 | 70 |
| 101-27c | 0.04 | 174 | 468 | 524 | 2.69 | 42550 | 0.1836 | 0.0024 | 13.21 | 0.19 | 0.5185 | 0.0085 | 0.66 | 2703 | 11 | 2687 | 36 | 2691 | 13 | 99 |
| 101-28b | 0.04 | 172 | 551 | 624 | 3.20 | 41700 | 0.1831 | 0.0020 | 13.18 | 0.19 | 0.5181 | 0.0086 | 0.77 | 2693 | 10 | 2689 | 36 | 2686 | 13 | 100 |
| 101-30b | 0.04 | 202 | 819 | 892 | 4.05 | 47500 | 0.1799 | 0.0023 | 12.64 | 0.20 | 0.5086 | 0.0087 | 0.74 | 2663 | 12 | 2647 | 37 | 2650 | 15 | 99 |

| | | | | | | | | | | | | | | | | | | | |
|---|---|---|---|---|---|---|---|---|---|---|---|---|---|---|---|---|---|---|---|
| 101-30c | 0.08 | 119 | 349 | 398 | 2.93 | 24000 | 0.1887 | 0.0024 | 11.18 | 0.17 | 0.4291 | 0.0074 | 0.72 | 2737 | 13 | 2302 | 33 | 2534 | 15 | 84 |
| 101-31c | 0.05 | 145 | 452 | 536 | 3.11 | 34600 | 0.1841 | 0.0023 | 13.28 | 0.19 | 0.5212 | 0.0075 | 0.67 | 2708 | 12 | 2706 | 32 | 2700 | 14 | 100 |
| 101-33b | 0.05 | 158 | 505 | 557 | 3.19 | 37050 | 0.1820 | 0.0022 | 12.99 | 0.16 | 0.5151 | 0.0077 | 0.61 | 2675 | 12 | 2675 | 33 | 2677 | 12 | 100 |
| 101-33c | 0.04 | 221 | 630 | 633 | 2.86 | 43350 | 0.1764 | 0.0019 | 10.55 | 0.23 | 0.4276 | 0.0088 | 0.87 | 2628 | 11 | 2288 | 40 | 2476 | 21 | 87 |

Amostra 98

| Zircão | *f*206 | (μg.g$^{-1}$) | | | | | Razão isotópica | | | | | | | Idade (Ma) | | | | | | Conc |
|---|---|---|---|---|---|---|---|---|---|---|---|---|---|---|---|---|---|---|---|---|
| spot | (%) | U | Th | Pb | Th/U | $^{206}Pb/^{204}Pb$ | $^{207}Pb/^{206}U$ | 2σ | $^{207}Pb/^{235}U$ | 2σ | $^{206}Pb/^{238}U$ | 2σ | Rho | $^{207}Pb/^{206}Pb$ | 2σ | $^{206}Pb/^{238}U$ | 2σ | $^{207}Pb/^{235}U$ | 2σ | (%) |
| 98-1 | 0.03 | 305 | 24 | 40 | 0.08 | 71750 | 0.1889 | 0.0035 | 13.00 | 0.25 | 0.505 | 0.012 | 0.66 | 2734 | 18 | 2627 | 50 | 2676 | 18 | 96 |
| 98-2b | 0.03 | 321 | 172 | 173 | 0.54 | 58550 | 0.1782 | 0.0027 | 9.12 | 0.20 | 0.370 | 0.009 | 0.79 | 2651 | 14 | 2013 | 40 | 2336 | 20 | 76 |
| 98-3 | 0.05 | 135 | 104 | 164 | 0.77 | 37350 | 0.1909 | 0.0036 | 14.39 | 0.30 | 0.545 | 0.015 | 0.74 | 2770 | 19 | 2786 | 62 | 2780 | 21 | 101 |
| 98-4 | 0.05 | 201 | 27 | 64 | 0.13 | 41100 | 0.1801 | 0.0025 | 10.70 | 0.19 | 0.429 | 0.009 | 0.74 | 2675 | 12 | 2306 | 41 | 2494 | 17 | 86 |
| 98-5c | 0.03 | 219 | 212 | 339 | 0.97 | 57950 | 0.1928 | 0.0026 | 14.36 | 0.26 | 0.536 | 0.011 | 0.75 | 2779 | 13 | 2767 | 46 | 2768 | 17 | 100 |
| 98-5b | 0.03 | 233 | 27 | 40 | 0.12 | 57700 | 0.1875 | 0.0023 | 13.62 | 0.19 | 0.523 | 0.008 | 0.70 | 2737 | 10 | 2722 | 35 | 2719 | 13 | 99 |
| 98-7 | 0.03 | 314 | 158 | 196 | 0.50 | 62950 | 0.1825 | 0.0026 | 10.44 | 0.22 | 0.409 | 0.009 | 0.79 | 2687 | 14 | 2197 | 42 | 2472 | 19 | 82 |
| 98-8 | 0.07 | 101 | 81 | 109 | 0.80 | 26800 | 0.1947 | 0.0034 | 14.79 | 0.34 | 0.546 | 0.012 | 0.67 | 2787 | 17 | 2794 | 51 | 2797 | 22 | 100 |
| 98-9 | 0.03 | 205 | 291 | 422 | 1.42 | 54750 | 0.1917 | 0.0030 | 14.59 | 0.25 | 0.549 | 0.011 | 0.64 | 2764 | 14 | 2823 | 44 | 2787 | 16 | 102 |
| 98-10 | 0.03 | 294 | 200 | 350 | 0.68 | 68550 | 0.1888 | 0.0039 | 13.62 | 0.33 | 0.522 | 0.016 | 0.72 | 2750 | 22 | 2704 | 66 | 2718 | 23 | 98 |
| 98-11 | 0.05 | 142 | 107 | 159 | 0.75 | 36550 | 0.1925 | 0.0025 | 14.81 | 0.19 | 0.555 | 0.008 | 0.58 | 2778 | 12 | 2840 | 33 | 2803 | 12 | 102 |
| 98-12c | 0.03 | 238 | 32 | 47 | 0.14 | 57150 | 0.1907 | 0.0023 | 14.16 | 0.19 | 0.536 | 0.008 | 0.68 | 2765 | 11 | 2757 | 34 | 2758 | 13 | 100 |

| | | | | | | | | | | | | | | | | | | | |
|---|---|---|---|---|---|---|---|---|---|---|---|---|---|---|---|---|---|---|---|
| 98-12b | 0.04 | 229 | 55 | 92 | 0.24 | 51700 | 0.1920 | 0.0032 | 13.74 | 0.23 | 0.516 | 0.010 | 0.60 | 2766 | 17 | 2671 | 44 | 2733 | 16 | 97 |
| 98-13 | 0.03 | 297 | 234 | 348 | 0.79 | 67100 | 0.1863 | 0.0032 | 13.05 | 0.26 | 0.515 | 0.013 | 0.67 | 2719 | 17 | 2680 | 54 | 2678 | 19 | 99 |
| 98-14 | 0.03 | 309 | 78 | 98 | 0.25 | 56500 | 0.1810 | 0.0025 | 9.87 | 0.20 | 0.392 | 0.008 | 0.78 | 2681 | 13 | 2133 | 39 | 2421 | 19 | 80 |
| 98-15 | 0.03 | 276 | 104 | 155 | 0.38 | 62950 | 0.1857 | 0.0025 | 13.40 | 0.24 | 0.521 | 0.010 | 0.70 | 2708 | 13 | 2706 | 41 | 2708 | 16 | 100 |
| 98-16 | 0.03 | 367 | 41 | 64 | 0.11 | 70850 | 0.1739 | 0.0020 | 10.76 | 0.24 | 0.434 | 0.010 | 0.88 | 2609 | 12 | 2327 | 44 | 2496 | 22 | 89 |
| 98-17 | 0.06 | 155 | 121 | 178 | 0.78 | 34000 | 0.1792 | 0.0029 | 12.69 | 0.28 | 0.509 | 0.010 | 0.71 | 2654 | 18 | 2643 | 43 | 2651 | 20 | 100 |
| 98-18c | 0.06 | 138 | 29 | 57 | 0.21 | 31000 | 0.1844 | 0.0034 | 13.42 | 0.36 | 0.521 | 0.012 | 0.74 | 2712 | 18 | 2710 | 51 | 2711 | 25 | 100 |
| 98-18b | 0.06 | 136 | 31 | 49 | 0.22 | 32650 | 0.1908 | 0.0026 | 14.64 | 0.20 | 0.550 | 0.009 | 0.60 | 2765 | 12 | 2821 | 35 | 2792 | 13 | 102 |
| 98-19 | 0.05 | 245 | 119 | 124 | 0.49 | 39700 | 0.1767 | 0.0027 | 9.36 | 0.17 | 0.378 | 0.008 | 0.67 | 2640 | 15 | 2060 | 35 | 2374 | 17 | 78 |
| 98-20c | 0.03 | 276 | 131 | 215 | 0.47 | 62500 | 0.1913 | 0.0029 | 14.35 | 0.27 | 0.538 | 0.010 | 0.67 | 2772 | 13 | 2771 | 43 | 2773 | 18 | 100 |
| 98-20b | 0.06 | 152 | 53 | 73 | 0.35 | 29900 | 0.1878 | 0.0030 | 11.79 | 0.21 | 0.458 | 0.010 | 0.68 | 2735 | 14 | 2420 | 43 | 2577 | 17 | 88 |
| 98-23 | 0.04 | 195 | 93 | 155 | 0.48 | 42450 | 0.1803 | 0.0024 | 13.00 | 0.21 | 0.518 | 0.009 | 0.69 | 2676 | 13 | 2678 | 36 | 2681 | 15 | 100 |
| 98-24 | 0.04 | 208 | 40 | 60 | 0.19 | 46200 | 0.1869 | 0.0023 | 13.96 | 0.19 | 0.535 | 0.009 | 0.70 | 2730 | 11 | 2756 | 36 | 2746 | 13 | 101 |
| 98-26 | 0.04 | 216 | 80 | 110 | 0.37 | 45500 | 0.1788 | 0.0030 | 12.63 | 0.23 | 0.504 | 0.010 | 0.63 | 2649 | 16 | 2622 | 43 | 2647 | 17 | 99 |
| 98-27 | 0.04 | 371 | 294 | 248 | 0.79 | 44500 | 0.1664 | 0.0028 | 7.04 | 0.16 | 0.305 | 0.007 | 0.70 | 2535 | 18 | 1707 | 34 | 2113 | 20 | 67 |
| 98-28 | 0.04 | 223 | 153 | 200 | 0.68 | 48300 | 0.1854 | 0.0021 | 13.56 | 0.17 | 0.525 | 0.008 | 0.65 | 2715 | 11 | 2715 | 33 | 2717 | 12 | 100 |
| 98-29b | 0.04 | 332 | 25 | 45 | 0.08 | 51750 | 0.1627 | 0.0025 | 7.99 | 0.29 | 0.341 | 0.011 | 0.90 | 2499 | 18 | 1876 | 51 | 2175 | 35 | 75 |

| | | | | | | | | | | | | | | | | | | | |
|---|---|---|---|---|---|---|---|---|---|---|---|---|---|---|---|---|---|---|---|
| 98-29c | 0.04 | 190 | 42 | 66 | 0.22 | 43250 | 0.1874 | 0.0025 | 14.85 | 0.20 | 0.571 | 0.009 | 0.61 | 2734 | 12 | 2911 | 36 | 2806 | 13 | 106 |
| 98-30 | 0.07 | 123 | 44 | 72 | 0.36 | 28150 | 0.1861 | 0.0026 | 14.61 | 0.23 | 0.564 | 0.010 | 0.67 | 2728 | 12 | 2873 | 39 | 2787 | 15 | 105 |
| 98-31 | 0.03 | 249 | 202 | 319 | 0.81 | 55000 | 0.1880 | 0.0031 | 14.07 | 0.24 | 0.535 | 0.011 | 0.64 | 2734 | 16 | 2761 | 45 | 2756 | 16 | 101 |

Amostra 69B

| Zircão | $f$206 | ($\mu g.g^{-1}$) | | | | | Razão isotópica | | | | | | | Idade (Ma) | | | | | | Conc |
|---|---|---|---|---|---|---|---|---|---|---|---|---|---|---|---|---|---|---|---|---|
| spot | (%) | U | Th | Pb | Th/U | $^{206}Pb/^{204}Pb$ | $^{207}Pb/^{206}U$ | 2σ | $^{207}Pb/^{235}U$ | 2σ | $^{206}Pb/^{238}U$ | 2σ | Rho | $^{207}Pb/^{206}Pb$ | 2σ | $^{206}Pb/^{238}U$ | 2σ | $^{207}Pb/^{235}U$ | 2σ | (%) |
| 69-12 | 0.1210 | 373.8 | 18.1 | 30.8 | 0.05 | 15450 | 0.0969 | 0.0019 | 1.539 | 0.035 | 0.1130 | 0.0027 | 0.67 | 1592 | 25 | 688 | 16 | 938 | 14 | 43 |
| 69-3 | 0.1123 | 465.0 | 195.9 | 68.9 | 0.42 | 16650 | 0.0899 | 0.0018 | 1.210 | 0.025 | 0.0962 | 0.0021 | 0.60 | 1438 | 21 | 591 | 12 | 803 | 11 | 41 |
| 69-4c | 0.0997 | 418.0 | 144.2 | 97.8 | 0.34 | 18750 | 0.1200 | 0.0026 | 2.108 | 0.049 | 0.1260 | 0.0027 | 0.53 | 1947 | 25 | 765 | 15 | 1143 | 16 | 39 |
| 69-4b | 0.0804 | 322.0 | 98.0 | 85.3 | 0.30 | 23250 | 0.1465 | 0.0027 | 4.002 | 0.096 | 0.1964 | 0.0045 | 0.71 | 2319 | 18 | 1155 | 24 | 1612 | 18 | 50 |
| 69-5c | 0.0557 | 215.7 | 138.3 | 181.1 | 0.64 | 33600 | 0.1853 | 0.0029 | 11.170 | 0.200 | 0.4325 | 0.0087 | 0.68 | 2727 | 15 | 2313 | 39 | 2527 | 17 | 85 |
| 69-5b | 0.1048 | 194.7 | 9.9 | 11.1 | 0.05 | 17850 | 0.1142 | 0.0016 | 4.129 | 0.066 | 0.2547 | 0.0043 | 0.63 | 1892 | 14 | 1463 | 22 | 1657 | 13 | 77 |
| 69-6 | 0.0557 | 180.4 | 53.7 | 93.3 | 0.30 | 33550 | 0.1922 | 0.0031 | 13.780 | 0.240 | 0.5150 | 0.0100 | 0.63 | 2785 | 15 | 2667 | 44 | 2732 | 17 | 96 |
| 69-8b | 0.0618 | 261.0 | 31.1 | 50.4 | 0.12 | 30250 | 0.1618 | 0.0022 | 7.220 | 0.140 | 0.3178 | 0.0065 | 0.78 | 2488 | 12 | 1778 | 31 | 2136 | 17 | 71 |
| 69-13 | 0.0413 | 235.5 | 41.7 | 75.5 | 0.18 | 45300 | 0.1830 | 0.0034 | 13.730 | 0.240 | 0.5370 | 0.0110 | 0.58 | 2695 | 16 | 2757 | 47 | 2728 | 17 | 102 |
| 69-14 | 0.0507 | 231.9 | 40.3 | 62.2 | 0.17 | 36900 | 0.1753 | 0.0031 | 10.710 | 0.240 | 0.4340 | 0.0110 | 0.74 | 2632 | 15 | 2304 | 48 | 2484 | 21 | 88 |
| 69-15 | 0.1054 | 372.0 | 102.5 | 78.6 | 0.28 | 17750 | 0.1419 | 0.0028 | 2.735 | 0.061 | 0.1384 | 0.0032 | 0.62 | 2267 | 20 | 834 | 18 | 1335 | 17 | 37 |
| 69-16c | 0.0765 | 368.0 | 143.2 | 97.7 | 0.39 | 24450 | 0.1402 | 0.0025 | 3.635 | 0.081 | 0.1860 | 0.0044 | 0.68 | 2257 | 19 | 1096 | 24 | 1548 | 18 | 49 |
| 69-16b | 0.0803 | 273.2 | 7.0 | 46.4 | 0.03 | 23300 | 0.1272 | 0.0026 | 3.935 | 0.088 | 0.2207 | 0.0055 | 0.70 | 2077 | 22 | 1277 | 29 | 1615 | 18 | 61 |
| 69-17 | 0.0738 | 407.0 | 68.5 | 68.5 | 0.17 | 25350 | 0.1469 | 0.0027 | 3.699 | 0.091 | 0.1785 | 0.0045 | 0.71 | 2328 | 19 | 1053 | 24 | 1556 | 19 | 45 |
| 69-18c | 0.0555 | 291.0 | 59.4 | 91.1 | 0.20 | 33700 | 0.1600 | 0.0029 | 7.100 | 0.290 | 0.3100 | 0.0120 | 0.87 | 2486 | 19 | 1709 | 56 | 2081 | 36 | 69 |
| 69-19b | 0.1218 | 188.0 | 24.5 | 36.4 | 0.13 | 15350 | 0.1376 | 0.0024 | 4.362 | 0.081 | 0.2243 | 0.0039 | 0.52 | 2211 | 18 | 1302 | 20 | 1704 | 15 | 59 |

| | | | | | | | | | | | | | | | | | | | |
|---|---|---|---|---|---|---|---|---|---|---|---|---|---|---|---|---|---|---|---|
| 69-12b | 0.0510 | 301.0 | 39.1 | 122.6 | 0.13 | 36650 | 0.1681 | 0.0027 | 7.870 | 0.180 | 0.3332 | 0.0084 | 0.77 | 2553 | 16 | 1839 | 40 | 2212 | 20 | 72 |
| 69-20 | 0.0507 | 235.9 | 100.3 | 127.7 | 0.43 | 36850 | 0.1757 | 0.0028 | 10.880 | 0.230 | 0.4430 | 0.0100 | 0.75 | 2635 | 17 | 2352 | 45 | 2497 | 19 | 89 |
| 69-22 | 0.0621 | 250.2 | 52.7 | 92.0 | 0.21 | 30100 | 0.1745 | 0.0030 | 8.050 | 0.150 | 0.3287 | 0.0069 | 0.62 | 2621 | 17 | 1827 | 34 | 2236 | 16 | 70 |
| 69-23b | 0.0680 | 157.6 | 22.0 | 76.1 | 0.14 | 27500 | 0.1900 | 0.0034 | 12.860 | 0.260 | 0.4780 | 0.0100 | 0.62 | 2763 | 17 | 2503 | 44 | 2664 | 19 | 91 |
| 69-24 | 0.0789 | 273.6 | 72.6 | 58.2 | 0.27 | 23700 | 0.1478 | 0.0027 | 4.910 | 0.110 | 0.2389 | 0.0062 | 0.74 | 2343 | 19 | 1370 | 32 | 1790 | 20 | 58 |
| 69-25 | 0.0844 | 462.0 | 133.6 | 106.9 | 0.29 | 22150 | 0.1423 | 0.0027 | 2.728 | 0.062 | 0.1360 | 0.0029 | 0.63 | 2259 | 22 | 819 | 16 | 1333 | 17 | 36 |
| 69-26c | 0.0469 | 213.1 | 57.8 | 94.3 | 0.27 | 39850 | 0.1841 | 0.0026 | 13.570 | 0.210 | 0.5205 | 0.0090 | 0.64 | 2699 | 13 | 2692 | 39 | 2716 | 15 | 100 |
| 69-26b | 0.0757 | 422.0 | 162.1 | 90.7 | 0.38 | 24700 | 0.1298 | 0.0023 | 2.944 | 0.068 | 0.1597 | 0.0039 | 0.70 | 2115 | 20 | 951 | 21 | 1386 | 18 | 45 |
| 69-27 | 0.0744 | 343.5 | 58.1 | 57.1 | 0.17 | 25150 | 0.1370 | 0.0025 | 4.000 | 0.130 | 0.2045 | 0.0062 | 0.81 | 2226 | 19 | 1190 | 33 | 1604 | 26 | 53 |
| 69-29 | 0.0808 | 199.6 | 171.3 | 178.4 | 0.86 | 23150 | 0.1734 | 0.0033 | 7.850 | 0.180 | 0.3217 | 0.0083 | 0.67 | 2614 | 18 | 1784 | 40 | 2207 | 20 | 68 |
| 69-30c | 0.1123 | 313.0 | 90.6 | 54.1 | 0.29 | 16650 | 0.1151 | 0.0025 | 2.333 | 0.060 | 0.1466 | 0.0038 | 0.71 | 1893 | 24 | 877 | 21 | 1209 | 18 | 46 |
| 69-34 | 0.0596 | 271.4 | 58.9 | 80.1 | 0.22 | 31400 | 0.1697 | 0.0030 | 7.530 | 0.240 | 0.3154 | 0.0095 | 0.82 | 2564 | 19 | 1748 | 46 | 2149 | 29 | 68 |
| 69-35 | 0.0757 | 439.0 | 74.2 | 70.2 | 0.17 | 24700 | 0.1417 | 0.0024 | 3.114 | 0.064 | 0.1562 | 0.0033 | 0.70 | 2266 | 19 | 932 | 18 | 1430 | 15 | 41 |
| 69-36 | 0.0711 | 344.0 | 51.2 | 57.8 | 0.15 | 26300 | 0.1604 | 0.0028 | 5.160 | 0.170 | 0.2267 | 0.0063 | 0.85 | 2473 | 21 | 1311 | 33 | 1810 | 29 | 53 |
| 69-12 | 0.1210 | 373.8 | 18.1 | 30.8 | 0.05 | 15450 | 0.0969 | 0.0019 | 1.539 | 0.035 | 0.1130 | 0.0027 | 0.67 | 1592 | 25 | 688 | 16 | 938 | 14 | 43 |
| 69-3 | 0.1123 | 465.0 | 195.9 | 68.9 | 0.42 | 16650 | 0.0899 | 0.0018 | 1.210 | 0.025 | 0.0962 | 0.0021 | 0.60 | 1438 | 21 | 591 | 12 | 803 | 11 | 41 |
| 69-4c | 0.0997 | 418.0 | 144.2 | 97.8 | 0.34 | 18750 | 0.1200 | 0.0026 | 2.108 | 0.049 | 0.1260 | 0.0027 | 0.53 | 1947 | 25 | 765 | 15 | 1143 | 16 | 39 |
| 69-4b | 0.0804 | 322.0 | 98.0 | 85.3 | 0.30 | 23250 | 0.1465 | 0.0027 | 4.002 | 0.096 | 0.1964 | 0.0045 | 0.71 | 2319 | 18 | 1155 | 24 | 1612 | 18 | 50 |

Amostra28

| Zircão | *f*206 | (μg.g$^{-1}$) | | | | | Razão isotópica | | | | | | | Idade (Ma) | | | | | | Conc |
|---|---|---|---|---|---|---|---|---|---|---|---|---|---|---|---|---|---|---|---|---|
| spot | (%) | U | Th | Pb | Th/U | $^{206}Pb/^{204}Pb$ | $^{207}Pb/^{206}U$ | 2σ | $^{207}Pb/^{235}U$ | 2σ | $^{206}Pb/^{238}U$ | 2σ | Rho | $^{207}Pb/^{206}Pb$ | 2σ | $^{206}Pb/^{238}U$ | 2σ | $^{207}Pb/^{235}U$ | 2σ | (%) |
| 28-1 | 0.09 | 97 | 96 | 139 | 0.99 | 21025 | 0.1845 | 0.0028 | 13.34 | 0.24 | 0.5226 | 0.0098 | 0.66 | 2701 | 16 | 2705 | 42 | 2705 | 17 | 100 |
| 28-3 | 0.14 | 93 | 146 | 76 | 1.56 | 13850 | 0.1560 | 0.0029 | 7.91 | 0.16 | 0.3681 | 0.0073 | 0.59 | 2425 | 20 | 2017 | 35 | 2214 | 18 | 83 |
| 28-5 | 0.15 | 59 | 76 | 108 | 1.28 | 12450 | 0.1808 | 0.0034 | 13.17 | 0.27 | 0.5390 | 0.0120 | 0.59 | 2676 | 19 | 2768 | 49 | 2693 | 19 | 103 |
| 28-6 | 0.04 | 213 | 132 | 189 | 0.62 | 43850 | 0.1776 | 0.0027 | 12.47 | 0.24 | 0.5050 | 0.0110 | 0.72 | 2647 | 16 | 2641 | 46 | 2638 | 18 | 100 |
| 28-7c | 0.17 | 54 | 41 | 60 | 0.76 | 11050 | 0.1846 | 0.0036 | 13.31 | 0.27 | 0.5230 | 0.0110 | 0.55 | 2723 | 21 | 2693 | 48 | 2691 | 19 | 99 |

| | | | | | | | | | | | | | | | | | | | |
|---|---|---|---|---|---|---|---|---|---|---|---|---|---|---|---|---|---|---|---|
| 28-8m | 0.14 | 70 | 107 | 139 | 1.54 | 13460 | 0.1863 | 0.0033 | 12.79 | 0.25 | 0.4950 | 0.0100 | 0.60 | 2729 | 18 | 2586 | 44 | 2655 | 18 | 95 |
| 28-8b | 0.04 | 240 | 174 | 257 | 0.73 | 48550 | 0.1752 | 0.0028 | 12.24 | 0.25 | 0.5040 | 0.0120 | 0.72 | 2619 | 15 | 2621 | 49 | 2618 | 19 | 100 |
| 28-9 | 0.11 | 73 | 59 | 86 | 0.82 | 16460 | 0.1853 | 0.0029 | 14.47 | 0.25 | 0.5630 | 0.0110 | 0.64 | 2720 | 15 | 2869 | 44 | 2780 | 16 | 105 |
| 28-10 | 0.13 | 71 | 65 | 95 | 0.92 | 14425 | 0.1904 | 0.0035 | 13.54 | 0.26 | 0.5120 | 0.0110 | 0.58 | 2775 | 17 | 2665 | 45 | 2710 | 18 | 96 |
| 28-11c | 0.11 | 80 | 66 | 99 | 0.83 | 16550 | 0.1820 | 0.0038 | 12.70 | 0.30 | 0.5110 | 0.0130 | 0.65 | 2688 | 22 | 2652 | 56 | 2649 | 22 | 99 |
| 28-11b | 0.06 | 145 | 122 | 205 | 0.84 | 30300 | 0.1868 | 0.0035 | 13.56 | 0.31 | 0.5250 | 0.0130 | 0.69 | 2732 | 18 | 2716 | 56 | 2713 | 21 | 99 |
| 28-12c | 0.28 | 31 | 45 | 61 | 1.47 | 6595 | 0.1798 | 0.0048 | 12.75 | 0.35 | 0.5110 | 0.0130 | 0.51 | 2666 | 25 | 2655 | 55 | 2650 | 25 | 100 |
| 28-12b | 0.13 | 64 | 61 | 84 | 0.95 | 14085 | 0.1841 | 0.0035 | 13.21 | 0.27 | 0.5200 | 0.0120 | 0.61 | 2715 | 18 | 2689 | 49 | 2691 | 20 | 99 |
| 28-13 | 0.08 | 108 | 120 | 282 | 1.11 | 23950 | 0.2006 | 0.0045 | 15.15 | 0.39 | 0.5530 | 0.0160 | 0.68 | 2844 | 21 | 2830 | 67 | 2827 | 25 | 100 |
| 28-14b | 0.16 | 64 | 34 | 86 | 0.53 | 12050 | 0.1804 | 0.0048 | 12.25 | 0.36 | 0.4870 | 0.0130 | 0.52 | 2663 | 28 | 2555 | 54 | 2616 | 27 | 96 |
| 28-14c | 0.12 | 79 | 95 | 141 | 1.21 | 16000 | 0.1839 | 0.0033 | 13.20 | 0.25 | 0.5210 | 0.0110 | 0.60 | 2708 | 17 | 2691 | 47 | 2693 | 18 | 99 |
| 28-15 | 0.31 | 29 | 40 | 58 | 1.39 | 5965 | 0.1893 | 0.0056 | 13.58 | 0.41 | 0.5320 | 0.0170 | 0.60 | 2757 | 28 | 2728 | 70 | 2718 | 29 | 99 |
| 28-16 | 0.30 | 32 | 28 | 39 | 0.87 | 6210 | 0.1825 | 0.0046 | 12.56 | 0.31 | 0.5090 | 0.0140 | 0.57 | 2692 | 25 | 2644 | 56 | 2647 | 23 | 98 |
| 28-17b | 0.24 | 38 | 33 | 52 | 0.85 | 7680 | 0.1831 | 0.0041 | 13.79 | 0.33 | 0.5470 | 0.0140 | 0.61 | 2711 | 23 | 2794 | 57 | 2724 | 22 | 103 |
| 28-21 | 0.35 | 27 | 30 | 43 | 1.11 | 5310 | 0.1909 | 0.0051 | 13.82 | 0.36 | 0.5340 | 0.0160 | 0.58 | 2773 | 27 | 2729 | 64 | 2724 | 25 | 98 |
| 28-22 | 0.15 | 74 | 63 | 87 | 0.85 | 12350 | 0.1837 | 0.0033 | 11.79 | 0.22 | 0.4639 | 0.0093 | 0.57 | 2706 | 17 | 2446 | 40 | 2584 | 17 | 90 |
| 28-23 | 0.10 | 104 | 84 | 130 | 0.81 | 19050 | 0.1802 | 0.0038 | 12.78 | 0.28 | 0.5080 | 0.0120 | 0.62 | 2681 | 22 | 2661 | 52 | 2662 | 20 | 99 |
| 28-24c | 0.17 | 57 | 44 | 66 | 0.77 | 11200 | 0.1861 | 0.0035 | 13.55 | 0.30 | 0.5230 | 0.0130 | 0.66 | 2737 | 19 | 2712 | 54 | 2712 | 21 | 99 |
| 28-24b | 0.10 | 95 | 58 | 100 | 0.61 | 17900 | 0.1786 | 0.0035 | 12.94 | 0.29 | 0.5170 | 0.0130 | 0.66 | 2653 | 18 | 2670 | 54 | 2666 | 21 | 101 |
| 28-25 | 0.39 | 25 | 34 | 51 | 1.37 | 4780 | 0.1896 | 0.0050 | 13.82 | 0.35 | 0.5320 | 0.0150 | 0.57 | 2758 | 24 | 2726 | 62 | 2722 | 24 | 99 |
| 28-26c | 0.35 | 27 | 17 | 38 | 0.65 | 5295 | 0.1879 | 0.0058 | 13.61 | 0.47 | 0.5240 | 0.0190 | 0.65 | 2743 | 29 | 2713 | 80 | 2719 | 33 | 99 |
| 28-26b | 0.28 | 35 | 14 | 33 | 0.39 | 6665 | 0.1766 | 0.0046 | 12.61 | 0.50 | 0.5090 | 0.0180 | 0.79 | 2648 | 27 | 2620 | 74 | 2616 | 37 | 99 |
| 28-28 | 0.12 | 83 | 87 | 135 | 1.04 | 15600 | 0.1801 | 0.0044 | 13.20 | 0.36 | 0.5230 | 0.0160 | 0.63 | 2692 | 23 | 2698 | 65 | 2698 | 26 | 100 |
| 28-30 | 0.10 | 117 | 138 | 177 | 1.18 | 18400 | 0.1706 | 0.0032 | 9.94 | 0.35 | 0.4050 | 0.0130 | 0.83 | 2597 | 21 | 2171 | 60 | 2388 | 34 | 84 |
| 28-31 | 0.14 | 61 | 56 | 182 | 0.92 | 12900 | 0.2090 | 0.0046 | 16.79 | 0.47 | 0.5730 | 0.0160 | 0.69 | 2918 | 23 | 2909 | 63 | 2904 | 27 | 100 |
| 28-32 | 0.28 | 37 | 31 | 50 | 0.83 | 6710 | 0.1876 | 0.0049 | 13.42 | 0.35 | 0.5030 | 0.0120 | 0.47 | 2715 | 23 | 2617 | 52 | 2674 | 24 | 96 |
| 28-33 | 0.16 | 79 | 81 | 116 | 1.02 | 11755 | 0.1816 | 0.0036 | 10.80 | 0.20 | 0.4213 | 0.0092 | 0.58 | 2687 | 18 | 2251 | 41 | 2499 | 17 | 84 |
| 28-34 | 0.07 | 170 | 99 | 142 | 0.58 | 27700 | 0.1514 | 0.0031 | 10.10 | 0.32 | 0.4600 | 0.0130 | 0.77 | 2385 | 22 | 2430 | 57 | 2420 | 29 | 102 |
| 28-35 | 0.28 | 37 | 38 | 58 | 1.04 | 6710 | 0.1874 | 0.0045 | 13.59 | 0.30 | 0.5240 | 0.0130 | 0.55 | 2737 | 24 | 2705 | 53 | 2706 | 21 | 99 |

Amostra 97A

| Monazita | $f$206 | | Razão isotópica | | | | | | | Idade (Ma) | | | | | | Conc |
|---|---|---|---|---|---|---|---|---|---|---|---|---|---|---|---|---|
| spot | (%) | $^{206}Pb/^{204}Pb$ | $^{207}Pb/^{206}U$ | 2σ | $^{207}Pb/^{235}U$ | 2σ | $^{206}Pb/^{238}U$ | 2σ | Rho | $^{207}Pb/^{206}Pb$ | 2σ | $^{206}Pb/^{238}U$ | 2σ | $^{207}Pb/^{235}U$ | 2σ | (%) |
| Mn-1 | 0.03 | 71450 | 0.1232 | 0.07 | 6.72 | 0.15 | 0.39 | 0.01 | 0.65 | 2026 | 21 | 2118 | 48 | 2070 | 20 | 105 |
| Mn-2 | 0.02 | 85400 | 0.1231 | 0.06 | 6.67 | 0.16 | 0.39 | 0.01 | 0.62 | 2025 | 22 | 2101 | 45 | 2066 | 21 | 104 |

| | | | | | | | | | | | | | | | | |
|---|---|---|---|---|---|---|---|---|---|---|---|---|---|---|---|---|
| Mn-3 | 0.03 | 68550 | 0.1231 | 0.08 | 6.44 | 0.16 | 0.38 | 0.01 | 0.58 | 2014 | 24 | 2077 | 51 | 2033 | 22 | 103 |
| Mn-4 | 0.04 | 48750 | 0.1245 | 0.07 | 6.70 | 0.15 | 0.38 | 0.01 | 0.55 | 2039 | 25 | 2084 | 45 | 2066 | 20 | 102 |
| Mn-5 | 0.05 | 38550 | 0.1256 | 0.07 | 6.81 | 0.19 | 0.39 | 0.01 | 0.47 | 2077 | 28 | 2120 | 50 | 2084 | 24 | 102 |
| Mn-6 | 0.03 | 59050 | 0.1238 | 0.08 | 6.51 | 0.16 | 0.38 | 0.01 | 0.56 | 2023 | 26 | 2057 | 51 | 2050 | 21 | 102 |
| Mn-7 | 0.03 | 60100 | 0.1265 | 0.08 | 6.54 | 0.16 | 0.38 | 0.01 | 0.62 | 2063 | 26 | 2077 | 53 | 2054 | 21 | 101 |
| Mn-8 | 0.03 | 72400 | 0.1271 | 0.06 | 6.61 | 0.14 | 0.38 | 0.01 | 0.62 | 2079 | 21 | 2090 | 43 | 2063 | 19 | 101 |
| Mn-9 | 0.03 | 64700 | 0.1269 | 0.11 | 6.52 | 0.22 | 0.38 | 0.02 | 0.60 | 2059 | 32 | 2069 | 74 | 2038 | 30 | 100 |
| Mn-10 | 0.04 | 52150 | 0.1256 | 0.07 | 6.66 | 0.15 | 0.38 | 0.01 | 0.58 | 2057 | 23 | 2064 | 48 | 2066 | 20 | 100 |
| Mn-11 | 0.03 | 53950 | 0.1263 | 0.06 | 6.56 | 0.15 | 0.38 | 0.01 | 0.61 | 2062 | 21 | 2067 | 42 | 2051 | 20 | 100 |
| Mn-12 | 0.02 | 89250 | 0.1283 | 0.07 | 6.79 | 0.14 | 0.38 | 0.01 | 0.60 | 2082 | 24 | 2078 | 48 | 2085 | 19 | 100 |
| Mn-13 | 0.03 | 63550 | 0.1283 | 0.06 | 6.62 | 0.14 | 0.38 | 0.01 | 0.57 | 2087 | 22 | 2074 | 43 | 2061 | 19 | 99 |
| Mn-14 | 0.03 | 61200 | 0.1258 | 0.07 | 6.44 | 0.15 | 0.37 | 0.01 | 0.65 | 2042 | 22 | 2014 | 44 | 2032 | 20 | 99 |
| Mn-15 | 0.03 | 69500 | 0.1279 | 0.08 | 6.51 | 0.18 | 0.38 | 0.01 | 0.66 | 2088 | 27 | 2059 | 57 | 2035 | 25 | 99 |
| Mn-16 | 0.02 | 80800 | 0.1299 | 0.06 | 6.69 | 0.16 | 0.38 | 0.01 | 0.61 | 2103 | 23 | 2072 | 42 | 2072 | 21 | 99 |
| Mn-17 | 0.03 | 66500 | 0.1292 | 0.07 | 6.63 | 0.16 | 0.37 | 0.01 | 0.58 | 2092 | 22 | 2055 | 44 | 2057 | 21 | 98 |
| Mn-18 | 0.02 | 87850 | 0.1316 | 0.06 | 6.70 | 0.15 | 0.38 | 0.01 | 0.64 | 2128 | 19 | 2087 | 43 | 2073 | 19 | 98 |
| Mn-19 | 0.03 | 64050 | 0.1264 | 0.09 | 6.52 | 0.17 | 0.38 | 0.01 | 0.72 | 2075 | 25 | 2035 | 60 | 2040 | 23 | 98 |
| Mn-20 | 0.03 | 53750 | 0.1309 | 0.09 | 6.79 | 0.17 | 0.37 | 0.01 | 0.59 | 2096 | 21 | 2054 | 59 | 2085 | 22 | 98 |
| Mn-21 | 0.03 | 61050 | 0.128 | 0.06 | 6.63 | 0.14 | 0.38 | 0.01 | 0.62 | 2105 | 21 | 2054 | 44 | 2061 | 19 | 98 |
| Mn-22 | 0.02 | 79350 | 0.1278 | 0.07 | 6.55 | 0.15 | 0.37 | 0.01 | 0.61 | 2090 | 21 | 2034 | 46 | 2046 | 21 | 97 |
| Mn-23 | 0.04 | 50950 | 0.1271 | 0.08 | 6.67 | 0.17 | 0.37 | 0.01 | 0.67 | 2090 | 22 | 2030 | 50 | 2070 | 22 | 97 |
| Mn-24 | 0.03 | 60100 | 0.1281 | 0.07 | 6.49 | 0.15 | 0.37 | 0.01 | 0.64 | 2103 | 22 | 2020 | 48 | 2044 | 21 | 96 |
| Mn-25 | 0.03 | 71950 | 0.129 | 0.11 | 6.35 | 0.22 | 0.37 | 0.02 | 0.66 | 2091 | 33 | 1998 | 68 | 2011 | 32 | 96 |
| Mn-26 | 0.03 | 72800 | 0.1274 | 0.09 | 6.40 | 0.20 | 0.36 | 0.01 | 0.66 | 2074 | 26 | 1976 | 56 | 2027 | 27 | 95 |
| Mn-27 | 0.03 | 58000 | 0.129 | 0.08 | 6.48 | 0.16 | 0.37 | 0.01 | 0.64 | 2097 | 21 | 1997 | 49 | 2041 | 22 | 95 |
| Mn-28 | 0.03 | 68000 | 0.1302 | 0.07 | 6.54 | 0.15 | 0.37 | 0.01 | 0.61 | 2119 | 19 | 2002 | 41 | 2047 | 20 | 94 |
| Mn-29 | 0.04 | 50300 | 0.1332 | 0.08 | 6.70 | 0.15 | 0.37 | 0.01 | 0.60 | 2153 | 26 | 2020 | 50 | 2072 | 21 | 94 |
| Mn-30 | 0.03 | 55050 | 0.132 | 0.08 | 6.69 | 0.16 | 0.37 | 0.01 | 0.60 | 2159 | 23 | 2020 | 49 | 2068 | 21 | 94 |